UNIVERSITÀ DEGLI STUDI DI MILANO

FACOLTÀ DI SCIENZE E TECNOLOGIE

Department of Chemistry

PhD Course in Chemistry – XXXII Cycle

HYBRID NANOMATERIALS in ELECTROCHEMISTRY and ELECTROANALYSIS: when the whole is greater than the sum

PhD Candidate: Anna TESTOLIN

Tutor: Prof. Luigi FALCIOLA

PhD School Coordinator: Prof. Emanuela LICANDRO

A.A. 2018-2019

"If I have seen further it is by standing on the shoulders of giants"

(Isaac Newton)

Table of Contents

1.

Extended Abstract

The scientific interest in nanotechnology and nanomaterials can be traced back to about sixty years ago (1959, in the occasion of the Annual Meeting of the American Physical Society), when a new approach for manipulating and controlling matter on a miniaturized scale rose. The subsequent huge increment in the involvement of nanomaterials in science is due to their peculiar properties: increased surface-to-volume ratio, quantum size effects, new physical and optical features, high active surface area, enhanced or different mass transport, improved selectivity and so on. All these characteristics make nanomaterials extremely suitable for a wide range of applications, from energetics to catalysis and sensing.

In the last few decades, apart from "single-component" nanomaterials, the use of "hybrids" (made of two or more components) is growing. This is connected to the fact that, since in a composite the instauration of synergistic effects is confined to the interfacial region of the mixed materials, in nanomaterials, because of the small size, these effects may become a dominant factor. The result is the instauration of new and unexpected properties (often sought and interesting) that are not only the sum of the individual contributions. Considering all these facts, hybrids are extremely good candidates to be applied in several fields.

In this PhD Thesis Project, hybrid nanomaterials are the subject of a deep electrochemical study with the final purpose of optimizing electroanalytical sensors for organic, inorganic and biological analytes, also at trace levels. The single components of the hybrids here presented are *metals, graphene* and *graphene-derivatives*, and *semiconductors.*

In more detail, *metal-metal* hybrids are gold-based bimetallic systems (AuPt, AuPd and AuAg), in different conformations (alloy or core-shell) that are characterized combining electrochemical results with those obtained by more conventional techniques (TEM, EXAFS). The use of electrochemistry for understanding the real structure of the hybrids is presented as a low-cost, easy to use and fast alternative technique, which allows also following in time the conformational evolution of selected bimetallic systems. The effect played also by

the possible presence of a support onto the electrochemical and electrocatalytic properties of the nanoparticles is considered, showing promising results in terms of selectivity of the materials. Moreover, the enhanced performances of the bimetallics instead of the monometallics in the detection of target analytes (cinnamyl alcohol and aldehyde in the case of AuPd systems and organic halides for what concern AuAg) is verified.

The interest is then moved to *metal-semiconductor* hybrids, particularly to Au/TiO_2 based devices, in which the presence of gold nanoparticles is exploited for the electroanalytical detection of a contaminant of emerging concern (diclofenac) while the presence of TiO_2 is essential in order to avoid problem of fouling and passivation of the electrode. The photo-renewability of the electrode is verified, allowing to restore the starting performances of the device even after the electroanalytical use. The instauration or not of a real interface between gold and TiO_2 is explored, analysing electrochemical results gained by Cyclic Voltammetry (CV) and Electrochemical Impedance Spectroscopy (EIS).

With regard to *graphene-metal* hybrids, two materials made of Reduced Graphene Oxide (RGO) decorated with gold nanoparticles are involved for the detection of both organic and inorganic molecules (dopamine and arsenic). In both cases, strong enhanced properties are highlighted in the use of the hybrid with respect to its single components, with low detection limits and high sensitivities reached.

A different material, also based on RGO platform, is used for the construction of a biosensor, labelled with gold nanoparticles, for the electroanalytical detection of the antigen H-IgG. In this case, the possibility to use paper-based electrodes is of particular interest for the construction of low-cost and user-friendly (in terms of facility of use) sensors.

Finally, *graphene-semiconductor* hybrids are analysed, starting from graphene/TiO_2 materials. Different electrodes modified with several layers of graphene (from one to five) decorated with titanium dioxide nanocrystals are

electrochemically characterized and differences in the electrochemical response and activity are highlighted passing from a graphene to a graphitic-like structure. The presence of TiO_2 nanocrystals is verified to act as a coverage of the defective site, changing again the reactivity of the device toward selected analytes. Moreover, the photo-renewability of the sensors is again exploited.

Another hybrid of this group is based on RGO and PbS nanocrystals, in which the light harvesting properties of the semiconducting particles are combined with the high conductivity of graphene in order to create a promising device to be applied from electronics to sensing fields. The electronic communication between the two materials and the hole transfer from photo-excited PbS nanocrystals to graphene is verified also allowing to claim the presence of an interface between the two components of the hybrid.

In conclusion, several hybrid materials are here investigated starting from their physico-chemical and electrochemical characterizations. Their application as electroanalytical sensors is explored, evidencing the presence of synergistic effects in the hybrid with respect to the single components, assuring enhanced properties and superior performances.

2.

Introduction

2.1 Nanotechnology and Nanomaterials in Electroanalysis

What is "nano"?

The advent of nanotechnology can be dated back to the famous lecture held by Richard Feynman, on the 29th December 1959, when, during the annual meeting of the American Physical Society, he told: "*There's plenty of room at the bottom*".[1] With this sentence, Feynman paved the way towards a new approach for manipulating and controlling properties about matter, on a miniaturized (atomic and molecular) scale. In general, he catalysed the attention to the nanotechnology field.

A more precise definition of "nanomaterial" was given later, from the European Commission on 18th October 2011. A nanomaterial was then named as a "*natural, incidental or manufactured material containing particles, in an unbound state or as an aggregate or as an agglomerate and where, for 50% or more of the particles in the number size distribution, one or more external dimensions is in the size range 1 nm – 100 nm*". So, it is possible to distinguish nanoparticles (zero dimensional), nanowires (one-dimensional) and nanosheets (two-dimensional). Lots of biological entities, like proteins, nucleic acids and viruses fall into the nanosized scale, but also a plethora of synthetic materials of various chemical compositions, from pure chemical elements (metals, carbon, silicon) to inorganic (metal oxides) and organic (polymers) compounds.

The application in science of nanomaterials are the most various ones, from sensing to catalysis, thanks to all their favourable features and above all, to the increased surface-to-volume ratio.

In the specific field of electrochemistry and electroanalysis, which are the main topic of this PhD Thesis, this peculiarity reflects in new quanto-mechanical (*quantum size effect*), physical and optical effects. Moreover, nanomaterials possess an enhanced mass transport (which facilitates the study of faster electrochemical processes), high

active surface area, improved selectivity and reduced cost. They are also characterized by a high signal-to-noise ratio and by an enhanced (or in general changed) diffusion mechanism. All these properties allow to provide control over the local microenvironment.[2,3] Considering all these facts, nanomaterials are good candidates to be applied in electroanalytical sensors.

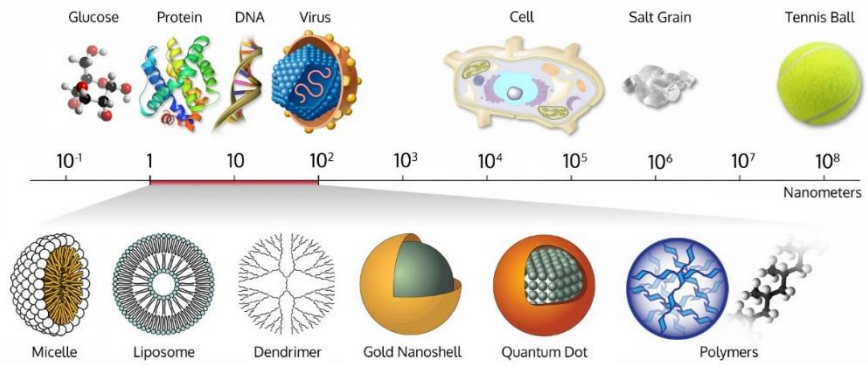

Figure 1.1: Different kind of natural and synthetic materials related to their size, with particular attention to the range of nanosized ones.

Diffusion Mechanisms from Macro to Nano-electrodes

The target of this PhD Thesis is the study of electroanalytical sensors with applications in liquids, using voltammetric experiments in particular. As a consequence, in this Paragraph, a general introduction on the phenomenon of diffusion in liquids will be developed, with a particular attention on the effect that the use of nanomaterials has in this field, starting from the related mathematical equations.

Diffusion phenomena were firstly been treated and studied in depth by the pioneering work of Adolf Fick, more than 150 years ago.[4] Diffusion is a phenomenon occurring when a concentration gradient is present. In more details, diffusion of a particular species toward an object is established from a zone of higher concentration to a one of lower concentration. It is possible to talk about a *diffusive flux*, at any point, described by Fick's first Law (**Eq. 1.1**):

$$j = -D\frac{\partial c}{\partial x} \tag{1.1}$$

where j is the flux (in mol cm^{-2} s^{-1}), describing the number of moles that pass through unit area in unit time, $\frac{\partial c}{\partial x}$ is the local concentration gradient at the x point and D (in cm^2 s^{-1}) is the *diffusion coefficient*, typical of the molecule that is under investigation and that it is diffusing in the environment. The minus sign is implying that the flux is on the opposite direction than the concentration gradient. It is worthwhile noticing that in a common voltammetric experiment, where the electrolyte solution is not particularly viscous, like some ionic liquids,[5] the values of D are commonly in the range of 10^{-6} to 10^{-5} cm^2 s^{-1}, and they are dependent from the temperature, often following an Arrhenius-type relationship. Moreover, following **Eq. 1.1**, it is evident that the flux is driven only by concentration differences in solution and no gradients of electrical potential is taken into consideration. This is correct in case of uncharged diffusing species, but in the case of ions (charged species), the electrical potential has a significant effect. By the way, it is common practice in a voltammetric experiment to work with sufficient quantities and concentrations of background electrolytes (*supporting electrolytes*) that eliminate the presence of significant electric fields in the solution except the one very close to the electrode surface. In this way, it is possible to assume that, in a conventional experiment, the materials in solution are brought towards the electrode only by diffusion (in a quiescent environment, at constant temperature, also the *convection* mechanism is suppressed). But how is the concentration changing with time? The answer to this question is given by the Fick's second law (**Eq. 1.2**), in one dimension:

$$\frac{\partial c}{\partial t} = D\frac{d^2c}{dx^2} \tag{1.2}.$$

Now that the equation for the flux are given, it is interesting to introduce them in a practical voltammetric experiment, where, in general, a potential is applied to an

electrode and the resulting current is measured, as a function of time. In more details, it follows the **Eq. 1.3**

$$I = nFAj \tag{1.3}$$

where *n* is the number of electrons that are involved in the electrode reaction and *F* is the Faraday's constant, *A* is the electrode area and finally *j* is the flux. By substituting the flux as expressed by the Fick's First law, it follows the *Cottrell Equation* (**Eq. 1.4**):

$$I = \frac{nFA\sqrt{D}c^*}{\sqrt{\pi t}} \tag{1.4}$$

from which it is easily to understand that the current of a reaction at an electrode, resulting from a potential step, decay to zero with an inversely proportional dependence to the square root of time. This equation is valid in the case of a planar macro-electrode. When dealing with spherical or hemispherical electrode, the equation that regulates the flux toward the surface is the following (**Eq. 1.5**), where r_e represents the radius of the electrode:

$$j = Dc^* \left[\frac{1}{\sqrt{D\pi t}} + \frac{1}{r_e}\right] \tag{1.5}.$$

In this case, it is evident that the flux, and so the current, are dependent both from the time and from the radius of the electrode (r_e). The first term is the "time-dependent" term, while the second one represents the "steady-state" condition, in which effectively the current is independent from the time and stay fixed at a certain value. In a "short-time" limit, when $\sqrt{D\pi t} \ll r_e$, the second term of **Eq. 1.5** is negligible and the flux is now descripted by **Eq. 1.6**, while in the "long-time" limit, when $\sqrt{D\pi t} \gg r_e$, the flux is descripted by **Eq. 1.7**:

$$j = \frac{c^* \sqrt{D}}{\sqrt{\pi t}} \tag{1.6}$$

$$j = D \frac{c^*}{r_e} \tag{1.7}$$

So, in the first case, an almost *linear diffusion* (or *planar*) is expected, meaning that the current lines are behaving like they are perpendicular to the surface of the electrode and parallel one to the other. In the second case, on the contrary, *convergent diffusion* (or *radial*) is established, where the current lines come to the electrode from every direction and they are not parallel one to the other (see **Figure 2.1**).

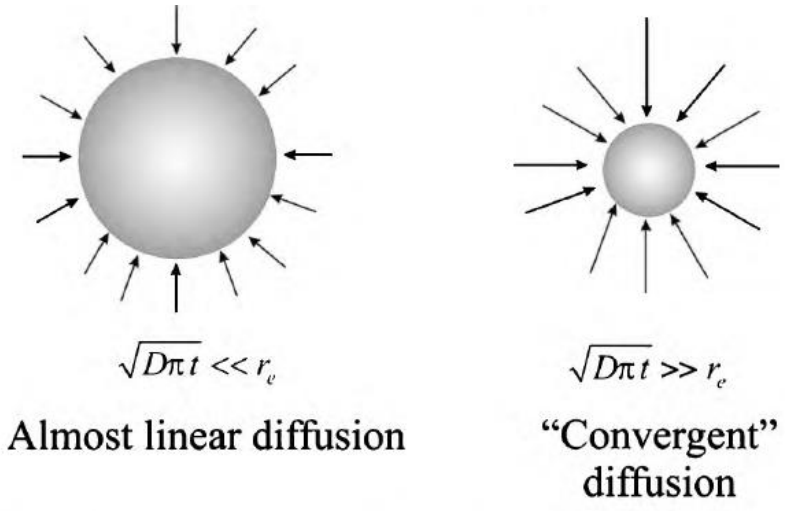

Figure 2.1: Schematical representation of two different diffusion mechanisms at a spherical electrode.[6]

In the "long time" limit, the diffusion layer thickness is high and it is higher than the time-scale of the performed voltammetry. In this case, a steady-state current is normally reached, resulting in a step-shaped voltammetric signal. **Figure 2.2** shows the relationship between the size of the electrode, with respect to the diffusion layer thickness, and the contribution of convergent diffusion to the observed voltammetry. It is evident how the convergent diffusion is responsible for a different shape of the voltammetric signal, but also for an enhancement of the current

intensity values. The magnitude of the flux under steady-state conditions is proportional to the size of the electrode: the smaller the electrode, the greater the current density and the faster the material diffuses to (and from) the electrode surface.

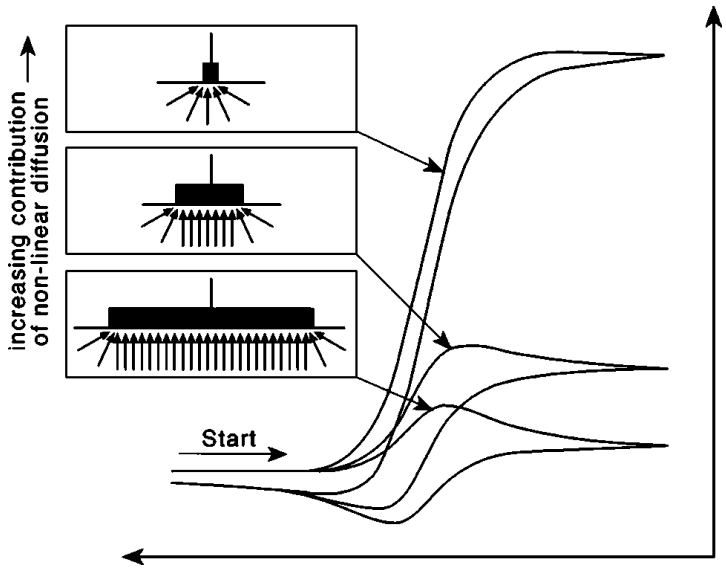

Figure 2.2: Schematic diagram showing the relationship between the size of the electrode (with respect to the diffusion layer thickness) and the contribution of convergent diffusion to the observed voltammetry.[6]

It is almost clear now that it is possible to have different diffusional mechanisms by changing the experimental conditions and the type of the electrode. In this context, the differences in the type of the electrode platforms, intended in their size and shape, is of particular interest. In fact, a macro electrode is completely different from a micro or a nano-electrode, starting from the diffusional mechanism that are involved at their surfaces. In more details, smaller electrodes lead to:

a) *Non planar diffusion*: microelectrodes favour faster rates of mass transport, leading to current lines that approach the electrode in a radial way and from every direction, with a diffusion layer thickness higher than the size of the electrodes itself.

b) *Reduced Capacitance*: The capacitance of the double layer is related to the electroactive area of the electrode. The reduction of the electrode area reduces the capacitance.

c) *Reduced Ohmic Drop*: The ohmic drop is proportional to the total current passed. Dealing with smaller electrodes, this current decreases.

The advantages in the use of microelectrodes is again enhanced if more than one electrode is involved in the experiment. In this case, it is created a so-called *microelectrodes array*. This definition refers to systems in which hundreds or even thousands of microdisc electrode wires are in parallel. They can be produced in several ways, from lithography to random assembly. The peculiarity of these systems is that they can provide a voltammetric response of similar magnitude to their macro counterparts, but with a considerably less background capacitive current.[6] For what concerns the redox reaction of a probe toward such electrodes, different situations can be imagined. In fact, in the case of an array of microdisc electrodes separated by an insulating material, individual diffusion layers will develop and growth during the experiment. Depending on the size and the reciprocal distance between the microelectrodes, the diffusive layers will overlap or not in different ways, resulting in different diffusional mechanisms of the redox reaction. A schematic representation is shown in **Figure 2.3**. In the first category (**Figure 2.3, 1**), the microelectrodes are so far apart that their diffusion layers do not interact and they are fully independent, since the time-scale of the voltammetry is short (fast scan rate). In this case, a planar diffusion to the electrode is expected, with a peak-shaped peak. In the second case **(Figure 2.3, 2**), the electrodes are sufficiently spaced like the situation 1, but now the time-scale is longer and the diffusional mechanism is radial (convergent), resulting in a step-shaped curve. In the third case (**Figure 2.3, 3**), the microelectrodes are closer and the diffusional layers are partially overlapped. This situation is a mixed one, with voltammetric properties that are not perfectly categorized. In the last category (**Figure 2.3, 4**), the microelectrodes are so close that there is a complete overlapping of the diffusional fields leading to a situation in which the array is

behaving like a macroelectrode (peak-shaped curves and peak current scaling with the square root of the voltage scan rate).

Considering all these facts on the diffusional mechanism and the size of the electrodes, it is possible to explain how the current intensity varies in the case of a macroelectrode and in the case of a spherical (or hemispherical) microelectrode.

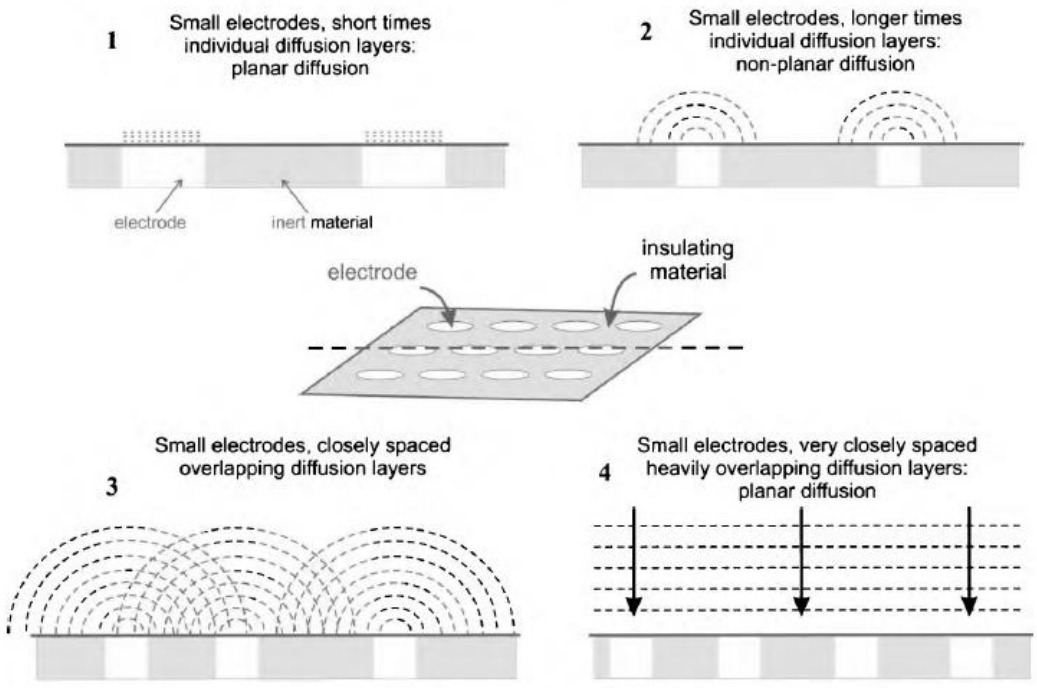

Figure 1.3: Different diffusion profile that can be present at an array of microelectrodes.[6]

For a macro-electrode, the current is governed by the Randles-Sevcik equation (Eq. 1.8):

$$I_{peak} = 2.69 \cdot 10^{-5}\, n^{3/2} D^{1/2} c_{bulk} v^{1/2} A \qquad (1.8)$$

where I_{peak} is the peak current, n is the number of electrons transferred in the rate determining step, D is the diffusion coefficient, C_{bulk} is the bulk concentration of active species in solution, v is the scan rate and A is the electrode surface area.

In the case of a hemispherical electrode, the limiting current (steady state) is explained by the equation 1.9:

$$I_{lim} = 2\pi nF c_{bulk} Dr \quad (1.9)$$

where *r* is the radius of the electrode. In the case of an array of microelectrodes, where actually their shape is a hemispherical one, it is considered that one electrode should be distant for at least a value equal to 10*r* to its nearest neighbour to be diffusionally independent. In this way, the total current for a particular area *A* of the nanoparticle array is:

$$I_{total} = I_{\lim} A(10r)^{-2} \quad (1.10)$$

Taking typical values for the parameters of n=1, D=1 10^{-5} cm^2 s^{-1}, C_{bulk}=1 10^{-6} mol cm^{-3}, v=1 10^{-2} V s^{-1} and A=1 cm^2, the peak current for different electrodes can be estimated as follow:

Macroelectrode: $\boldsymbol{I = 85 * 10^{-6}}$ **A**

Nanoparticles Array (*r* = 1 μm, 10 *r* spacing): $\boldsymbol{I = 6\ 10^{-4}}$ **A**

(*r* = 100 nm, 10 *r* spacing): $\boldsymbol{I = 6\ 10^{-3}}$ **A**

This calculation illustrates a potentially great advantage of reducing the size of the nanoparticles in an array in theory.[2,3]

2.2 Hybrid Nanomaterials

According to IUPAC Gold Book, an "Hybrid" is defined as a "*material composed of an intimate mixture of inorganic components, organic components, or both types of component. The components usually interpenetrate on scales of less than 1 μm*".

Nowadays, hybrid materials chemistry represents a common topic of the scientific domain for chemists. For this reason, it is obviously impacting numerous societal and industrial demands. Hybrid materials chemistry represents an inherent interdisciplinary field of research and development, since it links a huge variety of fields and applications.[7]

Starting from macroscopic structures, different materials can be integrated together to provide systems with tailored properties from the disparate components. In such systems, each component usually retains its original properties while modifications are confined to the interfacial region, which is much smaller than the entire system. In hybrid nanomaterials, defined as a class of materials made of two or more components in which at least one of them owe a dimension in the nanoscale regime, new properties can be attained. In fact, by combining several materials on the same nano-system, due to the small size, the effect of synergistic properties of the separate components may become a dominant factor.[8] In general, for a hybrid, the physico-chemical properties can be tuned and they are not only the sum of the individual contributions of both materials.

The single components of a hybrid nanostructures can be chosen from a wide range of materials like metals, metal oxides, metal chalcogenides, polymers, carbonaceous materials and so on.[9] They can be synthesized in several ways and with the most various size, shape and compositions. In the case of metal-metal hybrids, normally in the size and shape of nanoparticles, it is possible to found alloy, core-shell, Janus-type nanocomposites, synthesized via bottom-up or top-down approaches[10] (see for more details **Chapter 3**). Regarding other types of materials, among the most diffuse hybrids, the organic-inorganic nanomaterials, defined as nanocomposites with

intimately mixed organic and inorganic components, can be found. The control of the physico-chemical nature and the extension of hybrid organic/inorganic interfaces is of primary importance since it regulates the material's transparency, chemical homogeneity, and stability.[7,11] The inorganic part is normally composed by metal oxides and metal–oxo polymers, usually produced as amorphous networks, nanocrystalline networks or metal–oxo clusters via condensation of metal organic precursors or metallic salts. Organic components can be introduced into an inorganic network in two different ways, as network modifiers (molecules) or network formers (macromolecules).[7]

Another big component of the organic/inorganic materials are the colloidal heteronanocrystals, made of inorganic nanoparticles coated with an organic ligand.[12–15] One of the essential feature of these last materials is their nanoscale dimensions, which generate size effects to be exploited in order to engineer the material properties. Spatial confinement effects become increasingly important as the dimensions of a nanocrystal decrease below a certain critical limit, leading to size- and shape-dependent electronic structure.[12]

2.3 Focus of the Thesis

Considering all the above mentioned features, the great advantages in the use of nanomaterials in electrochemistry is clear and is the reason of the interest of many scientists in such a field. The number of works about nanomaterial-based electrodes are growing drastically over time and the potentialities of these devices are dramatically expanding. The applications are the most various ones, from sensing to catalysis, electrocatalysis and energetics. Apart from simple nanomaterials, also nano-hybrids are growing in interest over the last decades and their application is reasonably connected to the enhancement of all the properties of the starting

components in the final composite. Among all the applications, electrochemistry and electroanalysis play a crucial role.

The focus of this PhD thesis will be the sensors field. Different hybrid nanomaterials, based essentially on different combinations between metals, graphene and semiconductor materials will be studied in depth, starting from the single components and then to their combination in the final devices. In more details, Metal-Metal and Metal-Semiconductor Hybrids will be the subject of Chapter 3 and 4, Graphene-Metal and Graphene-Semiconductor Hybrids the ones investigated in Chapter 5 and 6, respectively. The enhanced performances of the hybrids will be highlighted, thanks to the application of these materials in the electroanalytical detection of different molecules, from inorganic, to organic and biomolecules.

Bibliography

(1) Feynman, R. P. Caltech Engineering and Science. *23:5*. 1960, pp 22–36.

(2) Welch, C. M.; Compton, R. G. The Use of Nanoparticles in Electroanalysis: A Review. *Anal. Bioanal. Chem.* **2006**, *384*, 601–619.

(3) Campbell, F. W.; Compton, R. G. The Use of Nanoparticles in Electroanalysis: An Updated Review. *Anal. Bioanal. Chem.* **2010**, *396* (1), 241–259.

(4) Fick, A. Uber Diffusion. *Poggendorff's Annel. Phys.* **1855**, *94*, 59.

(5) Buzzeo, M. C.; Evans, R. G.; Compton, R. G. Non-Haloaluminate Room-Temperature Ionic Liquids in Electrochemistry - A Review. *ChemPhysChem* **2004**, *5* (8), 1106–1120.

(6) Compton, R. G.; Banks, C. E. *Understanding Voltammetry*; Imperial College Press, London, 2001.

(7) Sanchez, C.; Belleville, P.; Popalld, M.; Lionel, N. Applications of Advanced Hybrid Organic–Inorganic Nanomaterials: From Laboratory to Market. *Chem. Soc. Rev.* **2011**, *40* (2), 588–595.

(8) Costi, R.; Saunders, A. E.; Banin, U. Colloidal Hybrid Nanostructures: A New Type of Functional Materials. *Angew. Chemie - Int. Ed.* **2010**, *49* (29), 4878–4897.

(9) Huang, X.; Tan, C.; Yin, Z.; Zhang, H. 25th Anniversary Article: Hybrid Nanostructures Based on Two-Dimensional Nanomaterials. *Adv. Mater.* **2014**, *26* (14), 2185–2203.

(10) Toshima, N.; Yonezawa, T. Bimetallic Nanoparticles: Novel Materials for Chemical and Physical Applications. **1998**, 1179–1201.

(11) Mann, S. Self-Assembly and Transformation of Hybrid Nano-Objects and Nanostructures under Equilibrium and Non-Equilibrium Conditions. *Nat. Mater.* **2009**, *8* (10), 781–792.

(12) Donegá, C. D. M. Synthesis and Properties of Colloidal Heteronanocrystals. *Chem. Soc. Rev.* **2011**, *40* (3), 1512–1546.

(13) Ingrosso, C.; Bianco, G. V.; Corricelli, M.; Comparelli, R.; Altamura, D.; Agostiano, A.; Striccoli, M.; Losurdo, M.; Curri, M. L.; Bruno, G. Photoactive Hybrid Material Based on Pyrene Functionalized PbS Nanocrystals Decorating CVD Monolayer Graphene. *ACS Appl. Mater. Interfaces* **2015**, *7* (7), 4151–4159.

(14) Corricelli, M.; Altamura, D.; De Caro, L.; Guagliardi, A.; Falqui, A.; Genovese, A.; Agostiano, A.; Giannini, C.; Striccoli, M.; Curri, M. L. Self-Organization of Mono- and Bi-Modal PbS Nanocrystal Populations in Superlattices. *CrystEngComm* **2011**, *13* (12), 3988–3997.

(15) Ingrosso, C.; Corricelli, M.; Bettazzi, F.; Konstantinidou, E.; Bianco, G. V.; Depalo, N.; Striccoli, M.; Agostiano, A.; Curri, M. L.; Palchetti, I. Au Nanoparticle: In Situ Decorated RGO Nanocomposites for Highly Sensitive Electrochemical Genosensors. *J. Mater. Chem. B* **2019**, *7* (5), 768–777.

3.

Metal-Metal Hybrids

Introduction

Monometallic vs Bimetallic Nanoparticles: Highlights

As already mentioned in the General Introduction (see **Chapter 2**), what is named "nano" is intended as a material of which a single unit is sized, in at least one dimension, between 1 and 100 nm (nanometer = 10^{-9} m). This feature reflects in a plethora of peculiar properties of nanomaterials, above all, the increased surface-to-volume ratio and quantum-size effects.[1] Focusing the attention on metal nanoparticles, it is important to underline the fact that they possess much larger surface area than the correspondent bulk materials. This evidence has led to widespread the applications of metal nanoparticles in a lot of field, from catalysis to sensing. Among them, electrochemistry, electrocatalysis and electroanalysis, which are the main areas of this PhD Thesis, have seen a huge evolution in the use of metal nanoparticles over the last decades. From an electrochemical point of view, it is important to highlight, among the unique properties of nanoparticles, the enhanced mass transport (which facilitates the study of faster electrochemical processes), the high surface area and the improved signal-to noise ratio. Moreover, nanosized electrode materials possess an enhanced (or in general changed) diffusion mechanism and they provide control over the local microenvironment.[2,3] Apart from monometallics, also bimetallic particles have attracted more and more interest from both the scientific and technological point of view. Bimetallic nanomaterials are composed by two metal elements and, thanks to the instauration of synergistic effects, they possess different and often enhanced performances than the correspondent monometallic counterparts, as reasonably expected when dealing with hybrid materials.[4]

Monometallic Nanoparticles: Preparation Methods

In general, the preparation methods of metal nanoparticles can be divided into two big families: *physical* and *chemical* techniques. The former includes evaporation and laser ablation methods; they can be defined more generally as "*top-down*" approaches, since they involve the subdivision of a bulk material into particles. The latter, "*bottom-up*" approaches, generally involves a first step of chemical reduction of an ion into a zero-valent metal followed by a particle-growth process. These methods can be classified as general chemical, sonochemical, photochemical and electrochemical ones. The main advantage of the chemical methods, apart of being more suitable for mass production, resides in the possibility to control the primary structure of the material, in terms of size, shape and composition. This aspect is of tremendous impact especially in the preparation of bimetallic particles (see next Paragraph "***Bimetallic Nanoparticles: Preparation Methods***"), because the structure affects the physical and chemical properties of the material itself.[5]

The first synthesis of metal nanoparticles traces back to 1857, when Michael Faraday prepared an Au colloidal solution, in which the dimension of the particles were found to be between 3 and 30 nm, by chemical reduction of an Au(III) precursor.[6] In that synthesis, the reducing agent were citrate ions, which also adsorb on the surface of gold nanoparticles acting as stabilizers. The presence of a stabilizing agent was then found to be crucial to prevent aggregation processes. Consequently, the use of synthetic polymers started to be more and more involved for the preparation of colloidal metal nanoparticles (called *polymer-stabilized* nanoparticles).[7,8] In these procedures, the reduction of ions into a zero-valent metal is then followed by the coordination of the stabilizing polymer to the metal particles. The protective properties of polymers used as ligands also reflect on the final dimensions of the nanoparticles.

Bimetallic Nanoparticles: Preparation Methods

Starting from the huge works of Toshima and others,[5] in the early 90's, a new era for the synthesis of hybrid nanoparticles systems born. The general synthetic procedures for bimetallic nanoparticles can be grouped essentially into two categories: *co-reduction* ("one-pot" synthesis strategy) or *subsequent reduction* ("two-step" synthesis strategy) of the two metals. Less used is the *galvanic replacement* method. Depending on the nature of the reducing agent, on the type of stabilizing agent, on the reaction temperature, time and so on, different bimetallic systems in terms of size, shape, metal loading, morphology and composition can be obtained.[4]

- **Co-Reduction Method**

Co-Reduction methods generally represent a single-step chemical reduction of two different metals (precursors) in a suitable selected solvent. It is a simple strategy, similar to the one involved in the synthesis of monometallic nanoparticles with the difference in the number of metal precursors.[5] This procedure normally favours the rapid nucleation of both metals making it suitable for the synthesis of *nanoalloys* (for more details see next Paragraph "**Bimetallic Nanoparticles: Structure**"). This happens when a strong reducing agent is involved, while the use of a reagent with a softer reducing power favours the delayed nucleation with the consequent formation of the so-called *core-shell* nanoparticles (for more details see next Paragraph "**Bimetallic Nanoparticles: Structure**").[9]

Considering the various synthetic parameters and the possibility to use different protecting agents and reducing reactants, the final combinations of metals in bimetallic structures can be the most various ones. To mention some examples, Toshima and others reported the synthesis of Pd-Pt, Pd-Au,[10,11] Pd-Rh[12] alloyed nanoparticles by the simultaneous reduction of the alcoholic solution of the metal salt precursors in the presence of poly(vinylpyrrolidone). Later, the same author proved the preparation of colloidal dispersion of Pd-Ni bimetallic clusters by the co-reduction of the metal salts with ethylene glycole.[13] Richard and co-workers reported

the preparation of Pt-Ru bimetallic systems using a different type of reducing agent: glucose.[14]

- **Successive (or Two-Step) Reduction Method**

The successive reduction method, as the definition suggests, involves the reduction of a first metal ion, followed by the reduction of a second metal ion. Thanks to the instauration of metal-metal bond, the second metal is normally deposited on the surface of the first one, creating a typical core-shell structure (for more details see next Paragraph "**Bimetallic Nanoparticles: Structure**"). The precise control of the core-shell structure is essential to obtain intended catalytic and electronic properties and represents a crucial issue in this context. In fact, the formation of the shell on the metal core is favoured when the internal metal ions have a high-redox potential. The preformed seed (internal core) should be chemically inert to the metal ions designed to be deposited to form the external shell and this happens if the external atoms possess a lower redox potential than the one of the internal core. Moreover, the external deposited metal atoms should stand on the surface of the metal core without migrating into the phase of the core under the preparation condition. For this reason, the synthesis of a metal core protected by strong organic ligands or protecting agents with strong coordination ability should be avoided. Some strategies were proposed to success in this aspect, for example, an "hydrogen-sacrificial" protective strategy as performed by Toshima et al.[15] In more details, hydrogen is adsorbed onto Pd or Pt surface and split in order to form metal hydrides on the metal surface. The adsorbed hydrogen atoms possess a very strong reducing ability since they have a quite low-redox potential. For this reason, the second metal ions that are added to form the shell are easily reduced by the presence of the adsorbed hydrogens and the bimetallic particles with a core-shell structure is successfully formed.

Bimetallic Nanoparticles: Structure

As already explained by exploring the different synthetic procedures for bimetallic nanoparticles, they can be grouped essentially into two big families, alloy or core-shell. The difference is in how the two metals are mutually distributed in space.

- **Alloy Nanoparticles (Nanoalloys)**

Nanoalloys, as the name suggest, are nanoparticles created by the simultaneous reduction of two metals, in which the starting materials are finally in intimate contact and connected one to the other, in order to form a completely different system. Alloy nanoparticles can be synthesized in a very wide range of combinations and compositions. The final structure, size, composition and degree of segregation or mixing strictly depend on several parameters. In more details, considering an A_nB_m nanoalloy (in which A and B represent the two metals), the degree of segregation/mixing and atomic ordering depends on the following factors:[16]

a) *Relative strenght of the A-A / B-B and A-B bonds*. As it can be easily imagined, if the A-B bond are stronger than the A-A and B-B ones, the mixing is favoured; otherwise, the nanoalloy overcomes segregation processes;

b) *Surface energies* of the two metals A and B. If an element has a low surface energy, it tends to segregate at the surface of the cluster;

c) *Relative A/B atomic sizes*. In this case, the smaller particles tend to stay in the external layer, particularly if they are subjected to compression;

d) *Charge transfer*. The mixing is generally favoured from less to more electronegative elements;

e) *Strength of binding to surface ligands*. If the strength of the bond between the metal and the ligand/support is too strong, the metal can be pulled out towards the surface;

f) *Specific electronic/magnetic effects*. Electronic shell structure or electron spin interaction can be responsible for changed composition, size and of segregation arrangements.

The balance of all these factors, together with the various preparation methods techniques and different experimental conditions, strongly affect the final alloy structures.

Nanoalloys can exist in various type of media such as colloidal solutions, cluster beams, supported on target surfaces or inside pores. By varying the composition, the atomic ordering and the size of cluster, the physico-chemical properties of the nanoalloys can be easily tuned and modified. As a result, the bimetallics often possess special stability or different chemical and catalytic activity that the correspondent components do not have. These enhanced properties, established thanks to the instauration of synergistic effects, represent the main interest in such materials.

- **Core-Shell Nanoparticles**

In this case, differently from nanoalloys, the bimetallic nanoparticles are composed by two metals that are distinct in the whole structure. In more details, the first metal represents the internal core, while the second one creates a shell around the core cluster. These structures are obtained by the "subsequent reduction" method, previously reported. Apart from the most typical spherical core-shell, these systems can be synthesized in several shape, as it can be seen in **Figure 3.1**.[17]

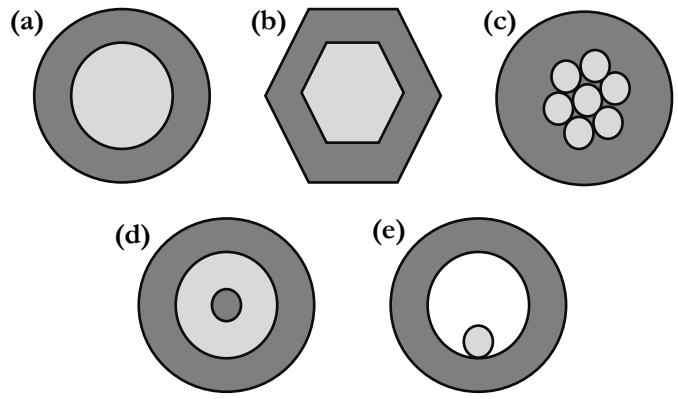

Figure 3.1: Core shell nanoparticles different in shape: **(a)** spherical, **(b)** hexagonal, **(c)** multiple small core materials coated by single shell material, **(d)** matryoshka, **(e)** movable core within hollow shell.

The different properties of core-shell particles are dependent not only to the different size of the components but also on their shape. In fact, the presence of anisotropy effect, due to changes in shape, can reflect in different magnetic and optical behaviour of the nanoparticles and in the presence of plasmon resonance effects. Not only, also catalytic activity and selectivity are shape-dependent properties.[18–20]

Core shell nanoparticles can be synthesized in a plethora of different composition, depending on the nature of the precursors. Bimetallic particles are comprised in the family of "inorganic/inorganic" core shell materials, even if other combinations with organic precursors can be easily found.

The interest in core-shell particles is rapidly growing, since they are highly functional materials with modified properties. In fact, the possibility to have distinct core and shell can be exploited in many ways. For example, because of the external coating, the properties of the internal core, like the reactivity, can be decreased or the thermal stability can be modified, with the result of an overall increase in the particle stability and reactivity. Moreover, the surface elements give to the material their peculiar properties like catalytic and optical activity, but these properties can be tuned by the presence of the internal metal core. In general, the hybrid particles show distinctive properties of the different materials employed together.[9,17]

Bimetallic Nanoparticles: Characterization Techniques

Characterization techniques commonly involved in the study of bimetallic nanoparticles are basically the same that are used for monometallic ones. They can be listed as follow:

a) *Transmission Electron Microscopy* (TEM), which can give the most important information on size, shape and distribution of the nanoparticles. This technique is normally associated to EDX (*Energy Diffraction X-Ray* analysis),

in order to have information on the crystal structure. *High Resolution TEM* (HRTEM), in addition, can give atomic resolution real-space imaging of the particles;[21,22]

b) *UV-Vis Spectroscopy,* which provides general information on the formation and final structure of the bimetallic nanoparticles, thanks to the presence, absence or changed position of the typical plasmonic band associated to selected metals, such as Au, Ag, Cu and Hg.[23–25] In fact, when a metal ion is gradually reduced to a zero-valent nanoparticle, the absorption plasmonic band of the zero valent metal appears, while the one relative to the metal ions disappears. By looking at the metal-to-ligand or ligand-to-metal charge transfer transition and the formation of band structure of nanoparticles, it is possible to follow the actual degree of consumption of the precursors and the formation of the final desired system;[26,27]

c) *X-Ray Diffraction* (XRD), which provides useful information on the crystal phase, lattice constant and average of the particle size in the sample. In the particular case of bimetallic systems, XRD is a precious tool to recognize the presence of an alloyed structure, simply by verifying the appearance of diffraction peaks in position between the ones of the pure constituent metals. In general, from the position of the peaks it is possible to know the nature of the particles while from the sharpness of the signals it is possible to gain information about the size of the particle itself;[28,29]

d) *X-Ray Photoelectron Spectroscopy* (XPS), from which it is possible to obtain information on the surface structure of the bimetallic material;[30]

e) *Extended X-Ray Absorption Fine Structure* (EXAFS); a powerful spectroscopy technique to evaluate the nature, the distance between atoms and their coordination sphere in a bimetallic sample. Absorption edges in an EXAFS spectrum of an element are related to the excitation of electrons from various electronic states at energy characteristic of that element (*i.e.* K edges derive from excitation of electrons in 1s states).[31,32] Apart from this, by analysing

the fine structure generated by the increased X-Ray energy on a selected edge, it is possible to have information about the environment of the absorbing atoms. In fact, the fine structure is generated by the interaction of the waves associated to the emitted photoelectrons and the ones to the backscattered neighbouring atoms.

f) *CO-IR Spectroscopy;* a technique that can give information on the surface structure of a bimetallic, thanks to the variability of the IR signal (wavenumber) of CO absorbed on a metal surface.[28,33]

Aim of the Project

In this part of the Thesis Project, the potentialities of bimetallic nanoparticles as electrodic platforms are investigated in depth. Different bimetallic systems (in particular, AuPt, AuPd and AuAg nanoparticles) are studied in order to clarify the effective structure and the possibility to undergo changes after aging time, being able to distinguish between alloyed or core-shell systems. What it is worthy to be underlined is the fact that electrochemistry is here proposed as an alternative, cost-effective and easy to use technique with respect to the commonly involved characterization tools for the study of bimetallic systems (see Paragraph "**Bimetallic Nanoparticles: Characterization Methods**"). The effect played by the possible presence of support is also investigated and final application in electrocatalytic experiments is considered. The general aim is to highlight any relevant difference among the bimetallic but, above all, to underline the presence of synergistic effects and the enhancement of the performances in the case of the hybrids with respect to the single components.

Bibliography

(1) Schmid, G. *Clusters and Colloids: From Theory to Application*; WCH Weinheim, 1994.

(2) Welch, C. M.; Compton, R. G. The Use of Nanoparticles in Electroanalysis: A Review. *Anal. Bioanal. Chem.* **2006**, *384*, 601–619. https://doi.org/10.1007/s00216-005-0230-3.

(3) Campbell, F. W.; Compton, R. G. The Use of Nanoparticles in Electroanalysis: An Updated Review. *Anal. Bioanal. Chem.* **2010**, *396* (1), 241–259. https://doi.org/10.1007/s00216-009-3063-7.

(4) Deepak, F. L. *Metal Nanoparticles and Clusters - Advances in Synthesis, Properties and Applications*; Springer International Publishing, 2018.

(5) Yonezawa, T.; Toshima, N. Bimetallic Nanoparticles-Novel Materials for Chemical and Physical Applications. *New J. Chem.* **1998**, *22* (11), 1179–1201. https://doi.org/10.1039/A805753B

(6) Faraday, M. Experimental Relations of Gold (and Other Metals) to Light. *Phil. Trans. R. Soc. Lond.* **1857**, *147*, 145–181. https://doi.org/10.1098/rstl.1857.0011 Phil. Trans. R. Soc. Lond. 1857 vol. 147 145-181.

(7) Rampino, L. D.; Nord, F. F. Preparation of Palladium and Platinum Synthetic High Polymer Catalysts and the Relationship between Particle Size and Rate of Hydrogenation. *J. Am. Chem. Soc.* **1941**, *63* (10), 2745–2749. https://doi.org/10.1021/ja01855a070.

(8) Toshima, N. Polymer-Protected Bimetallic Clusters. Preparation and Application to Catalysis. *J. Macromol. Sci. Part A - Chem.* **1990**, *27* (9–11), 1225–1238. https://doi.org/10.1080/00222339009349688.

(9) Toshima, N.; Yan, H.; Yukihide, S. Recent Progress in Bimetallic Nanoparticles: Their Preparation, Structures and Functions. In *Metal Nanoclusters in Catalysis and Materials Science: The Issue of Size Control*; Elsevier B.V., 2008.

(10) Harada, M.; Asakura, K.; Ueki, Y.; Toshima, N. Structure of Polymer-Protected Palladium/Platinum Bimetallic Clusters at the Oxidized State. Extended X-Ray Absorption Fine Structure Analysis. *J. Phys. Chem.* **1992**, *96* (24), 9730–9738. https://doi.org/10.1021/j100203a030.

(11) Toshima, N.; Harada, M.; Kushibashi, K.; Asakurat, K. Stuctural Analysis of Polymer-Protected Pd/Pt Bimetallic Clusters as Dispersed Catalysts by Using Extended X-Ray Absorption Fine Structure Spectroscopy. *J. Phys. Chem.* **1991**, *95* (14), 7448–7453. https://doi.org/ 10.1021/j100172a061

(12) Harada, M.; Asakura, K.; Toshima, N. Structural Analysis of Polymer-Protected Pd/Rh Bimetallic Clusters by Using Exafs Spectroscopy. *Jpn. J. Appl. Phys.* **1993**, *32*, 451–453. https://doi.org/10.7567/JJAPS.32S2.451.

(13) Toshima, N.; Lu, P. Synthesis and Catalysis of Colloidal Dispersions of Pd/Ni Bimetallic Clusters. *Chemistry Letters*. 2006, pp 729–730.

https://doi.org/10.1246/cl.1996.729.

(14) Richard, D.; Couves, J. W.; Thomas, J. M. Structural and Electronic Properties of Finely-Divided Supported Pt-Group Metals and Bimetals. *Faraday Discuss.* **1991**, *92*, 109–119. https://doi.org/10.1039/FD9919200109.

(15) Wang, Y.; Toshima, N. Preparation of Pd−Pt Bimetallic Colloids with Controllable Core/Shell Structures. *J. Phys. Chem. B* **2002**, *101* (27), 5301–5306. https://doi.org/10.1021/jp9704224.

(16) Ferrando, R.; Jellinek, J.; Johnston, R. L. Nanoalloys: From Theory to Applications of Alloy Clusters and Nanoparticles. *Chem. Rev.* **2008**, *108* (3), 845–910. https://doi.org/10.1021/cr040090g.

(17) Ghosh Chaudhuri, R.; Paria, S. Core/Shell Nanoparticles: Classes, Properties, Synthesis Mechanisms, Characterization, and Applications. *Chem. Rev.* **2012**, *112* (4), 2373–2433. https://doi.org/10.1021/cr100449n.

(18) Song, Q.; Zhang, Z. J. Shape Control and Associated Magnetic Properties of Spinel Cobalt Ferrite Nanocrystals. *J. Am. Chem. Soc.* **2004**, *126* (19), 6164–6168. https://doi.org/10.1021/ja049931r.

(19) Lee, H.; Habas, S. E.; Kweskin, S.; Butcher, D.; Somorjai, G. A.; Yang, P. Morphological Control of Catalytically ActivePlatinum Nanocrystals. *Angew. Chemie - Int. Ed.* **2006**, *118*, 7988–7992. https://doi.org/0.1002/ange.200603068.

(20) Wang, Z. L.; Ahmad, T. S.; El-Sayed, M. A. Steps, Ledges and Kinks on the Surfaces of Platinum Nanoparticles of Different Shapes. *Surf. Sci.* **1997**, *380* (2–3), 302–310. https://doi.org/10.1016/S0039-6028(97)05180-7.

(21) Wang, Z. L. Transmission Electron Microscopy of Shape-Controlled Nanocrystals and Their Assemblies. *J. Phys. Chem. B* **2002**, *104* (6), 1153–1175. https://doi.org/10.1021/jp993593c.

(22) Wang, Z. L. Structural Analysis of Self-Assembling Nanocrystal Superlattices. *Adv. Mater.* **1998**, *10*, 13–29. https://doi.org/10.1002/(SICI)1521-4095(199801)10:1<13::AID-ADMA13>3.0.CO;2-W

(23) Kokkinakis, T.; Papavassiliou, G. C. Surface Plasmons in Small Cu Particles. *Phys. Status Solidi* **1976**, *77* (1), K49–K51. https://doi.org/10.1002/pssb.2220770151.

(24) Link, S.; Wang, Z. L.; El-Sayed, M. A. Alloy Formation of Gold−Silver Nanoparticles and the Dependence of the Plasmon Absorption on Their Composition. *J. Phys. Chem. B* **1999**, *103* (18), 3529–3533. https://doi.org/10.1021/jp990387w.

(25) Han, S. W.; Kim, Y.; Kim, K. Dodecanethiol-Derivatized Au/Ag Bimetallic Nanoparticles: TEM, UV/VIS, XPS, and FTIR Analysis. *J. Colloid Interface Sci.* **1998**, *208* (1), 272–278. https://doi.org/10.1006/jcis.1998.5812.

(26) Yonezawa, T.; Toshima, N. Polymer- and Micelle-Protected Gold-Platinum Bimetallic Systems. **1993**, *83*, 167–181. https://doi.org/10.1016/0304-5102(93)87017-3

(27) Toshima, N.; Hirakawa, K. Polymer-Protected Bimetallic Nanocluster Catalysts Having Core/Shell Structure for Accelerated Electron Transfer in Visible-Light-Induced Hydrogen Generation. *Polymer Journal*. 2005, pp 1127–1132. https://doi.org/10.1295/polymj.31.1127.

(28) Alayoglu, S.; Eichhorn, B. Rh-Pt Bimetallic Catalysts: Synthesis, Characterization, and Catalysis of Core-Shell, Alloy, and Monometallic Nanoparticles. *J. Am. Chem. Soc.* **2008**, *130* (51), 17479–17486. https://doi.org/10.1021/ja8061425.

(29) Yan, S.; Sun, D.; Tan, Y.; Xing, X.; Yu, H.; Wu, Z. Synthesis and Formation Mechanism of Ag–Ni Alloy Nanoparticles at Room Temperature. *J. Phys. Chem. Solids* **2016**, *98*, 107–114. https://doi.org/10.1016/j.jpcs.2016.06.013.

(30) Prieto, P.; Nistor, V.; Nouneh, K.; Oyama, M.; Abd-Lefdil, M.; Díaz, R. XPS Study of Silver, Nickel and Bimetallic Silver-Nickel Nanoparticles Prepared by Seed-Mediated Growth. *Appl. Surf. Sci.* **2012**, *258* (22), 8807–8813. https://doi.org/10.1016/j.apsusc.2012.05.095.

(31) Sankar, G.; Vasudevan, S.; Rao, C. N. R. An EXAFS Investigation of Cu-ZnO Methanol Synthesis Catalysts. *J. Chem. Phys.* **1986**, *85* (4), 2291–2299. https://doi.org/10.1063/1.451126.

(32) Lee, P. A.; Citrin, P. H.; Eisenberger, P.; Kincaid, B. M. Extended X-Ray Absorption Fine Structure Its Strengths and Limitations as a Structural Tool. *Rev. Mod. Phys.* **1981**, *53* (4), 769–806. https://doi.org/10.1103/RevModPhys.53.769.

(33) Bradley, J. S.; Hill, E. W.; Behal, S.; Klein, C.; Chaudret, B.; Duteil, A. Preparation and Characterization of Organosols of Monodispersed Nanoscale Palladium. Particle Size Effects in the Binding Geometry of Adsorbed Carbon Monoxide. *Chem. Mater.* **1992**, *4* (6), 1234–1239. https://doi.org/10.1021/cm00024a023.

3.1 Gold and Platinum Bimetallic Systems

Focus

The aim of this part of the Thesis work is to deeply characterize bimetallic systems based on gold and platinum, in order to understand their final structure (*i.e.* alloy or core shell) and, above all, to follow their formation during the synthetic procedure and after aging time.

As already mentioned in the **Introduction** of **Chapter 3**, bimetallic systems (nanoparticles, in this case) are widely studied because of their attractive catalytic, magnetic and sensing properties, which are different and often better than the ones of the correspondent monometallic components[1–4]. These enhanced performances drove the attention of many scientists in the study of bimetallic nanoparticles for several applications such as sensors, catalysts, electrocatalysts, fuel cells[5–15]. Besides the type and the quantity of metals involved in the bimetallic structure, it is important to know the real final structure of the system, being able to discriminate between an alloy, a core-shell (intact or partially defective), a Janus-type system and so on. More interesting is the possibility to follow the formation morphology of bimetallic nanomaterials during their synthesis and after aging periods. In fact, since now, few papers in the literature can be found on this topic, which represents a remaining challenge and a gap to be fulfilled. Usually, some of the conventional techniques involved in the characterization of these systems, that are able to give information on the fine structure of the materials, are High Resolution Transmission Microscopy (HR-TEM) and Extended X-Ray Absorption Fine Structure (EXAFS) (for more information see Paragraph "**Bimetallic Nanoparticles: Characterization Techniques**" in **Chapter 3**). Despite being accurate and powerful techniques, they suffer from being expensive and not so easily accessible, especially for a general and first survey of the systems' characteristics[16–18]. Electrochemistry (in particular cyclic voltammetry) is here proposed as an alternative, easy to use, low-cost and fast characterization technique to this purpose. Over the last decades, electrochemistry

has been already employed to study alloyed systems[19,20] and, more recently, also to discriminate between alloyed or core-shell ones[21–25]. On the contrary, as previously mentioned, it has not been applied to follow the formation of the systems in time yet. In this context, the aim of this part of the Thesis work rose. At first, CVs on alloyed and core-shell AuPt nanoparticles are conducted on stabilized systems to understand their final structure; then, the attention is driven on the understanding their evolution in time, recording CVs of the samples at different fixed times from the reactants addition. The possibility to analyse the systems directly in their colloidal liquid form without supporting them (for example on carbon nanofibers or other solid materials), is another novel aspect of the work. TEM analyses and UV-Vis spectra are performed as supporting and complementary information tools.

Materials and Methods

Monometallic systems synthesis

- *AuNPs by chemical reduction in aqueous solution*

0.031 mmol of solid $NaAuCl_4 \cdot 2H_2O$ (Aldrich, Milan, Italy, 99.99 % purity) and polyvinylalcohol solution (PVA, MW(PVA) = 13,000 - 23,000, 87% - 89% hydrolysed, Aldrich; 1% w/w; Au/PVA 1:1, w/w) were added to 100 mL of H_2O. After 3 minutes, $NaBH_4$ (Fluka, Milan, Italy, >96%; Au/$NaBH_4$ 1/4 mol/mol) solution was added to the previous solution under vigorous magnetic stirring. A ruby red Au(0) sol was immediately formed.

- *PtNPs by chemical reduction in aqueous solution*

0.021 mmol of K_2PtCl_4 (Aldrich, Milan, Italy, 99.99 % purity) and polyvinylalcohol solution (PVA, MW(PVA) = 13,000 - 23,000, 87% - 89% hydrolysed, Aldrich; 1% w/w; Pt/PVA 1:1, w/w) were added to 100 mL of H_2O. After 3 minutes, $NaBH_4$ (Fluka, Milan, Italy, >96%; Pt/$NaBH_4$ 1/8 mol/mol) solution was added to the previous solution (yellow-brown coloured) under vigorous magnetic stirring. A black Pt(0) sol was immediately formed.

Bimetallic Systems Synthesis

AuPt nanoparticles (Au:Pt 6:4 molar ratio) were prepared by sol immobilization technique using PVA as protecting agent and $NaBH_4$ as reducer. The synthetic procedures are here described in more details:

- *(Au+Pt) NPs by co-reduction*

0.031 mol of solid $NaAuCl_4 * 2H_2O$, 0.021 mol of K_2PtCl_4 and PVA solution (1% w/w, metal/PVA 1:1 w/w) were added to 100 mL of H_2O. The yellow solution was

stirred for few minutes, after which $NaBH_4$ (metal/$NaBH_4$ = 1/8 mol/mol) solution was added under vigorous magnetic stirring.

- *(Au@Pt) NPs by two-step-reduction*

K_2PtCl_4 (Pt: 0.021 mmol) was dissolved in 40 mL of H_2O and PVA solution (1% w/w) (Pt/PVA= 1:1, wt/wt) was added. The yellow solution was stirred for few minutes, after which $NaBH_4$ (Pt/$NaBH_4$= 1:8 mol/mol) is added under vigorous magnetic stirring. $NaAuCl_4$* $2H_2O$ (Au: 0.031 mmol) was dissolved in 60 mL of H_2O and PVA solution (1% w/w) (Au:PVA= 1:1, wt/wt) was added, under stirring. The solution was then added to the Pt colloidal solution previously prepared and additional $NaBH_4$ (Au:$NaBH_4$= 1:4 mol/mol) was added under vigorous magnetic stirring.

- *(Pt@Au) NPs by two-step-reduction*

$NaAuCl_4$* $2H_2O$ (Au: 0.031 mmol) was dissolved in 60 mL of H_2O and PVA solution (1% w/w) (Au/PVA= 1:1, wt/wt) was then added. The yellow solution was stirred for few minutes, after which $NaBH_4$ (Au/$NaBH_4$= 1:4 mol/mol) was added under vigorous magnetic stirring. K_2PtCl_4 (Pt: 0.021 mmol) will be dissolved in 40 mL of H_2O and PVA solution (1% w/w) (Pt:PVA= 1:1, wt/wt) will be added, under stirring. The solution was then added to the Au colloidal solution previously prepared and additional $NaBH_4$ (Pt:$NaBH_4$= 1:8 mol/mol) was added under vigorous magnetic stirring.

The colloidal solutions have been kept under stirring for 24h. Sampling has been performed at 5 min, 2h, 4h and 24h from the time relative to the reactants' addition.

Morphological Characterization: TEM analyses

Pt+Au, Pt@Au and Au@Pt samples were characterized also by Transmission Electron Microscopy (TEM). In particular, detailed High Resolution High Angle

Annular Dark Field Scanning TEM (HAADF-STEM) imaging and energy-dispersive X-ray spectroscopy (XEDS) analyses were carried out using FEI Titan 80-300 cubed microscope operated at 200 kV accelerating voltage for a deeper investigation of the AuPt structure. This microscope is equipped with double aberration correctors, providing ultrahigh-resolution HAADF-scanning TEM (STEM) images, and an Oxford Inca energy dispersive X-ray (EDX) spectrometer equipped with a 30 mm^2 ultrathin window Si/Li X-ray detector. XEDS data were collected either as spectrum images, in which a focused electron probe was scanned across a region of interest during data collection, or in stationary spot mode, where an emitted X-ray spectrum from 0–20 keV energy range is acquired from a specific point on a particle using a probe size less than 0.5 nm. Spectra were acquired with a probe current of approximately 0.1 nA and dwell times between 200 and 400 ms per pixel, in the case of maps, and 20-30 seconds per analysis in spot mode. STEM HAADF images were acquired using FEI's TIA software and Oxford's INCA microanalysis software was used for XEDS acquisition and analysis. The atomic fractions of gold and platinum were quantified by the Cliff-Lorimer method on relative intensities of the Pt-Lα and Au-Lα peaks using k-factors provided by the XEDS system manufacturer.

Morphological Characterization: UV-Vis analyses

UV-Vis spectra of the monometallic (Au, Pt) and bimetallic (Au+Pt, Au@Pt and Pt@Au) nanoparticles were recorded using a UV-Vis spectrophotometer (Shimadzu). The colloidal solutions were diluted at a ratio 1:3 in milli-Q water and absorbance in the wavelength range 200 – 800 nm was registered.

Electrochemical Characterizations

Electrochemical measurements were performed using an AutoLab PGStat30 (EcoChemie, Utrecht, The Netherlands) equipped with the NOVA 2.1 Software.

Cyclic Voltammetry (CV) were recorded in a conventional three electrodes cell with a Saturated Calomel Electrode (SCE) and a Platinum wire used as Reference (RE) and Counter (CE) electrodes, respectively. The working electrode (WE) was a glassy carbon one modified with the different nanoparticles' solutions, after being polished with a Struers DP-Nap cloth and synthetic diamond powder (Sigma Aldrich, 1 μm) and finally rinsed with milli-Q water. The modified electrode was prepared by drop casting 20 μL of the sought metal nanoparticles' colloid using an automatic micropipette (Kartell, Noviglio, Milano, Italy) and letting it dry for one hour. The CVs were recorded in an aqueous solution with 0.1 M H_2SO_4 as supporting electrolyte. The potential was scanned between -0.25 V and +1.5 V (SCE) at a scan rate of 100 mV s^{-1}. In order to follow the evolution in time of the systems in the liquid form, the solutions were drop-casted on the electrode at different synthetic times (just after the start of the synthetic procedure and at two hours intervals) and then, once dried, analysed electrochemically.

Results and Discussion

Morphological Characterization: TEM Analyses

Transmission Electron Microscopy characterizations were conducted onto the bimetallic systems, after their complete stabilization, in order to understand the real final structure of the samples. High-Angle Annular Dark Field (HAADF) images showed AuPt nanoparticles with a mean diameter in the range of 3-4 nm. Energy Dispersive X-Ray Spectroscopy (XEDS) analyses from individual particles confirmed that most of the supported nanoparticles were bimetallic AuPt in nature, for all the three systems. In the case of Pt+Au and Au@Pt, XEDS maps of individual particles showed the coexistence of Pt and Au elements within the nanoparticle, suggesting the formation of random gold-platinum alloy structures (**Figure 3.1.1 (a)**). In contrast, the analysis performed on Pt@Au suggested the formation of an AuPt alloy core with an enrichment of Pt on the surface (**Figure 3.1.1 (b)**). EDX analysis confirmed that Au and Pt coexist with a ratio similar to the nominal one (6:4) (**Figure 3.1.2**).

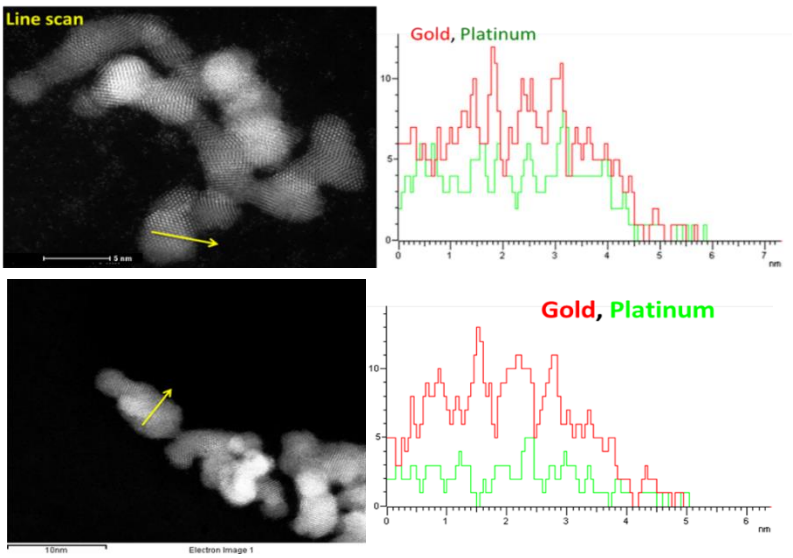

Figure 3.1.1: **(a)** HAADF images of Au+Pt nanoparticles, on the left, and representative XEDS maps of individual particle on the right. **(b)** HAADF images of Pt@Au nanoparticles, on the left, and representative XEDS maps of individual particle on the right.

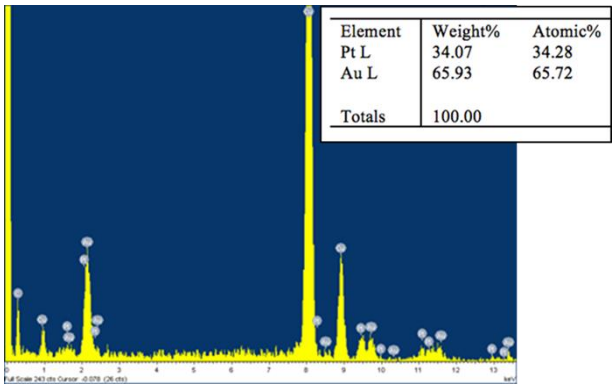

Figure 3.1.2: Representative EDX spectrum of AuPt particles.

Electrochemical Characterization

- *Final Structures of (Pt+Au), (Pt@Au) and (Au@Pt) Systems*

Following different synthetic procedures (see Paragraph **"Materials and Methods"** for more details), three different bimetallic structures were expected to be obtained, in particular an alloy (Pt+Au) and two core-shell (Au@Pt and Pt@Au) (**Figure 3.1.3 (a)**).[26–28] At first, these colloidal samples were analysed by cyclic voltammetry and compared among themselves and with the CV of their relative monometallic components (Au and Pt nanoparticles alone), after their complete stabilization, *i.e.* after more than 24 hours from the synthesis (**Figure 3.1.3 (b)**). These experiments allowed to do a preliminary screening of the final structures of the three bimetallic systems. In this context, it is important to find a way to understand the real structure of a bimetallic gold-based sample, because the thermodynamic tendency of gold to migrate to the surface of the systems[29] makes the control of the desired composition a challenge. Observing the voltammograms of (Pt+Au), (Au@Pt) and (Pt@Au) nanoparticles (**Figure 3.1.3 (b)**), a broad oxidation plateau in the anodic region can be seen. This signal, approximatively between +0.9 and +1.3 V (SCE), comprises the oxidation of both platinum and gold nanoparticles. In the cathodic region, two different reduction peaks for the bimetallic systems can be clearly distinguished. These peaks refer to the disruption of gold (at around +0.8 V (SCE)) and platinum

oxide (at around + 0.3 V (SCE)), respectively. The positions of these reduction peaks are compared among the bimetallic and monometallic samples and listed in **Table 3.1.1**. It is clear that (Pt+Au) and (Au@Pt) systems behave almost in the same way, having positions of the reduction peaks cathodically shifted with respect to the ones of the monometallic Au and Pt counterparts. This evidence yields to the conclusion that the materials behave like an alloy, with properties slightly different from the correspondent metal components [23]. The cathodic shifts of the reduction peaks in these bimetallic systems suggest a stabilization of both oxides in the composite, which are then harder to be reduced. This stabilization might be due to the intimate contact between the components, which results in a general enrichment of electrons in the oxide forms. In particular, Pt in these systems is more stabilised (ΔE (Pt_{RED}) = 100 mV) with respect to Au (ΔE (Au_{RED}) = 30-50 mV), suggesting an electron donation from Au to Pt, as already evidenced in the Literature[30,31]. In the (Pt@Au) case, the reduction peak of gold is fixed, while the platinum one shows a slight shift (ΔE (Pt_{RED}) = 40 mV). In this system the two metals appear less connected suggesting a possible and partial segregation of the materials.

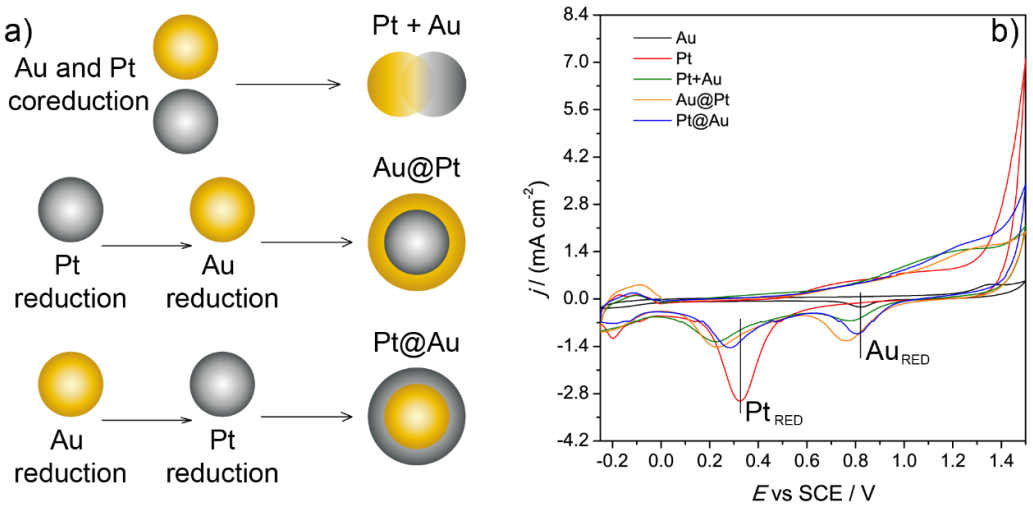

Figure 3.1.3: (a) A schematic representation of the expected morphology of the samples. **(b)** CV of the three bimetallic systems (Pt+Au, Au@Pt and Pt@Au) and the relative monometallic Au and Pt components, recorded at 100 mV s^{-1} in 0.1 M H_2SO_4.

Table 3.1.1: Reduction potential values of the bimetallic and monometallic systems. $\Delta E = E_{monometallic} - E_{bimetallic}$.

Electrode	E (Au_{RED}) / V	ΔE (Au_{RED}) / V	E (Pt_{RED})/ V	ΔE (Pt_{RED}) / V
Au	0.82	0.00	-	-
Pt	-	-	0.33	0.00
(Pt+Au)	0.79	0.03	0.23	0.10
(Au@Pt)	0.77	0.05	0.23	0.10
(Pt@Au)	0.82	0.00	0.29	0.04

- *Evolution in time of the Pt@Au System*

Since among the three bimetallic systems, Pt@Au showed more structural differences (evidenced from cyclic voltammetry experiments and confirmed by TEM analyses), this sample was studied following its evolution in time after reactants addition. The colloid was studied by CV as freshly-prepared (identified hereafter as "_5min") and after 2, 4 and 24 hours from the reactants addition (identified hereafter as "_2h", "_4h" and "_24h"). In order to make the necessary comparisons, the only Au and Pt nanoparticles systems were parallelly studied. It is important to underline that the indicated time is related to the moment in which the solution was deposited on the glassy carbon electrode; one additional hour was required to let the material dry.

Observing the behaviour of the only AuNPs (**Figure 3.1.4 (a)**), it can be claimed that the nanoparticles are in this case immediately formed and stable in time. In fact, they present oxidation and reduction peaks overlapping for all the solutions and no changes during time are visible. In contrast, PtNPs shows cyclic voltammograms which evolve in time (**Figure 3.1.4 (b)**): density current values for both oxidation and reduction peaks grow, evidencing a material that requires more time with respect to AuNPs to be formed and stabilized. Moreover, after 24 hours, it is reasonable to say that the colloid has not reached the final conformation, as evidenced by the slight shift of the reduction peak potential with respect to the one relative to the solution stabilized for more time (see **Figure 3.1.5 (a)**). In addition, in the region between 0

and -0.25 V (SCE), the typical peaks associated to hydrogen absorption and desorption processes on Pt electrodes are not so clear and defined, confirming that the material is still not like a pure Platinum bare system.

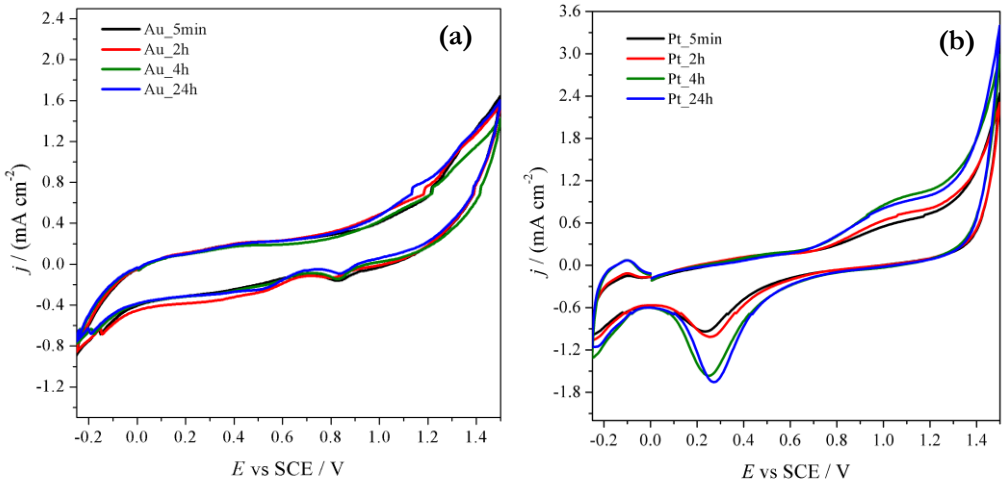

Figure 3.1.4: CV of the monometallic Au (**a**) and Pt (**b**) colloids, at different time from reactants addition, recorded at 100 mV s^{-1} in 0.1 M H_2SO_4.

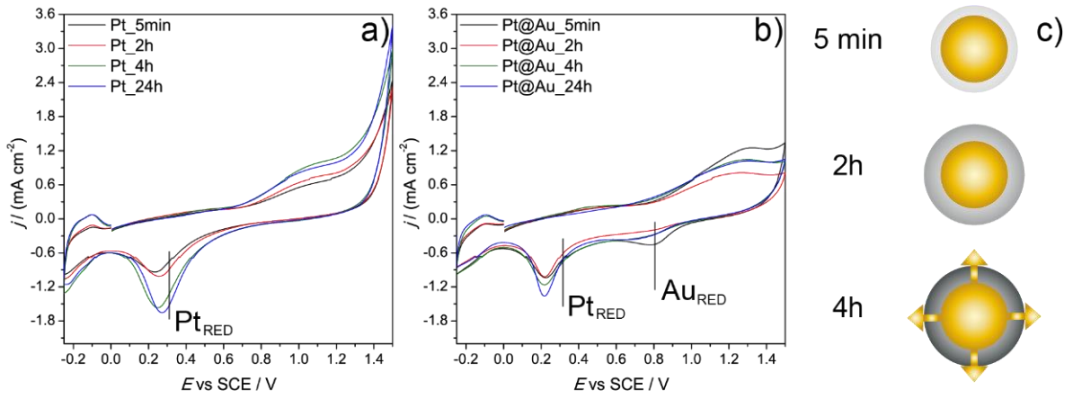

Figure 3.1.5: Evolution in time of the monometallic Pt system **(a)**. The line "Pt_{RED}" refers to the reduction potential of the PtNPs colloidal solution once completely stable in time, as shown in **Figure 3.1.3**. **(b)** Cyclic voltammetry showing the evolution in time of the bimetallic Pt@Au system, with the Au_{RED} and Pt_{RED} lines referring to the ones of **Figure 3.1.3**. **(c)** Schematic representation of Pt@Au formation.

The bimetallic Pt@Au system is compared internally at the four different times (**Figure 3.1.5 (b)**) and at every single time with the relative monometallic counterparts (**Figures 3.1.6 (a)-(d)**). Just after the reactants addition, the bimetallic system presents reduction peaks relative to gold and platinum, respectively, with comparable intensities in terms of current density (**Figure 3.1.5 (b) and 3.1.6 (a)**).

Bearing in mind that cyclic voltammetry is a surface-sensitive technique, able to detect electrochemical properties of surface atoms rather that bulk atoms [22], the presence of both gold and platinum reduction peaks suggests that the core-shell structure is not formed yet (**Figure 3.1.5 (c), 5 min**). However, a bimetallic structure has to be considered, as shown by the absence of the plasmonic band relative to gold and platinum in the UV-Vis spectra (**Figure 3.1.7 (a)**). After two hours (**Figure 3.1.5 (b) and 3.1.6 (b)**), the absence of the gold reduction peak and the decreased density current value of the oxidation plateau suggest the effective formation of the core-shell, in which the internal core made of gold is masked by the external shell of platinum (**Figure 3.1.5 (c), 2h**)[25]. After 4h (**Figure 3.1.5 (b) and 3.1.6 (c)**), the reduction peak relative to gold reappears slightly cathodically shifted, evidencing the tendency of the core-shell to turn into an alloy with the concomitant migration of gold to the surface (**Figure 3.1.5 (c), 4h**). This behaviour is confirmed also after 24 hours (**Figure 3.1.5 (b) and 3.1.6 (d)**).

In conclusion, in this system, segregation of the two metals never happens: gold is inside the structure or partially alloyed, as evidenced also by the absence in every case of the plasmonic band in the Pt@Au Uv-Vis spectra (**Figure 3.1.7**). Another interesting feature of the Pt@Au system is the position of the platinum reduction peak, which remains fixed in time due to the stabilizing effect of gold, as previously discussed for the final bimetallic structures (**Figure 3.1.3 (b)**).

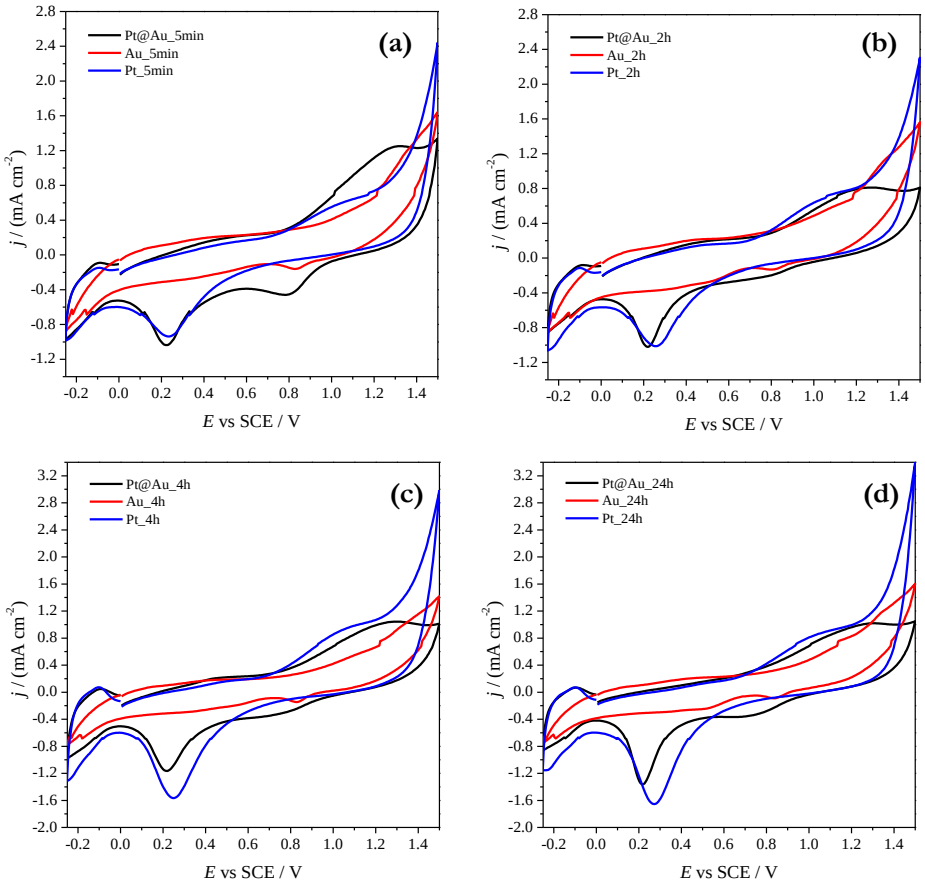

Figure 3.1.6: Evolution in time of the bimetallic systems Pt@Au with respect to its monometallic components (Au and Pt) at different times from the synthesis: deposited on the glassy carbon electrode as freshly prepared **(a)**, after 2h **(b)**, 4h **(c)** and 24h **(d)**. Cyclic voltammetry are recorded in H_2SO_4 0.1 M at 100 mV s^{-1}.

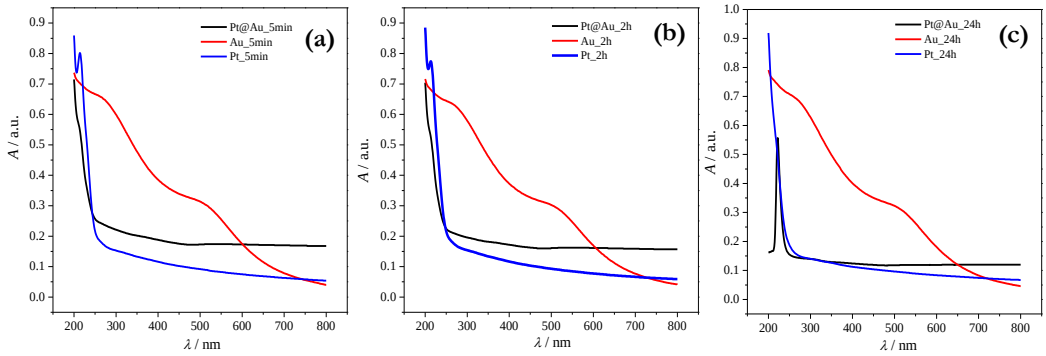

Figure 3.1.7: UV-Vis spectra of the Pt@Au bimetallic systems in colloidal solution compared with the monometallic Au and Pt NPs components at 5min **(a)**, 2h **(b)** and 24h **(c)** from the reactants addition.

Conclusions

In this part of the Thesis project, an electrochemical study of bimetallic systems based on Au and Pt nanoparticles (Pt+Au, Au@Pt, Pt@Au) is presented. As alternative or as complementary technique to the commonly used TEM and EXAFS characterization techniques, Cyclic Voltammetry has been used as an easy to use, low cost and fast methodology in order to discriminate between alloyed or core-shell systems, either perfect or defective. Moreover, and above all, electrochemistry revealed to be a suitable tool to evaluate the time evolution of the NPs systems. This aspect represents an easy and novel way to control the morphology of an investigated system and it eventually gives the possibility to fix the structure at the desired point.

The results show that, even if two different synthetic procedures have been followed, Pt+Au and Au@Pt behaves almost in the same way and particularly they act like an alloy. These alloys differ from the monometallic components, as evidenced by the different peak potential positions, and the cathodic shift of the reduction peaks reveals a stabilization of both metal oxides, addressed to the intimate contact between Pt and Au. On the other hand, Pt@Au behaves differently and resembles more a core-shell system, particularly at the beginning of its preparation, but it tends to an alloyed system with an enrichment of platinum at the surface. The results obtained by CV, in accordance with those obtained by TEM and UV-Vis techniques, can help the researchers to understand the behaviour of bimetallic systems with the final aim of applications in catalysis, electrocatalysis and electroanalysis.

Bibliography

(1) Sankar, M.; Dimitratos, N.; Miedziak, P. J.; Wells, P. P.; Kiely, C. J.; Hutchings, G. J. Designing Bimetallic Catalysts for a Green and Sustainable Future. *Chem. Soc. Rev.* **2012**, *41* (24), 8099–8139.

(2) Ferrando, R.; Jellinek, J.; Johnston, R. L. Nanoalloys: From Theory to Applications of Alloy Clusters and Nanoparticles. *Chem. Rev.* **2008**, *108* (3), 845–910.

(3) Toshima, N.; Yonezawa, T. Bimetallic Nanoparticles: Novel Materials for Chemical and Physical Applications. **1998**, 1179–1201.

(4) Villa, A.; Wang, D.; Su, D. S.; Prati, L. New Challenges in Gold Catalysis: Bimetallic Systems. *Catal. Sci. Technol.* **2015**, *5* (1), 55–68.

(5) Hu, Y.; Zhang, H.; Wu, P.; Zhang, H.; Zhou, B.; Cai, C. Bimetallic Pt-Au Nanocatalysts Electrochemically Deposited on Graphene and Their Electrocatalytic Characteristics towards Oxygen Reduction and Methanol Oxidation. *Phys. Chem. Chem. Phys.* **2011**, *13* (9), 4083–4094.

(6) Kim, C.; Dionigi, F.; Beermann, V.; Wang, X.; Möller, T.; Strasser, P. Alloy Nanocatalysts for the Electrochemical Oxygen Reduction (ORR) and the Direct Electrochemical Carbon Dioxide Reduction Reaction (CO_2 RR). *Adv. Mater.* **2018**, *1805617*, 1805617.

(7) Bracey, C. L.; Ellis, P. R.; Hutchings, G. J. Application of Copper-Gold Alloys in Catalysis: Current Status and Future Perspectives. *Chem. Soc. Rev.* **2009**, *38* (8), 2231–2243.

(8) Xia, Y.; Xiong, Y.; Lim, B.; Skrabalak, S. E. Shape-Controlled Synthesis of Metal Nanocrystals: Simple Chemistry Meets Complex Physics? *Angew. Chemie - Int. Ed.* **2009**, *48* (1), 60–103.

(9) Hernández-Fernández, P.; Rojas, S.; Ocón, P.; De La Fuente, J. L. G.; Fabián, J. S.; Sanza, J.; Peña, M. A.; García-García, F. J.; Terreros, P.; Fierro, J. L. G. Influence of the Preparation Route of Bimetallic Pt-Au Nanoparticle Electrocatalysts for the Oxygen Reduction Reaction. *J. Phys. Chem. C* **2007**, *111* (7), 2913–2923.

(10) Wu, M. L.; Chen, D. H.; Huang, T. C. Preparation of Au/Pt Bimetallic Nanoparticles in Water-in-Oil Microemulsions. *Chem. Mater.* **2001**, *13* (2), 599–606.

(11) Gong, J.; Zhou, T.; Song, D.; Zhang, L.; Hu, X. Stripping Voltammetric Detection of Mercury(II) Based on a Bimetallic Au-Pt Inorganic-Organic Hybrid Nanocomposite Modified Hlassy Carbon Electrode. *Anal. Chem.* **2010**, *82* (2), 567–573.

(12) Schrinner, M.; Proch, S.; Mei, Y.; Kempe, R.; Miyajima, N.; Ballauff, M. Stable Bimetallic Gold-Platinum Nanoparticles Immobilized on Spherical Polyelectrolyte Brushes: Synthesis, Characterization, and Application for the Oxidation of Alcohols. *Adv. Mater.* **2008**, *20* (10), 1928–1933.

(13) Suntivich, J.; Xu, Z.; Carlton, C. E.; Kim, J.; Han, B.; Lee, S. W.; Bonnet, N.; Marzari,

N.; Allard, L. F.; Gasteiger, H. A.; et al. Surface Composition Tuning of Au-Pt Bimetallic Nanoparticles for Enhanced Carbon Monoxide and Methanol Electro-Oxidation. *J. Am. Chem. Soc.* **2013**, *135* (21), 7985–7991.

(14) Howe, A. G. R.; Miedziak, P. J.; Morgan, D. J.; He, Q.; Strasser, P.; Edwards, J. K. One Pot Microwave Synthesis of Highly Stable AuPd@Pd Supported Core-Shell Nanoparticles. *Faraday Discuss.* **2018**, *208*, 409–425.

(15) Zhong, C. J.; Maye, M. M. Core-Shell Assembled Nanoparticles as Catalysts. *Adv. Mater.* **2001**, *13* (19), 1507–1511.

(16) Baer, D. R.; Amonette, J. E.; Engelhard, M. H.; Gaspar, D. J.; Karakoti, A. S.; Kuchibhatla, S.; Nachimuthu, P.; Nurmi, J. T.; Qiang, Y.; Sarathy, V.; et al. Characterization Challenges for Nanomaterials. *Surf. Interface Anal.* **2008**, *40* (3–4), 529–537.

(17) Villa, A.; Dimitratos, N.; Chan-Thaw, C. E.; Hammond, C.; Veith, G. M.; Wang, D.; Manzoli, M.; Prati, L.; Hutchings, G. J. Characterisation of Gold Catalysts. *Chem. Soc. Rev.* **2016**, *45* (18), 4953–4994.

(18) Wu, J.; Gao, W.; Wen, J.; Miller, D. J.; Lu, P.; Zuo, J. M.; Yang, H. Growth of Au on Pt Icosahedral Nanoparticles Revealed by Low-Dose in Situ TEM. *Nano Lett.* **2015**, *15* (4), 2711–2715.

(19) Breiter, M. W. Electrochemical Characterization of the Surface Composition of Heterogeneous Platinum-Gold Alloys. *J. Phys. Chem.* **1965**, *69* (3).

(20) Woods, R. Electrolytically Co-Deposited Platinum-Gold Electrodes and Their Electrocatalytic Activity for Acetate Ion Oxidation. *Electrochim. Acta* **1969**, *14*, 533–540.

(21) Tan, C.; Sun, Y.; Zheng, J.; Wang, D.; Li, Z.; Zeng, H.; Guo, J.; Jing, L.; Jiang, L. A Self-Supporting Bimetallic Au@Pt Core-Shell Nanoparticle Electrocatalyst for the Synergistic Enhancement of Methanol Oxidation. *Sci. Rep.* **2017**, *7* (1), 1–10.

(22) Kristian, N.; Wang, X. Ptshell-Aucore/C Electrocatalyst with a Controlled Shell Thickness and Improved Pt Utilization for Fuel Cell Reactions. *Electrochem. commun.* **2008**, *10* (1), 12–15.

(23) Plowman, B. J.; Sidhureddy, B.; Sokolov, S. V.; Young, N. P.; Chen, A.; Compton, R. G. Electrochemical Behavior of Gold–Silver Alloy Nanoparticles. *ChemElectroChem* **2016**, *3* (7), 1039–1043.

(24) Holt, L. R.; Plowman, B. J.; Young, N. P.; Tschulik, K.; Compton, R. G. The Electrochemical Characterization of Single Core-Shell Nanoparticles. *Angew. Chemie - Int. Ed.* **2016**, *55* (1), 397–400.

(25) Tschulik, K.; Ngamchuea, K.; Ziegler, C.; Beier, M. G.; Damm, C.; Eychmueller, A.; Compton, R. G. Core-Shell Nanoparticles: Characterizing Multifunctional Materials beyond Imaging - Distinguishing and Quantifying Perfect and Broken Shells. *Adv. Funct. Mater.* **2015**, *25* (32), 5149–5158.

(26) Dimitratos, N.; Messi, C.; Porta, F.; Prati, L.; Villa, A. Investigation on the Behaviour of Pt(0)/Carbon and Pt(0),Au(0)/Carbon Catalysts Employed in the Oxidation of Glycerol with Molecular Oxygen in Water. *J. Mol. Catal. A Chem.* **2006**, *256* (1–2), 21–28.

(27) Tiruvalam, R. C.; Pritchard, J. C.; Dimitratos, N.; Lopez-Sanchez, J. A.; Edwards, J. K.; Carley, A. F.; Hutchings, G. J.; Kiely, C. J. Aberration Corrected Analytical Electron Microscopy Studies of Sol-Immobilized Au + Pd, Au{Pd} and Pd{Au} Catalysts Used for Benzyl Alcohol Oxidation and Hydrogen Peroxide Production. *Faraday Discuss.* **2011**, *152*, 63–86.

(28) Peneau, V.; He, Q.; Shaw, G.; Kondrat, S. A.; Davies, T. E.; Miedziak, P.; Forde, M.; Dimitratos, N.; Kiely, C. J.; Hutchings, G. J. Selective Catalytic Oxidation Using Supported Gold-Platinum and Palladium-Platinum Nanoalloys Prepared by Sol-Immobilisation. *Phys. Chem. Chem. Phys.* **2013**, *15* (26), 10636–10644.

(29) Schwank, J. Gold in Bimetallic Catalysts. *Gold Bull.* **1985**, *18* (1), 2–10.

(30) Villa, A.; Jouve, A.; Sanchez Trujillo, F.; Motta, D.; Prati, L.; Dimitratos, N. Exploring the Effect of Au/Pt Ratio on Glycerol Oxidation in Presence and Absence of a Base. *Catalysts* **2018**, *8* (2), 54.

(31) Park, H. Y.; Jeon, T. Y.; Jang, J. H.; Yoo, S. J.; Choi, K. H.; Jung, N.; Chung, Y. H.; Ahn, M.; Cho, Y. H.; Lee, K. S.; et al. Enhancement of Oxygen Reduction Reaction on PtAu Nanoparticles via CO Induced Surface Pt Enrichment. *Appl. Catal. B Environ.* **2013**, *129*, 375–381.

Acknowledgements:

I gratefully acknowledge Dr. A. Villa from the Department of Chemistry of Università degli Studi di Milano (Milano, Italy) for the synthesis of the metallic nanoparticles, Dr. S. Prabhudev and G. A. Botton from Department of Materials Science and Engineering and Canadian Centre of Electron Microscopy (McMaster University, Ontario, Canada) for TEM measurements and data elaboration.

3.2 Gold and Palladium Bimetallic Systems

Focus

In this part of the Thesis Project, bimetallic systems based on gold and palladium, supported on different carbonaceous substrates, were deeply investigated in terms of electrochemical stability and electrocatalytic activities. The effect played by the support on the final properties of the metals was studied and differences between the monometallic and bimetallic hybrid materials were highlighted.

As already mentioned in the **Introduction** of **Chapter 3**, the interesting features of bimetallic systems, related to their enhanced performances with respect to the correspondent bulk materials, made them extremely attractive to many scientists.[1–3] The wide amount and variety of bimetallic samples, in terms of composition, structure, metal loading and morphology, has led to widespread applications in a lot of fields such as engineering, catalysis, electrocatalysis, sensors, electronics and so on.[4–6] In the particular fields of heterogeneous catalysis and electrocatalysis, metal nanoparticles are often supported on different kind of substrates, which themselves possess different characteristics and properties connected to the type and loading of the metal catalysts and/or to the nature and functionalization of the substrate itself.[7–13] However, the effect played by the support onto the properties of the metal loaded or the investigation of possible synergistic effects in bimetallic composites is still to be clarified and studied in depth. This part of the Thesis work aimed at fulfil this vacancy. In more details, three different types of carbon nanofibers (Pyrolitically Stripped carbon nanofibers (PS), Low-temperature Heat Treated (LHT) carbon nanofibers and High-temperature Heat Treated (HHT) carbon nanofibers) have been used as support for Au, Pd and bimetallic AuPd nanoparticles. The supports differ in terms of graphitization degree and surface chemistry. The focus of the work was to clarify how changes in the graphitization degree and in the amount of defects on the surface of the carbonaceous substrates reflect in different electrochemical activity and properties of the metal nanoparticles. Moreover, the presence of synergistic effects in the bimetallic with respect to the monometallic

systems was investigated, confirming the general trends already evidenced in several works in the literature.[14–18] Final application in the electroanalytical detection of cinnamyl alcohol and cinnamaldehyde was investigated, with the particular aim to highlight any enhancement in the addition of gold to palladium-based materials and so the increased performances of hybrids with respect to single components.

Materials and Methods

Detailed information at:

Testolin, A. Cattaneo, S., Wang, W., Wang, D., Pifferi, V., Prati, L., Falciola, L., Villa, A., "Cyclic Voltammetry Characterization of Au, Pd and AuPd Nanoparticles Supported on Different Carbon Nanofibers", *Surfaces* **(2019)**, 2, 205-215, doi:10.3390/surfaces2010016

Metal Nanoparticles/CNFs Preparation

Commercial carbon nanofibers (CNFs), PR24-PS (hereafter shortened as PS) from Applied Sciences, inc. (average diameter of 100 ± 30 nm and a specific surface area of 45 m^2/g); CNFs PR24-LHT (LHT) from Applied Sciences, inc. (average diameter of 100 ± 30 nm and a specific surface area of 43 m^2/g); and CNFs PR24-HHT (HHT) from Applied Sciences, inc. (average diameter of 100 ± 30 nm and a specific surface area of 41 m^2/g) were used as pristine carbon materials. $NaAuCl_4 \cdot 2H_2O$ (99%, Aldrich, St. Louis, MO, USA) and Na_2PdCl_4 (98 % Aldrich) were used as metal precursors, while $NaBH_4$ (> 98%, Ventron) and polyvinyl alcohol (PVA, MW = 9000–10,000, 80 % hydrolyzed, Aldrich) were used as reducing and protective agents, respectively.

- *CNF-AuNPs*

0.051 mol of solid $NaAuCl_4 *2H_2O$ and PVA solution (1% w/w, metal/PVA 1:1 w/w) were added to 100 mL of Milli-Q H_2O. The solution was stirred for few minutes, after which $NaBH_4$ (metal/$NaBH_4$ = 1/4 mol/mol) solution was added under vigorous magnetic stirring. Within a few minutes of sol generation, the sol was immobilized by adding the support (ca. 1 g) under vigorous stirring. The slurry was filtered, and the catalyst washed thoroughly with distilled water and dried at 80 °C for 4 h. The total nominal metal loading was 1 wt %.

- *CNF-PdNPs*

0.094 mol of Na_2PdCl_4 and PVA solution (1% w/w, metal/PVA 1:1 w/w) were added to 100 mL of Milli-Q H_2O. The solution was stirred for few minutes, after which $NaBH_4$

(metal/$NaBH_4$ = 1/8 mol/mol) solution was added under vigorous magnetic stirring. Within a few minutes of sol generation, the sol was immobilized by adding the support (ca. 1 g) under vigorous stirring. The slurry was filtered, and the catalyst washed thoroughly with distilled water and dried at 80 °C for 4 h. The total nominal metal loading was 1 wt %.

- *CNF-AuPdNPs*

0.037 mol of solid $NaAuCl_4$ *$2H_2O$, 0.025 mol of Na_2PdCl_4 and PVA solution (1% w/w, metal/PVA 1:1 w/w) were added to 100 mL of Milli-Q H_2O. The yellow solution was stirred for few minutes, after which $NaBH_4$ (metal/$NaBH_4$ = 1/8 mol/mol) solution was added under vigorous magnetic stirring. Within a few minutes of sol generation, the sol was immobilized by adding the support (ca. 1 g) under vigorous stirring. The slurry was filtered, and the catalyst washed thoroughly with distilled water and dried at 80 °C for 4 h. The total nominal metal loading was 1 wt %.

Morphological Characterizations

- Raman spectroscopy was performed with a Renishaw inVia Raman microscope for analysing the graphitisation degree of the carbon nanofibers. Bare supports and fresh and used catalysts were analysed. Typically, a sample of approximately 0.01 g was placed on a metal slide inside the spectrometer. The powder was analysed under an IR class laser (514 nm) with a laser intensity of 50 %. The sample was scanned at an attenuation time of 22 seconds, and 10 scans were carried out to give a spectrum.
- X-ray photoelectron spectroscopy (XPS) was performed on a Thermo Scientific K-alpha+ spectrometer (Thermo Fisher Scientific, Massachussetts, USA). Samples were analysed using a monochromatic Al x-ray source operating at 72 W (6 mA × 12 kV), with the signal averaged over an oval-shaped area of approximately 600 × 400 microns. Data were recorded at pass energies of 150

eV for survey scans and 40 eV for high resolution scan with a 1eV and 0.1 eV step size, respectively. Charge neutralization of the sample was achieved using a combination of both low energy electrons and argon ions (less than 1 eV), which gave a C(1s) binding energy of 284.8 eV.

All data were analysed using CasaXPS (v2.3.17 PR1.1, company, city, country) using Scofield sensitivity factors and an energy exponent of −0.6.

- The Au, Pd specimens were characterized by transmission electron microscopy (TEM, FEI Titan 80−300, Thermo Fisher Scientific, Massachussetts, USA). The samples were directly dispersed on copper grids covered with holey carbon film. Morphology of the catalysts was characterized by high angle annular dark-field (HAADF) scanning transmission electron microscopy (STEM), and its composition information was acquired by EDAX S-UTW EDX detector in a FEI Titan 80−300 microscope operating (Thermo Fisher Scientific, Massachussetts, USA) at 300 kV. Analysis of STEM-EDX spectrum imaging was carried out by using TEM image and analysis (TIA 4.7 SP3 version) software. Particle size of the specimens was measured on HAADF-STEM images by using the ImageJ software (National Institutes of Health, USA) fitting the particles with ellipsoid shapes.

Electrochemical Characterizations

Cyclo-voltammetric experiments were performed using an AutoLab PGStat128 (Metrohm AutoLab, Utrecht, The Netherlands) equipped with the NOVA 2.1 Software (Metrohm AutoLab, Utrecht, The Netherlands). The experimental setting was composed of a conventional three electrodes cell in which a saturated calomel electrode and a platinum wire were used as reference (RE) and counter (CE) electrodes, respectively. A glassy carbon (GC) modified with carbon nanofibers (CNFs) or with mono or bimetallic Au and Pd NPs supported on carbon nanofibers was used as working electrode (WE). Before the modification, GC was polished with diamond

powder (1 μm, Sigma Aldrich, Milan, Italy) on a Struers DP-Nap cloth and washed with milli-Q water. 5 mg of the different CNF-NPs powders were suspended in 1 mL EtOH (96 %, Sigma Aldrich) and 4.5 μL Nafion (5% solution in low aliphatic alcohols, Aldrich, Milan, Italy). Then, 20 μL of the suspension were deposited on GC using an automatic micropipette (Kartell, Noviglio, Milano, Italy) and allowed to dry for approximately 30 minutes. Cyclo-voltammetries were recorded in aqueous solution with 0.1 M H_2SO_4 as supporting electrolyte. The potential was scanned from −1 V (SCE) to +2 V (SCE), at a scan rate of 100 mV s^{-1} and a step potential of 5 mV.

Electroanalytical Applications

All the above-described samples (bare carbon nanofibers and nanofibers modified with gold and palladium nanoparticles), were applied as a preliminar proof of concept in the detection of cinnamyl alcohol and cinnamaldehyde. The electrochemical experimental setup is the same as the one previously explained in the "Electrochemical Characterization" paragraph. 3 mM of Cinnamyl Alcohol and Aldehyde (Sigma Aldrich, > 99%) were added in an aqueous solution with 0.1 M H_2SO_4 as supporting electrolyte. Cyclic voltammetry was recorded scanning the potential in the range -1 V (SCE) to +2 V (SCE), at a scan rate of 100 mV s^{-1} and a step potential of 5 mV. These experiments were repeated both in aerated and deareated, by bubbling N_2 in the environment, solution.

Results and Discussion

Detailed information at:

Testolin, A. Cattaneo, S., Wang, W., Wang, D., Pifferi, V., Prati, L., Falciola, L., Villa, A., "Cyclic Voltammetry Characterization of Au, Pd and AuPd Nanoparticles Supported on Different Carbon Nanofibers", **Surfaces 2019**, 2, 205-215, doi:10.3390/surfaces2010016

Morphological Characterizations

Commercial carbon nanofibers (CNFs), thermally processed at different severity degrees (PS < LHT < HHT)[19,20], were selected as supports. The strength of the thermal process reflects in different graphitization degrees of the supports, which were investigated via Raman spectroscopy. In more details, the ratio of the integral intensities of D and G bands (I_D/I_G), which is an index of the defectiveness of the graphite layers,[21] was measured and results are listed in **Table 3.2.1**. G band is related to structurally-ordered graphite domains, whereas D band can be associated with the turbostratic and/or disordered carbonaceous structures[22]. As expected, increasing the temperature of the heat treatment results in a higher graphitization degree (I_D/I_G = 0.75, 0.60, 0.11 for PS, LHT, HHT, respectively) (**Table 3.2.1**). In order to confirm the effective graphitization degrees of the three samples, X-ray photoelectron spectroscopy (XPS) has been used as a supporting characterization technique. XPS spectra of C1s show two main components: the first one at 284 eV, which can be attributed to sp^2-hybridised carbon species, and the second component at 285 eV ascribable to the presence of sp^3-hybridised carbon species[23] (**Figure 3.2.1** and **Tables 3.2.1** and **3.2.2**). It can be noticed that the sp^2/sp^3 ratio increases with increasing annealing temperature (in more details: 4.1, 7.0 and 16.8 for PS, LHT, HHT, respectively) (**Table 3.2.1**). Accordingly, a higher amount of oxygen has been observed decreasing the graphitization degree (C:O ratio of 88.3:11.7, 92.2:7.8, 97.3:2.7 for PS, LHT, HHT, respectively) (**Table 3.2.2**). **Table 3.2.2** summarizes the oxygen species observed on the surface, their concentration, and the overall elemental composition. Fitting the O1s peak, five contributions were observed (**Figure 3.2.2**). Binding Energy (BE) of 530.2–530.5 eV corresponds to highly

conjugated forms of carbonyl oxygen such as quinone[24]. The second contribution (531.6-531.9 eV) can be assigned to a carbon–oxygen double bond, whereas the one at 533.0-533.5 eV corresponds to an ether-like single bond C-O-C and to carbon oxygen single-bonds in hydroxyl groups C-O-H[25]. Oxygen species at 534.6–535.0 eV refers to the presence of carboxylic groups COOH[25]. The last signal at 536.7–537.1 eV can be assigned to adsorbed water[26]. C=O, C-O-H and C-O-C were the most abundant species present in all the CNFs (Table 2 and Figure 2).

Table 3.2.1: Atomic content of sp^2 and sp^3 carbon and ratio sp^2/sp^3 from X-ray photoelectron spectroscopy (XPS) and I_D/I_G ratio from Raman for the bare supports.

Catalyst	C sp^2 (%)	C sp^3 (%)	sp^2/sp^3	I_D/I_G
PS	75.8	18.6	4.1	0.75
LHT	83.8	12.0	7.0	0.60
HHT	90.8	3.4	16.8	0.11

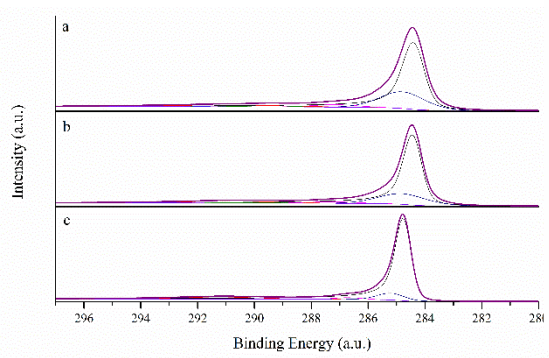

Figure 3.2.1: C1s XPS spectra of (**a**) PS, (**b**) LHT and (**c**) HHT

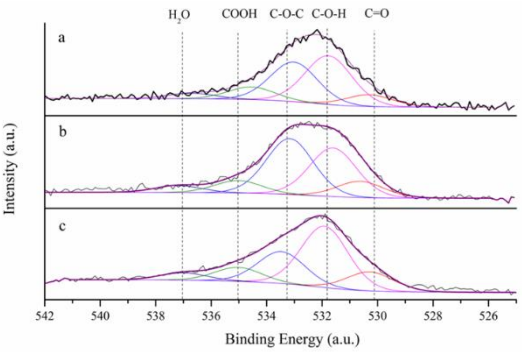

Figure 3.2.2: O1s XPS spectra of (**a**) PS, (**b**) LHT and (**c**) HHT

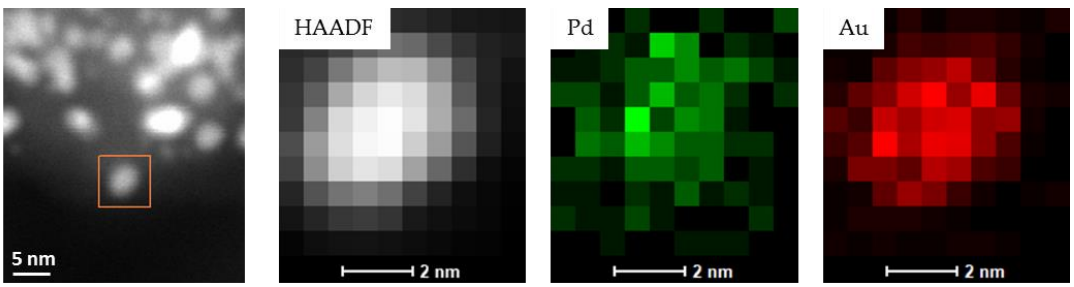

Figure 3.2.3: The element maps obtained from STEM-EDX spectrum imaging in the area marked box of AuPd nanoparticles.

Table 3.2.2. XPS analysis of the carbon nanofibers (CNFs).

Sample		$O1_S$					C1s				Atomic ratio % C:O
		C=O	**C-O-H**	**C-O-C**	**COOH**	**H_2O**	**sp^2**	**sp^3**	**C=O**	**C=C**	
PS	BE	530.2	531.8	533.0	534.6	536.7	284.4	284.9	287.2	290.0	88.3:11.7
	Atom %	(10.2)	(40.7)	(33.1)	(9.8)	(6.0)	(75.8)	(18.6)	(3.7)	(1.8)	
LHT	BE	530.5	531.6	533.1	535.0	537.1	284.5	284.9	287.4	290.1	92.2:7.8
	Atom %	(11.6)	(34.2)	(40.3)	(8.8)	(5.1)	(83.8)	(12.0)	(2.6)	(1.6)	
HHT	BE	530.2	531.9	533.5	535.0	537.0	284.7	285.2	287.9	290.6	97.3:2.7
	Atom %	(13.9)	(46.2)	(24.0)	(10.1)	(5.8)	(90.8)	(5.4)	(1.6)	(2.2)	

Monometallic Au and Pd, together with their corresponding bimetallic system (AuPd), were prepared by sol immobilization method using polyvinyl alcohol (PVA) as protective agent and $NaBH_4$ as reducing agent and immobilized on the three different CNFs. The monometallic and bimetallic systems consist of nanoparticles with an average size of 3–4 nm.[27,28] To investigate the morphology of the bimetallic systems, STEM-EDX spectrum imaging was performed on single nanoparticles to map the interior metal compositions. Element maps of one AuPd particle are reported in **Figure 3.2.3**, as example. Both Pd and Au signals were found in nanoparticles with a similar distribution, indicating the formation of AuPd alloyed nanoparticles. Quantification of the integrated EDX spectra of this nanoparticle indicates that the atomic ratio of Au and Pd is 64/36 close to the nominal 60/40 (**Figure 3.2.3**).

Electrochemical Characterizations

As already demonstrated by XPS results, the three types of carbon nanofibers differ from the ratio between the sp^2 and sp^3 conformation of carbon atoms. This ratio can be named as "graphitization" degree, which is an index of the order degree in carbon based materials[19,29,30]. It was observed that these differences reflect in different voltammetric behaviors, especially in the potential window width (that is the useful voltage range, between the anodic and cathodic reaction of the solvent/supporting electrolyte) and in electrocatalytic effects.

Regarding the potential window width, **Figure 3.2.4 (a)** shows that the order is PS < LHT < HHT (more clearly visible by looking at the zoom of the Figure itself, **Figure 3.2.4 (b)**), both in the cathodic and anodic side. This means that HHT fibers are the most electrochemically stable material and the most inert towards Oxygen Evolution Reaction (OER) and Hydrogen Evolution Reaction (HER) in the anodic and cathodic side, respectively. In fact, since the electrochemical experiments were conducted in an aqueous solution, OER and HER represent the background reactions.

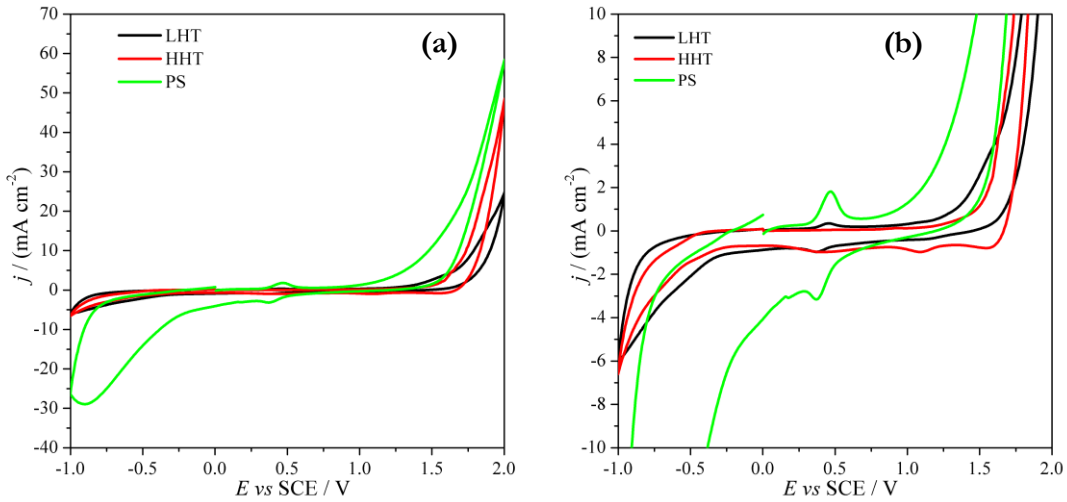

Figure 3.2.4: Cyclic Voltammetry recorded at 100 mv s^{-1} in 0.1 M H_2SO_4 of the three different carbon nanofibers supports. (**b**)Zoom of the region around +0.4 V (SCE).

Moreover, looking again at the zoomed graph in **Figure 3.2.4(b)**, the presence of small oxidation and reduction peaks in the region around +0.4 V (SCE) can be seen in the case of PS fibers, less marked in LHT and basically absent in HHT. Bearing in mind the surface morphology of the selected samples, already explained in the previous "Morphological Characterization" section, these signals have been addressed to the presence of oxygen functionalities of the carbonaceous structure[31,32], which are in higher concentration for PS, then followed by LHT and HHT. This aspect is in accordance with the graphitization degree, in fact, the lower the graphitization degree the higher the presence of surface impurities and defects[33]. The presence of these functionalities could also be reflected in the different potential window width.

The peculiarities of these carbon nanofibers drove the attention on a different and additional investigation. In fact, PS, LHT and HHT fibers were involved as support for metal nanoparticles, in particular, Au, Pd and alloyed AuPd NPs. The supported nanoparticles were used as electrode materials and the possible effect played by the carbonaceous support, with the instauration of synergistic effect were investigated. At first, the supported monometallic Au and Pd nanoparticles were studied, looking at their background patterns, *i.e.* cyclic voltammetry recorded in an aqueous solution with 0.1 H_2SO_4 as supporting electrolyte. As it can be seen in **Figure 3.2.5(a)**, representing supported Au nanoparticles, the smallest potential window width is again the one relative to PS carbon nanofibers, followed by LHT and HHT. Moreover, additional oxidation and reduction peaks relative to the presence of gold nanoparticles are present, as visible by looking at the zoomed cyclovoltammetries in **Figure 3.2.5(b**). In particular, apart from the same peaks of the bare nanofibers at +0.4 V (SCE), a well-defined signal (for LHT and HHT) at around +1.3 V (SCE) is evident, whose peak-shape confirms the nanosized structure of the gold particles[34]. This signal is less evident in the case of PS (it is more in a shape of a shoulder plateau) since it is partially covered by the reaction of the background. Looking at the oxidation peak position, a small catalytic effect for HHT can be highlighted, since

the position of the oxidation peak is shifted at +1.25 V (SCE) with respect to +1.31 V (SCE) of the LHT-supported sample. This effect could be related to the higher interaction of the HHT fibers and gold nanoparticles, thanks to the high graphitization degree of the material, which reflects in a favored electron transfer. A more interesting explanation could be done by looking at the main-oxide reduction signals, which are comprised in the region +0.5/+0.8 V (SCE). If they are compared to the reduction signal of analogous AuNPs without any support (see **Figure 3.2.8**), a strong shift in position can be highlighted[35]. In the case of non-supported gold nanoparticles, the reduction peak is registered at around +0.8 V (SCE) while in these supported systems the gold oxide reduction falls at lower potential and in the order PS < LHT < HHT. The shift at lower potential means that the oxide is more stable since it requires a higher energy to be disrupted. As a consequence, this evidence can be reasonably ascribed to a different stabilizing effect played by the different carbon nanofiber supports that can be further and conveniently exploited in sensing and catalytic applications.

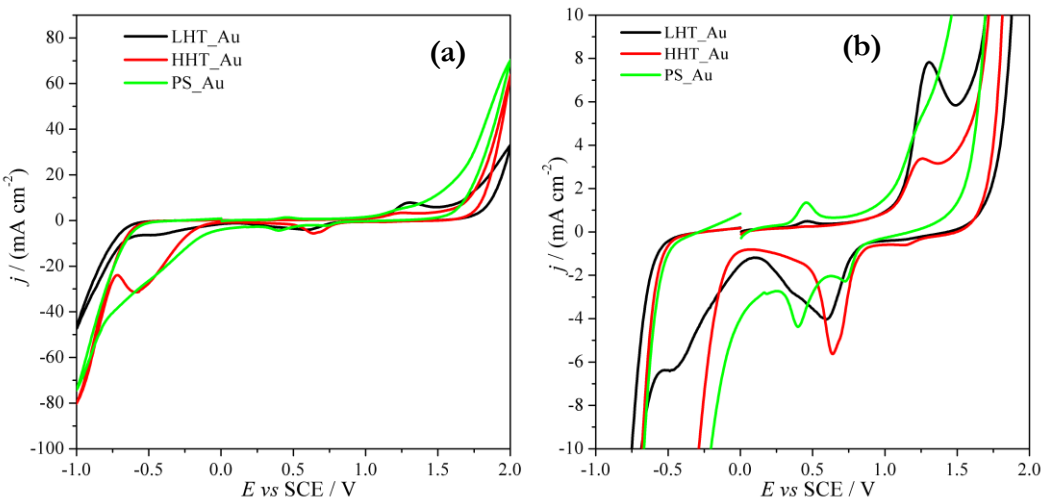

Figure 3.2.5: Cyclic Voltammetry recorded at 100 mv s^{-1} in 0.1 M H_2SO_4 of the three different carbon nanofibers supports modified with gold nanoparticles, with a zoom in (**b**).

In the case of Pd supported nanoparticles, the situation was more difficult to be clarified, maybe because of the intrinsic nature of the metal itself, which is more adaptable than the noble metal gold and so more susceptible of changes in its structure when it is in the presence of other materials like the support. Looking at the **Figure 3.2.6(a)**, a small oxidation peak around +1 V (SCE) is present, which is in line with the values of analogous colloidal (non-supported) PdNPs (**Figure 3.2.8**). In the case of the LHT- supported sample, more intense signal at +1.73 V (SCE) and +1.89 V (SCE) are present, probably due to the concomitant Pd oxidation together with O_2 evolution (background reaction).

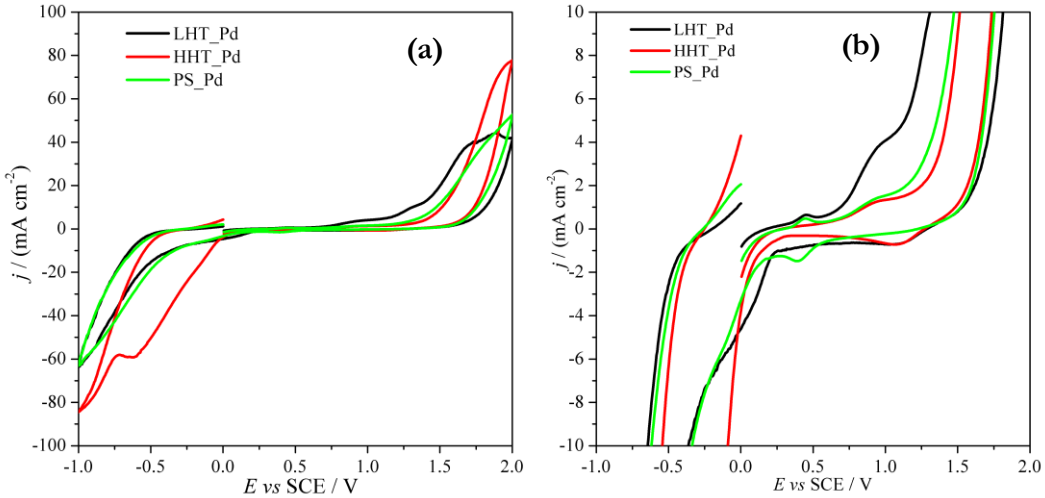

Figure 3.2.6: Cyclic Voltammetry recorded at 100 mv s^{-1} in 0.1 M H_2SO_4 of the three different carbon nanofibers supports modified with palladium nanoparticles, with a zoom in (**b**).

More interesting than the single monometallic supported nanoparticles, the CV patterns of the bimetallic AuPd alloyed nanoparticles supported on the three nanofibers are shown in **Figure 3.2.7(a)** and zoomed in **Figure 3.2.7(b).** Similarly to the other cases, the broad oxidation signal ascribable to the background reaction is predominant in the case of PS nanofibers, covering the peaks relative to the metal nanoparticles. In the case of LHT, two oxidation peaks at about +1.25 V (SCE) and +1.74 V (SCE) can be observed, related to the Pd and Au oxide formation, respectively. Both are shifted to higher anodic potentials with respect to the monometallic counterparts, in colloidal form (**Figure 3.2.8**)[35].

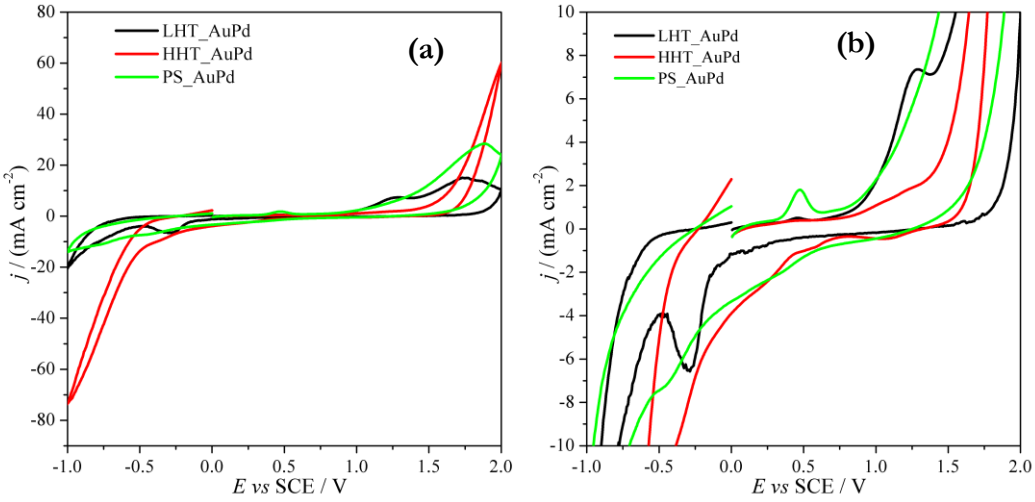

Figure 3.2.7: Cyclic Voltammetry recorded at 100 mv s^{-1} in 0.1 M H_2SO_4 of the three different carbon nanofibers supports modified with alloyed AuPd nanoparticles, with a zoom in (**b**).

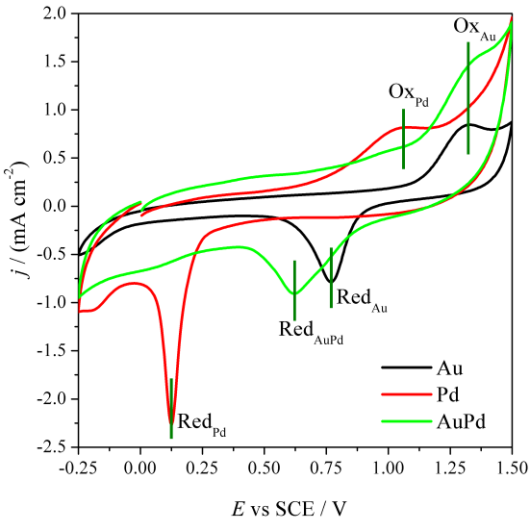

Figure 3.2.8: CV in 0.1 M H_2SO_4 of colloidal Au, Pd and alloyed AuPd nanoparticles.

This evidence could be justified by the presence of a stabilizing effect that the two metals exhibit when they are alloyed, as already known in the Literature[13]. Regarding the cathodic scan, only a single reduction signal at -0.29 V (SCE) is present, probably related to the reduction of the alloyed AuPd oxide. This reaction occurs at more cathodically shifted potential with respect to its monometallic references, being a confirmation of the high stability of the oxide, probably ascribable to the synergistic effect of the co-presence of the two metals and the contribution played by the carbonaceous support. This strong and unexpected potential shift of the main oxide-reduction peak (usually, on bare Pd, in this region it is more likely to have proton absorption), has been observed in other homogeneous noble metals alloys[36] and in other bimetallic Pd-based catalysts supported on carbon nanofibers.[37] Regarding HHT system, a small

oxidation peak around +1.2 V (SCE) is present, as evident by looking at the zoom of **Figure 3.2.7(b)**, which could be related to the formation of the palladium oxide. No signal related to the oxidation of gold can be seen, since it seems that AuNPs oxidation process occurs at higher potential with respect to +2 V (SCE) (the limit of the useful potential window), where the background reaction, OER, takes place. Moreover, the reduction peak in this case is not evident because it is probably too cathodically shifted to be seen, since it could be covered by the HER reaction of the background. These evidences are once more the confirmation of the greater stabilizing effect of HHT on the alloyed nanoparticles.

Electroanalytical Applications

Bare and modified carbon nanofibers were used for the preliminary detection of cinnamyl alcohol and cinnamaldehyde, in order to highlight any differences in the carbonaceous support and in the presence of monometallic or bimetallic nanoparticles. Differences in selectivity and catalytic activity were expected to be found, especially in the bimetallic-modified nanofibers, as already evidenced from the literature in the general filed of catalysis.[38–41] **Figure 3.2.9(a)** and **(b)** report the cyclic voltammetries of the three bare carbon nanofibers (LHT, HHT and PS) in the presence of 3 mM of cinnamaldehyde (**Figure 3.2.9(a)**, on the left) and alcohol (**Figure 3.2.9(b)**, on the right), respectively.

At a first glance, what it can be claimed is that also the bare nanofibers are able to detect the presence of these analytes in solutions. This fact is extremely interesting, since it opens the venue to a huge and interesting field of catalysis and electrocatalysis, based on *metal-free* materials. Moreover, differences in the behavior of the three carbonaceous supports both on the detection of alcohol and aldehyde can be found. In order to clarify better what is happening, each single support is analyzed comparing the answer toward the alcohol and aldehyde (**Figure 3.2.10 (a)**, **(b)** and **(c)**).

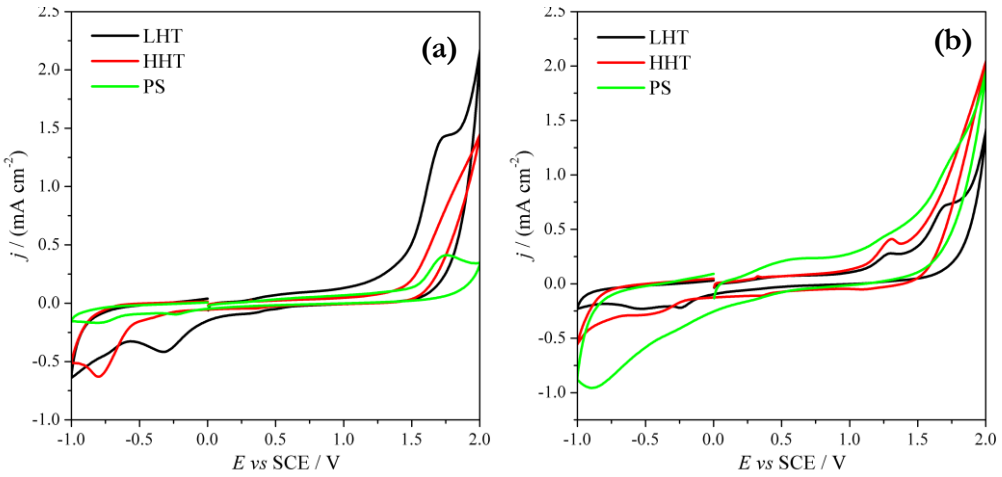

Figure 3.2.9: Cyclic Voltammetry of HHT, LHT and PS carbon nanofibers recorded at 100 mV s^{-1} in a 0.1 M H_2SO_4 solution in the presence of 3 mM cinnamaldehyde **(a)**, on the left, and cinnamyl alcohol **(b)**, on the right.

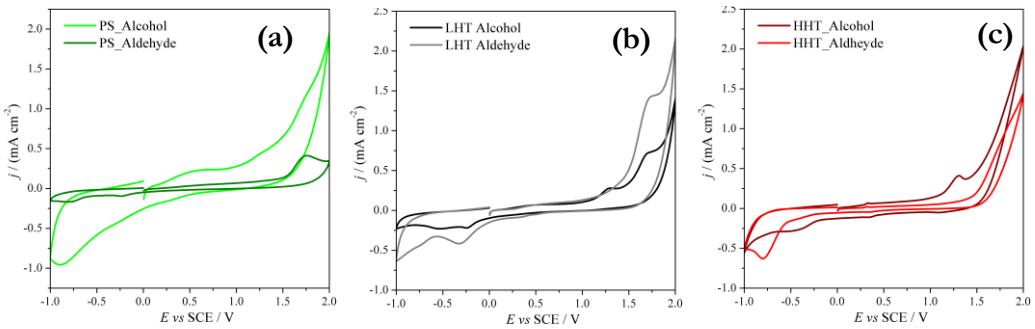

Figure 3.2.10: Cyclic Voltammetry of PS **(a)**, LHT **(b)** and HHT **(c)** carbon nanofibers recorded at 100 mV s^{-1} in a 0.1 M H_2SO_4 solution in the presence of 3 mM cinnamaldehyde or cinnamyl alcohol.

The clearest behavior (focusing for the moment on the anodic oxidation region) seems to happen for LHT nanofiber. In this case, when alcohol is added to the solution, the presence of two signal is highlighted, a first one at +1.30 V (SCE) and a second one at +1.70 V (SCE) (**Table 3.2.3**). The second signal is the same, both in the peak shape and position, when aldehyde is added to the solution. This aspect let us suppose that, in the case of the alcohol oxidation, the first step regards the formation of the aldehyde (**Figure 3.2.11** (**b**)), that is then oxidized again, probably to the carboxylic acid (**Figure 3.2.11** (**c**)). This is happening also in the case of PS,

even if, unfortunately, in the case of the alcohol oxidation the signals are not so clear because of a high capacitive current of the background (**Table 3.2.3**). By the way, regarding the oxidation of the aldehyde, the same peak shape and position observed for LHT is present, meaning that the same product is reasonably created. In this case, thanks to the presence of more defect sites, that are mainly oxygen-rich groups (see **Table 3.2.2**), the formation of the carboxylic acid (that requires, in fact, the addition of an oxygen in the chemical structure) is probably favored (**Figure 3.2.11**). HHT, on the contrary, seems to behave in a different manner. From **Figure 3.2.9** (**a**) it is evident that the oxidative path, especially for the aldehyde, is different from the one observed for the other carbon nanofibers. A shoulder, instead of a clear peak, is present at about +1.85 V (SCE) (**Table 3.2.3**). In addition, **Figure 3.2.10** (**c**) shows that the signal observed for the oxidation of aldehyde is different from the second one relative to the oxidation of alcohol, meaning that also the oxidative path followed by cinnamyl alcohol could be different from the one stated for PS and LHT. In more details, when alcohol is added to the solution, a first strong signal at +1.30 V (SCE) is present but then there are no other signal for a further oxidation, or maybe the relative reaction is covered by the one of the background above +2 V (SCE) (**Table 3.2.3**). Being HHT the most graphitized carbon nanofiber, it is reasonable to think about π–π stacking interaction between the graphitic plane of the support and the planar aldehyde or alcohol. In more details, a hydrogenation path, which leads to the breaking of the C=C double bond, is more likely to happen with this particular support. Moreover, less defect, and consequently less oxygen groups, are present on HHT. In conclusion, from the oxidation of cinnamyl aldehyde it is difficult to think about the formation of the relative carboxylic acid. In fact, the breaking of the C=C bond with the formation of the 3-phenyl propanal (**Figure 3.2.11** (**e**)) is the supposed reaction path (**Figure 3.2.11**). In parallel, in the presence of cinnamyl alcohol, the reaction could lead to the formation of 3-phenyl propanol (**Figure 3.2.11** (**d**)) instead of the cinnamyl aldehyde. For sure the products are concomitantly formed, but maybe in different ratio that the one observed for LHT and PS. The formation of

this alcohol could be the reason why the second peak is practically absent, or it is different from the one of LHT and PS, since it is impossible to create *via* electrochemical oxidation the carboxylic acid starting from this structure. Electrolysis experiments are now under study in order to confirm all these hypothesis.

Table 3.2.3: Voltage relative to the oxidation of cinnamyl alcohol and aldehyde with the three different carbon nanofiber supports.

	E_{ox} (cinnamyl alcohol) / V		E_{ox} (cinnamyl aldehyde) / V
PS	+1.29	+1.72	+1.74
LHT	+1.30	+1.70	+1.73
HHT	+1.30	/	+1.85

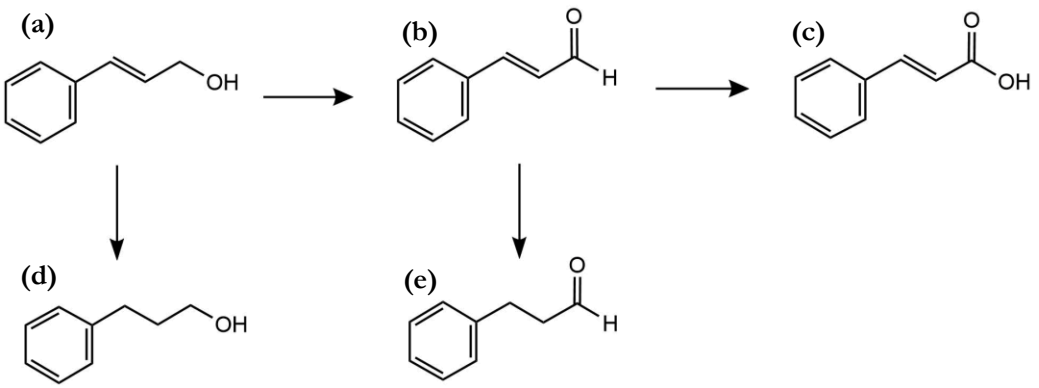

Figure 3.2.11: Schematic representation of the probable reaction path for the oxidation of cinnamyl alcohol (**a**) and aldehyde (**b**) on the three different carbon nanofibers to 3-phenylpropanol (d), 3-phenylpropanale (**e**) and cinnamic acid (**c**).

Regarding the modified carbon nanofibers with monometallic Au, Pd and bimetallic alloy AuPd, their behavior towards cinnamyl alcohol is reported in **Figure 3.2.12**. An aspect that is important to bear in mind, at this point of the dissertation, is that from the synthesis of the Pd-based catalysts, a high amount of hydrides on the surface of the metal are present. This aspect could reflect in a different reactivity of the Pd-modified materials, favoring the hydrogenation path instead of the oxidation

of the C-O ligand. Effectively, this can be observed if looking at the oxidative part of the voltammograms relative to LHT and HHT Pd-modified carbon nanofibers (**Figure 3.2.12 (e)** and **(f)**). In fact, in these cases the oxidative paths seem to be the same observed for the bare HHT nanofiber (**Figure 3.2.9**): the formation of the cinnamyl aldehyde (concomitantly with the hydrogenation to 3-phenyl propanol) than that could not produce the carboxylic acid but maybe creates the 3-phenyl propanal (**Figure 3.2.11 (e)**). Interestingly, Au- and AuPd-modified LHT and HHT carbon nanofibers show a different voltammetric shape and so they follow a different oxidative path.

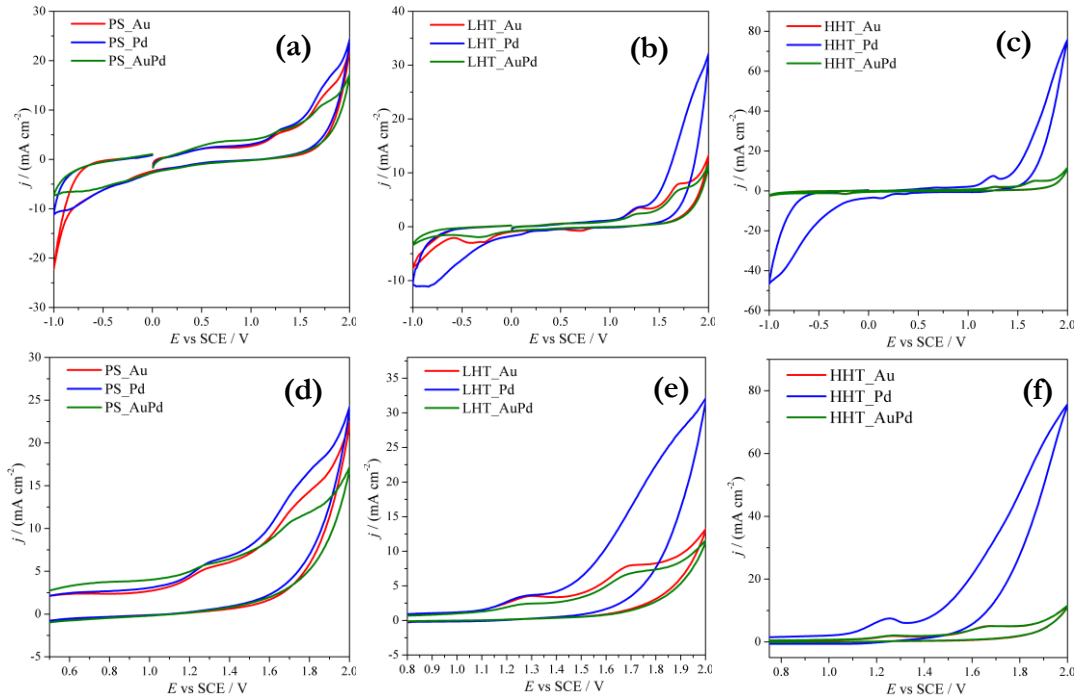

Figure 3.2.12: Cyclic Voltammetry of LHT **(a)**, with relative zoom of the oxidation part in **(d)**, HHT **(b)**, with zoom in **(e)**, and PS **(c)**, with zoom in **(f)**, carbon nanofibers modified with Au, Pd and AuPd nanoparticles in the presence of 3 mM cinnamyl alcohol.

In this case, it seems that it is the metal gold that governs the total activity of the material and leads to the formation of the cinnamyl aldehyde (**Figure 3.2.11 (b)**) and

than the carboxylic acid (**Figure 3.2.11 (c)**). In the case of the alloy, the selectivity of Palladium is so drastically changed and it is basically governed by the presence of gold.

In general, with LHT and HHT carbon nanofibers it seems that the electrochemical activity is based onto the one of the metals. On the contrary, in the case of PS modified carbon nanofibers, the peculiarity observed in the case of LHT-Pd and HHT-Pd modified electrodes are lost and the system behaves in the same way for all the three different materials. In this case, probably the defective structure of the carbonaceous support is dominant onto the electrochemical activity of the material and it governs the overall reaction, quenching the Pd peculiar activity. So, the oxidative pathway is the same one observed for the bare PS with alcohol: oxidation to cinnamyl aldehyde and than formation of the carboxylic acid (**Figure 3.2.11**).

Conclusions

Au, Pd and bimetallic AuPd alloy nanoparticle samples (3-4 nm diameter) have been studied after being supported on three types of carbon nanofibers (PS, LHT and HHT) characterized by a different degree of graphitization (HHT>LHT>PS). First of all, it was proved that the carbon materials are electrochemically more stable and inert in the HHT>LHT>PS order. The subsequent supporting of the metal NPs yields to a different behavior when compared with the non-supported systems. Anodic and cathodic shift in the oxidation and reduction potential positions, related to the formation and disruption of the main oxide is highlighted, in particular in the case of more graphitized HHT support. This effect can be explained considering a strong interaction between the metal systems and the carbon supports, which provides devices characterized by the presence of the metal catalyst, with an unexpected large potential window, which could be exploited for its peculiar activity in catalysis, electrocatalysis and sensing applications.

Preliminary results on the detection of cinnamyl alcohol and aldehyde showed at first that it is possible to open the venue to an interesting field of catalysis, based on *metal-free* materials. Different oxidative pathways could be supposed by changing the graphitization degree and the amount of defects of the carbonaceous support. Regarding the nanoparticle-modified systems, instead, it can be claimed that the electrochemical response seems to be governed by the carbonaceous support in the case of the more defective and less graphitic PS, while it is governed by the metal activity in the case of the more graphitic and less defective ones (LHT and HHT). Moreover, the answer of monometallic-supported-nanoparticles changes, in particular for Pd, when this metal is in the presence of another catalyst, in this case gold. This evidence is a strong support to the expected enhancement behavior of hybrids when compared with the relative counterparts. Further studies will be conducted in order to clarify better the mechanism under investigation, also comparing the catalytic performances with the electrocatalytic ones. In general, it seems that in the case of Palladium-based catalysts the reaction path is slightly different with respect to the gold one. Particularly interesting is, in this contest, the fact that the selectivity of Palladium could be changed by adding gold in its structure. Electrolysis at selected potentials in the presence of cinnamyl alcohol and aldehyde could be conducted, followed by chromatographic analysis on the electrolytic solution in order to understand the nature of the products and the specificity of the bimetallic *vs* monometallic supported nanoparticles. It is important to keep in mind, in fact, that the possibility to tune the selectivity of a catalyst is extremely powerful. Regarding the oxidation of cinnamyl alcohol, in particular, it is interesting to stop the reaction to the production of the cinnamyl aldehyde, which is reported to be an important intermediate in organic transformations and has wide applications in the food and perfume industries[42]. Considering the obtained results, it is possible to claim that electrochemistry could serve as a powerful tool to stop the reaction at the desired product, simply by selecting the right catalysts (bare or metal-modifed) and by conducting the reaction at the suitable potential.

Bibliography

(1) Silvestri, A.; Mondini, S.; Marelli, M.; Pifferi, V.; Falciola, L.; Ponti, A.; Ferretti, A. M.; Polito, L. Synthesis of Water Dispersible and Catalytically Active Gold-Decorated Cobalt Ferrite Nanoparticles. *Langmuir* **2016**, *32* (28), 7117–7126. https://doi.org/10.1021/acs.langmuir.6b01266.

(2) Sardar, R.; Funston, A. M.; Mulvaney, P.; Murray, R. W. Gold Nanoparticles: Past, Present, and Future. *Langmuir* **2009**, *25* (24), 13840–13851. https://doi.org/10.1021/la9019475.

(3) Campbell, F. W.; Compton, R. G. The Use of Nanoparticles in Electroanalysis: An Updated Review. *Anal. Bioanal. Chem.* **2010**, *396* (1), 241–259. https://doi.org/10.1007/s00216-009-3063-7.

(4) Hu, Y.; Zhang, H.; Wu, P.; Zhang, H.; Zhou, B.; Cai, C. Bimetallic Pt-Au Nanocatalysts Electrochemically Deposited on Graphene and Their Electrocatalytic Characteristics towards Oxygen Reduction and Methanol Oxidation. *Phys. Chem. Chem. Phys.* **2011**, *13* (9), 4083–4094. https://doi.org/10.1039/c0cp01998d.

(5) Kim, C.; Dionigi, F.; Beermann, V.; Wang, X.; Möller, T.; Strasser, P. Alloy Nanocatalysts for the Electrochemical Oxygen Reduction (ORR) and the Direct Electrochemical Carbon Dioxide Reduction Reaction (CO_2 RR). *Adv. Mater.* **2018**, *1805617*, 1805617. https://doi.org/10.1002/adma.201805617.

(6) Schrinner, M.; Proch, S.; Mei, Y.; Kempe, R.; Miyajima, N.; Ballauff, M. Stable Bimetallic Gold-Platinum Nanoparticles Immobilized on Spherical Polyelectrolyte Brushes: Synthesis, Characterization, and Application for the Oxidation of Alcohols. *Adv. Mater.* **2008**, *20* (10), 1928–1933. https://doi.org/10.1002/adma.200702421.

(7) Zhang, J. wei; Sun, K. kang; Li, D. dan; Deng, T.; Lu, G. ping; Cai, C. Pd-Ni Bimetallic Nanoparticles Supported on Active Carbon as an Efficient Catalyst for Hydrodeoxygenation of Aldehydes. *Appl. Catal. A Gen.* **2019**, *569* (October 2018), 190–195. https://doi.org/10.1016/j.apcata.2018.10.038.

(8) Gliech, M.; Klingenhof, M.; Görlin, M.; Strasser, P. Supported Metal Oxide Nanoparticle Electrocatalysts: How Immobilization Affects Catalytic Performance. *Appl. Catal. A Gen.* **2018**, *568* (August), 11–15. https://doi.org/10.1016/j.apcata.2018.09.023.

(9) Rodriguez, R. C.; Moncada, A. B.; Acevedo, D. F.; Planes, G. A.; Miras, M. C.; Barbero, C. A. Electroanalysis Using Modified Hierarchical Nanoporous Carbon Materials. *Faraday Discuss.* **2013**, *164*, 147–173. https://doi.org/10.1039/c3fd00018d.

(10) Bracey, C. L.; Ellis, P. R.; Hutchings, G. J. Application of Copper-Gold Alloys in Catalysis: Current Status and Future Perspectives. *Chem. Soc. Rev.* **2009**, *38* (8), 2231–2243. https://doi.org/10.1039/b817729p.

(11) Liu, X. Y.; Wang, A.; Zhang, T.; Mou, C. Y. Catalysis by Gold: New Insights into the Support Effect. *Nano Today* **2013**, *8* (4), 403–416. https://doi.org/10.1016/j.nantod.2013.07.005.

(12) Peneau, V.; He, Q.; Shaw, G.; Kondrat, S. A.; Davies, T. E.; Miedziak, P.; Forde, M.; Dimitratos, N.; Kiely, C. J.; Hutchings, G. J. Selective Catalytic Oxidation Using Supported Gold-Platinum and Palladium-Platinum Nanoalloys Prepared by Sol-Immobilisation. *Phys. Chem. Chem. Phys.* **2013**, *15* (26), 10636–10644. https://doi.org/10.1039/c3cp50361e.

(13) Villa, A.; Wang, D.; Su, D. S.; Prati, L. New Challenges in Gold Catalysis: Bimetallic Systems. *Catal. Sci. Technol.* **2015**, *5* (1), 55–68. https://doi.org/10.1039/c4cy00976b.

(14) Jin, C.; Wan, C.; Dong, R. Electrocatalytic Activity Enhancement of Pd Nanoparticles Supported on Reduced Graphene Oxide by Surface Modification with Au. *J. Electrochem. Soc.* **2017**, *164* (9), H696–H700.

(15) Romero Hernández, A.; Manríquez, M. E.; Ezeta Mejia, A.; Arce Estrada, E. M. Shape Effect of AuPd Core-Shell Nanostructures on the Electrocatalytical Activity for Oxygen Reduction Reaction in Acid Medium. *Electrocatalysis* **2018**, *9* (6), 752–761. https://doi.org/10.1007/s12678-018-0486-y.

(16) Yang, J.; Deng, S.; Lei, J.; Ju, H.; Gunasekaran, S. Electrochemical Synthesis of Reduced Graphene Sheet-AuPd Alloy Nanoparticle Composites for Enzymatic Biosensing. *Biosens. Bioelectron.* **2011**, *29* (1), 159–166. https://doi.org/10.1016/j.bios.2011.08.011.

(17) Mueller, J. E.; Krtil, P.; Kibler, L. A.; Jacob, T. Bimetallic Alloys in Action: Dynamic Atomistic Motifs for Electrochemistry and Catalysis. *Phys. Chem. Chem. Phys.* **2014**, *16* (29), 15029–15042. https://doi.org/10.1039/c4cp01591f.

(18) Pluntke, Y.; Kibler, L. A.; Kolb, D. M. Unique Activity of Pd Monomers: Hydrogen Evolution at AuPd(111) Surface Alloys. *PCCP* **2008**, *10*, 3684–3688. https://doi.org/doi:10.1039/b802915f.

(19) Campisi, S.; Sanchez Trujillo, F.; Motta, D.; Davies, T.; Dimitratos, N.; Villa, A. Controlling the Incorporation of Phosphorus Functionalities on Carbon Nanofibers: Effects on the Catalytic Performance of Fructose Dehydration. *C* **2018**, *4* (1), 9. https://doi.org/10.3390/c4010009.

(20) Tessonnier, J. P.; Rosenthal, D.; Hansen, T. W.; Hess, C.; Schuster, M. E.; Blume, R.; Girgsdies, F.; Pfänder, N.; Timpe, O.; Su, D. S. Analysis of the Structure and Chemical Properties of Some Commercial Carbon Nanostructures. *Carbon N. Y.* **2009**, *47*, 1779–1798. https://doi.org/10.1016/j.carbon.2009.02.032.

(21) Tasis, D.; Tagmatarchis, N.; Bianco, A.; Prato, M. Chemistry of Carbon Nanotubes. *Chem. Rev.* **2006**, *106* (3), 1105–1136. https://doi.org/10.1021/cr050569o.

(22) Tuinstra, F.; Koenig, J. L. Raman Spectrum of Graphite. *J. Chem. Phys.* **1970**, *53*, 1126–1130. https://doi.org/10.1063/1.1674108.

(23) Xie, F. Y.; Xie, W. G.; Gong, L.; Zhang, W. H.; Chen, S. H.; Zhang, Q. Z.; Chen, J. Surface Characterization on Graphitization of Nanodiamond Powder Annealed in Nitrogen Ambient. *Surf. Interface Anal.* **2010**, *42*, 1514–1518. https://doi.org/10.1002/sia.3350.

(24) Martínez, M. .; Callejas, M. .; Benito, A. .; Cochet, M.; Seeger, T.; Ansón, A.; Schreiber, J.; Gordon, C.; Marhic, C.; Chauvet, O.; et al. Sensitivity of Single Wall Carbon Nanotubes to Oxidative Processing: Structural Modification, Intercalation and Functionalisation. *Carbon N. Y.* **2003**, *41*, 2247–2256. https://doi.org/10.1016/S0008-6223(03)00250-1.

(25) Figueiredo, J. L.; Pereira, M. F. R.; Freitas, M. M. A.; Órfão, J. J. M. Modification of the Surface Chemistry of Activated Carbons. *Carbon N. Y.* **1999**, *37*, 1379–1389. https://doi.org/10.1016/S0008-6223(98)00333-9.

(26) Ketteler, G.; Ashby, P.; Mun, B. S.; Ratera, I.; Bluhm, H.; Kasemo, B.; Salmeron, M. In Situ Photoelectron Spectroscopy Study of Water Adsorption on Model Biomaterial Surfaces. *J. Phys. Condens. Matter* **2008**, *20*, 184024. https://doi.org/10.1088/0953-8984/20/18/184024.

(27) Sanchez, F.; Alotaibi, M. H.; Motta, D.; Chan-Thaw, C. E.; Rakotomahevitra, A.; Tabanelli, T.; Roldan, A.; Hammond, C.; He, Q.; Davies, T.; et al. Hydrogen Production from Formic Acid Decomposition in the Liquid Phase Using Pd Nanoparticles Supported on CNFs with Different Surface Properties. *Sustain. Energy Fuels* **2018**, *2* (12), 2705–2716. https://doi.org/10.1039/c8se00338f.

(28) Wang, D.; Villa, A.; Su, D.; Prati, L.; Schlögl, R. Carbon-Supported Gold Nanocatalysts: Shape Effect in the Selective Glycerol Oxidation. *ChemCatChem* **2013**, *5* (9), 2717–2723. https://doi.org/10.1002/cctc.201200535.

(29) Franklin, R. E. Homogeneous and Heterogeneous Graphitization of Carbon. *Nature* **1956**, *177*, 239. https://doi.org/10.1038/177239a0.

(30) Chen, X.; Deng, X.; Kim, N. Y.; Wang, Y.; Huang, Y.; Peng, L.; Huang, M.; Zhang, X.; Chen, X.; Luo, D.; et al. Graphitization of Graphene Oxide Films under Pressure. *Carbon N. Y.* **2018**, *132*, 294–303. https://doi.org/10.1016/j.carbon.2018.02.049.

(31) Wilgosz, K.; Chen, X.; Kierzek, K.; Machnikowski, J.; Kalenczuk, R. J.; Mijowska, E. Template Method Synthesis of Mesoporous Carbon Spheres and Its Applications as Supercapacitors. *Nanoscale Res. Lett.* **2012**, *7*, 269. https://doi.org/10.1186/1556-276X-7-269.

(32) Andreas, H. A.; Conway, B. E. Examination of the Double-Layer Capacitance of an High Specific-Area C-Cloth Electrode as Titrated from Acidic to Alkaline PHs. *Electrochim. Acta* **2006**, *51*, 6510–6520. https://doi.org/10.1016/j.electacta.2006.04.045.

(33) Tasis, D.; Tagmatarchis, N.; Bianco, A.; Prato, M. Chemistry of Carbon Nanotubes Chemistry of Carbon Nanotubes. *Chem. Rev.* **2006**, *106*, 1105–1136. https://doi.org/10.1021/cr050569o.

(34) Bonanni, A.; Pumera, M.; Miyahara, Y. Influence of Gold Nanoparticle Size (2-50 Nm) upon Its Electrochemical Behavior: An Electrochemical Impedance Spectroscopic and Voltammetric Study. *Phys. Chem. Chem. Phys.* **2011**, *13* (11), 4980–4986. https://doi.org/10.1039/c0cp01209b.

(35) Pifferi, V.; Chan-Thaw, C.; Campisi, S.; Testolin, A.; Villa, A.; Falciola, L.; Prati, L.

Au-Based Catalysts: Electrochemical Characterization for Structural Insights. *Molecules* **2016**, *21* (3), 261. https://doi.org/10.3390/molecules21030261.

(36) Grdeń, M.; Łukaszewski, M.; Jerkiewicz, G.; Czerwiński, A. Electrochemical Behaviour of Palladium Electrode: Oxidation, Electrodissolution and Ionic Adsorption. *Electrochim. Acta* **2008**, *53* (26), 7583–7598. https://doi.org/10.1016/j.electacta.2008.05.046.

(37) Maiyalagan, T.; Scott, K. Performance of Carbon Nanofiber Supported Pd-Ni Catalysts for Electro-Oxidation of Ethanol in Alkaline Medium. *J. Power Sources* **2010**, *195* (16), 5246–5251. https://doi.org/10.1016/j.jpowsour.2010.03.022.

(38) Lee, J. H.; Kattel, S.; Jiang, Z.; Xie, Z.; Yao, S.; Tackett, B. M.; Xu, W.; Marinkovic, N. S.; Chen, J. G. Tuning the Activity and Selectivity of Electroreduction of CO2 to Synthesis Gas Using Bimetallic Catalysts. *Nat. Commun.* **2019**, *10* (1), 1–8. https://doi.org/10.1038/s41467-019-11352-0.

(39) Yu, H.; Yang, X.; Wu, Y.; Guo, Y.; Li, S.; Lin, W.; Li, X.; Zheng, J. Bimetallic Ru-Ni/TiO2 Catalysts for Hydrogenation of N-Ethylcarbazole: Role of TiO2 Crystal Structure. *J. Energy Chem.* **2020**, *40*, 188–195. https://doi.org/10.1016/j.jechem.2019.04.009.

(40) Khawaji, M.; Zhang, Y.; Loh, M.; Graça, I.; Ware, E.; Chadwick, D. Composition Dependent Selectivity of Bimetallic Au-Pd NPs Immobilised on Titanate Nanotubes in Catalytic Oxidation of Glucose. *Appl. Catal. B Environ.* **2019**, *256* (May), 117799. https://doi.org/10.1016/j.apcatb.2019.117799.

(41) Yan, H.; Yao, S.; Yin, B.; Liang, W.; Jin, X.; Feng, X.; Liu, Y.; Chen, X.; Yang, C. Synergistic Effects of Bimetallic PtRu/MCM-41 Nanocatalysts for Glycerol Oxidation in Base-Free Medium: Structure and Electronic Coupling Dependent Activity. *Appl. Catal. B Environ.* **2019**, *259* (August), 118070. https://doi.org/10.1016/j.apcatb.2019.118070.

(42) Wu, G.; Brett, G. L.; Cao, E.; Constantinou, A.; Ellis, P.; Kuhn, S.; Hutchings, G. J.; Bethell, D.; Gavrilidis, A. Oxidation of Cinnamyl Alcohol Using Bimetallic Au-Pd/TiO2 Catalysts: A Deactivation Study in a Continuous Flow Packed Bed Microreactor. *Catal. Sci. Technol.* **2016**, *6*, 4749–4758. https://doi.org/10.1039/c6cy00232c.

Acknowledgements:

I gratefully acknowledge Dr. A. Villa and Dr. S. Cattaneo from the Department of Chemistry of Università degli Studi di Milano (Milano, Italy) for the synthesis of the metallic nanoparticles and XPS measurements, Dr. W. Wang and Dr. D. Wang from Institute of Nanotechnology and Karlsruhe Nano Micro Facility, Karlsruhe Institute of Technology (Eggenstein-Leopoldshafen, Germany) for TEM analyses.

3.3 Gold and Silver Bimetallic Systems

Focus

In this part of the PhD Thesis, bimetallic systems based on gold and silver are deeply investigated, both from a physico-chemical point of view and from an electrochemical one. Finally, their possible application in the electrochemical detection of organic halides, with the concomitant highlight of synergistic electrocatalytic effects are taken into consideration.

The interest in Au-Ag based materials arise from the same motivations listed for the other gold-based systems, mentioned in **Paragraph 3.1** and **3.2**, namely AuPt and AuPd nanoparticles. Briefly, the general consideration of gold being an inactive catalyst has been overcome, thanks to the pioneering works done by Haruta. [1–5] In these studies it was remarked that the catalytic activity of gold is strictly dependent on the size of the gold particles,[6–10] on the preparation method [11–13] and on the nature of the support.[12,14–17] In addition, a part from the use of single gold catalysts, it was found and demonstrated that the combination of gold with another metal, different and even less noble than Au, reflects in enhanced performances of the system in general. This aspect is the reason of the studies conducted on bimetallic systems paying attention to their *size*, *shape*, *composition* and *nature of the support*.

In this case, three kind of bimetallic AuAg samples, in alloy or core-shell form, are supported onto carbon nanofibers and deeply analysed by physico-chemical and electrochemical techniques. The initial interest is in the discrimination between the three different compositions (alloy Au+Ag and core shells Au@Ag or Ag@Au), also looking at their modification after aging periods. Electrochemical considerations are compared with Transmission Electron Microscopy (TEM) results and Extended X-Ray Absorption Fine Structure (EXAFS) analyses. The possibility to draw the same conclusion from the three techniques represent a strong demonstration on how Cyclic Voltammetry could represent a valid alternative, cost-effective, simple and easy to use technique to the other normally involved in the study of the morphology

of a bimetallic system. For sure, electrochemistry cannot be considered as the unique source of information, but it represents the perfect tool to be involved for a preliminary screening of the sample, without the need of more sophisticated, time consuming and expensive techniques.

The three above-mentioned systems are finally applied in electroanalytical experiments, particularly in the reduction of organic halides in aprotic solvents. The interest is here focused on the revealing of any synergistic effect present in case of the bimetallic samples (Au+Ag, Ag@Au and Au@Ag), reflecting in electrocatalysis with respect to the single monometallic counterparts (Au and Ag supported nanoparticles). Any difference among the three bimetallics is also investigated, trying to discriminate between the alloyed or core shell morphologies by looking at the shape, position and number of signals relative to the reduction of the target analyte.

Materials and Methods

Metal Nanoparticles – HHT CNFs Preparation

Commercial carbon nanofibers (CNFs), PR24-HHT (here after shortened as HHT) from Applied Sciences, inc. (average diameter of 100 ± 30 nm and a specific surface area of 41 m^2/g) were the pristine carbonaceous materials used as support for metallic nanoparticles. $NaAuCl_4 \cdot 2H_2O$ (99%, Aldrich, St. Louis, MO, USA) and $AgNO_3$ (99%, Aldrich) were used as metal precursors, while $NaBH_4$ (> 98%, Ventron) and polyvinyl alcohol (PVA, MW = 9000–10,000, 80 % hydrolyzed, Aldrich) were used as reducing and protective agents, respectively.

- *Synthesis of Au/HHT, Ag/HHT and AuAg/CNFs*

Monometallic Au and Ag and bimetallic random alloy AuAg catalysts were prepared with a sol-immobilisation technique. In a typical synthesis of Au_xAg_y/CNFs catalyst, the appropriated amount of metal precursor ($HAuCl_4$ and $AgNO_3$) was dissolved in deionised water (Au + Ag concentration 5 x 10^{-4} mol L^{-1}). The stabilising agent, polyvinyl alcohol (PVA, PVA:metal 0.5 wt/wt), was then added and the solution was vigorously stirred. A fresh 0.1 mol L^{-1} aqueous solution of $NaBH_4$ was then prepared and the required amount of reducing agent ($NaBH_4$:metal 4 mol/mol) was rapidly added to the metal precursor solution; a change in colour indicated the successful synthesis of metal nanoparticles. The colloid was left to stir for either 5 min, 2h or 24 h. After the desired ageing time, an aliquot of colloid was withdrawn and rapidly added to a beaker containing 0.5 g of support suspended in 50 mL of deionised water. The amount of colloid was calculated in order to get a final metal loading of 2 wt%. After the addition, the suspension was acidified with 2 drops of concentrated H_2SO_4 in order to decrease the pH to ca. 2. The catalyst was left to stir for 15 minutes, then it was filtered, washed thoroughly with 1 L of deionised water and dried in oven for 4 h at 80 °C.

- *Synthesis of Au@Ag/CNFs and Ag@Au/CNFs*

Bimetallic core-shell Au@Ag and Ag@Au catalysts were prepared with a sol-immobilisation technique. In a typical synthesis, the appropriated amount of metal precursor ($HAuCl_4$ and $AgNO_3$) of the core metal was dissolved in deionised water (in order to have a final Au + Ag concentration of 5×10^{-4} mol L^{-1}). The stabilising agent, polyvinyl alcohol (PVA, PVA:core metal 0.5 wt/wt), was then added and the solution was vigorously stirred. A fresh 0.1 mol L^{-1} aqueous solution of $NaBH_4$ was then prepared and the required amount of reducing agent ($NaBH_4$:core metal 4 mol/mol) was rapidly added to the metal precursor solution; a change in colour indicated the successful synthesis of metal nanoparticles. A new fresh solution of the shell metal precursor was then prepared in deionised water (in order to have a final Au + Ag concentration of 5×10^{-4} mol L^{-1}) and PVA was added (PVA:shell metal 0.5 wt/wt). This solution was then rapidly added to the colloid previously prepared. $NaBH_4$ was finally added ($NaBH_4$:shell metal 4 mol/mol) and the final colloid was left to stir for either 5 min, 2h or 24 h. After the desired ageing time, an aliquot of colloid was withdrawn and rapidly added to a beaker containing 0.5 g of support suspended in 50 mL of deionised water. The amount of colloid was calculated in order to get a final metal loading of 2 wt%. After the addition, the suspension was acidified with 2 drops of concentrated H_2SO_4 in order to decrease the pH to ca. 2. The catalyst was left to stir for 15 minutes, then it was filtered, washed thoroughly with 1 L of deionised water and dried in oven for 4 h at 80 °C.

The three different bimetallic samples were analysed at different "aging" time, meaning that the carbonaceous support was added after 5 min of the nanoparticles reactants' addition, after 2 hours and after 24 hours. These samples, filtered and dried in the oven, were collected and used for the physico-chemical and electrochemical characterizations.

Electrochemical Characterizations

Cyclic voltammetric experiments were performed using an AutoLab PGStat30 (Metrohm AutoLab, Utrecht, The Netherlands) equipped with the NOVA 2.1 Software (Metrohm AutoLab, Utrecht, The Netherlands). The experimental setting was composed of a conventional three electrodes cell in which a saturated calomel electrode and a platinum wire were used as reference (RE) and counter (CE) electrodes, respectively. A glassy carbon (GC) modified with the different carbon nanofiber-supported nanoparticles was used as working electrode (WE). Before the modification, GC was polished with diamond powder (1 μm, Sigma Aldrich, Milan, Italy) on a Struers DP-Nap cloth and rinsed in milli-Q water. 5 mg of the different CNF-NPs powders were suspended in 1 mL EtOH (96 %, Sigma Aldrich) and 4.5 μL Nafion (5% solution in low aliphatic alcohols, Aldrich, Milan, Italy). Then, 20 μL of the suspension were deposited on GC using an automatic micropipette (Kartell, Noviglio, Milano, Italy) and allowed to dry for approximately 30 minutes. Cyclic voltammetries were recorded in aqueous solution with 0.1 M H_2SO_4 as supporting electrolyte. The potential was scanned from −0.3 V (SCE) to +1.5 V (SCE), at a scan rate of 100 mV s^{-1} and a step potential of 5 mV.

Electrochemical Impedance Spectroscopy analyses were conducted on the same above-mentioned set-up (three-electrode cell with SCE, Pt wire and modified Glassy Carbon as RE, CE and WE, respectively) and using an aqueous solution with 0.1 M H_2SO_4 as supporting electrolyte. The experiments were conducted using an AutoLab PGStat30, equipped with a FRA (Frequency Response Analyzer) Apparatus (Metrohm AutoLab, Utrecht, The Netherlands). EIS spectra were recorded at different fixed values of potential (*E*), frequency was varied between 0.1 Hz and 65000 Hz, with an amplitude of 10 mV.

Electroanalytical Applications

All the "5 min" samples were used in the electrochemical reduction of organic halides (Acetobromo-α-D-glucose, ≥ 95 % TLC, Sigma Aldrich, and Benzyl bromide, reagent grade 98 %, Sigma Aldrich) using an AutoLab PGStat128 (Metrohm AutoLab, Uthrecht, The Netherlands) equipped with the NOVA 2.1 Software. The same cell configuration already described in the previous sub-Paragraph was used as experimental set up. Acetonitrile (ACN, ≥ 99.9 %, Sigma Aldrich) was selected as solvent with 0.1 M tetrabutylammonium perchlorate (TBAP, ≥ 99%, Fluka) as supporting electrolyte. Cyclic Voltammetries were performed scanning the potential between -0.5 V (SCE) and -2 V (SCE), at a scan rate of 100 mV s^{-1}, in a deaerated environment: N_2 was bubbled in the solution for 5 min before starting the analysis and the experiments were conducted in a closed cell under N_2 atmosphere.

TEM Analysis

Electron micrographs were obtained using a ZEISS LIBRA200FE microscope equipped with a 200 kV FEG source. Energy-dispersive X-ray spectra (EDS – Oxford INCA Energy TEM 200) and elemental maps were collected along with HAADF-STEM (high angular annular dark field scanning transmission electron microscopy) images. Before the analysis, the samples were finely smashed in an agate mortar, suspended in isopropanol and sonicated. Each suspension was then dropped onto a holey carbon-coated copper grid (300 mesh) and the solvent was evaporated. Histograms of the particle size distribution were obtained by counting onto the micrographs at least 300 particles. The mean particle diameter (d_m) was calculated by using the formula $d_m = \sum d_i n_i / \sum n_i$ where n_i is the number of particle of diameter d_i. The standard deviation was calculated by using the formula $S_d = [\sum n_i (d_i - d_m)^2 / n_i]^{0.5}$.

EXAFS (XAFS and XANES Analyses)

X-Ray Absorption Fine Structure (XAFS) measurements were taken at the BM08 LISA CRG beamline[18] of the European Synchrotron Radiation Facility (ESRF) at Grenoble (France). All catalysts (Au, Ag, Au@Ag, Ag@Au, Au+Ag) and reference samples (Au and Ag foils, Ag_2O and AgCl) were measured in transmission mode, but the catalysts were measured also in fluorescence mode, using at the Au L_3 edge a large-area Si photodiode (thickness 300 μm)[19] and at the Ag K edge a 13-element high purity Ge solid state detector. All spectra were measured at liquid nitrogen temperature (LNT) to reduce the thermal effects that are surely very important for these XAFS measurements, specially at the Au L_3[20]. The absorption coefficient was calculated as $\mu(E) = \ln(I_0/I)$ in transmission mode and as $\mu(E) = I_F/I_0$ in fluorescence mode where I_0, I are the intensities of the incoming and of the transmitted X-ray beams, measured by two ionization chambers, while I_F represents the fluorescence intensity. For energy calibration, using a third ionization chamber the reference Au and Ag foils were measured together with the samples in transmission mode. The reference samples were also used to determine the S_0^2 values[21]. The catalytic samples were prepared pressing into pellets their fine powders with no need of supporting agents like boron nitride or cellulose and the powder amounts were chosen to achieve appropriate edge jumps[22]. In the data analysis both the near edge region (X-Ray Absorption Near Edge Structure, XANES) and the Extended X-ray Absorption Fine Structure (EXAFS) were taken into account. EXAFS data, usually indicated as $\chi(k)$, where k is the photoelectron wave vector[23], were extracted using the ATHENA program[24] and the least-square parameter fitting was performed using the ARTEMIS program[24] both implemented in the IFEFFIT package[25]. The fitting procedure was used to determine the coordination numbers (N), the interatomic distances (R) and Debye-Waller factors (σ^2) of the coordination shells around the absorbing Au and Ag atoms. In the fitting procedure of the reference samples and of many catalysts at the Au L_3 edge, single and multiple-scattering contributions

calculated by the FEFF6 software package[26], were used. At the Ag K edge, only single scattering contributions were included for the bimetallic catalysts. In all cases an estimation of the accuracy of the obtained structural parameters, compatible with data quality and range[27] used, was achieved.

Results and Discussion

In the following paragraph, the analysis of the catalysts by means of the three different characterization techniques (CV, EXAFS and TEM) were at first kept separated. Efforts in the understanding the bimetallic structures compared to the relative monometallics were made, and only after the independent evaluation of the systems, a general comparison of the results were done. Particular attention was paid on the electrochemical characterizations, since the main goal of this work is to justify how electrochemistry could be an alternative, easy to use and low cost tool to know the structure of a hybrid system.

Electrochemical Characterizations – Evolution in time

As previously mentioned, the three bimetallic systems were analysed at different time from their synthesis in order to see if some modifications of the structure is occurring during their formation. 5 minutes, 2 hours and 24 hours were chosen as standard time to be compared internally. The selected samples were analysed by cyclic voltammetry, performing five cycles for each sample, scanning the potential at first in the anodic way and coming back with the cathodic scan. The cycles were not continuous: after one cycle the system was let a couple of seconds in quiescent environment and then another cycle, with the same parameters of the previous one, was performed. In **Figure 3.3.1(a)** the first cycle of the system Ag@Au, (which is supposed to be a core-shell with an external layer of silver, as the synthetic procedure asserts) at the three different times is reported. The same is done for the inverted core-shell system Au@Ag, in **Figure 3.3.1(b)** and for the alloy Au+Ag in **Figure 3.3.1(c)**.

At a first glance, not so many differences can be highlighted between the different times. It seems that the shape of the oxidation and reduction peaks is basically the same for the systems at 5min, 2h and 24h. These considerations are valid for all the

three bimetallics. The differences in the density current values can be ascribed to the quantity of material deposited onto the glassy carbon support. In fact, the suspension of the powder in EtOH is not always homogeneous. Current values, in fact, are normalised for the geometric area of the glassy carbon (0.071 cm^2), even if the active surface area is related to the quantity of the carbonaceous material effectively deposited, which is at the moment hard to be quantified.

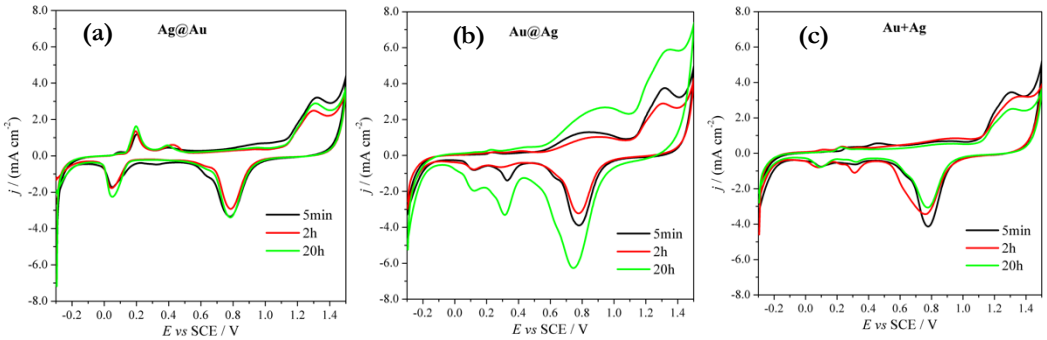

Figure 3.3.1: Cyclic Voltammetry in 0.1 M H_2SO_4 recorded at 100 mV s^{-1} for the three bimetallic systems Ag@Au**(a)**, Au@Ag**(b)** and Au+Ag**(c)** at three different times from the reactants' addition.

Since the systems behave in the same way at the three different times, a different comparison is done, by looking only the "5 min" systems and comparing the three bimetallics at this time from their synthesis. In the next Paragraph a deeper investigation is done.

Electrochemical Characterization – 5 min systems

Ag@Au, Au@Ag and Au+Ag bimetallics are compared at their first voltammetric cycle and results are shown in **Figure 3.3.2**.

Considering that cyclic voltammetry is a surface-sensitive technique, the signals related to the first cycle can be reasonably ascribed to the external structure of the systems. What can be easily seen from the voltammograms in **Figure 3.3.2** is that the **Ag@Au** system is the one with the most marked signals in the region between 0

V (SCE) and +0.4 V (SCE), which corresponds to the oxidation and reduction region of silver. This aspect is a supporting evidence to the fact that the bimetallic system is composed by an external shell made of silver. The presence of the oxidation peak typically ascribed to gold, at around +1.3 V (SCE), is probably due to the fact that the silver-based shell is not perfectly intact or it is too thin to hide the internal core made of gold.[28]

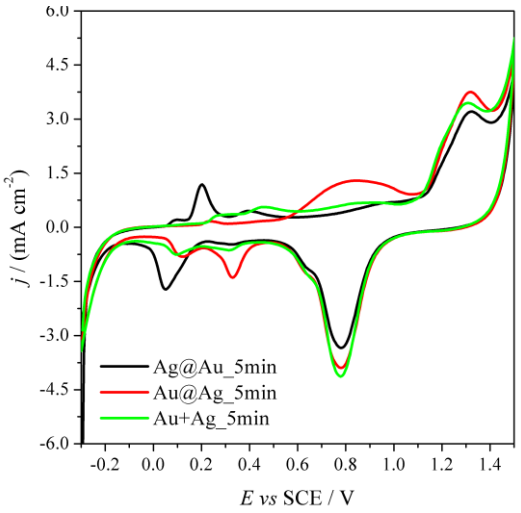

Figure 3.3.2: First CV of the three different bimetallic systems at "5min" from the reactants addition.

Regarding the **Au@Ag** structure, it seems that no signals in the oxidation region of silver are present, meaning that the metal is masked by the external shell, but a broad oxidation signal in the region in between the oxidation of gold and silver is present, at about +0.8 V (SCE). The related reduction peak is reasonably ascribed to the signal at about +0.3 V (SCE), which is absent on the case of the Ag@Au system. These additional signals could be ascribed to a mixed phase of Au and Ag, reasonably in the external shell. Then, the typical oxidation and reduction peak of gold are present. It could happen that the oxidation and reduction of gold lead to a stripping of the external layer, which reveals the internal core made of silver, evident from the presence of a reduction peak at around +0.1 V (SCE). The supposed alloy Au+Ag, instead, has a behaviour which is intermediate between the one of the two core-shell systems. It seems that effectively this material is an alloy, with signals ascribable to gold and silver, a little bit shifted and in some case splitted with respect to the ones of the monometallic counterparts (see for more details the next sub-paragraph "*Au+Ag systems*").

At this point, in order to better clarify the structure of the bimetallics, a deeper investigation of the three systems at 5 min from the reactants addition is conducted, by cycling each sample for 5 times and observing how the voltammetric profiles are changing upon cycling.

- *Ag@Au system*

Figure 3.3.3(a), with details in **(b)** and **(c)**, reports the voltammograms relative to the core-shell Ag@Au system.

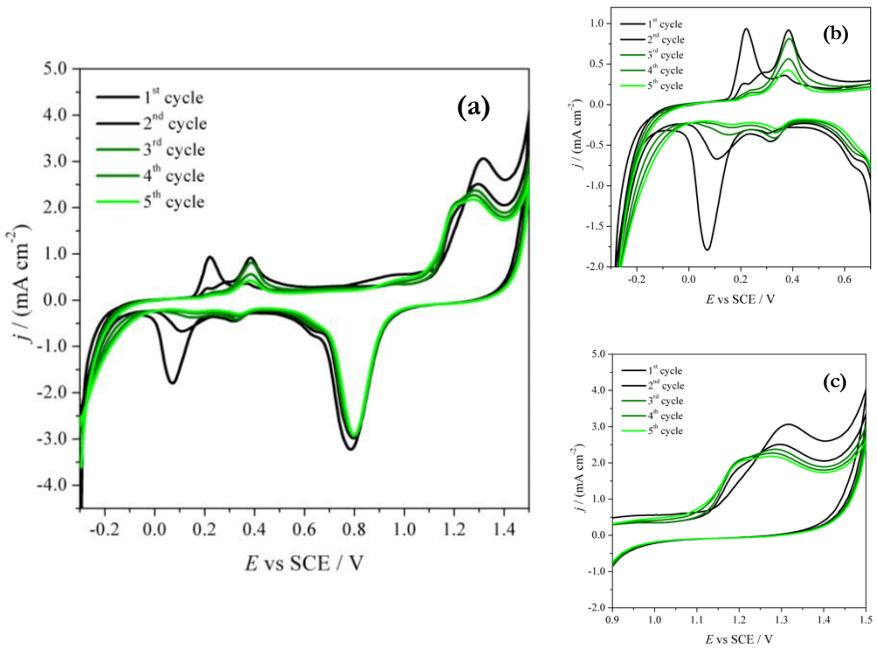

Figure 3.3.3: Cyclic Voltammetry in 0.1 M H_2SO_4 recorded at 100 mV s^{-1} of the bimetallic system Ag@Au**(a)**, with details of the oxidation part relative to silver **(b)** and gold**(c)**.

What is clearly visible from these graphs is that the system is drastically modified when cycling the potential. The first cycle, that should be representative of the external layer, shows a first oxidation peak, at about + 0.2 V (SCE), relative to the oxidation of silver, which is followed by another less intense peak at around +0.4 V (SCE), always related to a Ag specie.[29,30] At around +1.3 V (SCE) the oxidation of

gold occurs, followed by the reduction at +0.8 V. Reduction of silver seems to occur again in two steps, or two different species of silver are reduced, since a small peak at +0.30 V is present, followed by a more intense one at +0.07 V (SCE). This fact is in accordance to what happens in the related oxidation range, where a first intense peak is followed by a smaller one.

Table 3.3.1 reports in detail the values of the peak positions. An interesting feature is that, when cycling, the first oxidation signal of silver is reducing in current intensity values and concomitantly the second one, at higher potential, is growing. It seems like there is a more external layer of Ag, and a second type of silver more internal, which is cycle by cycle more exposed to oxidation and reduction processes. The same happens in the case of gold, since after the first cycle the oxidation peak slightly shifts to lower potential and seems to be splitted in two. This aspect could be ascribable again to the presence of the second metal, Ag, which is affecting the electronic structure of Au.

Table 3.3.1: Oxidation potential values of the bimetallic Ag@Au catalyst compared with the ones of the monometallic Ag and Au nanoparticles.

System	E (Ag_{OX}) / V	E (Ag_{OX}) / V	E (Au_{OX}) / V	E (Au_{OX}) / V
Ag@Au 1st cycle	+ 0.22	+ 0.37	+ 1.18	+ 1.32
Ag 1st cycle	-	+ 0.46	-	-
Au 1st cycle	-	-	-	+ 1.28

In order to clarify this aspect, an in depth look at the positions of the signals in the voltammograms is necessary. The first oxidation peak is related to the oxidation of the first external layer of silver and is drastically different from the Ag monometallic, in particular, it is energentically stabilized by the presence of gold in the structure. In fact, since the oxidation of the bimetallic silver occurs at lower potentials, it means that the process is energetically favoured. It could be present a sort of electron transfer from gold to silver, which is, in this case, more charged in electrons and so it requires less energy to be oxidised by an external power. The hypotesis about the

donation, or the condivision, of electrons from gold to silver is supported also by the observation of a delay in the oxidation potential of gold. In fact, this metal should be less charged in electrons after the donation to silver and so it should require more energy to be oxidised. Looking at the potential values of the bimetallic gold and the monometallic one, in fact, a slight shift from + 1.32 V (SCE) to + 1.28 V (SCE) is observed (see **Table 3.3.1**). When gold is oxidised and reduced, after a complete CV cycle, it seems that the electronic structure is partially recovered. In fact, from the second to the fifth cycle, silver is oxidised at higher potential, being less stabilised by gold, and gold is oxidised at lower potential, donating less electrons and being more stable than that in the first cycle. **Figure 3.3.4 (a)** and **(b)** reports the related voltammograms (of the bimetallic compared to the monometallics).

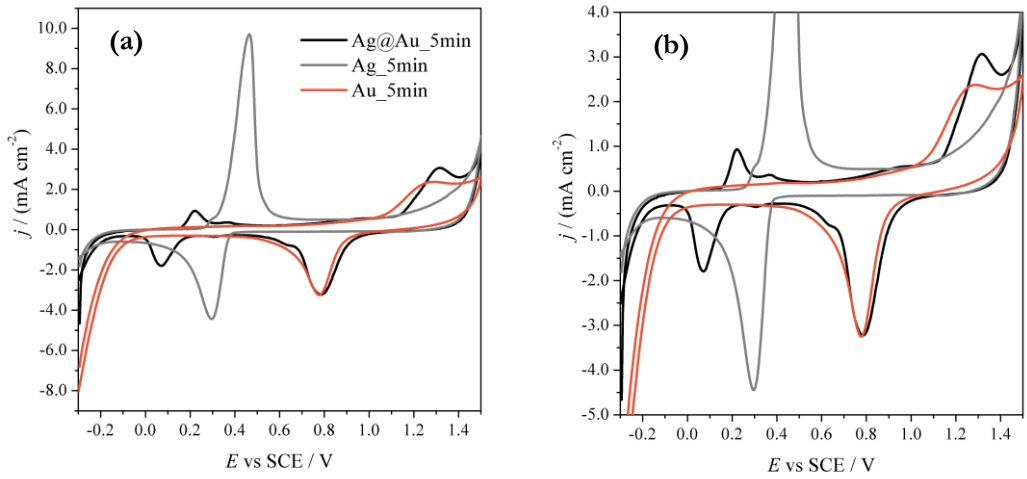

Figure 3.3.4: Cyclic Voltammetry in 0.1 M H_2SO_4 recorded at 100 mV s^{-1} of the Ag@Au bimetallic system compared with monometallic Au and Ag nanoparticles **(a)**, zoom in **(b)**.

In order to better understand the aspect of condivision of electrons, and in general to clarify the influence of one metal to the other, Linear Sweep Voltammetry (LSV) on the whole range or half range of the potential scan were conducted. **Figure 3.3.5 (a)** reports the LSV on the whole oxidation range, while **Figure 3.3.5 (b)** shows the graph obtained when the potential was scanned only between -0.3 V (SCE) and +0.5 V (SCE), in order to comprise only the region relative to the oxidation of silver. It can be noticed how the trend is different from the one observed in the CVs. At the first cycle, as expected, the shape of the curve is the same one of the CV, from the

second to the fifth cycle, instead, there is not the growing of the second peak, but a general drop in the intensity of the current of the first peak and almost the disappearence of the second one.

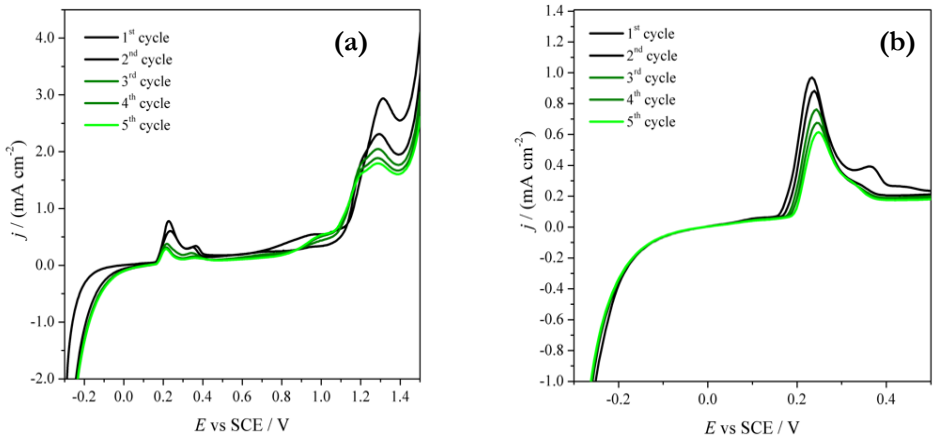

Figure 3.3.5: LSV in 0.1 M H_2SO_4 recorded at 100 mV s^{-1} of the bimetallic system Ag@Au on the whole oxidation potential range **(a)** and only in the first potential range **(b)**.

This is more evident when the oxidation is done only in the shorter potential range (**Figure 3.3.5 (b)**), when gold is not oxidised. What can be hypotised is that the first signal, ascribable to the more external layer, is lowered especially when it is reduced with a complete cycle, and consequently consumed/stripped. About the second peak (at around +0.4 V (SCE)) it seems that it is necessary to involve the oxidation and reduction of gold to let it growing.

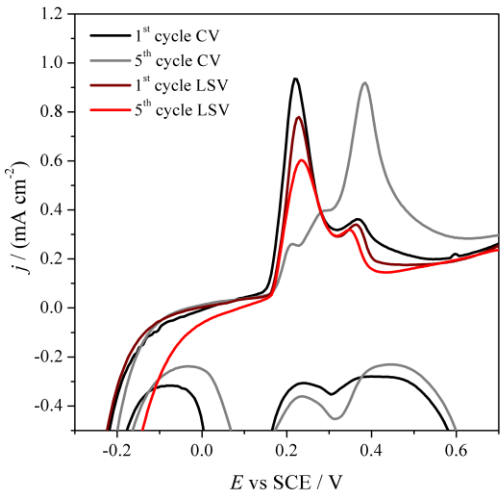

Figure 3.3.6: First and fifth CV compared with the first and fifth LSV of the Ag@Au system.

It is possible at this point to assume that, when cycling the potential, it is like silver is "removed from the clutches" of gold and it is then transformed in a silver species more similar to the monometallic one. If the potential is not scanned until the oxidation and reduction of gold, the

passage from one type of silver to the other is less marked, as it can be seen also in **Figure 3.3.6**.

In conclusion, considering all these observations and considerations, the structure of the bimetallic can be supposed as it follows:

- External shell made of Ag, not intact. It is reasonable to think about a "pure" silver, with Ag-Ag bond, but for sure this species is electronically influenced by gold, more internal in the structure;
- Internal core made of gold, which can be seen from the first cycle because the external shell is not perfectly intact. Also this metal is affected by the presence of silver;
- Mixed phase, in between the external shell and internal core, made of silver and gold, in which the two metals are in intimate contact and connected one to the other, presenting mixed behaviour.

Generally, it can be stated that, passing from the core to the shell, there is a compositional gradient from pure Au to Au-Ag to pure Ag.

- *Au@Ag system*

Figure 3.3.7 (a), with details in **(b)** and **(c)**, reports the voltammograms relative to the core-shell Au@Ag system.

At a first glance, the system behaves in a different way with respect to the Ag@Au previously explained. In this case, what is clearly visible in the first scan, is the presence of a small signal relative to the oxidation of silver, at around +0.22 V (SCE), similar but with lower intensity than the one previously attributed to the external shell of silver, and the presence of a broad oxidation peak at around +0.8 V (SCE). The zone relative to the oxidation of gold seems really similar to the other bimetallic core-shell Ag@Au. From the second cycle, the broad oxidation peak disappears, and

it another peak appears, at +0.39 V (SCE), which gradually loses its current intensity, cycle by cycle. This last signal could be related to a silver specie more similar to the monometallic one, which is found to be oxidised at +0.46 V (SCE), as previously reported in **Table 3.3.1**.

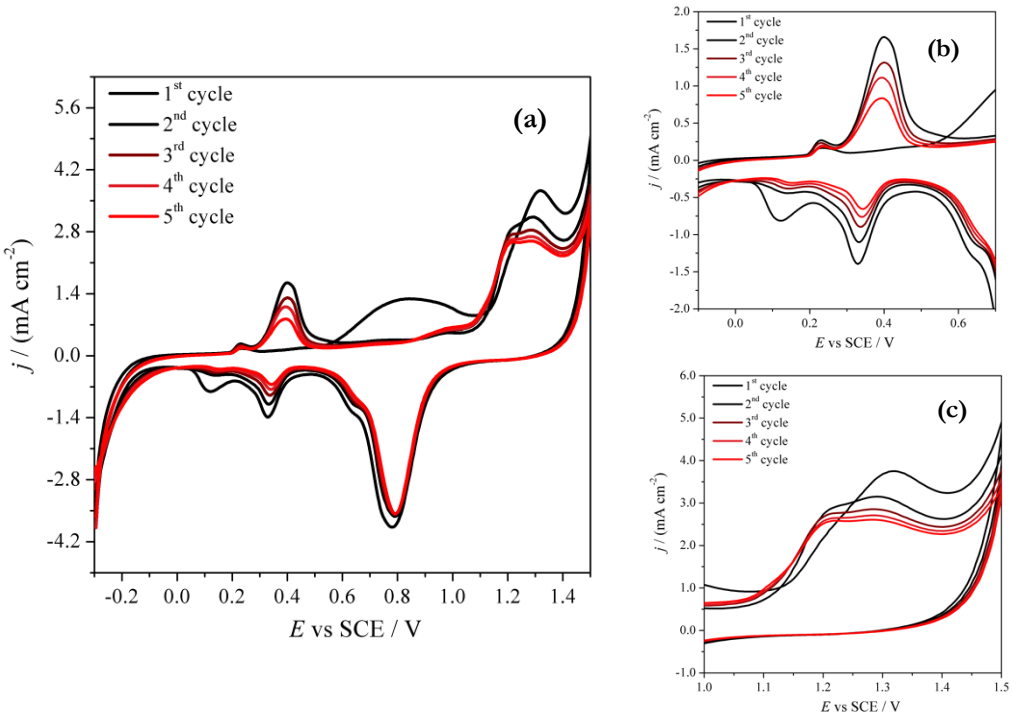

Figure 3.3.7: Cyclic Voltammetry in 0.1 M H_2SO_4 recorded at 100 mV s^{-1} of the bimetallic system Au@Ag**(a)**, with details of the oxidation part relative to silver **(b)** and gold**(c)**.

In this case, the first cycle act as a properly stripping of the external layer. This layer can reasonably be ascribed to a mixed AuAg phase, since the oxidation at +0.89 V is in the middle between the oxidation of the relative monometallic counterparts (+0.46 V for silver and +1.28 V for gold). Values relative to the oxidation voltage of monometallics and Au@Ag bimetallics are reported in **Table 3.3.2** and the relative voltammograms in **Figure 3.3.8 (a)** and **(b)**. As already observed for the Ag@Au, also in Au@Ag case, the oxidation of Ag-related species appears at lower potential with respect to the monometallic Ag, while the oxidation of the Au-related species occurs at higher voltage. This fact is again a confirmation of a possible passage of

electrons from gold to silver and a general sharing of electrons among the two metals in the bimetallic structure.

Table 3.3.2: Oxidation potential values of the bimetallic Ag@Au catalyst compared with the ones of the monometallic Ag and Au nanoparticles.

System	***E*** **(Agox) / V (SCE)**	***E*** **mixed / V (SCE)**	***E*** **(Auox) / V (SCE)**
Au@Ag 1st cycle	+ 0.23	+0.89	+ 1.32
Ag 1st cycle	+0.46	-	-
Au 1st cycle	-	-	+ 1.28

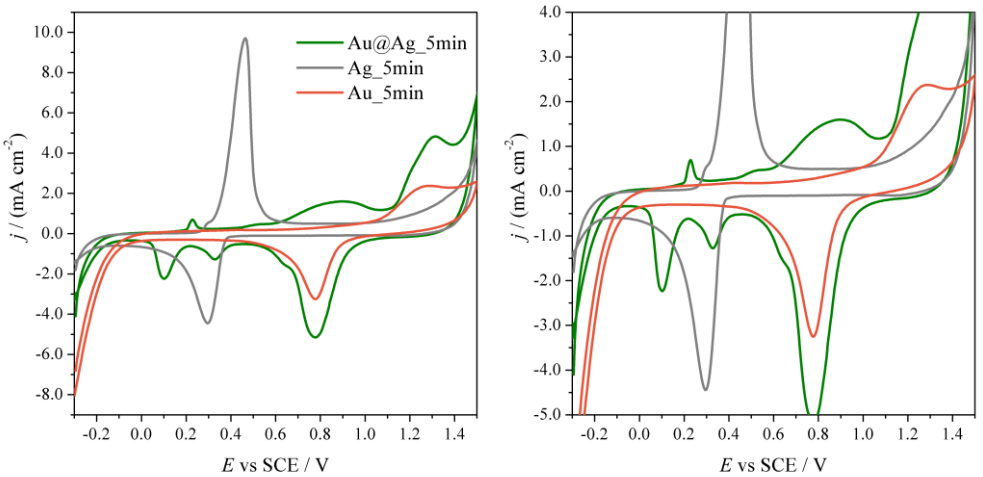

Figure 3.3.8: Cyclic Voltammetry in 0.1 M H_2SO_4 recorded at 100 mV s^{-1} of the Ag@Au bimetallic system compared with monometallic Au and Ag nanoparticles**(a)**, zoom in **(b)**.

The presence of the signal at +0.39 V (SCE) (appearing more intense from the second cycle) is again related to Ag-Ag species. It is possible to imagine a mixed shell that, unlike the previous case, is less rich in silver. The strong signal of the mixed phase is probably due to the fact that in this system the interaction between the two metals is stronger, the interphase is probably more extended and it can be considered as effectively bimetallic.

Also in this case, Linear Sweep Voltammetry on the whole range of potential (**Figure 3.3.9 (a)**) and on restricted one was conducted. It can be noticed how, by looking at

the range which comprises the oxidation of silver, there is only a sharp peak at +0.22 V (SCE), which increases in current intensity with increasing the cycles (**Figure 3.3.9 (b)**). This behaviour is different from what is happening in the cyclic voltammetries. In fact, no peak at +0.4 V are here present. It seems that, when gold is not involved in the potential scan, it is not affecting the electrochemical behaviour of silver, which is just oxidised and maybe cleaned and so it increases in the intensity current response. As for the previous Ag@Au case, the position of the oxidation peak is shifted to lower potential, meaning that this metal is influenced by the presence of gold, being more stabilized. What is different from the previous case is the relative quantity of the metal. In fact, considering the current intensities, for Au@Ag the amount of silver is much less than in the case of Ag@Au. Looking at the range comprising the oxidation of gold, it is evident the presence of the broad oxidation peak at intermediate position (at about +0.8 V (SCE)) ascribable to the mixed phase, and then it is present the typical signal relative to oxidation of gold (**Figure 3.3.9 (c)**). In this case the shape of the signal remains the same even cycling and it is not splitted, as previously observed for the Ag@Au system, also when scanning the potential in the whole range (**Figure 3.3.9 (a)**). It seems that, apart from the general bimetallic system evidenced by the presence of intermediate signals, both Ag and Au exist as "pure" species, with a higher amount of gold with respect to silver. It is gold that governs the whole electrochemical behaviour of this bimetallic, as expected by the fact that it is in the external layer.

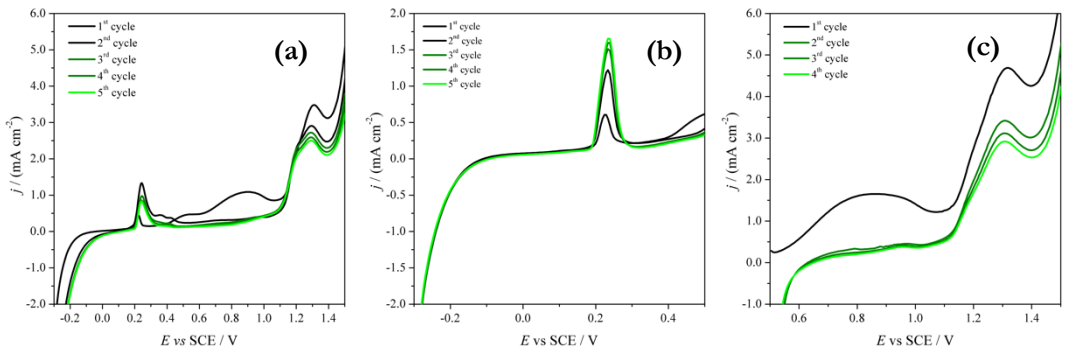

Figure 3.3.9: LSV in 0.1 M H_2SO_4 recorded at 100 mV s^{-1} of the bimetallic system Au@Ag on the whole oxidation potential range **(a)** and only in the first **(b)** and second **(c)** potential range.

- *Au+Ag system*

Figure 3.3.10 (a), with details in **(b)** and **(c)**, reports the voltammograms relative to the bimetallic Au+Ag system.

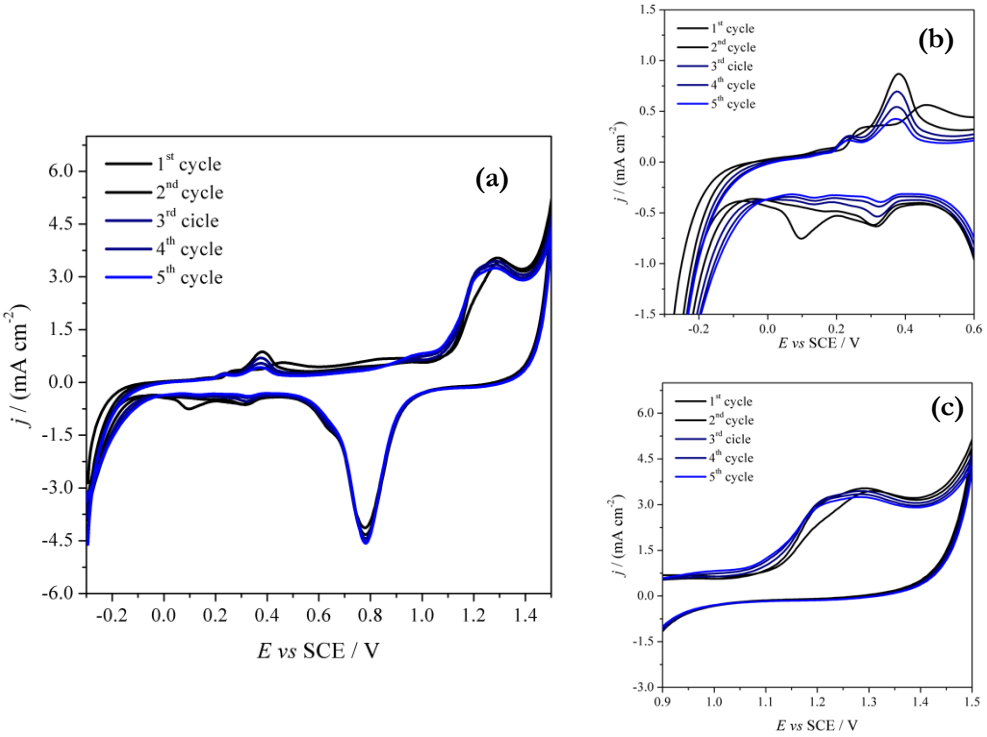

Figure 3.3.10: Cyclic Voltammetry in 0.1 M H_2SO_4 recorded at 100 mV s^{-1} of the bimetallic system Au+Ag **(a)**, with details of the oxidation part relative to silver **(b)** and gold **(c)**.

At a first glance, this system appears as an intermediate situation between the other two (Ag@Au and Au@Ag). In fact, it seems that there is less silver, compared to the Ag@Au core-shell and the signals are more than a single one, in the region +0.2 / +0.5 V (SCE). This is reasonably ascribable to the presence of silver influenced by gold. The oxidation of gold is present as in the other two systems, but this is the only case in which the signal seems splitted in two already in the first cycle. Probably, in this structure, gold is affecting silver, but also silver is affecting gold in the same way and intensity, being a confirmation of the fact that this system act as an alloy, where the metals are in an intimate contact and act differently from the correspondent

monometallic counterparts. For more details, see the potential values in **Table 3.3.3** and the related voltammograms in **Figure 3.3.11 (a)** and **(b)**. As in the Au@Ag system, a broad oxidation plateau at about +0.8 V is present, although of lower intensity. This is probably due to the fact that the bimetallic is well distributed in the whole structure and it is also more masked than the one of the previous system.

Table 3.3.3: Oxidation potential values of the bimetallic Au+Ag catalyst compared with the ones of the monometallic Ag and Au nanoparticles.

System	E (Ag_{OX}) / V	E (Ag_{RED}) / V	E (Au_{OX}) / V	E (Au_{RED}) / V
Au+Ag	+ 0.27 and + **0.45**	**+ 0.31** and + 0.10	+ 1.19 and + **1.30**	+ 0.78
Au	-	-	**+ 1.28**	+ 0.78
Ag	**+ 0.46**	**+ 0.29**		

Regarding the peak potential, one of the two is close to the one of the relative monometallic, while the other is strongly shifted. It seems that there is a mixed phase made of Au and Ag, and the concomitant presence of single phase of gold and silver, maybe segregated metals, in the general alloyed phase.

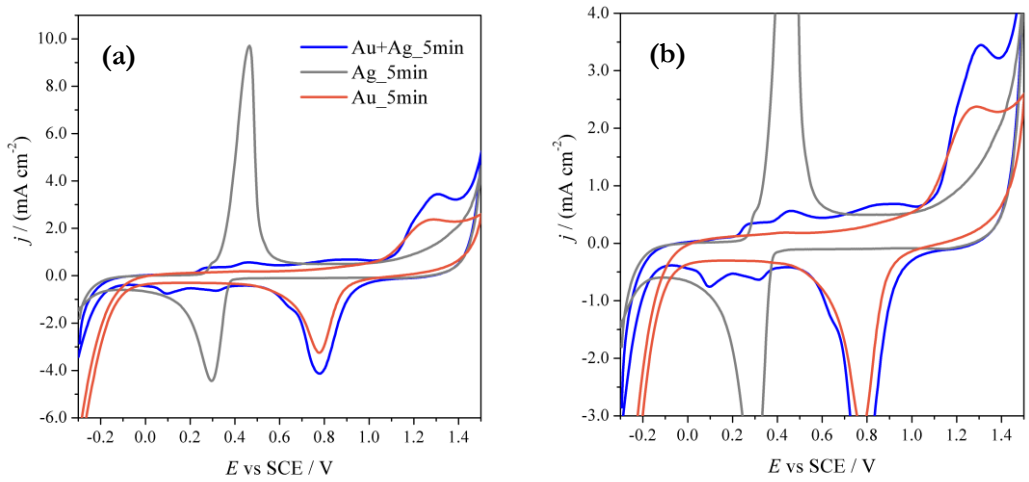

Figure 3.3.11: Cyclic Voltammetry in 0.1 M H_2SO_4 recorded at 100 mV s^{-1} of the Au+Ag bimetallic system compared with monometallic Au and Ag nanoparticles **(a),** with a zoom in the silver oxidation region **(b)**.

Also in this case, Linear Sweep Voltammetry was conducted onto the complete oxidation scan and on the restricted ones (from -0.3 V to +0.5 V (SCE) and from +0.5 V to +1.5 V (SCE)). **Figure 3.3.12 (a)** and **(b)** report the complete range and the first restricted one (*i.e.* the potential comprising the region of silver oxidation), since they are the only situation in which anomalous behaviour (different from the one observed since now) are present.

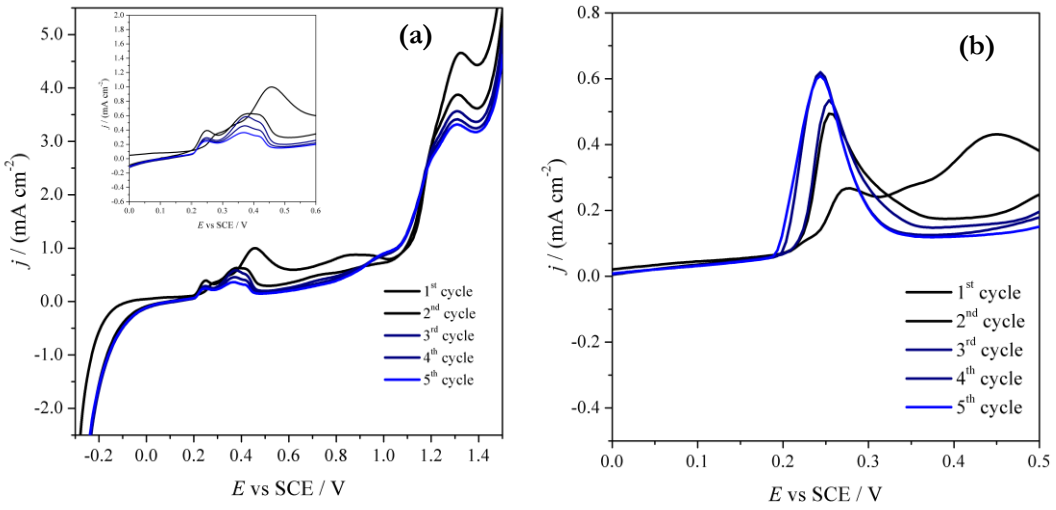

Figure 3.3.12: LSV in 0.1 M H_2SO_4 recorded at 100 mV s^{-1} of the bimetallic system Au+Ag on the whole oxidation potential range **(a)**, with a zoom in the inset, and only in the first **(b)** potential range.

In this system, differently from Ag@Au and Au@Ag, after the first linear scan the fusion of the oxidation peaks relative to silver is absent. On the contrary, the second oxidation signal in the region of silver seems to split, scan by scan, with a general drop in the intensity current values. On the contrary, if the LSV is conducted only in the first scan, the peak fusion of the oxidation of silver is observed, with the current intensity increasing. This fact means that if gold is not oxidised, the presence of silver remains marked (**Figure 3.3.12** (**b**)), while if gold is oxidised, the signals of silver are drastically affected (**Figure 3.3.12** (**a**), inset), attesting a strong relationship among the two metals in this structure.

Electrochemical Characterizations: Summary

Table 3.3.4: Current intensity values of the oxidation peak of silver and gold compared to the reduction peak of gold for the three bimetallic catalysts.

Ag@Au			
***-i (Au$_{RED}$)* = 2.20 10^{-04}**			
	***E* / V**	***i* / A**	***i* / *i*(Au$_{RED}$)**
Ag$_{ox,1}$	+ 0.22	5.72 10^{-05}	**0.26**
Au$_{OX}$	+1.32	1.57 10^{-04}	**0.72**
AgAu$_{OX}$	-	-	-
Au@Ag			
***-i (Au$_{RED}$)* = 3.50 10^{-04}**			
	***E* / V**	***i* / A**	***i* / *i*(Au$_{RED}$)**
Ag$_{ox,1}$	+ 0.23	3.08 10^{-05}	**0.09**
Au$_{OX}$	+1.31	2.36 10^{-04}	**0.67**
AgAu$_{OX}$	+0.89	7.36 10^{-05}	**0.21**
Au+Ag			
***-i (Au$_{RED}$)* = 3.68 10^{-04}**			
	***E* / V**	***i* / A**	***i* / *i*(Au$_{RED}$)**
Ag$_{ox,1}$	+ 0.28	2.00 10^{-05}	**0.05**
Au$_{OX}$	+1.31	2.37 10^{-04}	**0.64**
AgAu$_{OX}$	+0.85	1.48 10^{-05}	**0.04**

In general, it can be observed that in all the three bimetallics, the signal that seems to be more constant both in position and in current intensity, is the reduction peak of gold. For this reason, ratio between the oxidation peaks of silver and gold (single or splitted ones) are calculated with respect to the one of the reduction peak of gold. This ratio can be an indication of the relative quantities of the two metals in the structure. It must be kept in mind that considering the first cycle of the CV, what it is concerned is the external layer. Therefore, the information about the metal quantities we are referring is related to the external layer. Results are listed in **Table 3.3.4**. In particular, the first signal encountered for the oxidation of silver (**Ag$_{ox,1}$** at around +0.2 V (SCE)), the one of the oxidation of gold (**Au$_{ox}$** at around +1.3 V

(SCE)) and the one attributed to the mixed phase (**$AgAu_{ox}$** at around +0.8 V (SCE)) are considered for the three different systems. From the values reported in **Table 3.3.4,** it is evident that the system in which the external amount of silver is the highest one is the Ag@Au core shell ($Ag_{OX,1}/Au_{RED}$ ratio of 0.26 *vs* 0.09 for Au@Ag and 0.05 for Au+Ag), as expected from the synthesis, and as already evidenced from the cyclic voltammetries. The amount of gold (looking at Au_{OX}/Au_{RED}) seems not so different for the three systems (0.72, 0.67 and 0.64 ratios): the slight increased value for Ag@Au could be maybe related to the absence of any contribution of gold to the "mixed" phase, whose signal is absent at the first cycle differently from the other two systems. The amount of this mixed phase is more marked for Au@Ag with respect to the Au+Ag (0.21 *vs* 0.04 ratio), as already evidenced from the cyclic voltammetries.

Electroanalytical Applications – 5 min systems

The three bimetallic systems previously analysed in depth (5 min) were involved in the detection of organic halides, with the aim to highlight any electrocatalytic effect when compared with the monometallic counterparts. The presence of synergistic effects between the two metals, clearly evidenced by the characterization in cyclic voltammetry, is expected to play a key role when the materials are applied as active electrodic systems towards a selected analyte. In this specific case, the reduction of two organic halides (Acetobromo-α-D-glucose and Benzyl Bromide) was studied. As already reported in the Literature, it is known that silver has a strong electrocatalytic effect toward organic halide, when compared to other metals like Au, Cu, Pb and other carbonaceous materials like Boron Doped Diamond (BDD) and Glassy Carbon (GC)[31,32]. According to this fact, the idea of this part of the work is to study the effect of the co-presence of two active metals and to see if their interactions can be practically beneficial.

In **Figure 3.3.13** the response of the three bimetallic systems towards the reduction of acetobromo-α-D-glucose is reported, compared with the relative monometallics Ag and Au ones. It is evident that Ag reacts with the analyte at a more favourable potential with respect to Au, but what it is important to underline is that all the three bimetallics react at potential even more favourable than the Ag alone. Surprisingly, the signal is not in the middle between those of the two single metals, but it is drastically anticipated with respect to both (see **Table 3.3.5**). This is a confirmation of the synergistic effect and of the enhanced performances of these hybrid systems.

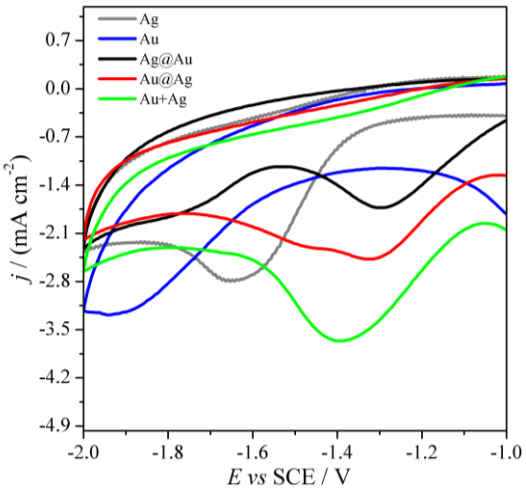

Table 3.3.5: Reduction potential values for the bimetallic and monometallic catalysts towards Acetobromo-α-D-glucose.

System	E_{red} / V
Au	-1.94
Ag	-1.65
Ag@Au	-1.30
Au@Ag	-1.33
Au+Ag	-1.39

Figure 3.3.13: CV of bimetallic and monometallic catalysts registered in ACN with 0.1 M TBAP solution as supporting electrolyte, at 100 mV s^{-1}, in the presence of 2 mM of Acetobromo-α-D-glucose.

At this point, due to an observed poisoning effect of the electrode due to the subsequent addition of the analyte in solution, it was decided to try these systems with another molecule, similar in the electrochemical reductive behaviour, *i.e.* benzyl bromide. The reduction of benzyl bromide is shown in **Figure 3.3.14**. To see more clearly the effects, the answer towards the monometallics is shown in a separated graph (**Figure 3.3.14** (**a**)) with respect to the one of the bimetallics (**Figure 3.3.14** (**b**)). In this case, the situation is even more interesting than the previous one, since it can be possible to distinguish more clearly between the three bimetallics. In fact, also in this case Au reacts at the lowest potentials, followed by Ag and then by the

bimetallics (see **Table 3.3.6**). Bimetallic systems react more or less at the same potential, but with different peak shapes. In fact, it is evident that there are two peaks in the case of bimetallics, reasonably ascribable to Ag and Au in the hybrid, respectively. In the core-shell systems, these peaks are not so clearly separated, while in the case of the Au+Ag alloy they are more defined. In the case of Ag@Au system, it seems that the first peak is prevailing on the second, while the opposite is happening in the case of Au@Ag.

Table 3.3.6: Reduction potential values for the bimetallic and monometallic catalysts towards Benzyl bromide, Δ*E* refers to the difference, in mV, between the monometallic and bimetallic peak positions.

System	E_{red} / V		ΔE_{Au} / mV	ΔE_{Ag} / mV
Au	-1.55			
Ag		-1.36		
Ag@Au	-1.37	-1.19	180	170
Au@Ag	-1.43	-1.20	120	160
Au+Ag	-1.38	-1.11	170	250

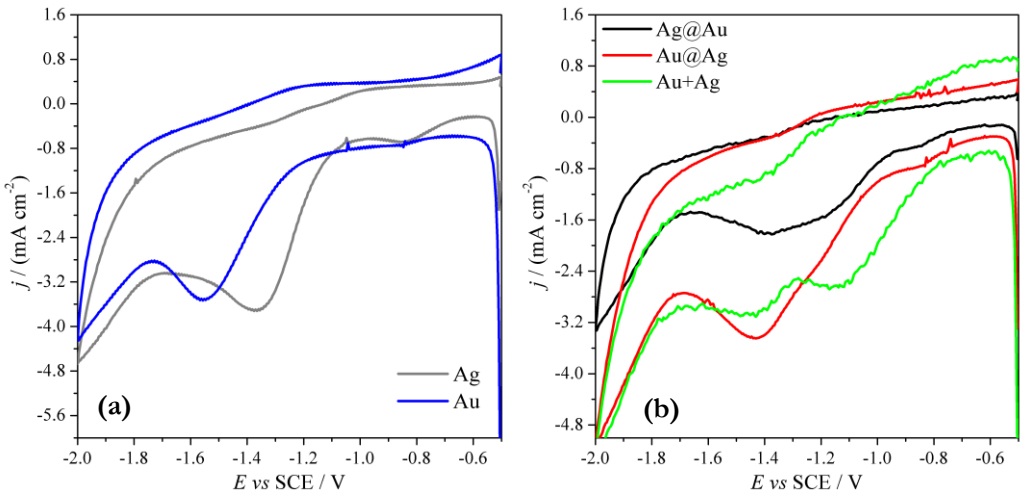

Figure 3.3.14: CV of monometallic (a) and bimetallic (b) catalysts in ACN with 0.1 M TBAP solution as supporting electrolyte, recorded at 100 mV s^{-1}, in the presence of 2 mM of Benzyl bromide.

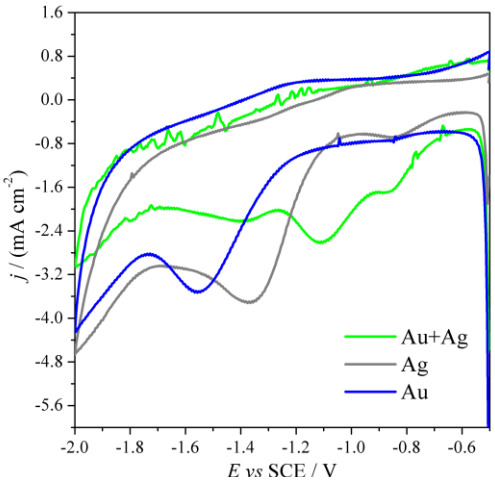

Figure 3.3.15: CV of Au, Ag and Au+Ag catalysts in ACN + 0.1 M TBAP solution, at 100 mV s^{-1}, in the presence of 2 mM of benzyl bromide

In general, it seems that, from an electrocatalytic point of view, the best system is the Au+Ag alloy. These experiments were repeated again by using this hybrid and the results are reproducible and even more clear, as shown in **Figure 3.3.15**.

XAFS Analysis – 5 min systems

XAFS spectroscopy was quite useful in the study of the structure of the monometallic Au, Ag and bimetallic Au-Ag catalysts. In particular, taking into account that Au and Ag have the same FCC structures and very similar lattice parameters, since they have very different backscattering functions this makes XAFS spectroscopy able to distinguish their different contributions[33].

- *Monometallic Au and Ag catalysts*

The monometallic Au sample shows (see **Table 3.3.7** and **3.3.9**) the presence of small FCC Au nanoparticles (N= 9.6) with a small contraction of the nearest neighbour distance. Taking into account the coordination number found and a spherical shape, an estimation of a mean particle dimension gives a $D_{mean} \approx 25$ Å. On the contrary the FCC monometallic Ag nanoparticles (see **Table 3.3.7** and **3.3.10**) are surely bigger (N=11.5) and an estimation of a mean particle dimension gives a $D_{mean} > 80$ Å.

Table 3.3.7: Results of the fitting procedure on the **5min** catalysts Δk= (2.5-14.5) $Å^{-1}$, k^3 for Au and Δk= (2.0-11.8) $Å^{-1}$, k^2 for Ag

Sample	N_1	R_1	σ_1^2	NN_1
Au Foil	12	2.870	0.0038	**Au-Au**
Au	9.6	2.856	0.0051	**Au-Au**
Ag Foil	12	2.872	0.0037	**Ag-Ag**
Ag	11.5	2.872	0.0043	**Ag-Ag**

- *Bimetallic catalysts*

In order to understand the structure of the bimetallic catalyst, it was firstly considered the sum of the coordination numbers (first shell) at the two absorption edges for the three samples. Values are listed in **Table 3.3.8** and in more details in **Table 3.3.9** and **3.3.10**. In all examined spectra **A** is bigger than **B** meaning that in all the bimetallic samples the Au contribution is bigger.

Table 3.3.8: Coordination number of the bimetallic catalysts at the first shell named as **A**= (N_{Au-Au} + N_{Au-Ag}) (Au L_3 edge) and **B**= (N_{Ag-Ag} + N_{Ag-Au}) (Ag K edge)

Sample	A	N_{Au-Au}	N_{Au-Ag}	B	N_{Ag-Ag}	N_{Ag-Au}
Ag@Au	10.3	7.4	2.9	5.7*	2.3	3.3
Au@Ag	10.6	7.3	3.3	9.2	6.5	2.7
Au+Ag	10.7	8.2	2.5	8.0	5.7	2.3

**only for this sample there is a first shell Ag-Cl contribution not included in the sum*

Table 3.3.9: Summary of the results of the fitting procedure on the **5min** catalysts Δk= (2.5-14.5) $Å^{-1}$, k3. **BOLD NN= N_{TOT}(AuAu+AuAg)**

Sample	N_1	R_1	σ_1^2	NN_1
Au Foil	12	2.870	0.0038	**Au-Au**
Au	9.6	2.856	0.0051	**Au-Au**
Ag@Au	7.4 (**10.3**)	2.859	0.0039	**Au-Au**
	2.9	2.8597	0.0039	**Au-Ag**
Au@Ag	7.3(**10.6**)	2.857	0.0041	**Au-Au**
	3.3	2.859	0.0038	**Au-Ag**
Au+Ag	8.2(**10.7**)	2.858	0.0042	**Au-Au1**
	2.5	2.861	0.0048	**Au-Ag**
	4.0	4.050	0.0084	**Au-Au2**

Table 3.3.10: Results of the fitting procedure on the **5m** catalysts Δk= (2.0-11.8) $Å^{-1}$, k^2. **BOLD NN= N_{TOT}(AgAg+AgAu)**

Sample	N_1	R_1	σ_1^2	NN_1
Ag Foil	12	2.872	0.0037	**Ag-Ag**
Ag	11.5	2.872	0.0043	**Ag-Ag**
Ag@Au	2.3 (**5.7**)	2.865	0.0041	**Ag-Ag**
	3.4	2.86	0.0043	**Ag-Au**
	1.6	**2.74**	**0.0067**	**Ag-Cl**
Au@Ag	6.5 (**9.2**)	2.87	0.0055	**Ag-Ag**
	2.7	2.86	0.0041	**Ag-Au**
Au+Ag	5.7(**8**)	2.87	0.0058	**Ag-Ag**
	2.3	2.86	0.0050	**Ag-Au**
AgCl	6	2.76	0.0079	**Ag-Cl**

- *Au + Ag system (AuAg)*

The Au+Ag sample (in the graph named as AuAg) is the one with the highest N_{Au-Au} coordination number and also the one with the smallest Au-Ag contribution (N_{Au-Ag} (Au+Ag) < N_{Au-Ag} (Ag@Au) and N_{Au-Ag}(Au@Ag)), as listed in **Table 3.3.8**.

As **Figure 3.3.16** (**a**) shows for this sample (**EXAFS** spectra), it was possible to fit also the highest coordination shells and, as **Figure 3.3.17** (**a**) shows (**XANES** spectra), there is an Au-Ag interaction, although smaller than the one present in the other two samples. The N_{Ag-Ag} (5.7) of the AuAg sample (see **Figure 3.3.16** (**b**)) is smaller than N_{Au-Au}(8.2), but it can indicate the presence of small Ag cores. Taking both this information into account, it is possible to imagine a structure in which there are big Au cores with an Ag shell, but also small Ag cores surrounded by a Au shell. In this sample **A>B,** means that the gold contribution is higher than the Ag one.

- *Ag@Au system*

In the Ag@Au sample the N_{Au-Au} coordination number is smaller than the one of the previous Au+Ag sample (7.4 < 8.2). Moreover, also the second coordination shell

can be fitted using an Au-Au contribution, but it is not possible to fit the highest coordination shells. Things are clearly changing if compared to the Au+Ag sample, since there is a decrease of the Au-Au contribution and an increase of the Au-Ag one. Only in this sample the Ag-Ag coordination number is very small and the Ag-Ag distance is shorter. Considering this information, it is possible to think about a structure in which there are Au cores surrounded by rich Ag shells. Moreover, the external Ag atoms or segregated ones have also Cl atoms as nearest neighbours, probably deriving from the synthetic procedure (See **Figure 3.3.17 (b)** and **3.3.16 (c)**). In this sample **A>>B,** means that the Au contribution is much higher than the Ag one, probably also due to the presence of Cl atoms.

- *Au@Ag system*

In the Au@Ag samples it seems that there are Au and Ag cores of comparable dimensions, with a slight increase in the case of gold. By the way, even if the contribution of gold is bigger, the value of A and B are almost comparable (**A= 10.6 and B= 9.2)**. In fact, in this configuration, the Ag- Ag contribution is the biggest (but smaller than the Au-Au one) of the three different bimetallics, as it can be seen in **Figure 3.3.16** (**b**). In this sample the presence of Ag is more "invasive" and it is also visible from the shape of the FT at the Au L_3 edge reported in **Figure 3.3.16** (**a**). In this sample it is more difficult to define only the presence of Au-cores and Ag-shells, because also the Ag contribution is relevant.

XANES Analysis – 5 min systems

Concerning the XANES spectra at the Au L_3 edge, as **Figure 3.3.17 (a)** shows, the Au@Ag and the Ag@Au samples are very similar, probably due to their comparable Au-Au and Au-Ag contributions. On the other hand, at the Ag K edge**,** as **Figure 3.3.17 (b)** shows, the Ag@Au sample is the one showing a big difference due to the presence of a AgCl phase, while the XANES spectra of the AuAg and Au@Ag

samples are very similar.

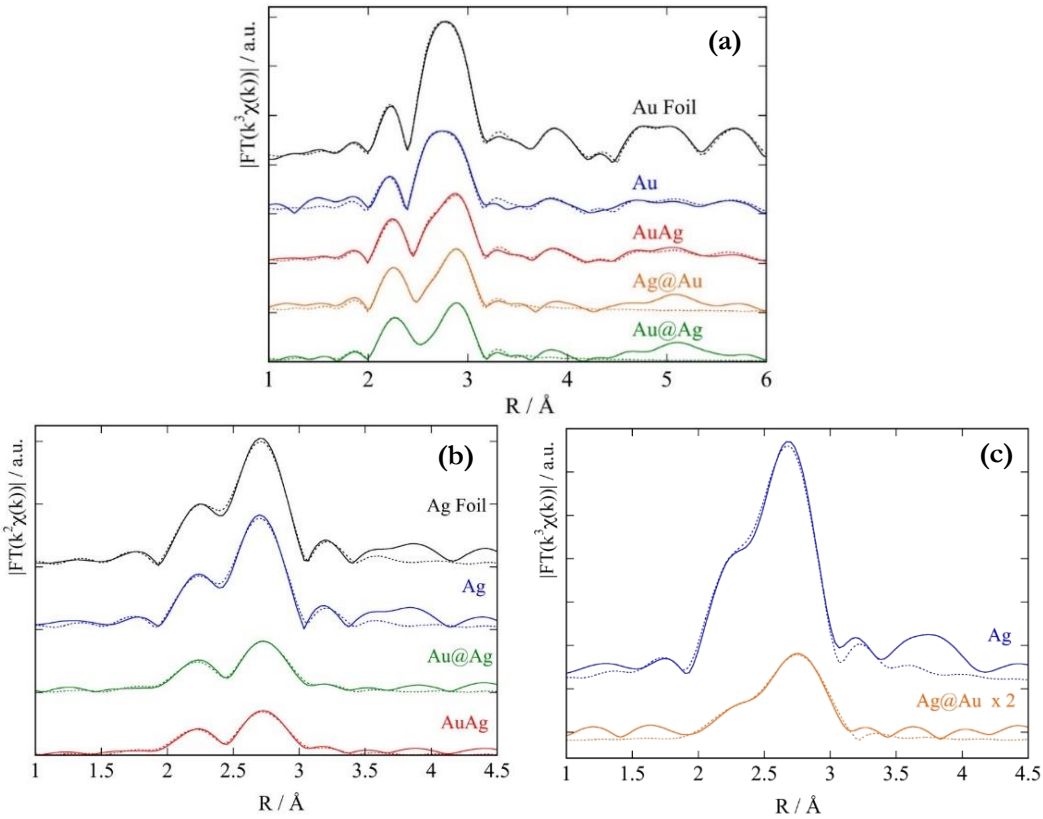

Figure 3.1.16: Fourier transforms of the experimental (full lines) and theoretical (dashed lines) EXAFS spectra of the monometallic and bimetallic samples compared to the one of the Au (a) and Ag (b) and (c) reference sample.

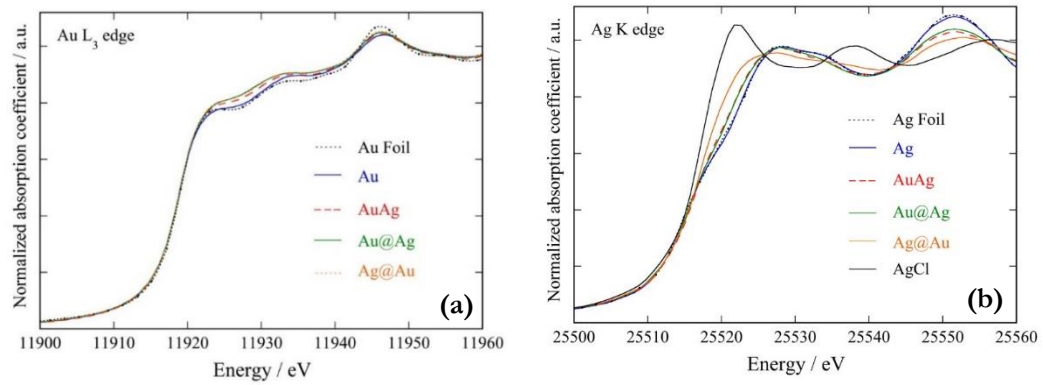

Figure 3.3.17: XANES spectra of the monometallic and bimetallic samples compared to the one of the Au (a) and Ag(b) reference sample.

TEM Analysis

Transmission Electron Microscopy (and High Resolution TEM), together with the previously explained EXAFS, is one of the most powerful technique to characterize nanomaterials. For this reason, it was here involved as an additional technique to understand the structures of mono and bi-metallic AuAg systems under investigation.

Figure 3.3.22 reports TEM images at different magnitude of the supported monometallic Au nanoparticles, with the relative particle size distribution (**Figure 3.3.21**), from which it was found a mean diameter of 2.8 nm. This result is in accordance with the results obtained from XAFS analyses, which gave a mean size of 2.5 nm (see previous Paragraph).

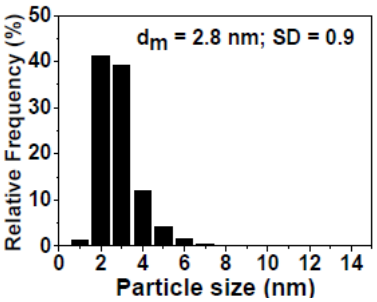

Figure 3.3.21: Size ditribution of Au catalyst.

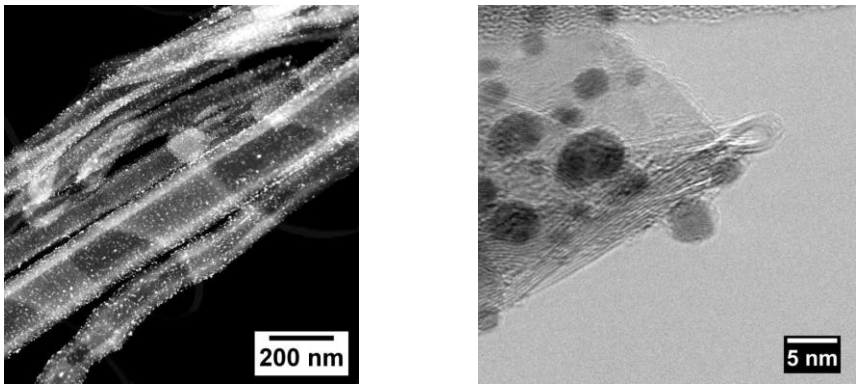

Figure 3.3.22: TEM images at different magnitude of the monometallic Au nanoparticles catalyst.

Concerning the bimetallic structure, a deep investigation of the three systems at 5 min from the synthesis were done, for the final comparison with the other two characterization tools.

Au+Ag system

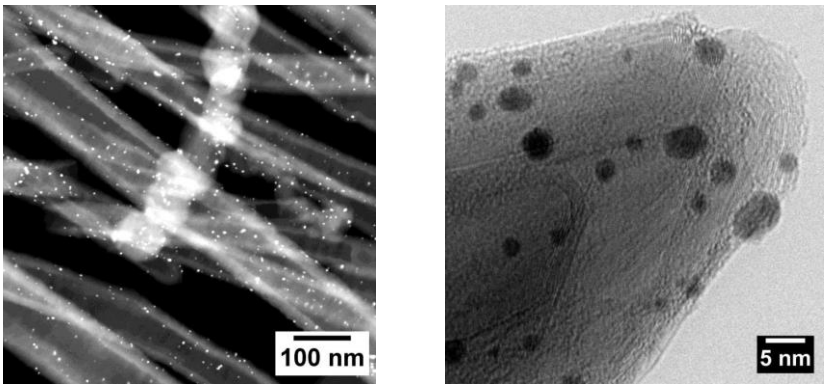

Figure 3.3.23: TEM images at different magnitude of the bimetallic Au+Ag nanoparticles catalyst.

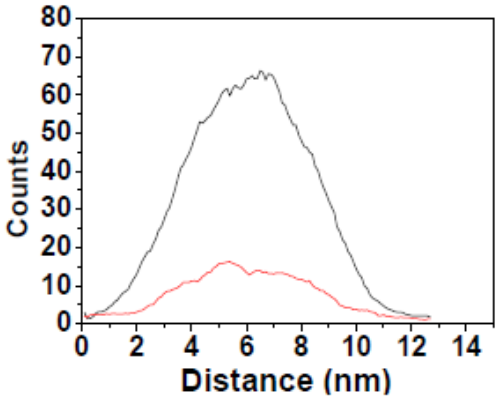

Figure 3.3.24: EDS spectra of Au+Ag catalyst.

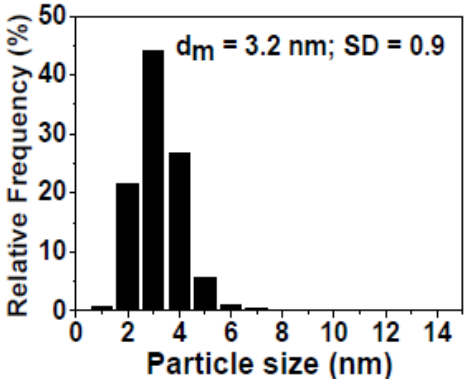

Figure 3.3.25: Size distribution of Au+Ag catalyst.

TEM images of this system (**Figure 3.3.23**) show the presence of an alloy, in which Au and Ag are both present from the internal core to the external shell, as evidenced from the EDS profile on a single particle, in **Figure 3.3.24**. In fact, looking at the shape of the curve (the black one refers to Au, while the red one refers to Ag), it is possible to claim that in the core both metals are present, since there are two lines with a Gaussian shape. This means that, thinking to move from the external to the internal part of the nanoparticle the counts of the metals are increasing from the shell to the core. If there was a core shell structure, the shape of the line would have been flatter. It seems, by the way, focusing on the ratio between the counts of the two metals, that there is an

enrichment of gold (mean composition: atomic gold 59%). In this system, the composition is really close to the nominal one, 50% of Au and 50% of Ag. The particle size distribution (**Figure 3.3.25**) gives a mean diameter of 3.2 nm.

The HADDF profile is reported in **Figure 3.3.26 (a) and Figure 3.3.27 (a)**. The carbon element contribution is shown in **Figure 3.3.26 (b)**, related to the presence of the carbonaceous support (carbon nanofibers, HHT). **Figure 3.3.26 (c)** highlights the contribution of silver atoms (green spots), while **(d)** is related to the gold one (red spots). Line analysis on some particles were conducted, showing that gold and silver are equally distributed (**Figure 3.3.27 (a)** with relative EDX spectra **(b)** and **(c)**).

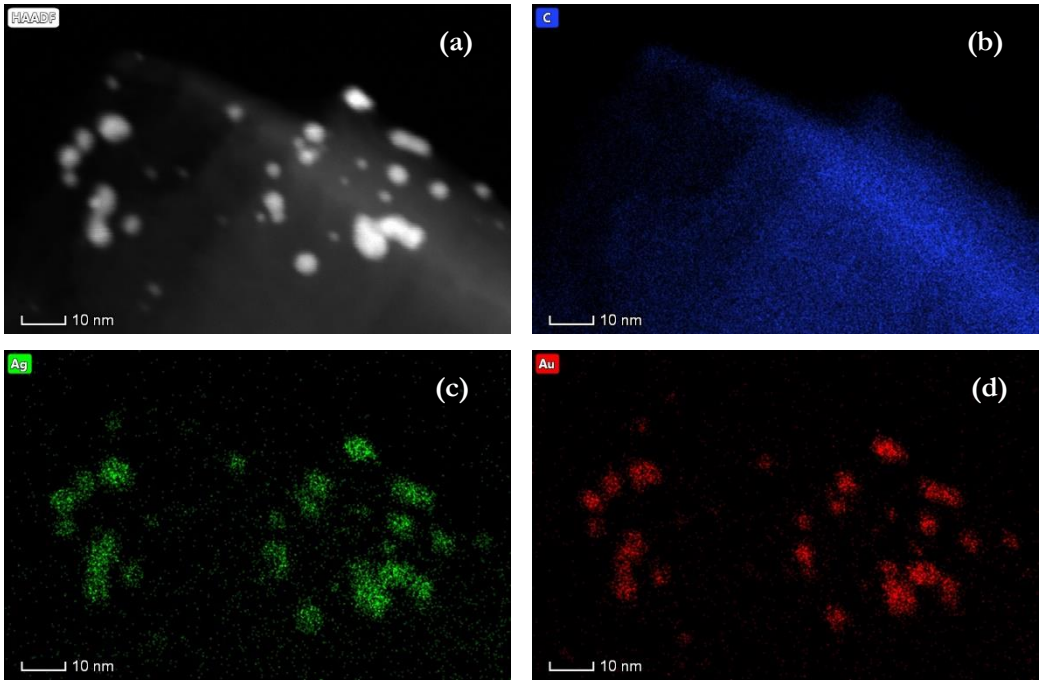

Figure 3.3.26: HAADF images of the bimetallic catalyst Au+Ag with elemental analysis: C **(b)**, Ag **(c)** and Au **(d)**

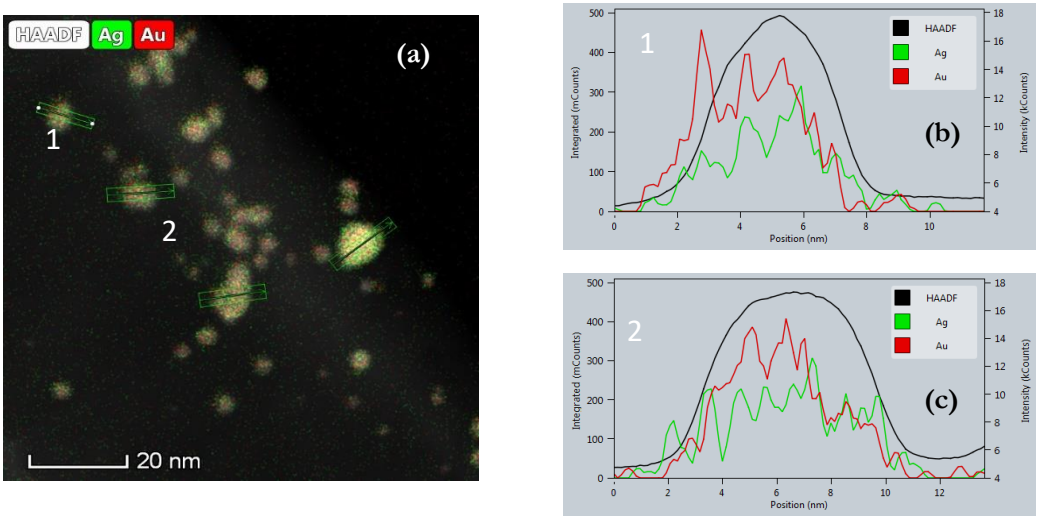

Figure 3.3.27: HAADF analysis of particles of Au+Ag system, with relative line analysis **(b)** and **(c)**

Ag@Au system

Figure 3.3.28 reports TEM images of the bimetallic Ag@Au system. As in the previous Au+Ag case, the nanoparticles are again really small. From the size distribution counts (**Figure 3.3.29**) it was found a mean diameter of 2.8 nm.

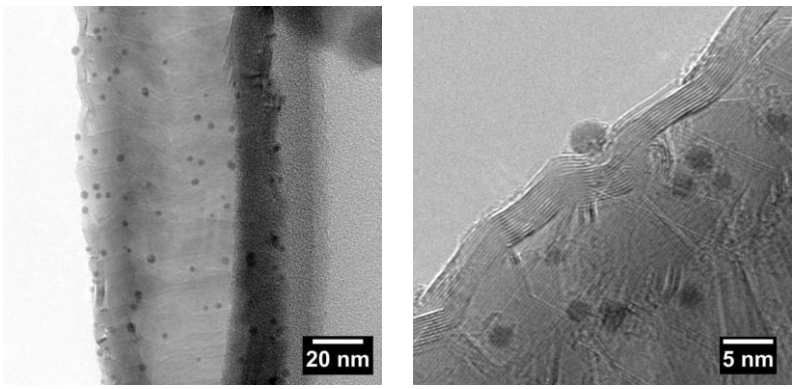

Figure 3.3.28: TEM images at different magnitude of the bimetallic Ag@Au nanoparticles catalyst.

Regarding the EDS profile (**Figure 3.3.30**) on a single particle, in this case it seems that in the core there are both gold and silver, maybe alloyed, but the silver profile is flatter than the one of the Au+Ag system. This evidence could be related to a higher amount of silver also in the shell. HAADF and line analysis (**Figure 3.3.31**) support the hypothesis of having both gold and silver, but if compared with the previous system, the amount of silver seems higher.

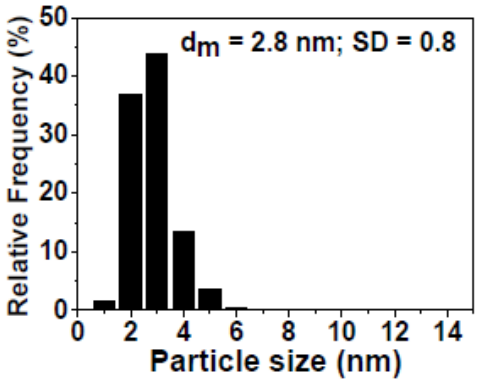

Figure 3.3.29: Size distribution of Ag@Au catalyst nanoparticles.

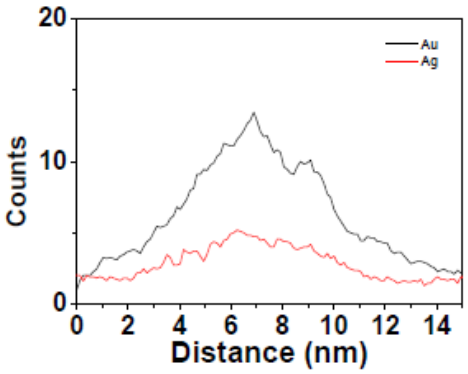

Figure 3.3.30: EDS spectra of Ag@Au catalyst.

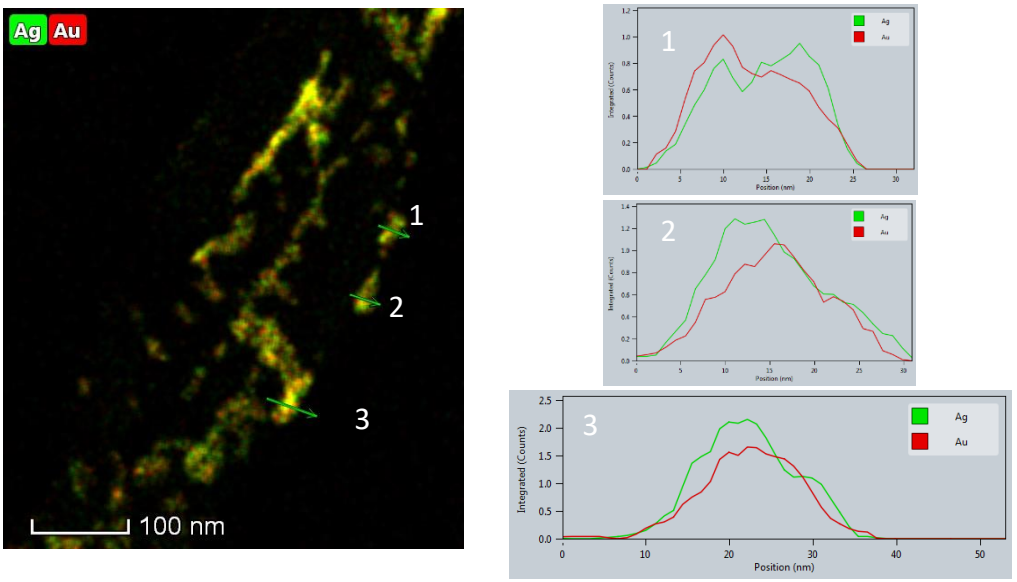

Figure 3.3.31: HAADF analysis of particles of Ag@Au system, on the left with relative line analysis on the right.

Au@Ag system

Figure 3.3.32 reports TEM images of the Au@Ag bimetallic catalyst. Particle size (**Figure 3.3.33**) are in accordance with the other two samples, a little bit higher, with a mean diameter of 3.5 nm. EDS spectra (**Figure 3.3.34**) shows particles that are bimetallic in the whole structure, but with a core that is richer in silver and a shell richer in gold, with respect to the previous samples.

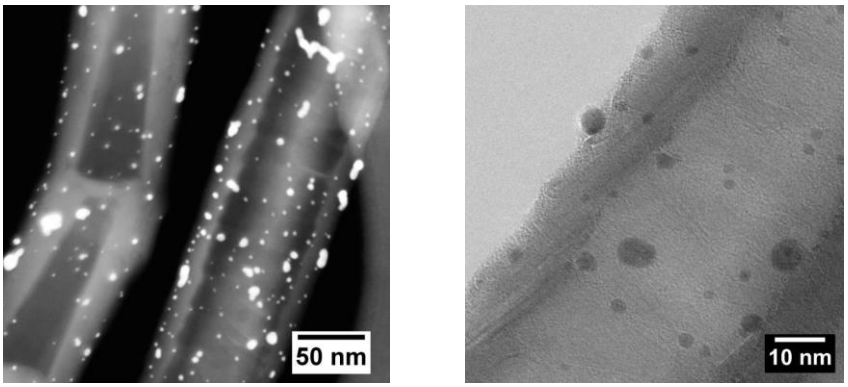

Figure 3.3.32: TEM images at different magnitude of the bimetallic Au@Ag nanoparticles catalyst.

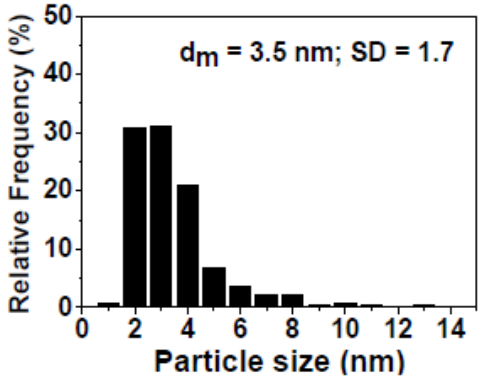

Figure 3.3.33: Size distribution of Au@Ag catalyst nanoparticles.

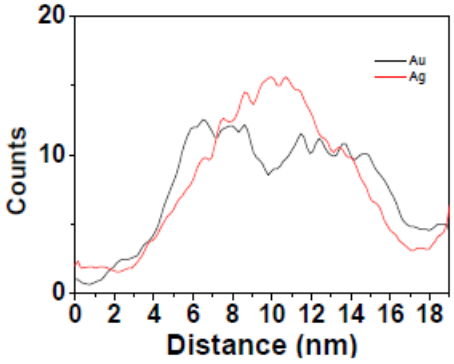

Figure 3.3.34: EDS spectra of Au@Ag catalyst.

HAADF images, supported also in this case by elemental map and line analysis (EDX), show that both gold and silver are present, but for some particles it is possible to clearly see an enrichment of gold in the shell, as evidenced in **Figure 3.3.35**. EDX spectra clearly show that moving from the external to the internal part

of a particle, the amount of silver is prevailing with respect to gold, meaning that the presence of silver cores is reasonably verified.

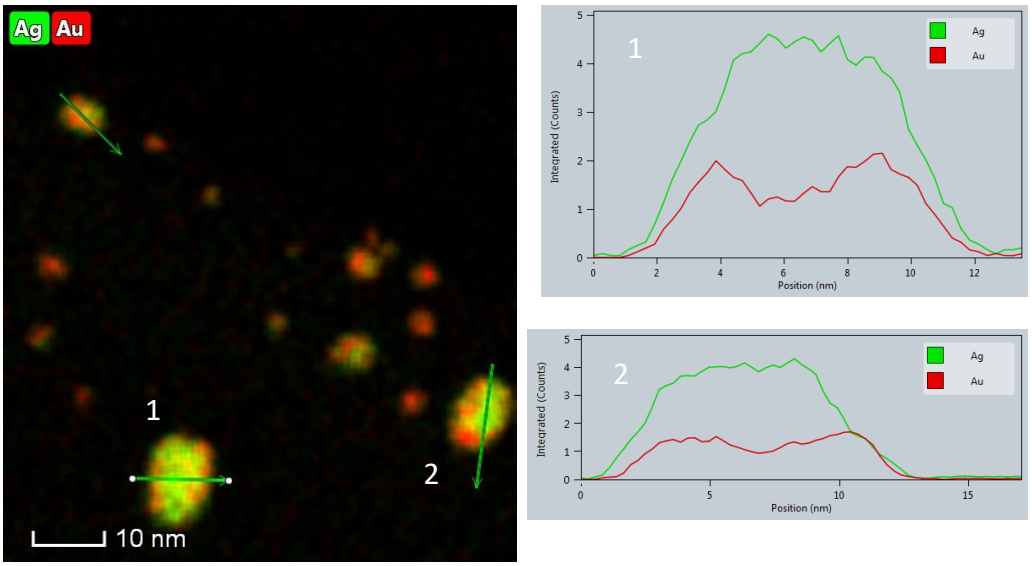

Figure 3.3.35: HAADF analysis of particles of Ag@Au system, on the left with relative line analysis on the right.

Comparison of the three techniques

- *Ag@Au system*

CV experiments showed a structure in which the amount of silver in the external layer is the highest of the three bimetallics. For sure the shell is not intact, since the internal Au is evident from oxidation and reduction peaks. The external shell of silver is then drastically changed after a CV cycle, meaning that it is not so thick and not stable.

EXAFS analyses are in accordance, since they highlighted an external thin layer of silver, maybe due to the presence of Cl atoms deriving from the synthetic procedure. This could reflect also in the low coordination number for Ag-Ag and it is also

responsible of the difficultly encountered in understanding the real structure of the shell.

TEM results seems to confirm what shown from the other two techniques. In fact, from this characterization, the presence of bimetallic AuAg cores is highlighted, but a higher amount of silver, especially when compared with the relative alloyed Au+Ag system is evidenced.

In conclusion, it could be claimed that in this case a perfect core shell is not formed, since the presence of silver is verified also in the cores. Moreover, gold is external too, but in this case the amount of silver seems to be more relevant. It seems that silver shell, really thin and not perfect, are covering bimetallic AuAg clusters.

- *Au@Ag system*

CV experiments showed a system which is different from the Ag@Au core-shell especially looking at the silver part. A bimetallic composite seems to be present even if in low quantities. After a first cycle the presence of silver, similar to the monometallic, is evident, meaning that probably there is the presence of a silver core, in higher amount than the other bimetallics.

EXAFS is in accordance with these considerations because from the coordination number extrapolated from here, the values of N_{Au-Au} and N_{Ag-Ag} are similar, supporting the idea of having Au and Ag nuclei of consistent dimensions. Moreover, N_{Ag-Ag} is the biggest of the three systems, confirming the hypothesis of having silver cores.

TEM images and EDS analysis are again in accordance, showing from line section that the amount of silver is for sure higher in the core, while gold is higher in the shell.

- *Au+Ag system*

CV experiments showed an intermediate structure, in which the external layer seems to be composed by silver and gold, concomitantly, and affected one by the other. In fact, the signals are slightly different in shape and position from the ones of the relative monometallics. It is reasonable to think about a relation between Au-Ag and Ag-Au of comparable intensity, with an enrichment of the contribution given from gold.

EXAFS analyses support what it was observed with CV. In fact, in this material the coordination number of Au-Ag and Ag-Au, even if lower with respect to the other two systems, are internally the most similar when compared one to the other (2.5 vs 2.3), meaning that the relation between the two metals is more or less the same. Also in this case it seems that there is an enrichment of the contribution of gold, but both Au and Ag cores are present.

TEM analyses are again in accordance. In fact, an alloyed structure is proposed, simply by looking at the EDS profile, from which both Au and Ag seems to be present from the shell to the core, with comparable intensities. Only a small enrichment of gold is reported, again confirming what it was previously claimed from CV and EXAFS considerations.

In conclusion, it seems that this system is effectively an alloy, in which there are both core of gold and silver, but for sure there is the highest relation between the two metals and the most distributed mixed AuAg phase in the whole system.

Conclusions

In general, the three techniques are in accordance one to the other. It could be claimed that in all the three bimetallic systems the presence of AuAg particles is high and there is not a clear distinction between the core and the shell. The alloy seems

effectively a bimetallic, but the two supposed core shell show some contamination with the metal that should be in the core present also in the shell.

What is really interesting to underline is the fact that it is possible to draw the same conclusion also from a simple and not so commonly involve technique like cyclic voltammery. In fact, electrochemistry is here proposed as a successful tool for a general and preliminary survey of bimetallic catalysts. The technique is easy to use, low cost, not requiring expensive equipment.

Bibliography

(1) Haruta, M.; Kobayashi, T.; Sano, H.; Yamada, N. Novel Gold Catalysts for the Oxidation of Carbon Monoxide at a Temperature Far Below 0 °C. *Chem. Lett.* **1987**, 405–408. https://doi.org/10.1002/asia.201100575.

(2) Bond, G. C.; Thompson, D. T. Catalysis by Gold. *Catal. Rev.* **2002**, *41* (3–4), 319–388. https://doi.org/10.1081/cr-100101171.

(3) Haruta, M. Size- and Support-Dependency in the Catalysis of Gold. *Catal. Today* **1962**, *36*, 153–166. https://doi.org/10.1016/s0920-5861(96)00208-8.

(4) Kung, H. H.; Kung, M. C.; Costello, C. K. Supported Au Catalysts for Low Temperature CO Oxidation. *J. Catal.* **2003**, *216* (1–2), 425–432. https://doi.org/10.1016/S0021-9517(02)00111-2.

(5) Haruta, M. When Gold Is Not Noble: Catalysis by Nanoparticles. *Chem. Rec.* **2003**, *3* (2), 75–87. https://doi.org/10.1002/tcr.10053.

(6) Boccuzzi, F.; Chiorino, a; Manzoli, M.; Lu, P.; Akita, T.; Ichikawa, S.; Haruta, M. Au/TiO2 Nanosized Samples: A Catalytic, TEM, and FTIR Study of the Effect of Calcination Temperature on the CO Oxidation. *J. Catal.* **2001**, *202* (2), 256–267. https://doi.org/10.1006/jcat.2001.3290.

(7) Valden, M.; Lai, X.; Goodman, D. W. Onset of Catalytic Activity of Gold Clusters on Titania with the Appearance of Nonmetallic Properties. *Science (80-.).* **1998**, *281* (5383), 1647–1650. https://doi.org/10.1126/science.281.5383.1647.

(8) Meier, D. C.; Goodman, D. W. The Influence of Metal Cluster Size on Adsorption Energies: CO Adsorbed on Au Clusters Supported on TiO 2 . *J. Am. Chem. Soc.* **2007**, *126* (6), 1892–1899. https://doi.org/10.1021/ja030359y.

(9) Lopez, N.; Janssens, T. V. W.; Clausen, B. S.; Xu, Y.; Mavrikakis, M.; Pedersen, T. B.; Nørskov, J. K. On the Origin of the Catalytic Activity of Gold Nanoparticles for Low-Temperature CO Oxidation. *J. Catal.* **2004**, *223*, 232–235.

(10) Wallace, W. T.; Whetten, R. L. Carbon Monoxide Adsorption on Selected Gold Clusters: Highly Size-Dependent Activity and Saturation Compositions. *J. Phys. Chem. B* **2000**, *104* (47), 10964–10968. https://doi.org/10.1021/jp002889b.

(11) Moreau, F.; Bond, G. C.; Taylor, A. O. The Influence of Metal Loading and PH during Preparation on the CO Oxidation Activity of Au/TiO2 Catalysts. *Chem. Commun.* **2004**, *4* (14), 1642–1643. https://doi.org/10.1039/b404769a.

(12) Schubert, M. M.; Hackenberg, S.; Van Veen, A. C.; Muhler, M.; Plzak, V.; Behm, J. J. CO Oxidation over Supported Gold Catalysts -"Inert" and "Active" Support Materials and Their Role for the Oxygen Supply during Reaction. *J. Catal.* **2001**, *197* (1), 113–122. https://doi.org/10.1006/jcat.2000.3069.

(13) Chen, Y. J.; Yeh, C. T. Deposition of Highly Dispersed Gold on Alumina Support. *J. Catal.* **2001**, *200* (1), 59–68. https://doi.org/10.1006/jcat.2001.3199.

(14) Kozlov, A. I.; Kozlova, A. P.; Asakura, K.; Matsui, Y.; Kogure, T.; Shido, T.; Iwasawa, Y. Supported Gold Catalysts Prepared from a Gold Phosphine Precursor and As-Precipitated Metal-Hydroxide Precursors: Effect of Preparation Conditions on the Catalytic Performance. *J. Catal.* **2000**, *196* (1), 56–65. https://doi.org/10.1006/jcat.2000.3033.

(15) Arrii, S.; Morfin, F.; Renouprez, A. J.; Rousset, J. L. Oxidation of CO on Gold Supported Catalysts Prepared by Laser Vaporization: Direct Evidence of Support Contribution. *J. Am. Chem. Soc.* **2004**, *126* (4), 1199–1205. https://doi.org/10.1021/ja036352y.

(16) Epling, W. S.; Hoflund, G. B.; Weaver, J. F.; Tsubota, S.; Haruta, M. Surface Characterization Study of Au / α-Fe 2 O 3 and Au/Co 3 O 4 Low-Temperature CO Oxidation Catalysts . *J. Phys. Chem.* **2002**, *100* (23), 9929–9934. https://doi.org/10.1021/jp960593t.

(17) Schumacher, B.; Plzak, V.; Kinne, M.; Behm, R. J. Highly Active Au/TiO2 Catalysts for Low-Temperature CO Oxidation: Preparation, Conditioning and Stability. *Catal. Letters* **2003**, *89* (1–2), 109–114. https://doi.org/10.1023/A:1024731812974.

(18) D'Acapito, F.; Lepore, G. O.; Puri, A.; Laloni, A.; La Manna, F.; Dettona, E.; De Luisa, A.; Martin, A. The LISA Beamline at ESRF. *J. Synchrotron Rad.* **2019**, *26*. https://doi.org/10.1107/S160057751801843X.

(19) D'Acapito, F.; Davoli, I.; Ghigna, P.; Mobilio, S. The ReflEXAFS Station at the GILDA Beamline (BM08) of ESRF. *J. Synchrotron Rad.* **2003**, *10*, 260–264.

(20) Comaschi, T.; Balerna, A.; Mobilio, S. Thermal Dependent Anharmonicity Effects on Gold Bulk Studied by Extended X-Ray-Absorption Fine Structure. *J. Phys. Condens. Matter* **2009**, *21*, 325404.

(21) Rehr, J. J.; Albers, R. C. Theoretical Approaches to X-Ray Absorption Fine Structure. *Rev. Mod. Phys.* **2000**, *72*, 621.

(22) Lee, P. A.; Citrin, P. H.; Eisenberger, P.; Kincaid, B. M. Extended X-Ray Absorption Fine Structure—Its Strengths and Limitations as a Structural Tool. *Rev. Mod. Phys.* **1981**, *53*, 769.

(23) Evangelisti, C. et al. Bimetallic Gold–Palladium Vapor Derived Catalysts: The Role of Structural Features on Their Catalytic Activity. *J. Catal.* **2012**, *286*, 224–236. https://doi.org/10.1016/j.jcat.2011.11.007.

(24) Ravel, B.; Newville, M. ATHENA, ARTEMIS}, HEPHAESTUS: Data Analysis for X-Ray Absorption Spectroscopy Using IFEFFIT. *J. Synchrotron Radiat.* **2005**, *12* (4), 537–541. https://doi.org/10.1107/S0909049505012719.

(25) Newville, M. IFEFFIT: Interactive XAFS Analysis and FEFF Fitting. *J. Synchrotron Radiat.* **2001**, *8* (2), 322–324. https://doi.org/10.1107/S0909049500016964.

(26) Zabinsky, S. I.; Rehr, J. J.; Ankudinov, A.; Albers, R. C.; Eller, M. J. Multiple-Scattering Calculations of x-Ray-Absorption Spectra. **1995**, *52* (4). https://doi.org/10.1103/PhysRevB.52.2995.

(27) Li, G. G.; Bridges, F.; Booth, C. H. XAFS Standards: A Comparison of Experiment and Theory. *Phys. Rev. B* **1995**, *52* (9). https://doi.org/10.1103/PhysRevB.52.6332.

(28) Tschulik, K.; Ngamchuea, K.; Ziegler, C.; Beier, M. G.; Damm, C.; Eychmueller, A.; Compton, R. G. Core-Shell Nanoparticles: Characterizing Multifunctional Materials beyond Imaging - Distinguishing and Quantifying Perfect and Broken Shells. *Adv. Funct. Mater.* **2015**, *25* (32), 5149–5158. https://doi.org/10.1002/adfm.201501556.

(29) Giovanni, M.; Pumera, M. Size Dependant Electrochemical Behavior of Silver Nanoparticles with Sizes of 10, 20, 40, 80 and 107nm. *Electroanalysis* **2012**, *24* (3), 615–617. https://doi.org/10.1002/elan.201100690.

(30) Goda, T.; Oohashi, M.; Matsumoto, A.; Hoshi, T.; Sawaguchi, T.; Pumera, M.; Miyahara, Y. Chemical Optimization for Simultaneous Voltammetric Detection of Molybdenum and Silver Nanoparticles in Aqueous Buffer Solutions. *ChemElectroChem* **2014**, *1* (12), 2110–2115. https://doi.org/10.1002/celc.201402269.

(31) Bellomunno, C.; Bonanomi, D.; Falciola, L.; Longhi, M.; Mussini, P. R.; Doubova, L. M.; Di Silvestro, G. Building up an Electrocatalytic Activity Scale of Cathode Materials for Organic Halide Reductions. *Electrochim. Acta* **2005**, *50* (11), 2331–2341. https://doi.org/10.1016/j.electacta.2004.10.047.

(32) Isse, A. A.; Berzi, G.; Falciola, L.; Rossi, M.; Mussini, P. R.; Gennaro, A. Electrocatalysis and Electron Transfer Mechanisms in the Reduction of Organic Halides at Ag. *J. Appl. Electrochem.* **2009**, *39* (11), 2217–2225. https://doi.org/10.1007/s10800-008-9768-z.

(33) Jouve, A.; Nagy, G.; Somodi, F.; Tiozzo, C.; Villa, A.; Balerna, A.; Beck, A.; Evangelisti, C.; Prati, L. Gold-Silver Catalysts: Effect of Catalyst Structure on the Selectivity of Glycerol Oxidation. *J. Catal.* **2018**, *368*, 324–335. https://doi.org/10.1016/j.jcat.2018.10.019.

Acknowledgements:

I gratefully acknowledge Dr. A. Villa and Dr. S. Cattaneo from the Department of Chemistry of Università degli Studi di Milano (Milano, Italy) for the synthesis of the metallic nanoparticles, Dr. C. Evangelisti from CNR-ISTM, Milano (Italy), for TEM analyses and Dr. A. Balerna from Istituto Nazionale di Fisica Nucleare (Frascati, Italy) for EXAFS data elaboration.

4.

Metal-Semiconductor Hybrids

4.1 Au/TiO_2 Hybrid Materials

Focus

In this part of the PhD Thesis, a hybrid based on AuNPs and a TiO_2 layer is the material under investigation. At the beginning, the interest is focused onto the properties that each single component possess and on how the two materials (AuNPs and TiO_2) interact. Therefore, a deep investigation on the instauration of an effective heterojunction is done, trying to fulfil the gap of the actual research on hybrid materials, which is often dominated by trial and error procedures, missing a deep atomistic understanding of the phenomena located at the heterojunctions. The results are compared with the ones obtained in a previous work conducted on a similar device, modified with silver nanoparticles instead of gold,[1] highlighting strong differences among the two devices.

The final application of this material is the detection of contaminants of emerging concern (in particular, diclofenac). Emerging Contaminants (EC) represent pollutants of new interest due to their recent findings in environmental matrices, especially water, and they have potential human health effects after a chronic exposure. Since now, they are not included in the current legislation for Drinking Water Quality (WHO, 2011) and the Drinking Water Directive – Council Directive 98/83/EC (EC, 1998).[2–7] Only a restricted number of agencies proposed some guidelines for detecting and establishing a provisional safety level, the Drinking Water Guidelines Levels (DWGLs). Among the emerging contaminants, personal care products (PCPs), pharmaceuticals and hormones, illicit drugs, pesticides, artificial sweeteners, perfluorinated compounds, disinfection by-products and sun screen agents can be listed.[8] They are worldwide used substances, almost indispensable for modern societies and it can be assumed that their concentration is going to raise as a result of the increasing trend of urbanisation. All these compounds, and their metabolites, can be introduced into the aquatic environment in complex mixtures via different routes, but especially they derive from effluents of

wastewater treatment plants and from agricultural and industrial activities. In fact, the main problem related to this family of pollutants is that they cannot be removed from water with the conventional treatments (active carbons, flocculation, disinfection).

Diclofenac (IUPAC name: 2-[2-(2,6-dichloroanilino)phenyl]acetic acid) is a Non-Steroidal Anti-Inflammatory Drug (NSAID), used mainly to treat pain and inflammatory diseases. Intercontinental Medical Statistics (IMS) health database reports that, analysing the two-year period 2011-2013 in 86 nations, the global annual consumption of this drug was about 1450 tons (data referring only to the human consumption, not taking into account the animal related consumption). In 2013, diclofenac has been put, along with other pharmaceuticals, into a Watch List by the European Union of "European Water Framework Directive", containing all those emerging compounds that are supposed to be harmful for the environment. According to this document, an Environmental Quality Standard has been set for Diclofenac: the maximum concentrations allowed are 0.1 μg/L in fresh waters and 0.01 mg/L in marine waters (2013/39/EC, European Directive, Diclofenac EQS Dossier 2011). The presence of diclofenac in the environment is mainly due to its excretion, together with its metabolites, by humans and animals. These compounds reach the conventional wastewater treatment plant (WWTP) where they can follow two different routes. On one side, part of Diclofenac is adsorbed by the sludge that, eventually, ends up in a landfill, from where, by percolation, enters in the surface waters; on the other side, it remains in the wastewaters and it is discharged directly into the surface waters. Diclofenac is a fairly persistent drug in the environment, since conventional wastewater treatment systems do not provide a good percentage of removal, as previously mentioned.[9,10]

Nowadays, the detection methods commonly involved for the analysis of emerging contaminants are especially chromatographic ones, usually coupled with mass spectrometry, in order to reach lower detection limits. Extraction methods,

microwave assisted[11] or in combination with rotating disk technologies[12], are other detection tools for these emerging contaminants. Electrochemistry is proposed as low-cost analytical technique for the creation of an "alarm" sensor, for a preliminary screening of the environmental sample, suitable for *on-line*, *on-site* and *continuous* monitoring. In this context, this part of the PhD project rises. The transparent Au/TiO_2 hybrid here proposed, in fact, resulted to be particularly suitable for the detection of diclofenac thanks to the presence of gold nanoparticles, reported to be electroactive towards such analyte.[13] The presence of TiO_2, in addition, allow to create a photo-renewable sensor, whose surface properties and electrochemical response could be restored simply by an UV-light treatment.

Materials and Methods

Synthesis

- *AuNPs synthesis*

0.06 g $AuCl_3$ (≥ 99.99 %, Sigma Aldrich), 0.088 g trisodium citrate (≥ 99%, Sigma Aldrich) and 0.055 g PVP10 (Sigma Aldrich) are separately dissolved in 200 mL Milli-Q and the resulting solution is poured in a three-necked, round-bottomed 500

mL flask equipped with a mechanical stirrer. The solution is cooled in an ice bath, then 0.0075 g $NaBH_4$ (≥ 98%, Sigma Aldrich) dissolved in 5 mL Milli-Q are added dropwise under good stirring. The solution immediately turns red. After the borohydride addition the suspension is left under stirring for additional 10 min. The deep red suspension is transferred in a clean plastic bottle and stored first at room temperature in the dark for a couple of hours (to decompose the excess of borohydride) and then in the fridge.

- *TiO_2 sol synthesis*

TiO_2 sol is synthesized following a known procedure[14]. Briefly, 0.9 mL of HCl 37% (Sigma Aldrich) are added to a solution of $Ti(OC_3H_7)_4$ (Sigma Aldrich) in ethanol (99,8 %, Sigma Aldrich) (0.1 mol in 100 mL) under stirring. Then, 0.47 g of Lutensol ON70 (BASF) are added to the sol after being dissolved in 100 mL of EtOH (99.8 %, Sigma Aldrich). The sol is left under stirring for one hour and then stored in a closed bottle avoiding humidity.

- *Device Assembly*

At first, FTO glass (Sigma-Aldrich (~ 7 (Ω sq)) is sonicated in a cleaning solution (H_2O: 2-propanol (Carlo Erba reagents): Acetone (Sigma Alrdich), 1: 1: 1) and then irradiated for one hour under UV light. Once that the FTO glass is cleaned, it is immersed by dip coating in a solution of H_2SO_4 (97-99%, Sigma Aldrich) for approximatively one minute, in order to favour the cleaning and concomitant

acidification of the support. The support is dried under nitrogen flux. At this point, the conducting glass is dipped in an *ad-hoc* cell containing 18 mL of anhydrous toluene. The environment inside the cell is degassed with nitrogen stream and then the reactor, carefully closed, is immersed in a bath at 70°C for one hour. Then, 36 mL of MPTMS ((3-mercaptopropyl)trimethoxysilane, 95%, Sigma Aldrich) and 4 mL of APTES ((3-aminopropyl)triethoxysilane, 99%, Sigma Aldrich) (9:1 volume ratio) are mixed in 2 mL of toluene (Sigma Aldrich) and added in the reactor, in order to reach a total volume of 20 mL of toluene in the cell. The reactor is then left again at 70°C for three hours. After that, the conducting glass (now functionalized with the binders) is taken off the reactor and cleaned by subsequent sonication step in toluene (Sigma Aldrich), EtOH (96 %, Sigma Aldrich) and Milli-Q water, for five minutes each. These steps contribute to the creation of a single monolayer of binders and to the removal of the un-grafted silane. The device is then immersed in a solution of gold nanoparticles for one hour. After that, the device is washed with Milli-Q water and dried under nitrogen flux. The final step regards the immersion by dip coating of the device in the previously prepared TiO_2 sol, for approximatively one minute. A fast calcination (using a FORNO MAB calcination oven) for one hour at 400°C, under N_2 flow (200 cm^3/min) is conducted, allowing the organic compounds mineralization and the growth of oxide crystallinity, without altering the film transparency.

Physico-Chemical Characterizations

- *UV-Vis*

UV-Vis analyses on the AuNPs sol were performed using a UV-2600 Spectrophotometer, Schimadzu. The synthetic sols were diluted in Milli-Q water in a 1:3 ratio and quartz cuvette were used to register the spectra, in a wavelength range from 200 – 800 nm.

- *Transmission Electron Microscopy (TEM)*

TEM Images of the AuNPs were recorded, using a Zeiss EFTEM LEO 912AB (120 kV). The processing of the dimensions was done using the Image J software.

- *Dynamic Light Scattering (DLS) and Zeta Potential*

DLS analyses were performed onto the AuNPs sol using a Zeta-Sizer Nano ZS Instrument (Malvern Instruments Corp., Malvern, Worcestershire, UK) equipped with a solid state He-Ne laser (λ = 633 nm). In the instrument, the detector is placed at an angulation of 173° in order to detect the backscattered light, excluding in this way excess scattered light. 1 mL of AuNPs was placed into a disposable optical translucent plastic cuvette without any further dilution at a temperature of 298 K. Each hydrodynamic diameter was averaged from three measurements. Fitting was performed using the correlation function $G(t) = 0.15 \cdot \left(A_i \cdot e^{-D_i \cdot q^2 \cdot x}\right)$, where $G(t)$ is the correlation coefficient, A_i the pre-exponential term, D_i the diffusion coefficient, x the time and q the wave vector. q is calculated as $q = \frac{4 \cdot \pi \cdot n}{\lambda} \cdot \sin\frac{\theta}{2}$ where λ is the wavelength of the laser (633 nm), θ the collection angle (173°) and n the reflex index of the medium (in this analysis, since the dispersant is water, n = 1.33).[15]

With the same instrument used for the DLS analysis, also Zeta potential measurements on the AuNPs sol were performed, the only difference is in the cell used for the measurement, which is here a dip-cell suitable for this particular analysis.

Electrochemical Characterizations

All the electrochemical characterizations were carried out using an Autolab PGStat 30 (EcoChemie, Utrecht, The Netherlands) potentiostat/galvanostat equipped with the Nova 2.0 Software (Metrohm Autolab). All the measurements were done in a conventional three-electrode cell equipped with a Saturated Calomel Electrode

(SCE) and a Platinum wire as Reference (RE) and Counter (CE) electrodes, respectively. The working electrode (WE) was the selected FTO glass (2 x 3 cm dimensions), functionalized with only AuNPs, only TiO_2 sol or with the final Au/TiO_2 hybrid. An aqueous solution with 0.1 M $NaClO_4$ was chosen as supporting electrolyte and $K_4[Fe(CN)_6]$ was the selected redox probe for the characterization of the materials. Cyclic Voltammetry (CV) was performed by scanning the potential in a selected potential range with a step of 5 mV at different voltage scan rates (form 0.01 V s^{-1} to 1 V s^{-1}). Electrochemical Impedance Spectroscopy (EIS) was performed at different potentials in the presence and in the absence of the redox probe. Frequencies were varied between 650000 and 0.1 Hz and a sinusoidal potential curve with an amplitude of 10 mV was applied in all cases. All the impedance data were processed by using Z-View 3.1 software.

Photocurrent measurements were performed registering the current at an applied potential (+ 1 V). Initially, the electrode was maintained at the chosen potential in the dark for 600 s; then an halogenide UV lamp (Jelosil HG500) was switched on for 200 s and off for 100 s, repeating 6 times these two steps.

Electroanalytical Applications

The as created electrodes were used as electroanalytical sensors for Diclofenac. A Diclofenac Sodium (DS, Sigma Aldrich) solution has been prepared dissolving the necessary amount of salt in Milli-Q water. The electrochemical analyses were performed in a PBS (Phosphate Buffer) solution as supporting electrolyte at a desired pH of about 4 (reached by adding to the solution the suitable amount of HCl (37%, Sigma Aldrich) and HCl 0.1 M). All the electrochemical measurements were performed with the same instrument used for the electrochemical characterizations, namely an AutoLab PGStat 30 (MetrOhm AutoLab, Utrecht, The Netherlands) and with the same cell configuration (using a platinum wire as Counter electrode, a Saturated Calomel as Reference electrode and the modified FTO as Working

electrode). The experimental parameters were adapted from the Literature[13], briefly, a Cyclic Voltammetry between 0.3 V (SCE) and 1.2 V (SCE) was recorded, with a voltage scan rate of 100 mV s^{-1}.

UV-light treatment

The synthesized devices, after being used as electroanalytical sensors, were subjected to a UV-light treatment in order to investigate the possibility to photo-renovate the surface. In more details, the electrodes were irradiated using an iron-halogenide lamp (with a power of 45 mW cm^2) for different times and in different conditions (in air, in water and in water with stirring). In the last part of the work, it also a commercially available IP95 waterproof ultraviolet Light Emitting Diode (385-400 nm, UV-A level) with a maximum of intensity located at ca. 390 nm was involved. The light power intensity checked by a power meter corresponded to ca. 14 mW cm^{-2}.

Results and Discussion

AuNPs Physico-Chemical Characterization

The synthesized AuNPs, which are expected to have an average diameter of 10 nm, were deeply characterized by UV-Vis, TEM, DLS and Zeta Potential measurements.

UV-Vis spectroscopy is one of the most common technique involved to characterize gold nanoparticles, since from the shape of the spectra it is possible to estimate the size, the concentration and the aggregation of the colloidal solution. The big advantages of this characterization technique is that it requires short time, it is user-friendly and it does not lead to alteration of the sample during and after the analysis.[16] The optical responses of AuNPs are governed by the collective response of conduction electrons, which form an electron gas. When this gas interacts with an external light field, it moves away from equilibrium position, creating a surface polarization charge that acts as a restoring force on the electron gas. The result is a collective oscillatory motion of electrons, called *"plasmonic excitation"*. This motion is characterized by an absorption band, which, for gold, lies in the vis-NIR region of the spectrum. This is the reason why colloidal suspensions of gold nanoparticles are normally red. The plasmonic excitation depends on the characteristics of the particles: any change in shape, size or functionalization alters the electric field on the surface resulting in a change in the oscillatory frequency.[17] As the dimensions of the particles increase, the plasmonic band is red-shifted and it becomes broader: this is why UV-Vis spectroscopy is a valid method to assess the stability and the aggregation of the nanoparticles. In this work, UV-Vis spectra have been recorded monthly in order to evaluate the stability of the colloidal AuNPs sol over time. The related spectra are shown in **Figure 4.1.1**. As it can be seen, a maximum is observed at an average value of 522 nm (see **Table 4.1.1**), which is stable both in the shape and in the position even after several months from the synthesis of the colloid, meaning that the solution is highly stable in time. The first red-shifted value (13_Nov_2018, 526 nm) can be ascribed to an initial instability of the sample and to a consequent non-homogeneous size distribution of AuNPs.

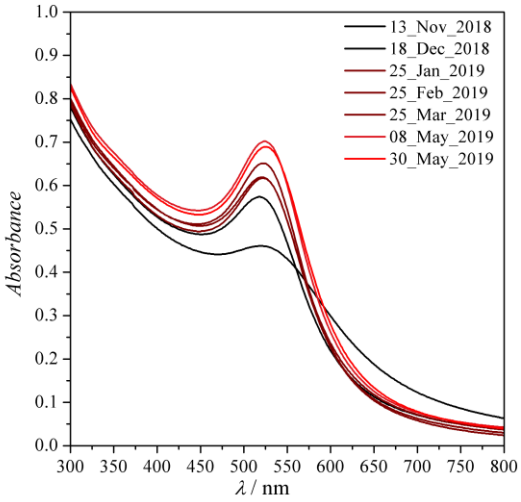

Figure 4.1.1: UV-Vis spectra of the AuNPs colloidal sol at different times from the synthesis.

Table 4.1.1: λ_{max} of the AuNPs colloidal solution recorded monthly.

DATE	λ_{max} / nm
13_Nov_2018	526
18_Dec_2018	518
25_Jan_2019	520
25_Feb_2019	522
25_Mar_2019	522
08_May_2019	524
30_May_2019	525
	λ_{max} mean = 522 nm

In order to evaluate in a more accurate way the dimension of the nanoparticles, TEM images were recorded and the average size was calculated by using the Image J software, sampling a total number of 150 entities. **Figure 4.1.2 (a)** shows the morphology of the nanoparticles, which are spherical in shape. It seems that the dimensions are not homogeneous and from the calculated average size (see **Figure 4.1.2 (b)**) the mean diameter is higher than the expected one (around 30 nm). It must be underlined that some problems were encountered in the preparation of the sample on the TEM grid and so some aggregation phenomena could have taken place.

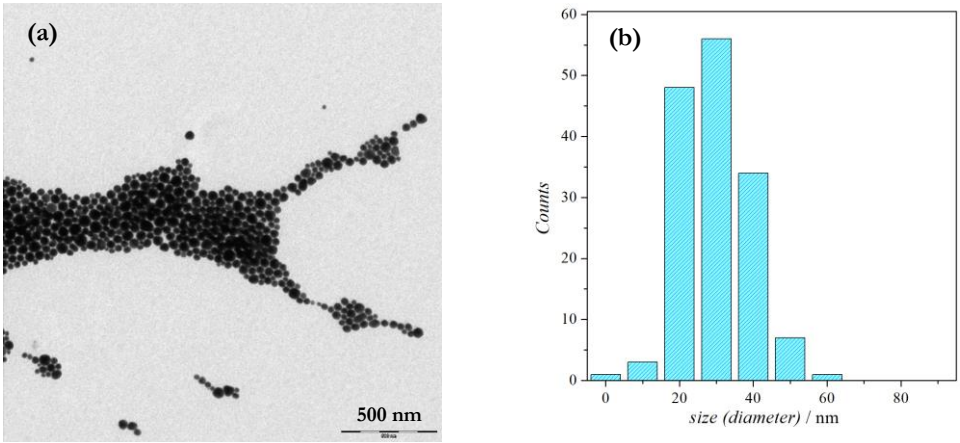

Figure 4.1.2: (**a**) TEM Image of AuNPs colloidal solution and (**b**) their size distribution

Since from TEM analysis the size of the nanoparticles was not in accordance to what expected, also DLS measurements were conducted onto the colloidal sol of gold nanoparticles. Results are shown in **Figure 4.1.3** (**a**), (**b**) and (**c**). The first graph (**Figure 4.1.3** (**a**)) shows the intensity of the light scattered by the nanoparticles. As it can be easily seen, since the light intensity depends on the sixth power of the radius, larger particles scatter much more light than those with smaller diameters. This is why the peak centred at 80 nm is higher than the one at around 8 nm. This could lead to the wrong assumption that most of the particles contained in the sol have a diameter of about 80 nm. However, looking at **Figure 4.1.3** (**b**), related to volumes, it is evident a solitary peak at about 10 nm. This type of graph shows how much each population weighs in mass on the total volume: this means that, within the sol of AuNPs, almost all the nanoparticles are very small. The analysis is further confirmed by **Figure 4.1.3** (**c**), related to the "numbers" of nanoparticles, whose result is consistent with the others. From the fitting of the spectra, the average size of the nanoparticles resulted to be (6.6 ± 0.7) nm.

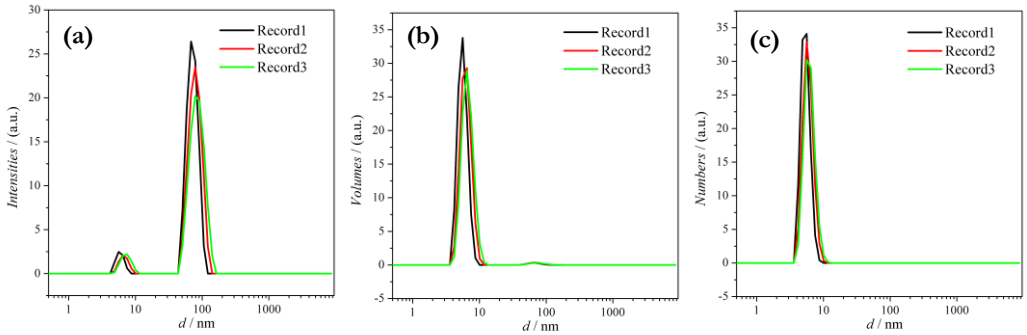

Figure 4.1.3 DLS analysis of the AuNPs colloidal sol. (**a**) Intensities (**b**) Volumes and (**c**) Numbers.

In addition to these characterizations, also Zeta potential measurements were conducted onto the AuNPs colloidal sol, in order to have information of their surface charge. Zeta potential, termed also as *electrokinetic potential*, is the potential measured at the slipping plane of a colloidal particle, which is moving under an electric field. It can be thus considered as the potential difference between the electric double layer of the particle and the layer of dispersant around it.[18] During the analysis,

an electric field is applied to the colloidal solution and the electrophoretic mobility of the particles is measured. The electrophoretic mobility (μ) is proportional to the Zeta Potential (ζ) according to the equation $\zeta = \frac{4 \cdot \pi \cdot \eta \cdot \mu}{\varepsilon}$ where η is the viscosity of the solution and ε the dielectric constant. The surface charge of the particles can be easily determined by the direction in which they move during electrophoresis. **Figure 4.1.4** reports the Zeta potential graph of the investigated sample.

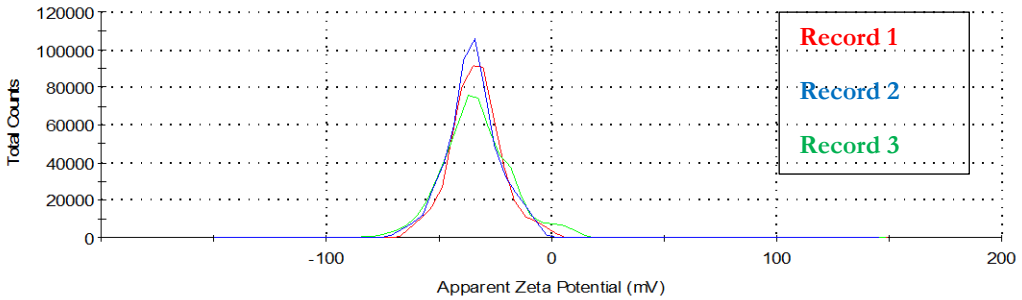

Figure 4.1.4: Zeta Potential measurements of AuNPs colloidal sol.

Table 4.1.2: Zeta Potential results from the three records registered on the AuNPs sample.

ANALYSIS	Zeta Potential / mV
RECORD 1	-33.5
RECORD 2	-33.2
RECORD 3	-34.9
AVERAGE	(-33.9 ± 0.9)

The surface charge of gold nanoparticles is negative: this is consistent with what was expected since these nanoparticles were synthesized using citrate, which is a negatively charged molecule. Moreover, the absolute value of zeta potential is greater than 30 mV, which means that the suspension of AuNPs can be considered very stable.[18]

Au/TiO_2 *vs* Ag/TiO_2 Hybrids

As previously mentioned (see ***Focus***), the first hybrid material that serves as reference for the object of study of this Chapter, is a composite material based on silver nanoparticles and titanium dioxide (anatase phase) layer. A similar device has been already used for several photocatalytic purposes and engineered for the electrochemical detection of relevant neurotransmitters,[19–21] also proving its photorenewable characteristics[22]. A theoretical and electrochemical concerted study showed that the two materials are in deep contact one to the other and that a real interface is created, where the electrochemical properties of silver are drastically changed with respect to the expected ones. **Figure 4.1.5** (**a**) reports the cyclic voltammetry patterns of the Ag/TiO_2 hybrid with respect to its single components (AgNPs and TiO_2 alone), recorded in 0.1 M $NaClO_4$. As expected, no faradaic current is detected for the wide band-gap titanium dioxide semiconductor nanoparticles, while, in the case of the Ag-modified electrode, a typical plateau at positive potentials (associated to the formation of Ag oxides on the silver surface) and the relative reduction peak are present. The Ag/TiO_2 hybrid voltammogram presents a sharp oxidation peak for silver, shifted at more favourable potential, with an area higher than that of the reduction counterpart (even if the Ag quantity that is deposited on the bare Ag-modified FTO and on the hybrid is the same). This effect is ascribed to a charge donation from Ag to Titania, where the most external atoms of silver release their electrons to the top layer of titania. Ag is then poor in electrons and more easily oxidised. This electron transfer phenomenon is again confirmed by photocurrent experiments (**Figure 4.1.5** (**b**)), in which it is clear that the Ag/TiO_2 hybrid possesses a lower photocurrent density compared to the bare TiO_2, meaning that part of the electrons do not participate to the formation of a photocurrent, but are simply donated from Ag to TiO_2. The strong adaptation of silver to titania is also confirmed by looking at the shape of the Bode plots, in **Figure 4.1.5** (**c**), where it is evident that the hybrid material is practically the same of the single TiO_2 and differs from the single Ag. Moreover, looking at the equivalent circuits derived by using the

Software ZView, the presence of an additional circuit in the case of the hybrid could be a proof of the effective formation of an interface (**Figure 4.1.6**)

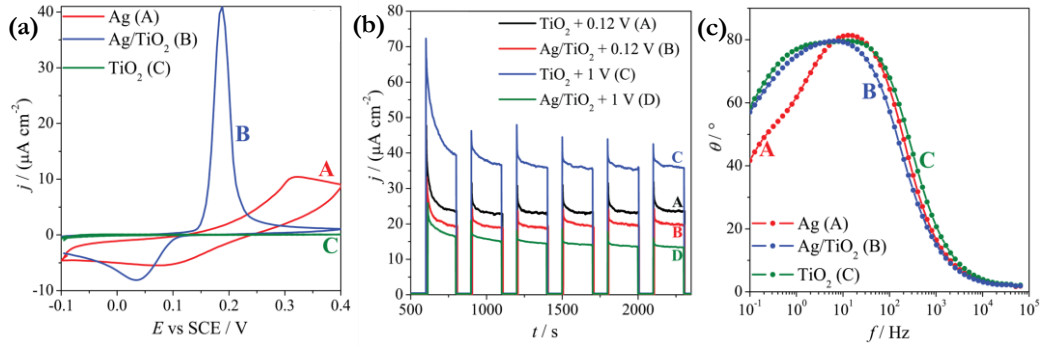

Figure 4.1.5: (**a**) CV patterns in $NaClO_4$ 0.1 M of the single Ag, single TiO_2 and hybrid modified FTO, recorded at 100 mV s^{-1}. (**b**) Photocurrent experiments of the hybrid compared with the bare TiO_2 electrode, recorded at two different potential (+1 V (SCE) and +0.12 V (SCE)) in 0.12 M $NaClO_4$. (**c**) EIS spectra, Bode plots, on $NaClO_4$ 0.1 M, at 0.1 V (SCE) for the hybrid compared with the single components.[1]

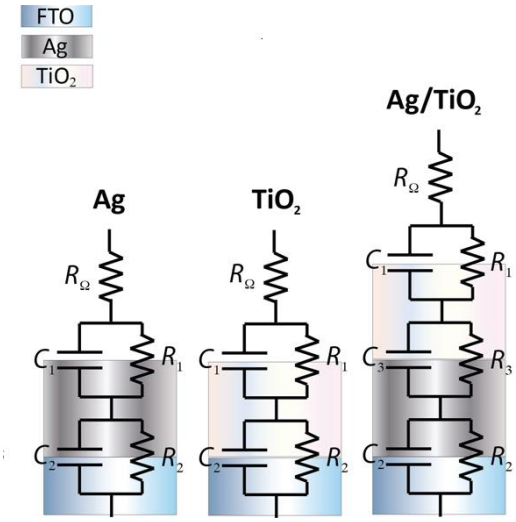

Figure 4.1.6: Equivalent circuits for the Ag, TiO_2 and the hybrid Ag/TiO_2, respectively.[1]

In comparison with what happens with Ag/TiO_2 hybrids, similar experiments were conducted on the Au/TiO_2 system and results are shown in **Figure 4.1.7** (**a**), (**b**) and (**c**). In this case it is clear, starting from the CV pattern, that the hybrid is more similar to the FTO modified with only AuNPs, meaning that the intrinsic properties of gold are maintained. The different shape of the oxidation plateau could be addressed to a different disposition of gold nanoparticles, that could aggregate in the absence of the

titania layer on top. By the way, also looking at the reduction peak, no strong differences are highlighted: the peak of the single AuNPs and of the hybrid are at the same position and the ratio between the area of the oxidation and reduction peak is similar and not unbalanced as happened in the case of the Ag/TiO_2 system. This fact let us suppose that no charge transfer is happening between the two materials of the composite and a confirmation is obtained from the photocurrent experiments (**Figure 4.1.7** (**b**)). In this case, the hybrid and the bare TiO_2 possess the same photocurrent density, meaning that in the case of the hybrid all the electrons involved are used for the generation of the anodic photocurrent and no donation from gold to titania is present. **Figure 4.1.7** (**c**) shows the Bode plots recorded on the background, from which is again possible to assert that the hybrid is really similar to the bare gold, that is not adapting to titania as previously observed in the case of silver. **Figure 4.1.8** reports the related equivalent circuits. All these evidences let reasonably claim that in this system both the components are retaining their peculiar characteristics and are not affecting each other. Preliminary results from theoretical calculation are supporting this hypothesis, since it seems really difficult to grow an interface between gold and titania, conversely on what observed for silver. This could be due to the more "noble" characteristic of gold as metal, which is less adaptable than silver.

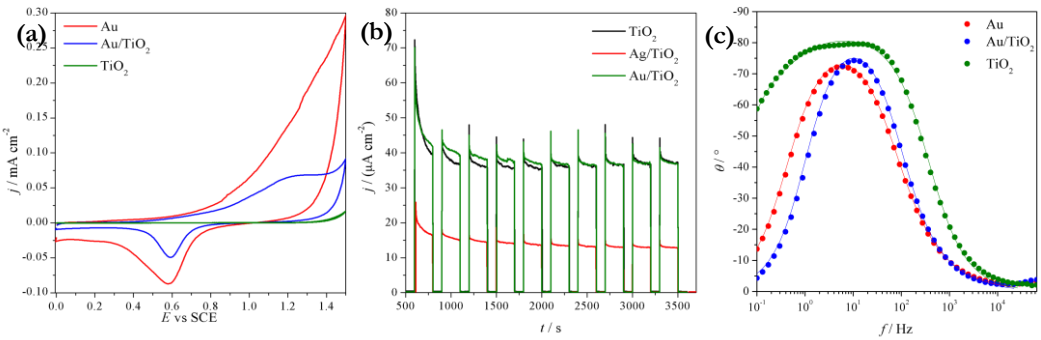

Figure 4.1.7: (**a**) CV patterns in $NaClO_4$ 0.1 M of the single Au, single TiO_2 and hybrid modified FTO, recorded at 100 mV s^{-1}. (**b**) Photocurrent experiments of the hybrid (both made of Au and Ag nanoparticles) compared with the bare TiO_2 electrode, recorded at two different potential (+1 V (SCE) and +0.12 V (SCE)) in 0.1 M $NaClO_4$. (**c**) EIS spectra, Bode plots, on $NaClO_4$ 0.1 M, at - 0.1 V (SCE) for the hybrid compared with the single components.

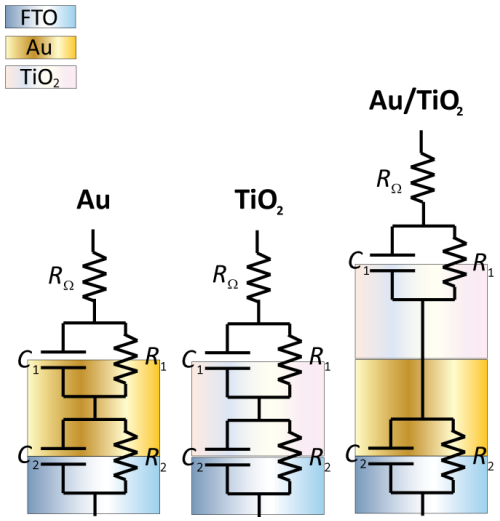

Figure 4.1.8: Equivalent circuits for the Au, TiO_2 and the system Au/TiO_2, respectively.

Table 4.1.3: EIS parameters from the fitting of the equivalent circuits in **Figure 4.1.8**.

	R_Ω / (Ω cm^2)	CPE$_1$ / (μF cm^{-2} s$^{\alpha-1}$)	α_1	R_1 / (kΩ cm^2)	CPE$_2$ / (μF cm^{-2} s$^{\alpha-1}$)	α_2	R_2 / (kΩ cm^2)
Au	98.5	576	0.56	0.0394	25.3	0.92	15.7
Au/TiO_2	92.9	335	0.65	0.0209	17.0	0.97	9.42
TiO_2	56.7	54.9	0.88	8.64	16.6	0.94	207

From EIS fitting results (**Table 4.1.3**), what it can be immediately seen is that the Au/TiO_2 system possesses parameters that are in the same order of magnitude than the ones of the single Au, and not of the single TiO_2, confirming what previously supposed: gold is not adapting to titania and it is behaving like the bare metal. A slight influence of TiO_2 onto the composite final performance could be seen in its CPE$_1$ value, that is a little bit lowered with respect to the one of the bare Au system, even if it is still far from the one of bare TiO_2. The low resistance values (R_1) of Au, and also of the Au/TiO_2 composite, are due to the intrinsic characteristic of gold: being a highly conductive metal it favours the reaction of the probe.

In general, the presence of two equivalent circuits could be ascribed to a first contact between the electrode surface and the electrolyte solution and a second one due to the contact between the ITO support and the materials deposited on it. As already

underlined, the presence of the interface between Au and TiO_2 in the composite is not highlighted from these data.

Au/TiO_2 Electroanalytical Applications

The composite material, as previously mentioned (see ***Focus***), is applied in the electroanalytical detection of diclofenac, a molecule that belongs to the family of emerging contaminants. It is a NSID (Non-Steroidal Inflammatory Drug) and it is widely used to treat pain and inflammatory disease, being the 10th most sold drug in Italy in 2018. Since it is only classified as emerging contaminant, a specific maximum level of its concentration in water is still to be defined from Laws, but its dangerous effects for human health under chronic exposure are almost clear. For this reason, the necessity to construct a sensor able to detect such molecules in environmental samples is a topic of growing interest in the last few years.

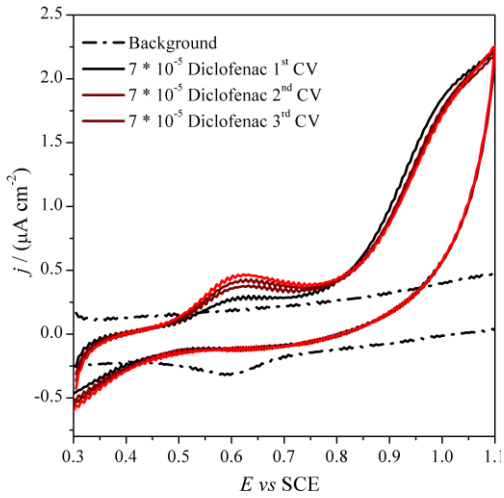

Figure 4.1.9: Subsequent CVs of the hybrid Au/TiO_2 in the presence of a 7*10^{-5} M of Diclofenac, in PBS at pH 4.

In this work, the presence of AuNPs is exploited since their affinity towards Diclofenac is known from the Literature.[13] The presence of TiO_2, instead, is thought in order to recover the electrode surface which could undergo fouling and passivation, after diclofenac detection and polimerization on the electrode platform.[13,21,22] In **Figure 4.1.9** the cyclic voltammograms registered in the presence of a fixed concentration (7 * 10^{-5} M) of diclofenac, in a Phosphate Buffer Solution, at pH 4, previously prepared for the intended experiment are reported. As it can be observed from the voltammograms in **Figure 4.1.9**, the target molecule is strongly detected by the electrode, with an oxidation

signal (resembling a shoulder) at about + 1 V (SCE) at the first scan, and a small signal at about +0.6 V (SCE), which is growing cycle by cycle. This signal is related to the by-products of diclofenac, which are known to deposit onto the surface of the electrode and to be responsible of its fouling and passivation.[13,23] A possible oxidative path followed by Diclofenac is reported in **Figure 4.1.10**.

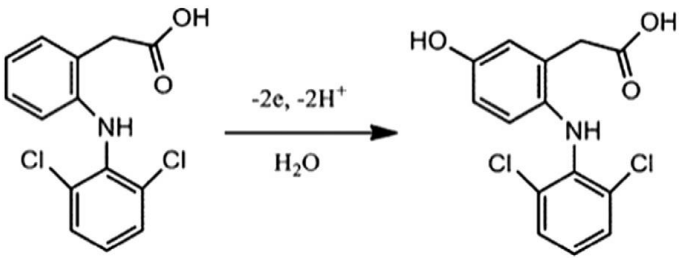

Figure 4.1.10: Schematic representation of the possible oxidative path followed by Diclofenac. Used with permission, Copyright 2015 ©, Elsevier.[13]

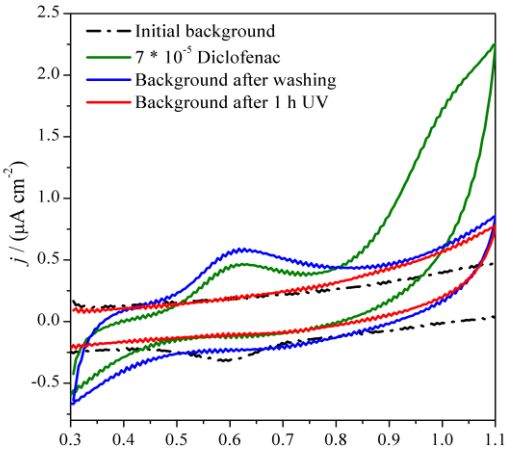

Figure 4.1.11: Device recovery with 1h treatment with UV lamp (λ max = 365 nm).

The fouling effect was later on verified, since if the electrode was washed and then re-used in a background solution in the absence of diclofenac, the signal relative to the by-product was still present in the voltammetric pattern (**Figure 4.1.11**). The electrode was then subjected to a UV-light treatment: it was left for one hour under irradiation with an UV lamp (λ_{max} = 365 nm) and then a CV on the background was performed. As **Figure 4.1.11** show, the complete recovery of the initial background was achieved, with the disappearance of the signal relative to diclofenac.

This cleaning step was performed by leaving the electrode in air, directly irradiated from the lamp, at a distance of about 20 cm. This step was then repeated also by leaving the electrode in the background solution and so with the addition of the glass

and the liquid medium as an "obstacle" between the light source and the device. Also in this case, a complete recovery of the electrode surface was achieved.

The same procedure was repeated also leaving the electrode in the background solution, under stirring, during the hour of irradiation. In this way, a possible "real" situation is reproduced, if thinking about the creation of a sensor to be implemented in a water pipe for a continuous monitoring of the pollutant in the environment. Concerning this last point, for the cleaning of the electrode surface, a big UV lamp like the one used in the laboratory cannot be employed for *on-site* measurements. For this reason, the use of a small LED, with a specific emitting wavelength (in this case, 390 nm), was employed in the same configuration of the UV lamp. The perfect recovery of the electrode surface was verified also in this case, as clearly shown in **Figure 4.1.12**.

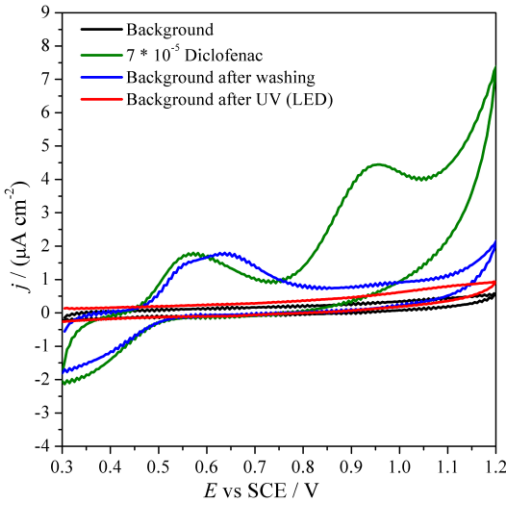

Figure 4.1.12: Device recovery with 1h treatment with UV lamp (λ max = 365 nm).

TiO_2 aging time: effect on the electroanalytical applications

By performing several electrochemical characterizations on different devices, it was oberved, by chance, a different response of the electrodes towards the $K_4[Fe(CN)_6]$ redox probe (see **Figure 4.1.13** (**a**)). These results were surprising because the devices were expected to be identical, since the followed synthetic procedure was the same for all the electrodes (see "**Materials and Methods**" Paragraph of this Chapter for more details). The only thing that it was noticed to be different is the aging time of the AuNPs and TiO_2 sols. In fact, both the solutions were synthetised once, stored in selected bottles, and used when necessary to create the final devices. The three

systems that are here under investigation were synthesized the **same day**, **9 days** and **15 days** after the synthesis of TiO_2 sol. AuNPs were synthesized proviously and so the aging time taken as reference is the one of the titanium dioxide sol. The stability in time of the AuNPs sol was already discussed and verified in this section (by means of UV-Vis analyses and confirmed by Zeta-potential results) and so the only parameters that is still to be analysed is the stability in time of the TiO_2 sol. **Figure 4.1.13** (**a**) shows the behavior of three different devices toward the redox probe $K_4[Fe(CN)_6]$ and from this graph it can be immediately observed how the position and the shape of the voltammetric pattern is changing, by changing the device. In more details, focusing the attention on the oxidation step, for the systems synthesized the same day of TiO_2 (dark line), a step-shaped curve is registered. This curve is shifted at more favourable potentials in the case of the system synthesized 9 days after TiO_2 (red line), and the shape is no more a perfect step. Then, after 15 days from TiO_2 synthesis (blue line), the signal is a peak and it is again shifted at voltage closer to zero with respect to the previous one.

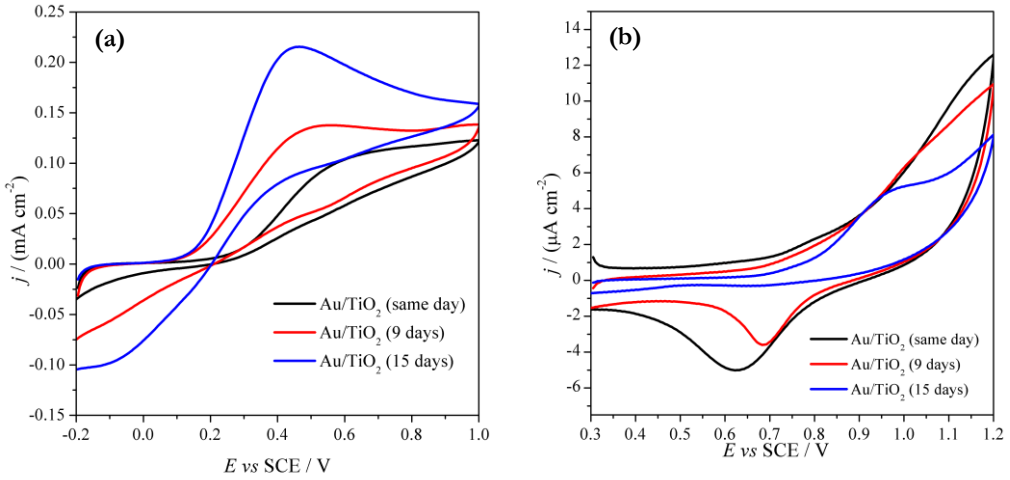

Figure 4.1.13: Effect of the TiO_2 aging onto the response of the electrodes towards (**a**) $K_4[Fe(CN)_6]$ and (**b**) Diclofenac.

An hypotesis on what is happening is that the TiO_2 particles in the sol are changing over time and they are probably aggregating, passing from a first situation chacarcterized by very small particles to a system in which the particles are bigger.

When the sol is deposited onto the electrode and then it is subjected to the calcination step, it is possible to imagine the creation of a more compact layer in the case of smaller nanoparticles and a less compact layer, with a more porous pattern, for what concern particles of bigger dimensions. In this way, the final device presents a smaller porosity when it is synthesized the same day of the TiO_2 sol and a bigger porosity when it is finalized after 15 days. The smaller porosity could lead to a mechanism of *convergent diffusion* of the probe towards the electrode, in which the Au layer of nanoparticles (that are the electroactive species of the device) is resembling a *microarray* of electrodes (see **Chapter 2** for more details on the mechanism) where the conducting materials is covered by a porous insulating layer. In the case of bigger porosity, the electroactive layer of Au nanoparticles is no more hindered by TiO_2 like the previous case and the electroactive spots are big enough to generate a *planar diffusion* mechanism. This fact is reflected by the shape of each voltammetric pattern, that is a step when there is the convergent diffusion mechanism and a peak in the case of the planar one. In a situation of higher porosity, morover, a higher amount of electroactive surface area is avaiable for the probe to react and this could be the reason why the current values are higher for the "15 days" materials with respect to the "same day" one. In fact, the density current values reported in the graph are normalized by the electrode geometric area, which is the same for all the three materials, and not for the real surface area (since this value is still unknown). The peak current density gap "same day-9 days" (25 $\mu A\ cm^{-2}$) is lower than the one of "9 days-15 days" (80 $\mu A\ cm^{-2}$) even if the time among the proof is slightly lower. This could be explained by the fact that in case of convergent diffusion, normally, an enhanchment of the current is registered and so the values for the "same day" material could have been enhanced for this reason. An aspect that is still to be clarified is the anticipation of the oxidation peak. Normally, this is due to electrocatalytic effects of the electrode material but in this situation, the electrodes are made of the same components. The only thingh that could be responsible of this effect is the exposition of different gold cistallographic faces, that are known from

the Literature to possess a different electrocatalytic activity[24,25]. Considering all these facts, the effective dimension of titania nanoparticles in the colloidal sol needs to be verified and for this reason DLS studies are on-going. Meanwhile, since this effect seemed interesting on the simple redox probe, also the answer of the same electrodes towards the analyte Diclofenac was conducted (**Figure 4.1.13** (**b**)). As it can be noticed, also in this case a change in the signal was obtained, with a more marked oxidation peak, at lower potential values, instead of a shoulder, for the system synthesized 15 days after the TiO_2 sol. The same above-mentioned considerations could be done also for this case. These results, even if are still to be verified and supported by other characterization techniques, are promising since the device coul be synthesized at different times and a *size exclusion* effect coul be exploited. In this way, the device could be appositely designed and created to be extremely selective toward a particular analyte simply by playing with the size of the particles and consequently with the size of the pores of the final titania layer on top.

Conclusions

In this part of the Thesis project, a material based on gold nanoparticles, covered by a top layer of titanium dioxide is at first studied in depth in order to clarify the mutual influence of one material to the other and then is applied as electroanalytical sensor for the detection of Diclofenac. Comparing the results with the ones obtained in a previous work onto a similar material based on silver nanoparticles, it can be claimed that in this case it is not possible to talk about a real hybrid material, since the presence of an interface between Au and TiO_2 is still to be found. In fact, from the preliminary results gained from the electrochemical characterization of the material, it seems that gold is not adapting to titania, like silver did, while it retains its own characteristic being unperturbed in its electrochemical behaviour by the presence of the top layer of TiO_2. By the way, advantages in having gold nanoparticles and titanium dioxide together in the same system were gained with the final application

of the device. The presence of AuNPs was exploited in order to detect Diclofenac and the presence of TiO_2 was exploited to restore the electrode surface after processes of fouling and passivation. In this way, a suitable device for *on-line, on-site* and *continuous* monitoring of contaminants in water is created. The aging effect of the top layer of titania will be also a key factor for the creation of selective sensors with *size exclusion* potentialities. The work is still in progress, since the best electroanalytical technique is still to be found, with the aim of lowering the limit of detection and increasing the sensitivity of the device, but preliminary results are promising.

Bibliography

(1) Di Liberto, G.; Pifferi, V.; Lo Presti, L.; Ceotto, M.; Falciola, L. Atomistic Explanation for Interlayer Charge Transfer in Metal-Semiconductor Nanocomposites: The Case of Silver and Anatase. *J. Phys. Chem. Lett.* **2017**, *8* (21), 5372–5377. https://doi.org/10.1021/acs.jpclett.7b02555.

(2) Noguera-Oviedo, K.; Aga, D. S. Lessons Learned from More than Two Decades of Research on Emerging Contaminants in the Environment. *J. Hazard. Mater.* **2016**, *316*, 242–251. https://doi.org/10.1016/j.jhazmat.2016.04.058.

(3) Naidu, R.; Arias Espana, V. A.; Liu, Y.; Jit, J. Emerging Contaminants in the Environment: Risk-Based Analysis for Better Management. *Chemosphere* **2016**, *154*, 350–357. https://doi.org/10.1016/j.chemosphere.2016.03.068.

(4) Taheran, M.; Naghdi, M.; Brar, S. K.; Verma, M.; Surampalli, R. Y. Emerging Contaminants: Here Today, There Tomorrow! *Environ. Nanotechnology, Monit. Manag.* **2018**, *10* (May), 122–126. https://doi.org/10.1016/j.enmm.2018.05.010.

(5) Riva, F.; Castiglioni, S.; Fattore, E.; Manenti, A.; Davoli, E.; Zuccato, E. Monitoring Emerging Contaminants in the Drinking Water of Milan and Assessment of the Human Risk. *Int. J. Hyg. Environ. Health* **2018**, *221* (3), 451–457. https://doi.org/10.1016/j.ijheh.2018.01.008.

(6) Riva, F.; Zuccato, E.; Davoli, E.; Fattore, E.; Castiglioni, S. Risk Assessment of a Mixture of Emerging Contaminants in Surface Water in a Highly Urbanized Area in Italy. *J. Hazard. Mater.* **2019**, *361* (July 2018), 103–110. https://doi.org/10.1016/j.jhazmat.2018.07.099.

(7) Gogoi, A.; Mazumder, P.; Tyagi, V. K.; Tushara Chaminda, G. G.; An, A. K.; Kumar, M. Occurrence and Fate of Emerging Contaminants in Water Environment: A Review. *Groundw. Sustain. Dev.* **2018**, *6* (September 2017), 169–180. https://doi.org/10.1016/j.gsd.2017.12.009.

(8) Daughton, C. G.; Ternes, T. A. Pharmaceuticals and Care Products in the Environment. **2001**, *791*. https://doi.org/10.1021/bk-2001-0791.

(9) Lonappan, L.; Brar, S. K.; Das, R. K.; Verma, M.; Surampalli, R. Y. Diclofenac and Its Transformation Products: Environmental Occurrence and Toxicity - A Review. *Environ. Int.* **2016**, *96*, 127–138. https://doi.org/10.1016/j.envint.2016.09.014.

(10) Mohapatra, D. P.; Kirpalani, D. M. Advancement in Treatment of Wastewater: Fate of Emerging Contaminants. *Can. J. Chem. Eng.* **2019**, *2019* (October), 2621–2631. https://doi.org/10.1002/cjce.23533.

(11) Llompart, M.; Celeiro, M.; Dagnac, T. Microwave-Assisted Extraction of Pharmaceuticals, Personal Care Products and Industrial Contaminants in the Environment. *TrAC - Trends Anal. Chem.* **2019**, *116*, 136–150. https://doi.org/10.1016/j.trac.2019.04.029.

(12) Arismendi, D.; Becerra-Herrera, M.; Cerrato, I.; Richter, P. Simultaneous

Determination of Multiresidue and Multiclass Emerging Contaminants in Waters by Rotating-Disk Sorptive Extraction–Derivatization-Gas Chromatography/Mass Spectrometry. *Talanta* **2019**, *201* (January), 480–489. https://doi.org/10.1016/j.talanta.2019.03.120.

(13) Afkhami, A.; Bahiraei, A.; Madrakian, T. Gold Nanoparticle/Multi-Walled Carbon Nanotube Modified Glassy Carbon Electrode as a Sensitive Voltammetric Sensor for the Determination of Diclofenac Sodium. *Mater. Sci. Eng. C* **2016**, *59*, 168–176. https://doi.org/10.1016/j.msec.2015.09.097.

(14) Maino, G.; Meroni, D.; Pifferi, V.; Falciola, L.; Soliveri, G.; Cappelletti, G.; Ardizzone, S. Electrochemically Assisted Deposition of Transparent, Mechanically Robust TiO2 Films for Advanced Applications. *J. Nanoparticle Res.* **2013**, *15* (11). https://doi.org/10.1007/s11051-013-2087-2.

(15) Maggioni, D.; Arosio, P.; Orsini, F.; Ferretti, A. M.; Orlando, T.; Manfredi, A.; Ranucci, E.; Ferruti, P.; D'Alfonso, G.; Lascialfari, A. Superparamagnetic Iron Oxide Nanoparticles Stabilized by a Poly(Amidoamine)-Rhenium Complex as Potential Theranostic Probe. *Dalt. Trans.* **2014**, *43* (3), 1172–1183. https://doi.org/10.1039/c3dt52377b.

(16) Amendola, V.; Meneghetti, M. Size Evaluation of Gold Nanoparticles by UV-Vis Spectroscopy. *J. Phys. Chem. C* **2009**, *113* (11), 4277–4285. https://doi.org/10.1021/jp8082425.

(17) Myroshnychenko, V.; Rodríguez-Fernández, J.; Pastoriza-Santos, I.; Funston, A. M.; Novo, C.; Mulvaney, P.; Liz-Marzán, L. M.; García de Abajo, F. J. Modelling the Optical Response of Gold Nanoparticles. *Chem. Soc. Rev.* **2008**, *37* (9), 1792–1805. https://doi.org/10.1039/b711486a.

(18) Bhattacharjee, S. DLS and Zeta Potential - What They Are and What They Are Not? *J. Control. Release* **2016**, *235*, 337–351. https://doi.org/10.1016/j.jconrel.2016.06.017.

(19) Hirakawa, T.; Kamat, P. V. Charge Separation and Catalytic Activity of Ag@TiO 2 Core-Shell Composite Clusters under UV-Irradiation. *J. Am. Chem. Soc.* **2005**, *127* (11), 3928–3934. https://doi.org/10.1021/ja042925a.

(20) Lu, Q.; Lu, Z.; Lu, Y.; Lv, L.; Ning, Y.; Yu, H.; Hou, Y.; Yin, Y. Photocatalytic Synthesis and Photovoltaic Application of Ag-TiO2 Nanorod Composites. *Nano Lett.* **2013**, *13* (11), 5698–5702. https://doi.org/10.1021/nl403430x.

(21) Soliveri, G.; Pifferi, V.; Panzarasa, G.; Ardizzone, S.; Cappelletti, G.; Meroni, D.; Sparnacci, K.; Falciola, L. Self-Cleaning Properties in Engineered Sensors for Dopamine Electroanalytical Detection. *Analyst* **2015**, *140* (5), 1486–1494. https://doi.org/10.1039/c4an02219j.

(22) Pifferi, V.; Soliveri, G.; Panzarasa, G.; Cappelletti, G.; Meroni, D.; Falciola, L. Photo-Renewable Electroanalytical Sensor for Neurotransmitters Detection in Body Fluid Mimics. *Anal. Bioanal. Chem.* **2016**, *408* (26), 7339–7349. https://doi.org/10.1007/s00216-016-9539-3.

(23) Yang, X.; Wang, F.; Hu, S. Enhanced Oxidation of Diclofenac Sodium at a Nano-

Structured Electrochemical Sensing Film Constructed by Multi-Wall Carbon Nanotubes-Surfactant Composite. *Mater. Sci. Eng. C* **2008**, *28* (1), 188–194. https://doi.org/10.1016/j.msec.2006.11.006.

(24) Chen, Y.; Schuhmann, W.; Hassel, A. W. Electrocatalysis on Gold Nanostructures: Is the {1 1 0} Facet More Active than the {1 1 1} Facet? *Electrochem. commun.* **2009**, *11* (10), 2036–2039. https://doi.org/10.1016/j.elecom.2009.08.046.

(25) Hebié, S.; Kokoh, K. B.; Servat, K.; Napporn, T. W. Shape-Dependent Electrocatalytic Activity of Free Gold Nanoparticles toward Glucose Oxidation. *Gold Bull.* **2013**, *46* (4), 311–318. https://doi.org/10.1007/s13404-013-0119-4.

5.

Graphene-Metal Hybrids

Introduction

According to IUPAC definition (1995), graphene is "*a single carbon layer of graphite structure, describing its nature by analogy to a polycyclic aromatic hydrocarbon of quasi-infinite size*".[1] More specifically, it is a two-dimensional material based on a honeycomb structure formed of sp^2-hybridized carbon atoms.[2–4] Graphene has attracted enormous interest over the last decades due to its unique properties: a large surface area, excellent thermal and electrical conductivities and high mechanical strength.[5,6] Thanks to its properties (superior than that of other carbon allotropes),[5] graphene has had a great impact in the field of electrochemistry.[5–9] It has a theoretical surface area of 2630 $m^2 g^{-1}$, overcoming that of graphite (almost 10 $m^2 g^{-1}$), and it is two times larger than that of carbon nanotubes (1315 $m^2 g^{-1}$).[10] Additionally, the electrical conductivity of graphene has been calculated to be almost 64 mS cm^{-1}, which is sixty times more than that of single walled carbon nanotubes.[11,12] Moreover, it has a thermal conductivity of up to 5000 W $m^{-1} K^{-1}$ and a breaking strength of 42 N m^{-1}.[7] As a consequence, graphene has been used for the fabrication of novel and improved energy storage and energy production devices, which are of vital importance considering the increasing demand for greener energy related devices with high power output and efficiency.[13,14] Moreover, it is used as sensing and biosensing platform for the detection of bio-molecules and substances harmful to human health and to environment.[5,15,16]

Nowadays, graphene can be produced by different synthetic routes. These methods are mainly subdivided into two categories: *top-down* or *bottom-up* approaches. Among the "top down" ones, there is the famous "scotch tape" method, developed by Geim and Novoselov in 2004,[17] which is basically a dry exfoliation of graphite, in which it is possible to control the number of graphene layers simply by controlling the number of repeated peeling steps. This technique, even if it is a cost-effective method allowing to obtain high-quality single graphene sheets,[9] suffers from lack of reproducibility and it is not suitable for large-scale and mass production. Other approaches in the "top down" category are the chemical and electrochemical

exfoliation of graphite (in the first one, graphite is dispersed in a water-surfactant solution[18] or in an organic solvent[19] and then transformed in monolayer graphene by the application of ultrasound, while in the second one cathodic or anodic potentials or currents in aqueous or organic electrolytes to a graphite based working electrode are applied). Last, but not least, since it is one of the most applied approach, there is the possibility to synthesized graphene starting form one of its most famous precursor, that is GO, graphene oxide. This is considered one of the most inexpensive way to produce graphene[20,21] and with this technique it is possible to obtain graphene with a higher amount of structural defects and functional groups, essential for possible further modifications and advantageous for electrochemical applications.[22,23] The "bottom up" approaches, on the contrary, involve the use of small carbon-containing molecules that combine to form the sp^2-honeycomb structure. They include: organic synthesis[9], epitaxial growth on SiC[24], Chemical Vapour Deposition[6], and so on.

The development of graphene in a wide range of applications and fields is a suggestion of its great potentialities. However, pure graphene sheets are limited for many applications despite their excellent characteristics.[25] For example, having a weak light-absorption, pure graphene sheets are not the perfect candidate for efficiently collect solar light. Moreover, the capacitance of graphene is limited by the electronic double layer regime and it is very low, inducing the need of the introduction of some modification on the bare sheets. In this context, graphene hybrids and nanocomposites in general are subjected to increasing efforts for subsequent real applications, from energetics to environmental and sensoristics.

Graphene Nanocomposites: Preparation methods

Over the last decades, many methods have been developed to prepare functionalized graphene nanocomposites. Each of these techniques presents advantages and drawbacks as evidenced in the following points::

a) Non-covalent Interactions

This method represents one of the most commonly involved approach. In general, non covalent interactions between organic molecules and graphene are the responsible forces to attach organic species (surfactants and polymers, above all) on the graphene platform. In this case, the aromatic ligand interacts with the honeycomb structure of graphene via π–π stacking, electrostatic or hydrophobic interactions. Many works report the use of pyrene-based ligands (pyrene-butirric acid, pyrene-carboxylix acid, aminopyrene and so on) to functionalize graphene and to obtain soluble solutions, processable and adabtable to the most various applications.[26–31] Non covalent approach can involve also the functionalization of graphene with metal ions, to form three-dimensional composites or hydrogels.[32,33] Moreover, the functionalzation of graphene could also occur via biomolecules such as nucleotides, peptides and proteins.[34–36]

b) Covalent Methods

As the definition suggests, in this way the graphene platform is modified via covalent interactions with other molecules. In more details, graphene and graphene oxide can be bonded to the surface *via* covalent interactions by amide bonding, diazonium salts, atom transfer radical polymerization or click chemistry.[37–40]

c) In situ Chemical Electroless Deposition

This method is relative to a direct depostion and functionalization of the graphene platform, via *in situ* modification. This route is particularly suited for the modification of graphene with metals, metal oxides and dichalcogenides nano-objects. In general, it involves a reduction step induced by the addition of selected reducing agents (such as $NaBH_4$) or, sometimes, a reduction induced and assisted by microwaves.[41,42]

d) Hydrothermal and solvothermal growth

With these methods, in general, the precursors are mixed together with graphene or graphene oxide and then the process is done in an autoclave, with high temperature and pressure. The high pressure reached during these syntheses permit to obtain composites where the components are in close contact one to the other, with eventual covalent connections, to be conveniently applied in various applications. The solvothermal and hydrothermal methods are, in fact, really versatile and can be applied to synthesized the most various composites, such as graphene with metal and alloy nanoparticles,[43] metal oxides,[44] metal calchogenides[45].

e) Electrochemical and Electrophoretic deposition

With electrochemical deposition methods, graphene composites (in particular those based on metals, metal alloys and oxides)[46–48] are synthesized upon the application of a potential or a current, that induces an electrochemical reaction, normally a reduction, and a subsequent deposition.

f) Photochemical Reactions

With this approach, the graphene composite is prepared by mixing graphene or graphene oxide with the precursors under light irradiation, in order to let some photochemical reactions to occur and to create the final hybrid.[49]

g) Physical deposition and mixing

Physical deposition, as the name suggests, is a simple technique based on the functionalization of graphene via physical vapour deposition or atomic layer deposition. With these approaches, it is normally preferred having a graphene structure with defects, since the functionalization preferentially takes place on edge planes and defects instead of basal planes, typical of a perfect flat graphene layer.[50] Physical mixing is again one of the easiest technique to functionalize graphene, usually based on the mixing of the precursors, spray drying and annealing processes.[51]

b) Chemical Vapor Deposition (CVD)

With this already known technique to prepare bare graphene, it is also possible to prepare functionalized graphene platforms. In this case, graphene is used as a substrate in the normal CVD process, resulting in graphene heterostructures with other materials.[52]

Graphene Nanocomposites: Functionalizations

The functionalization of graphene can occur via different routes, in order to reach materials with enhanced properties. The modification of graphene is normally done with:

a) *Molecules:* surfactants, proteins, biological matters. The purpose is mainly to improve the solubility of graphene and in general to change its properties by an optical, electrical, electronical and bio-related point of view;[25]
b) *Nanoscale objects:* nanoparticles, nanowires, nanorods and nanosheets. These objects can provide peculiar optical and electronic properties to graphene, which, combined with the outstanding feature of the carbonaceous matrix, can create a really performant hybrid;[25]
c) *Polymers:* they are applied normally, as other molecules, to improve the solubility of graphene. In general, in such composite, the electrical and electrochemical performances of the pristine graphene are changed and enhanced.[25]

Among the graphene-based materials modified with nanoscale objects, it is of huge interest the possibility to modify graphene with metal nanoparticles such as Au, Pt, Pd, Ag and so on. In fact, especially in catalysis and electrocatalysis, noble metal nanoparticles still possess the best activity. However, their efficiency is relatively low if they are unsupported onto suitable platform. The possibility to functionalize graphene with these materials is a way to produce interesting hybrids, exploiting the

peculiar properties of metals enhancing the ones of the pristine graphene.[53] Such composites are interesting also for sensing applications, since they can act as a dual detection tool.

Aim of the Project

In this part of the Thesis Project, hybrid nanomaterials based on graphene platform (especially Reduced Graphene Oxide, RGO) modified with gold nanoparticles are the main subject of the study. Different synthetic routes will be taken into consideration and the final application of the hybrid materials as electroanalytical sensors is investigated. In particular, they will be applied in the detection of organic molecules (dopamine), inorganic ions (arsenic) and biomolecules (antigen H-IgG), showing the wide range of applications that such materials could embrace.

The peculiar properties of each component of the hybrid will be taken into consideration, with the general aim to highlight the enhancement of the performances of the hybrid with respect to the single components.

Bibliography

(1) Fitzer, E.; Köchling, K. H.; Boehm, H. P.; Marsh, H. Recommended Terminology for the Description of Carbon as a Solid. *Pure Appl. Chem.* **1995**, *67* (3), 473–506.

(2) Novoselov, K. S.; Geim, A. K.; Morozov, S. V; Jiang, D.; Katsnelson, M. I.; Grigorieva, I. V; Dubonos, S. V; Firsov, A. A. Two-Dimensional Gas of Massless Dirac Fermions in Graphene. *Nature* **2005**, *438* (7065), 197–200.

(3) Geim, A. K., Novoselov, K. S. The Rise of Graphene. *Nat. Mater.* **2007**, *6*, 183–191.

(4) Geim, A. K. Graphene : Status and Prospects. *Science (80-.).* **2009**, *324*, 1530–1535.

(5) Brownson, D. A. C.; Banks, C. E. Graphene Electrochemistry: An Overview of Potential Applications. *Analyst* **2010**, *135* (11), 2768–2778.

(6) Brownson, D. a. C.; Banks, C. E. The Electrochemistry of CVD Graphene: Progress and Prospects. *Phys. Chem. Chem. Phys.* **2012**, *14* (23), 8264.

(7) Brownson, D. a. C.; Kampouris, D. K.; Banks, C. E. *Graphene Electrochemistry: Fundamental Concepts through to Prominent Applications*; 2012; Vol. 41.

(8) Ambrosi, A.; Pumera, M. Electrochemistry at CVD Grown Multilayer Graphene Transferred onto Flexible Substrates. *J. Phys. Chem. C* **2013**, *117* (5), 2053–2058.

(9) Ambrosi, A.; Chua, C. K.; Bonanni, A.; Pumera, M. Electrochemistry of Graphene and Related Materials. *Chem. Rev.* **2014**, *114* (14), 7150–7188.

(10) Pumera, M. Electrochemistry of Graphene: New Horizons for Sensing and Energy Storage. *Chem. Rec.* **2009**, *9* (4), 211–223.

(11) Liu, C.; Alwarappan, S.; Chen, Z.; Kong, X.; Li, C. Z. Membraneless Enzymatic Biofuel Cells Based on Graphene Nanosheets. *Biosens. Bioelectron.* **2010**, *25* (7), 1829–1833.

(12) Wang, X.; Zhi, L.; Müllen, K. Transparent, Conductive Graphene Electrodes for Dye-Sensitized Solar Cells. *Nanoletters* **2007**, *8*, 323–327.

(13) Stoller, M. D.; Park, S.; Yanwu, Z.; An, J.; Ruoff, R. S. Graphene-Based Ultracapacitors. *Nano Lett.* **2008**, *8* (10), 3498–3502.

(14) Brownson, D. A. C.; Kampouris, D. K.; Banks, C. E. An Overview of Graphene in Energy Production and Storage Applications. *J. Power Sources* **2011**, *196* (11), 4873–4885.

(15) Pumera, M.; Ambrosi, A.; Bonanni, A.; Chng, E. L. K.; Poh, H. L. Graphene for Electrochemical Sensing and Biosensing. *TrAC - Trends Anal. Chem.* **2010**, *29* (9), 954–965.

(16) Xiao, X.; Beechem, T. E.; Brumbach, M. T.; Lambert, T. N.; Davis, D. J.; Michael, J. R.; Washburn, C. M.; Wang, J.; Brozik, S. M.; Wheeler, D. R.; et al. Lithographically Defined Three-Dimensional Graphene Structures. *ACS Nano* **2012**, *6* (4), 3573–3579.

(17) Novoselov, K. S.; Geim, A. K.; Morozov, S. V.; Jiang, D.; Zhang, Y.; Dubonos, S. V.; Grigorieva, I. V.; Firsov, A. A. Electric Field Effect in Atomically Thin Carbon Films. *Science (80-.).* **2004**, *306* (5696), 666–669.

(18) Lotya, M.; King, P. J.; Khan, U.; De, S.; Coleman, J. N. High-Concentration, Surfactant-Stabilized Graphene Dispersions. *ACS Nano* **2010**, *4* (6), 3155–3162.

(19) Hernandez, Y.; Nicolosi, V.; Lotya, M.; Blighe, F.; Sun, Z.; De, S.; McGovern, I. T.; Holland, B.; Byrne, M.; Gunko, Y.; et al. High Yield Production of Graphene by Liquid Phase Exfoliation of Graphite. *Nat. Nanotechnol.* **2008**, *3* (9), 563–568.

(20) Geim, A. K. Graphene: Status and Prospects. *Science (80-.).* **2009**, *324* (5934), 1530–1534.

(21) Park, S.; Ruoff, R. S. Chemical Methods for the Production of Graphenes. *Nat. Nanotechnol.* **2009**, *4* (4), 217–224.

(22) McCreery, R. L. Advanced Carbon Electrode Materials for Molecular Electrochemistry. *ChemInform* **2008**, *39* (41), 2646–2687.

(23) Brownson, D. A. C.; Kampouris, D. K.; Banks, C. E. *Graphene Electrochemistry: Fundamental Concepts through to Prominent Applications*; 2012; Vol. 41.

(24) Berger, C.; Song, Z.; Li, T.; Li, X.; Ogbazghi, A. Y.; Feng, R.; Dai, Z.; Alexei, N.; Conrad, M. E. H.; First, P. N.; et al. Ultrathin Epitaxial Graphite: 2D Electron Gas Properties and a Route toward Graphene-Based Nanoelectronics. *J. Phys. Chem. B* **2004**, *108* (52), 19912–19916.

(25) Chang, H.; Wu, H. Graphene-Based Nanocomposites: Preparation, Functionalization, and Energy and Environmental Applications. *Energy Environ. Sci.* **2013**, *6* (12), 3483–3507.

(26) Enhanced Photoactivity and Conductivity in Transparent TiO2 Nanocrystals/Graphene Hybrid Anodes. *J. Mater. Chem. A* **2017**, *5* (19), 9307–9315.

(27) Curri, M. L.; Comparelli, R.; Striccoli, M.; Agostiano, A. Emerging Methods for Fabricating Functional Structures by Patterning and Assembling Engineered Nanocrystals. *Phys. Chem. Chem. Phys.* **2010**, *12* (37), 11197–11207.

(28) Ingrosso, C.; Bianco, G. V.; Corricelli, M.; Comparelli, R.; Altamura, D.; Agostiano, A.; Striccoli, M.; Losurdo, M.; Curri, M. L.; Bruno, G. Photoactive Hybrid Material Based on Pyrene Functionalized PbS Nanocrystals Decorating CVD Monolayer Graphene. *ACS Appl. Mater. Interfaces* **2015**, *7* (7), 4151–4159.

(29) Ingrosso, C.; Corricelli, M.; Bettazzi, F.; Konstantinidou, E.; Bianco, G. V.; Depalo, N.; Striccoli, M.; Agostiano, A.; Curri, M. L.; Palchetti, I. Au Nanoparticle: In Situ Decorated RGO Nanocomposites for Highly Sensitive Electrochemical Genosensors. *J. Mater. Chem. B* **2019**, *7* (5), 768–777.

(30) Ingrosso, C.; Corricelli, M.; Disha, A.; Fanizza, E.; Bianco, G. V.; Depalo, N.; Panniello, A.; Agostiano, A.; Striccoli, M.; Curri, M. L. Solvent Dispersible Nanocomposite Based on Reduced Graphene Oxide in Situ Decorated with Gold

Nanoparticles. *Carbon N. Y.* **2019**, *152*, 777–787.

(31) Ingrosso, C.; Bianco, G. V; Pifferi, V.; Guffanti, P.; Petronella, F.; Comparelli, R. TiO2 Nanocrystals Decorated CVD Graphene Based Hybrid for UV- Light Active Photoanodes. *Procedia Eng.* **2016**, *168*, 396–402.

(32) Tang, Z.; Shen, S.; Zhuang, J.; Wang, X. Noble-Metal-Promoted Three-Dimensional Macroassembly of Single-Layered Graphene Oxide. *Angew. Chemie - Int. Ed.* **2010**, *49* (27), 4603–4607.

(33) Cong, H. P.; Ren, X. C.; Wang, P.; Yu, S. H. Macroscopic Multifunctional Graphene-Based Hydrogels and Aerogels by a Metal Ion Induced Self-Assembly Process. *ACS Nano* **2012**, *6* (3), 2693–2703.

(34) Han, T. H.; Lee, W. J.; Lee, D. H.; Kim, J. E.; Choi, E. Y.; Kim, S. O. Peptide/Graphene Hybrid Assembly into Core/Shell Nanowires. *Adv. Mater.* **2010**, *22* (18), 2060–2064.

(35) Tang, L.; Chang, H.; Liu, Y.; Li, J. Duplex DNA/Graphene Oxide Biointerface: From Fundamental Understanding to Specific Enzymatic Effects. *Adv. Funct. Mater.* **2012**, *22* (14), 3083–3088.

(36) Zhang, L.; Lu, Z.; Zhao, Q.; Huang, J.; Shen, H.; Zhang, Z. Enhanced Chemotherapy Efficacy by Sequential Delivery of SiRNA and Anticancer Drugs Using PEI-Grafted Graphene Oxide. *Small* **2011**, *7* (4), 460–464.

(37) Stankovich, S.; Piner, R. D.; Nguyen, S. B. T.; Ruoff, R. S. Synthesis and Exfoliation of Isocyanate-Treated Graphene Oxide Nanoplatelets. *Carbon N. Y.* **2006**, *44* (15), 3342–3347.

(38) Fang, M.; Wang, K.; Lu, H.; Yang, Y.; Nutt, S. Covalent Polymer Functionalization of Graphene Nanosheets and Mechanical Properties of Composites. *J. Mater. Chem.* **2009**, *19* (38), 7098–7105.

(39) Wang, H. X.; Zhou, K. G.; Xie, Y. L.; Zeng, J.; Chai, N. N.; Li, J.; Zhang, H. L. Photoactive Graphene Sheets Prepared by "Click" Chemistry. *Chem. Commun.* **2011**, *47* (20), 5747–5749.

(40) Si, Y.; Samulski, E. T.; Hill, C.; Carolina, N. Synthesis of Water Soluble Graphene. *Nano Lett.* **2008**, *8* (6), 1679–1682.

(41) Liu, X.; Pan, L.; Lv, T.; Zhu, G.; Sun, Z.; Sun, C. Microwave-Assisted Synthesis of CdS–Reduced Graphene Oxide Composites for Photocatalytic Reduction of Cr(Vi). *Chem. Commun.* **2011**, *47* (43), 11984–11986.

(42) Li, Y.; Tang, L.; Li, J. Preparation and Electrochemical Performance for Methanol Oxidation of Pt/Graphene Nanocomposites. *Electrochem. commun.* **2009**, *11* (4), 846–849.

(43) Shen, J.; Shi, M.; Yan, B.; Ma, H.; Li, N.; Ye, M. One-Pot Hydrothermal Synthesis of Ag-Reduced Graphene Oxide Composite with Ionic Liquid. *J. Mater. Chem.* **2011**, *21* (21), 7795–7801.

(44) Dong, J. J.; Zhen, C. Y.; Hao, H. Y.; Xing, J.; Zhang, Z. L.; Zheng, Z. Y.; Zhang, X. W. Controllable Synthesis of ZnO Nanostructures on the Si Substrate by a Hydrothermal Route. *Nanoscale Res. Lett.* **2013**, *8* (1), 1–7.

(45) Cao, A.; Liu, Z.; Chu, S.; Wu, M.; Ye, Z.; Cai, Z.; Chang, Y.; Wang, S.; Gong, Q.; Liu, Y. A Facile One-Step Method to Produce Craphene-CdS Quantum Dot Nanocomposites as Promising Optoelectronic Materials. *Adv. Mater.* **2010**, *22* (1), 103–106.

(46) Yang, J.; Deng, S.; Lei, J.; Ju, H.; Gunasekaran, S. Electrochemical Synthesis of Reduced Graphene Sheet-AuPd Alloy Nanoparticle Composites for Enzymatic Biosensing. *Biosens. Bioelectron.* **2011**, *29* (1), 159–166.

(47) Wu, S.; Yin, Z.; He, Q.; Lu, G.; Yan, Q.; Zhang, H. Nucleation Mechanism of Electrochemical Deposition of Cu on Reduced Graphene Oxide Electrodes. *J. Phys. Chem. C* **2011**, *115* (32), 15973–15979.

(48) Huang, X.; Tan, C.; Yin, Z.; Zhang, H. 25th Anniversary Article: Hybrid Nanostructures Based on Two-Dimensional Nanomaterials. *Adv. Mater.* **2014**, *26* (14), 2185–2203.

(49) Williams, G.; Seger, B.; Kamat, P. V. UV-Assisted Photocatalytic Reduction of Graphene Oxide. *ACS Nano* **2008**, *2* (7), 1487–1491.

(50) Wang, X.; Tabakman, S. M.; Dai, H. Atomic Layer Deposition of Metal Oxides on Pristine and Functionalized Graphene. *J. Am. Chem. Soc.* **2008**, *130* (26), 8152–8153.

(51) Zhou, X.; Wang, F.; Zhu, Y.; Liu, Z. Graphene Modified LiFePO4 Cathode Materials for High Power Lithium Ion Batteries. *J. Mater. Chem.* **2011**, *21* (10), 3353–3358.

(52) Paul, R. K.; Ghazinejad, M.; Penchev, M.; Lin, J.; Ozkan, M.; Ozkan, C. S. Synthesis of a Pillared Graphene Nanostructure: A Counterpart of Three-Dimensional Carbon Architectures. *Small* **2010**, *6* (20), 2309–2313.

(53) Xia, B. Y.; Yan, Y.; Wang, X.; Lou, X. W. Recent Progress on Graphene-Based Hybrid Electrocatalysts. *Mater. Horizons* **2014**, *1* (4), 379–399.

5.1 PA-RGO/OLEAM-AuNPs Hybrids

Focus

Over the last decades, gold-decorated graphene hybrids have attracted increasing attention as electrochemical and bio-electrochemical platforms for sensing and diagnostic applications. In this part of the Thesis Project, the attention is focused on the production of an electrochemical device for point-of-care diagnosis through disease biomarkers detection for biomedical applications, starting from the well-known dopamine. Dopamine is an important neurotransmitter, which is part of the catecholamine group, distributed in the mammalian central nervous system for message transfer. For this reason, it plays a crucial role in brain functions modulation[1] and altered level of its concentration are clinical features of neurological disorders, like Parkinson's, Alzheimer's, schizophrenia, depression and addiction.[2–6] Moreover, dopaminergic neurons were found to be predicting reward signals.[7] Considering all these facts, the development of diagnostic tools for monitoring such biomarkers, providing technically insights into the mechanisms of its formation, changes of its body quantities and role is a topic of high interest in the scientific community. Moreover, the possibility to investigate the dynamics of biomarkers like dopamine in the extracellular space in biological fluids could be useful for preventing and treating human patho-physiological alterations. In this context, electrochemical (bio)sensors have seen a huge increment in their use for point-of-care diagnosis of disease, practically performed in clinical laboratories. This is due to their easiness of operation, fast response, low detection limits (LOD), excellent selectivity, good sensitivity and low cost. Moreover, they can be miniaturized and implemented in portable instrumentations.[8–10]

Here the use of an electrochemical sensor based on a graphene platform (in particular, reduced graphene oxide (RGO)) functionalized with gold nanoparticles (AuNPs) is proposed. The powerful properties of graphene in electrochemical and

chemical (bio)sensors were already discussed in the Introduction of this Chapter 5, together with the beneficial support from AuNPs for analytical purposes. The functionalization of graphene platforms could happen in different ways, thanks to their high chemical reactivity that makes them robust scaffolds for manufacturing with inorganic nanoparticles. Here a non-covalent functionalization method is proposed. The aim is to obtain original and highly functional hybrid nanocomposite materials, exhibiting enhanced properties that the pristine components do not intrinsically possess. Such routes rely on binding the nanostructures by "soft" π–π stacking interactions or hydrophobic forces, which do not affect the structural properties of graphene that are strictly dependent on its sp^2 carbon atom conjugation extent.[11] The coordination of organic molecules to the surface of nano-objects can be exploited to anchor the particles to the graphene sheets, thus conveying to graphene their unique size and shape dependent properties.[12–14] Sometimes, functional linkers immobilized onto graphene can be essential for chemically binding the ligands coordinated to the nano-objects surface, or directly for coordinating the particles surface, leading to their anchoring onto the graphene platform.[15]

The choice related to the use of gold nanoparticles rises from their demonstrated effectiveness in chemical and electrochemical (bio)sensors, as also discussed in the next **Paragraph 5.2**, **5.3** and the previous **Chapter 4**. Briefly, they possess intense and narrow absorption plasmon, they have strong capability in specifically detecting (bio)molecules (binding them by means of chemical moieties or undergoing surface redox electrocatalytic processes) and they are characterized by a high rate of heterogeneous electron transfer kinetics.[16] In electrochemical (bio)sensors, in fact, the hybridization of graphene with AuNPs provides a very large electrochemically active surface area and effectively accelerates electron transfers between the electrode and the target molecule, leading to a rapid and sensitive current response.[17,18] Due to all these interesting properties of nanocomposites formed of graphene and gold nanoparticles, a great deal is devoted in the last years in the development of advanced synthetic approaches. The general aim is to improve the control of the *size* of the

nanoparticles immobilized onto the graphene platforms, their *dispersion* and the general *uniformity of their coating*.

An *in-situ* synthesis is here reported as a novel route in order to obtain a hybrid with enhanced performances with respect to its relative components alone. In this particular case, gold nanoparticles (AuNPs) are functionalized with an organic ligand, oleylamine (OLEAM), and the RGO platform is functionalized with amino-pyrene (PA). Interactions between PA and OLEAM lead to the effective functionalization of the graphene platform with gold nanoparticles. Amino-pyrene is selected for its capability to exfoliate the RGO flakes and strongly interact with RGO surface by $\pi-\pi$ interactions. As a result, the RGO flakes serves a high density of NH_2 sites for the heteronucleation and growth of oleylamine-functionalized AuNPs. Moreover, PA linker is essential to channel the charge transfer between the nanoparticles and the graphene sheets. The hybrid was synthesized by varying several synthetic conditions, from the gold precursor to the RGO and oleylamine concentrations. A systematic study of the spectroscopic, morphological and electrochemical properties of the nanocomposite enabled the elucidation of the mechanism involved in the *in situ* formation of the nanoparticles onto graphene sheets. As expected, the results showed that a careful control of the concentrations of gold precursor, OLEAM and PA lead to a good control over the AuNPs morphology and size distribution. The synthetic route finally brought to a PA-RGO flakes, coated by a dense and uniform layout of monodisperse AuNPs of about 10 to 20 nm size, functionalized with OLEAM ligand that allowed the formation of a multilayer network of nanoparticles. The hydrophobic forces, which are responsible of the interconnection between the nanoparticles and the graphene flakes, allow long-term stability of the hybrid in organic solvents. The colloid is then used to modify Carbon Screen Printed Electrodes and tested as sensitive platform for dopamine detection.

Focus of this part of the Thesis work is to study in depth the effectiveness of the synthetic route in the final hybrid electrochemical and electroanalytical

performances. The role played by the capping agent OLEAM is investigated, together with the size and distribution of the nanoparticles on the graphene platform. The enhanced performances (from sensitivity to electrocatalytic features) of the hybrid with respect to its component are highlighted, especially looking at its electrochemical features and electroanalytical answer towards dopamine.

Materials and Methods

Chemicals

Commercial Reduced Graphene Oxide (RGO) (1.6 nm flakes) was purchased from Graphene Supermarket. 1-Aminopyrene (PA, 97%), n-methyl-2-pyrrolidone (NMP, 99%), tetrachloroaurate(III) trihydrate ($HAuCl_4 \times 3H_2O$, 99.999%), oleylamine (OLEAM, 70%), toluene and methanol were purchased from Sigma Aldrich.

Exfoliation and functionalization of RGO

Commercial RGO was exfoliated and functionalized with 1-Aminopyrene (PA), by following an already known procedure[19] with minor modification, that is by sonicating a mixture of RGO powder and PA, prepared in a 1:8 molar ratio, in n-methyl-2-pyrrolidone (NMP). NMP was chosen as solvent, because of its ability to disperse RGO flakes.[20] The excess of PA was removed by cycles of centrifugation and re-dispersion in methanol, until the UV-Vis absorption spectra of the PA-RGO complex, collected after each washing step, remain unchanged, and until the TEM images of the dispersion do not show PA crystallites onto the flakes.[19] Finally, the purified PA-RGO powder was dispersed in NMP.

Synthesis of the PA-RGO/AuNPs hybrid material

For the preparation of the PA-RGO/AuNPs hybrid nanocomposites, the colloidal synthesis of amino-coated Au NPs, of Hiramatsu H. et al.[21], was followed with minor modifications. In a typical experiment, a reaction flask was added by 1 - 5 mg of PA-RGO powder dispersed in 15 mL of toluene, by 5-7.5 mL of OLEAM and 240-340 mg $HAuCl_4 \times 3H_2O$ in 35 mL of toluene. At first, the reaction flask was heated up to 110°C under vacuum, and then, the synthesis was allowed to proceed for 5 hours at this temperature. The obtained PA-RGO/Au NPs hybrid nanocomposite was purified from the excess of OLEAM, by four cycles of centrifugation at 3000 rpm, using a non-solvent precipitation procedure, which is carried out by re-dispersing the pellet in methanol. Finally, the isolated hybrid nanocomposite was dispersed in

toluene, to achieve optically transparent solutions for spectroscopy and morphological investigation.

Characterization techniques

- **UV-Vis-NIR** absorption spectroscopy was performed to characterize the PCA-RGO/Au NP hybrid material dispersed in toluene, by using a Cary Varian 5000 spectrophotometer.
- **Mid-infrared** spectra were acquired with a Varian 670-IR spectrometer equipped with a DTGS (Deuterated Tryglycine Sulfate) detector, having a spectral resolution of 4 cm^{-1}. For attenuated total reflection (ATR) measurements, the used internal reflection element (IRE) was a one-bounce 2 mm diameter diamond microprism. The samples were cast directly on the upper face of the diamond crystal and the solvent was allowed to evaporate.
- **Transmission Electron Microscopy** (TEM) images of the PA-RGO/AuNP hybrid flakes were acquired by using a JEOL JEM-1011 microscope, working at an accelerating voltage of 100 kV and equipped with a high-contrast objective lens, and a W filament as electron source. Under these conditions, the ultimate point resolution of the microscope was equal to 0.34 nm. The TEM images were collected by a Gatan SC-1000 Orius Camera, equipped with a fiber-optical coupled 11 Mp CCD. The samples were prepared by dipping the 300 mesh amorphous carbon-coated Cu grid in PA-RGO/Au NP toluene dispersions, and letting the solvent to evaporate. Size statistical analysis (NP average size and size distribution) of the samples was performed by means of a freeware Image J analysis program.
- Topography and phase mode **Atomic Force Microscopy** (AFM) measurements were performed in air and at room temperature, by means of a PSIA XE-100 SPM system operating in tapping mode. A silicon Scanning Probe Microscope (SPM) sensor for noncontact AFM (Park Systems), having a spring constant of 42 N m^{-1} and a resonance frequency of 330 kHz,

was used. Micrographs were collected on six distinct areas of the sample, with a scan size area of 5 μm × 5 μm, by sampling the surface at a scan rate between 1.0–0.5 Hz, and a resolution of 256 × 256 pixels. Topography AFM images were processed by using the XEI software to obtain statistical data.

Electrodes Preparation

The colloidal dispersions in toluene of the PA-RGO_AuNPs hybrid samples were drop casted onto C-SPEs (purchased from Metrohm DropSens) and let them dry in air at room temperature. The modified electrodes were treated by spin coating a mixture of CH_3OH/CH_3COOH or by casting onto the surface a 1 mM solution of mercaptohexanol, MCH, (97%, Sigma Aldrich, Milano, Italy) and let under controlled humidity for one hour. The colloidal dispersions composed by only PA-RGO and only AuNPs were investigated too. In this case, the suspension was left under stirring for one hour; then, 1.8 μL of the colloid were deposited by drop casting, using an automatic micropipette (Kartell, Noviglio, Milan, Italy), onto the C-SPE surface and let them dry in air at room temperature. Apart from RGO and AuNPs samples alone, also a subsequent deposition of RGO and then AuNPs was done, by drop casting 1.8 μL of RGO first and then, when dried, the same amount of AuNPs colloidal solution. The ligand-exchange procedure with MCH was performed also on these last modified electrodes (bare AuNPs, RGO and AuNPs deposited one over the other).

Electrochemical Characterizations

Electrochemical Characterizations by Cyclic Voltammetry (CV) and Electrochemical Impedance Spectroscopy (EIS) were performed using a PGStat30 (Metrohm AutoLab, Utrecht, The Netherlands) equipped with NOVA 2.1 Software (Metrohm AutoLab, Utrecht, The Netherlands). The experiments were carried out in a conventional three electrode cell using a Saturated Calomel Electrode (SCE) and a Platinum wire as reference (RE) and counter (CE) electrodes, respectively. The

working electrode (WE) was the Carbon Screen Printed Electrode (C-SPE) modified with the different RGO and AuNPs colloidal solutions. 0.1 M solution of KCl, $NaClO_4$ and PBS (Phosphate Buffer, pH 7.4) were used as supporting electrolyte and $K_4[Fe(CN)_6]$ as molecular redox probe. Cyclic Voltammetry was performed both on the background and on a solution of 3 mM redox probe, in the range -0.3 V (SCE) and +0.7 V (SCE). EIS measurements were conducted at -0.1 V, +0.1 V and +0.25 V (SCE).

Electroanalytical Applications

Electrochemical detection of dopamine was performed using a μ-AutoLab III (Metrohm AutoLab, Uthrecht, The Netherlands), equipped with the NOVA 2.1 Software (Metrohm AutoLab, Utrecht, The Netherlands). Differential Pulse Voltammetry (DPV) was used as electroanalytical technique, scanning the potential between -0.2 V and +0.6 V (SCE), with a pulse of 5 mV and an amplitude of 50 mV. Dopamine Hydrochloride (Sigma Aldrich, Milano, Italy) solutions were prepared in 0.1 M PBS (pH 7.4) as supporting electrolyte.

Results and Discussion

Synthesis and Characterization of the PA-RGO/AuNPs Hybrids

Commercial Reduced Graphene Oxide (RGO) powder has been functionalized and exfoliated with the functional aromatic ligand 1-aminopyrene (PA) by following the approach reported in [19] with little modifications. In particular, RGO powder was dissolved in an n-methyl-2-pyrrolidone (NMP) solution of PA and subjected to successive cycles of sonication and stirring. Then, purification of the flakes from the excess of PA was achieved by centrifugation steps. The 1-aminopyrene linker is able to anchor the RGO flakes through π–π stacking interactions, opening small gaps at the graphene sheets edges and penetrating deeper in the graphene multilayers.[19] It is important to underline that PA is able to preserve the C sp^2 structure, grafting $–NH_2$ groups into the platform. These groups, acting as out-of-plane moieties, keep separated the RGO sheets preventing their re-stacking and concomitantly they allow the dispersion of the synthesized PA-RGO sheets in solvents.[20]

Figure 5.1.1 (a) reports Transmission Electron Microscopy image of the PA-RGO flakes. The TEM micrograph shows a micro-meter sized sheet-like structure, almost transparent. The lack of PA crystallites chemisorbed onto the RGO sheets is a proof of the effectiveness of the centrifugation step of purification previously explained. Panel **(b)** and **(c)** of **Figure 5.1.1** report the Atomic Force Microscopy (AFM) images and cross section profiles (correspondent to the red line in panel (b)) of the PA-RGO material, from which a sheet-like nanostructure is confirmed to be present, with a thickness of about 4-6 nm. Considering that the thickness of a single RGO sheet is more than 1 nm and the interlayer distance between the RGO platform and PA molecules is between 0.35 and 0.8 nm, it is possible to assert that the arrangment of the PA-RGO flakes in the hybrid is of single or few-layered sheets [22,23].

The PA-RGO/AuNPs hybrid flakes have been obtained synthesizing OLEAM-coated AuNPs *in situ*, i.e. in the presence of the PA-RGO flakes. In this process, the gold precursor ($HAuCl_4 \times 3H_2O$) is reduced by the oleylamine agent, which behaves

also as capping ligand, controlling the synthesis process.[21] Au(III) is completely reduced to Au(0) without the need of addiction of any other reducing agent. In concomitance, the $–NH_2$ moieties of the PA-RGO complex act as heteronucleation, growth and coordination sites for the AuNPs synthesis. In this way, gold nanoparticles are finally anchored to the RGO platform.[24]

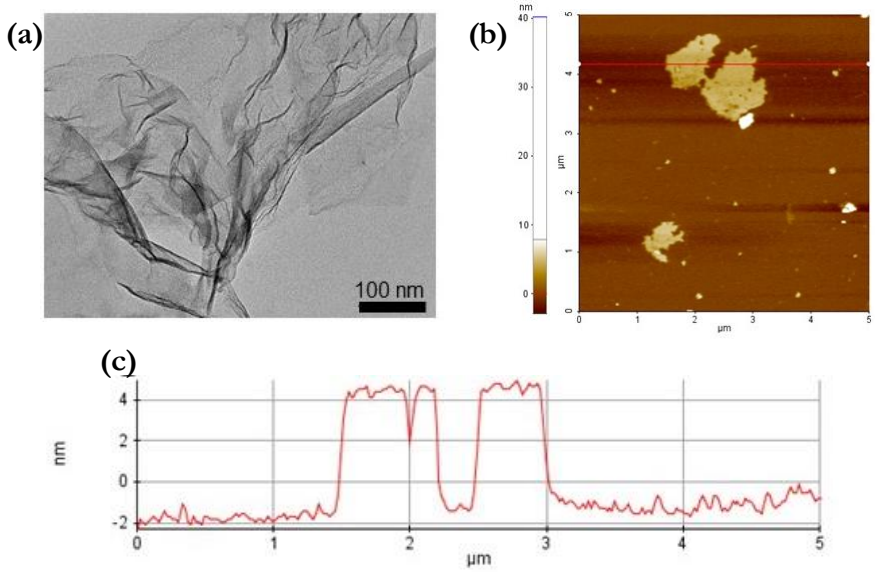

Figure 5.1.1: (a) TEM micrograph, **(b)** AFM topography and **(c)** Cross sectional line profile taken on the red line in **(b)** of the PA-RGO complex.

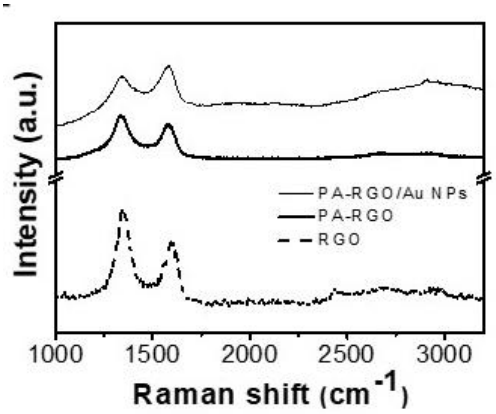

Figure 5.1.2: Raman spectra of the bare RGO, the modified PA-RGO and the final hybrid PA-RGO/AuNPs.

Figure 5.1.2 reports the Raman spectra of the bare RGO, the PA-RGO and the final PA-RGO/AuNPs hybrid. In the RGO spectra, the typical G and D peaks of the graphene derivative platform, at about 1580 cm^{-1} and 1340 cm^{-1}, respectively, are present. The first one refers to the stretching of the C-sp^2 bonds and the second to the vibrational "breathing modes" of C-sp^2 atoms in the

hexagonal rings. The D peak is of particular interest, since its intensity gives information on the structural quality of the carbon lattice.[25] In this case, in particular, it could refer to the presence of defects in RGO like ripples, edges or impurities, including oxygen functionalities (like hydroxyl, epoxy, carbonyl and carboxyl groups) as well as C heteroatoms and hydrocarbon possibly deriving from the synthetic conditions for the reduction from GO to RGO.[26] This defective structure of RGO sheets is verified again by the low intensity of the 2D peak at around 2700 cm^{-1}, and by the presence of the D+D' signal below 3000 cm^{-1}. Regarding the exfoliated and functionalized RGO (PA-RGO complex spectrum) there are no significant changes in the D and G intensities ratio. However, this intensity (D/G) is lowered when dealing with the final hybrid PA-RGO/AuNPs. This change could be ascribed to a healing effect played by the OLEAM capping agent during the synthesis of the AuNPs at 110 °C. The broad background signal in the hybrid flakes spectrum is due to the typical photoluminescence emission of 1-amynopyrene.[27]

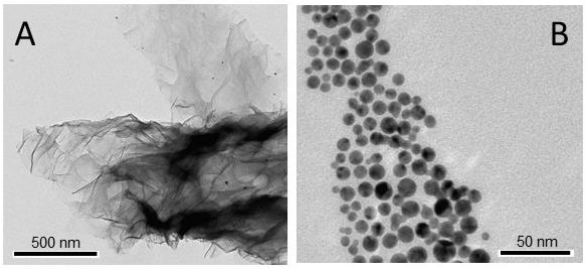

Figure 5.1.3: TEM images of the AuNPs grown onto bare RGO (**a**) and (**b**) in the surnatant solution of (**a**).

The effective role played by the pyrene linker has been verified by a control experiment in which gold nanoparticles were synthesised in the same way of the final hybrid, but in the presence of the only RGO sheets, without any pyrene functionalities on them. TEM images clearly show that in the absence of PA linker, gold nanoparticles do not grow onto the graphene platform (**Figure 5.1.3 (a)**). This experiment and other preliminary studies show that gold nanoparticles do not heteronucleate onto the bare RGO flakes and, consequently, underlines the crucial role of the pyrene linker in both the synthesis and then anchoring of AuNPs onto

the graphene platform. On the contrary, nanoparticles homonucleate when in solution, in the absence of the PA-RGO flakes, under the control of the OLEAM capping ligand (**Figure 5.1.3 (b)**).

In order to have a reliable control onto the synthesis of the PA-RGO/AuNPs hybrid nanocomposite, the effects of the different synthetic parameters on the morphological and spectroscopic properties of the nanoparticles have been explored. The OLEAM:$HAuCl_4$ x $3H_2O$ molar ratio together with the PA-RGO:$HAuCl_4$ x $3H_2O$ w/w ratio have been varied until the most suitable conditions were achieved. The optimized process is necessary in order to achieve organic solvent dispersible hybrid flakes, in which the PA-RGO flakes are densely and uniformly decorated with AuNPs, that are capped with OLEAM ligand and with a narrow size distribution and regular morphology.

It was observed that, keeping fixed the concentration of heteronucleation sites (and so the PA-RGO quantity), the increase in the OLEAM:$HAuCl_4$ x $3H_2O$ molar ratio favours the growth of the nanoparticles rather than the heteronucleation, resulting in AuNPs larger in size or distributed with a bimodal population. The same happens when the PA-RGO:$HAuCl_4$ x $3H_2O$ increase when OLEAM:$HAuCl_4$ x $3H_2O$ is kept fixed, meaning that PA acts as coordinating ligand and its -NH_2 moieties favour the growth of the nanoparticles rather than their heteronucleation.

From the morphology investigation, also multilayer of OLEAM-AuNPs were found, reasonably ascribed to the occurrence of hydrophobic forces between the long alkyl chain of the amino ligand molecules that are coordinating the AuNPs surface. The effective presence of OLEAM ligand onto the nanoparticles was verified by recording IR spectra of the bare OLEAM ligand and of the PA-RGO/OLEAM-AuNPs final hybrid (**Figure 5.1.4**). What can be immediately seen from FTIR spectrum of the hybrid, is that the two signals relative to -NH stretching, which are located at 3370 cm^{-1} and 3293 cm^{-1} in the case of OLEAM spectrum, are absent. On the contrary, bands relative to the alkyl groups of OLEAM (the peak relative to the

asymmetric stretching of $–CH_3$, at 2962 cm^{-1} and the two peaks relative to the asymmetric and symmetric stretching of $–CH_2$, at 2922 cm^{-1} and 2852 cm^{-1}, respectively) are visible. The -C=C- stretching of the bare OLEAM molecule, at 3005 cm^{-1} and 1657 cm^{-1} are absent when the ligand is bound to AuNPs to form the hybrid. Other differences in the two spectra can be found in the low wavenumber region, where the typical bending of the neat OLEAM, at 1613 cm^{-1}, is absent in the hybrid, like the symmetric bending signals of $-CH_2$ and $-CH_3$ (at 1467 cm^{-1} and 1378 cm^{-1}, respectively). In the hybrid, and so when OLEAM is coordinated to AuNPs, the –C-N- stretching vibrations signals are at 1259 cm^{-1}, 1084 cm^{-1} and 1015 cm^{-1}, instead of the single signal at 1071 cm^{-1} in the case of the bare ligand. At 795 cm^{-1} the –NH bending is evident in the spectrum of the hybrid, while the same band is at 792 cm^{-1} in the spectrum of OLEAM.

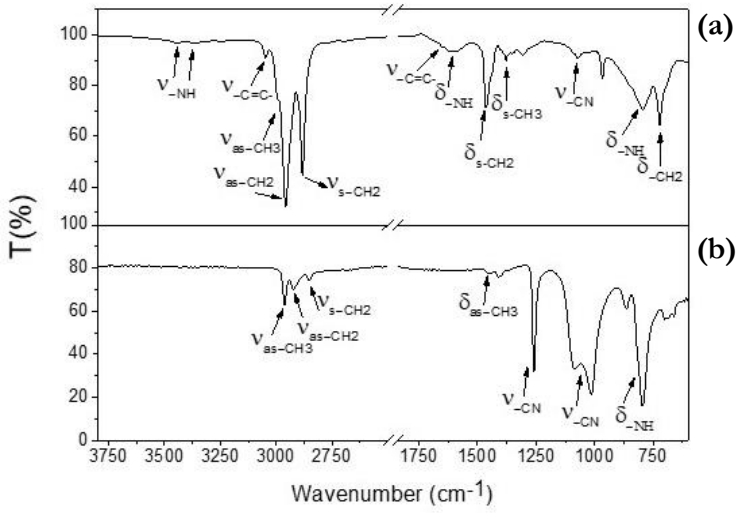

Figure 5.1.4: FTIR-ATR spectra of the OLEAM ligand alone (**a**) and PA-RGO/OLEAM-AuNPs (**b**) flakes.

In general, it can be claimed that the functionalization of the nanoparticles with the OLEAM ligand is effective and leads to a new and different material with respect to the starting components, as already evidenced by the morphological characterization.

The coordination of the organic ligand, oleylamine, onto the surface of gold nanoparticles allows to disperse the hybrid flakes into organic solvents, giving a colloidal solution that results stable in time over several months.

PA-RGO/AuNPs Hybrids: understanding the role of each component

Two of the different hybrid materials previously synthesized have been used to modify the electrode platforms, *i.e.* Carbon Screen Printed Eletrodes. The two hybrids differ in the mean nanoparticles size, that are about 12 nm and 19 nm, hereafter named as "Au2" and "Au3". Here the study of the materials is done in order to understand how the different properties of the hybrids reflect in different electrochemical and electroanalytical performances. At first, the effect of morphology and size of the nanoparticles is considered; then, the effect played by the presence or the absence of the OLEAM capping agent is investigated. In fact, since oleylamine is composed by a long carbonaceous chain (see **Figure 5.1.5 (a)**), this ligand may affect the performance of the electrode, covering gold nanoparticles and leaving them less available to react with the target analyte.

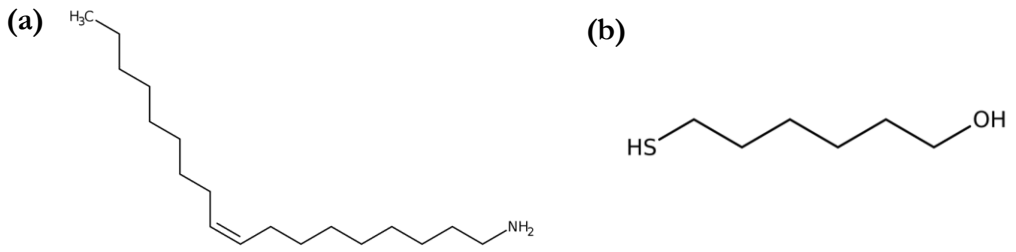

Figure 5.1.5. Chemical structure of oleylamine (OLEAM) (**a**) and 6-mercapto-1-hexanol (MCH) (**b**).

In order to explore this fact, the electrodes were treated in several ways after their modification (via drop casting of the colloidal solutions, as previously reported in the "Materials and Methods" Paragraph of this Chapter 5.1). In more details, they were used as they were after the casting or they were subjected to:

a) Spin coating procedure with a mixture of MeOH/CH_3COOH
b) Casting of a solution of 1 mM 6-mercapto-1-hexanol (MCH) (see **Figure 5.1.5 (b)**).

The first treatment, by spin-coating of a mixture of ligand molecules onto colloidal nanocrystals/nanoparticles (NC/NP) films, is a procedure typically performed to enhance the electron conductivity of the NC/NP films integrated in optoelectronic devices as photodectectors, sensors and photovoltaic cells.[28] Here, in particular, the treatment of the Au NP film by spin-coating a mixture of acetic acid/methanol was performed to displace at the surface of the Au NPs the pristine insulating long alkyl chain oleylamine ligand with short chain acetate ions. In this way, the interparticles charge transfers and the charge transfers at the interphase electrode/electrolyte solution was expected to be improved, resulting in an enhancement of the electron conductivity of the PCA-RGO/Au NP based electrodes.[29] The second treatment, instead, regards a ligand-exchange procedure which leaves AuNPs coated with the new MCH ligand.

Figure 5.1.6 (a) reports the typical surface morphology, obtained with Scanning Electron Microscopy measures, of the bare C-SPEs. **Figure 5.1.6 (b)**, instead, shows the surface of the electrode after the modification with the colloidal solution (in toluene) of the PA-RGO/AuNPs hybrid. What it can be observed is that the modified electrode (**Figure 5.1.6 (b)** presents a high nanoporous surface area, due to the bright contrast spherical in shape nanostructures, reasonably ascribed to the presence of AuNPs. After treatment of the hybrid modified C-SPEs surface by spin-coating the mixture of CH_3OH/CH_3COOH, a partial aggregation of the Au nanostructures (**Figure 5.1.6 (c)**) can be observed. Such aggregation effect drastically increases after casting onto the modified electrode surface the solution of mercaptohexanol (MCH) (**Figure 5.1.6 (d)**). The high affinity of -SH groups for gold nanoparticles could be responsible, in this case, also of the breaking of the ligand between the NH_2 moieties of PA and AuNPs, leading to an effective aggregation of

AuNPs, with the detachment from the graphene platform and the effective detriment of the hybrid structure.

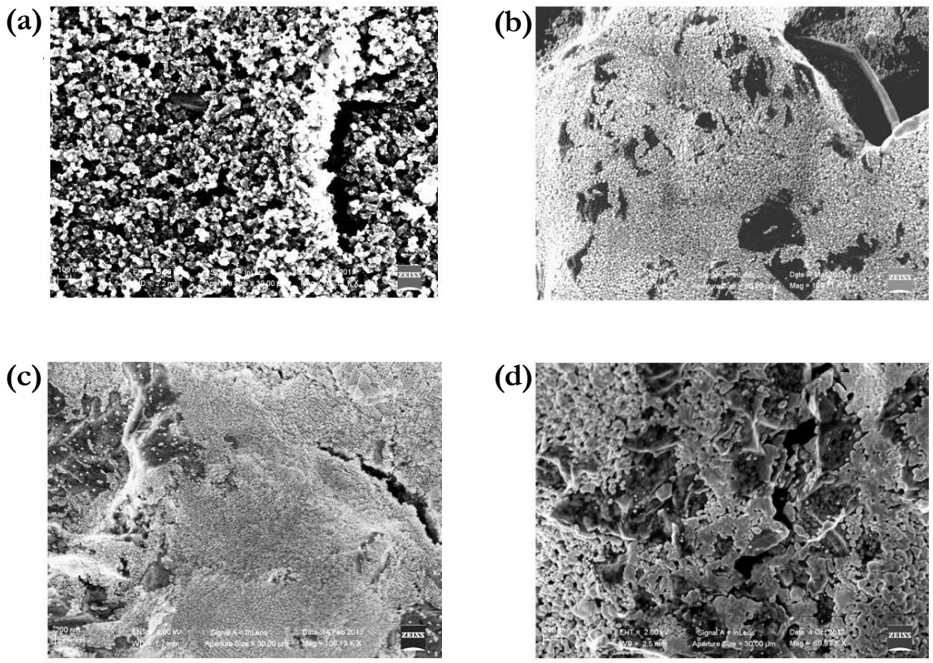

Figure 5.1.6. SEM micrographs of C-SPEs, as bare (**a**) and modified with the hybrid solution, before (**b**) and after spin-coating a CH_3OH/CH_3COOH mixture (**c**) and after casting MCH (**d**).

As previously mentioned, the effect played by the different dimensions of gold nanoparticles is at first investigated. Cyclic Voltammetry (CV) and Electrochemical Impedance Spectroscopy (EIS) measurements on different modified electrodes have been recorded and their relative behavior is compared. In this part of the characterization data, the electrochemical results shown are all conducted in a solution of Phosphate Buffer (PBS) at a pH value of 7.4, since it represents the most suitable electrolyte solution for the final application in the detection of dopamine. In the next Paragraph, all the other electrochemical characterizations, conducted in different supporting electrolytes and conditions, are deeply discussed.

In the next graphs, the electrodes will be named as follow:

- **RGO_Au2_OLEAM**: represent the C-SPE modified with the hybrid solution with AuNPs of mean size equal to 12 nm. No further treatments are

done on this electrode. The "_OLEAM", in fact, represent the idea that the ligand is already present onto the AuNPs surface,

- **RGO_Au3_OLEAM**: system analogous to the previous one, with the only difference that the AuNPs are bigger, with a mean size of 19 nm,
- **RGO_Au2**: it represents the electrode in which the treatment with spin coating of the mixture of MeOH/CH_3COOH is done and the OLEAM ligand is removed. Gold nanoparticles are here the "Au2" (12 nm),
- **RGO_Au3**: analogous to the previous system RGO_Au2, with the difference in the gold nanoparticles size, here about 19 nm,
- **RGO_Au2_MCH**: hybrid with the smaller nanoparticles deposited onto the C-SPE support and then subjected to the ligand exchange procedure with MCH,
- **RGO_Au3_MCH**: analogous to the previous modified electrode, but with the bigger nanoparticles "Au3",
- **RGO**: the only PA-RGO colloidal solution, without any modification with gold nanoparticles,
- **Au2_OLEAM**: the only gold nanoparticles solution, in which the size is the same of the "Au2" in the hybrid. The nanoparticles, in order to be stable in time in the organic solvent, are functionalized with the OLEAM ligand,
- **RGO,Au2_OLEAM**: system in which the electrode is modified with two subsequent depositions, the first one of the "RGO" solution and the second of the only "Au2_OLEAM" one. This system represents a layer-by-layer creation of the composite, instead of the *in situ* synthesis of the hybrid.

Cyclic Voltammetry of different modified electrodes is shown in **Figure 5.1.8 (a)**. At a first glance, it can be noticed how the two samples treated with MCH behave differently from the others. In particular, the total capacitive current is drastically increased and the signals relative to oxidation and reduction of gold are more visible, but with a shape different from the typical one (see **Figure 5.1.7**).

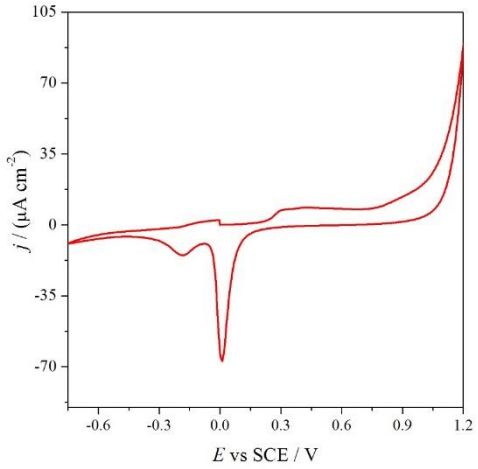

Figure 5.1.7: CV pattern of a bulk gold electrode in 0.1 M NaOH

Moreover, in the cathodic region it can be observed the presence of two reduction peaks, both shifted at more negative potentials than the one of the other samples, at ca. +0.4 V (SCE). This aspect could be ascribed to the presence of AuNPs aggregates of different dimensions. So far, the general trend of these two hybrids let us suppose that the surface of the electrode is drastically modified by the ligand exchange procedure: the nanoparticles are not well distributed on the surface, as confirmed by the SEM images of the electrode morphology in **Figure 5.1.6 (d)**, where aggregation phenomena are clearly visible. Looking at the inset of **Figure 5.1.8 (a)**, particularly focusing on the cathodic peaks, it can be noticed how the hybrids in which no treatments have been done (**RGO_Au2_OLEAM** and **RGO_Au3_OLEAM**) behave basically in the same way. Both the peak positions and the density current values are quite similar for the samples with two different dimensions of gold nanoparticles ("Au2", 12 nm and "Au3", 19nm). On the contrary, in the case of the hybrids that have been treated by spin coating the mixture of methanol and acetic acid (**RGO_Au2** and **RGO_Au3**) more appreciable differences in peak positions and density current values can be noticed. It means that without the oleylamine capping agent it is possible to obtain a different electrochemical response by tuning the nanoparticles size.

These considerations are confirmed also by the Electrochemical Impedance Spectroscopy results. **Figure 5.1.8 (b)** shows Bode plots recorded on the background solution (PBS, 0.1 M) at +0.25 V for the different hybrid materials. In an analogous way from the CVs, the two samples treated with MCH are totally different from the others, in which more differences can be appreciated in the

samples composed by AuNPs of different dimensions, after the spin coating treatment (**RGO_Au2** and **RGO_Au3**).

Figure 5.1.9 (a) and **(b)** report the analogous CV and EIS plots of the other electrodes under investigation: only **RGO**, only AuNPs (**Au2_OLEAM** and **Au2_MCH**) and subsequent depositions of RGO and AuNPs before and after the ligand exchange procedure with MCH (**RGO,Au2_OLEAM** and **RGO,Au2_MCH**).

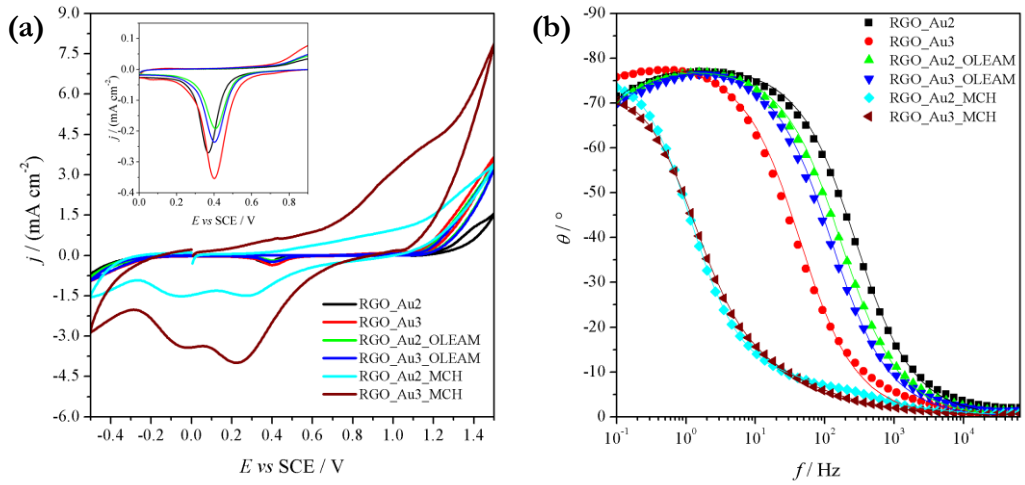

Figure 5.1.8: (**a**) Cyclic Voltammetry of the hybrid materials recorded in 0.1 M PBS as supporting electrolyte, At 100 mV s^{-1}. In the inset, CVs without the ones treated with MCH, zoomed in the reduction region of gold. (**b**) Bode plots recorded in 0.1 M PBS at +0.25 V.

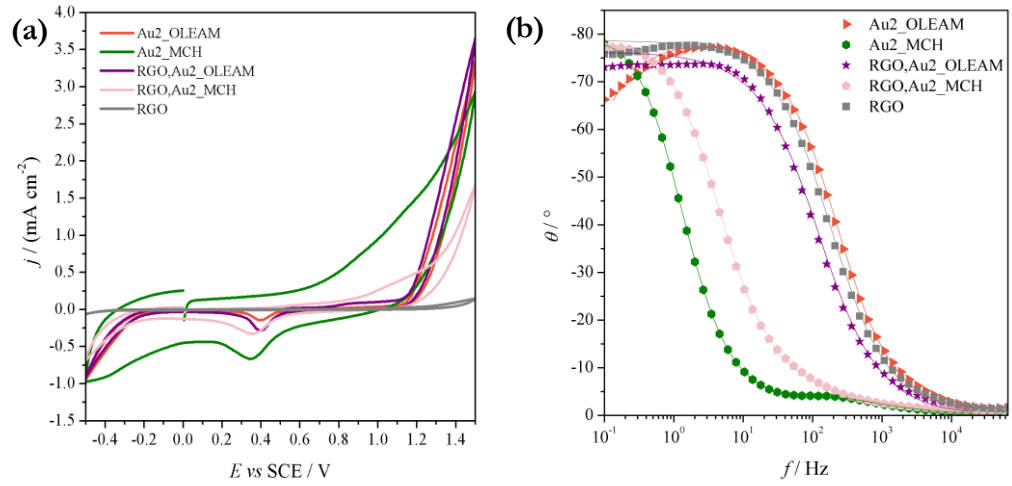

Figure 5.1.9: (**a**) Cyclic Voltammetry of the hybrid materials recorded in 0.1 M PBS as supporting electrolyte, At 100 mV s^{-1} (**b**) Bode plots recorded in 0.1 M PBS at +0.25 V.

Also in these cases, the samples treated with MCH are drastically different from the others. In the case of the "RGO,AuNPs" materials, in which the AuNPs are casted on graphene and not grown *in situ* on the platform, as happens for the hybrids, it is clearly visible how the answer is basically equal to the only AuNPs ones. This fact means that the synthetic procedure is essential in order to achieve a real hybrid. It is not sufficient just casting one layer over the other, but it is fundamental that gold nanoparticles grow onto the PA-RGO sheets, assisted by the OLEAM reducing and capping agent. In fact, the answer of the layer-by-layer modified electrode is equal to the one of only gold, meaning that the effect played by the RGO platform is completely lost and hide.

Cyclic Voltammetry and Electrochemical Impedance Spectroscopy were performed also in the presence of 3 mM of $K_4[Fe(CN)_6]$ as molecular redox probe (see **Figure 5.1.10 (a)** and **(b)**). As already observed in the case of the analysis performed on the background, also in this case the answer of the electrode treated with MCH are the most different from the others. There is a general increase in the capacitive current, but also the reaction towards the oxidation and reduction of the redox probe is changed, as evident by the shape of the voltammetric curves (more similar to a step than a peak). In the cases of the hybrid treated with CH_3OH and CH_3COOH and without any treatment, the differences among them follow the trend observed in the background, but in a more appreciable way. The treated hybrids (**RGO_Au2** and **RGO_Au3**), the ones in which the AuNPs are free from the OLEAM ligand, show CV and EIS that differ one from the other, in terms of potential peak position, density current and frequency shifts. These differences are not appreciable in the case of the hybrid that are not treated and so the ones that retains the oleylamine ligand. It is reasonable to think that the long aromatic chain of the capping agent act as a partial coverage and suppress the peculiar electrochemical properties of nanoparticles of different dimensions, showing them like they have all the same characteristics.

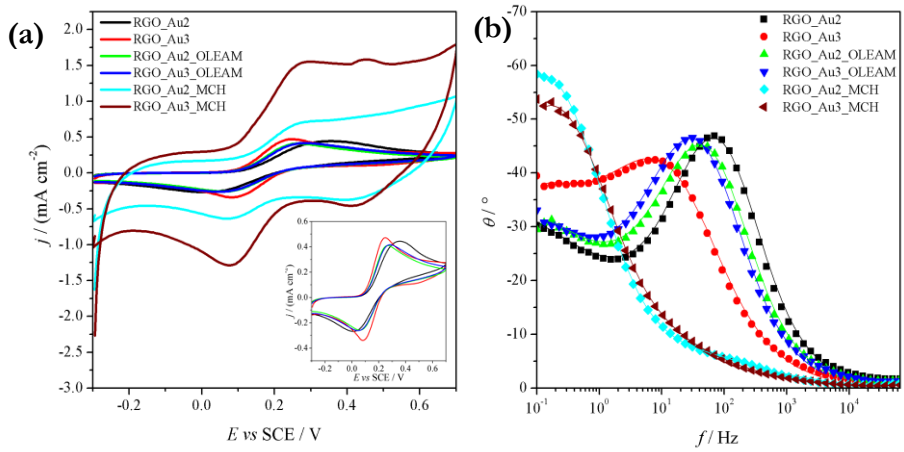

Figure 5.1.10: (**a**) Cyclic Voltammetry of the hybrid materials recorded in 0.1 M PBS as supporting electrolyte, at 100 mV s^{-1}, in the presence of 3mM of $K_4[Fe(CN)_6]$. In the inset, CVs without the ones treated with MCH. (**b**) Bode plots recorded at +0.25 V.

For what concern the other material under investigation, as a comparison with the experiments done on the background, CV and EIS of the single RGO, of the only AuNPs and of the two solutions casted one over the other, before and after the ligand exchange procedure, are reported in **Figure 5.1.11 (a)** and **(b)**. Also in this case, analogous to the background situation, the materials which are modified with MCH treatment show the highest capacitive current. It can be observed that in all the gold-containing samples, the reaction of the probe occurs at potential values closer to zero with respect to the only RGO platform. This effect could be ascribed to the intrinsic electrocatalytic activity played by gold nanoparticles as electroactive material. For what concern the materials treated with 6-mercapto-1-hexanol, a higher capacitive current is reflecting in an overall high activity, even if the Faradaic contribution is higher for the materials with the OLEAM ligand. The aggregation phenomena are, also in this case, detrimental for the final electrochemical response of the electrode material. From the impedance spectra (Bode Plots) the different behaviors of the MCH-treated materials are again more evident, since the maximum of the phase angle is registered at frequency values much lower than the other materials (**Figure 5.1.11 (b)**). From the electrochemical results, it is clear how the treatment to remove or change the capping agent of AuNPs affects the performances of the systems. In particular, the ligand exchange procedure with MCH is not

beneficial, since it creates on the surface of the electrode big aggregates of nanoparticles, with uncontrollable dimensions (for sure much more than 12 nm or 19 nm, typical of the samples "Au2" and "Au3", respectively). This aspect reflects in a completely different morphology of the system and also results in a change of the redox levels of the AuNPs anchored on RGO.[30,31] On the contrary, the spin-coating treatment is beneficial. In fact, without the oleylamine capping agent, it is possible to see differences between the two samples characterized by different AuNPs dimensions, meaning that the nanoparticles are less hindered and maybe more active for further electroanalytical applications. These differences are not clear when the hybrids are used as they are, without any treatment, because oleylamine, made of a long aromatic chain, could hide the fine differences between the AuNPs dimensions and make the two hybrids as "globally" equal. Another interesting aspect is the similar behavior of the only AuNPs systems and the related layer-by-layer modified electrodes, in which the RGO solution is deposited before the AuNPs one. In this case, a complete coverage of the graphene platform with AuNPs could be present and no enhanced performances with respect to the single components, as observed for the hybrid, are verified. This means that it is important to follow the particular synthetic procedure in order to achieve a suitable functionalization of RGO with AuNPs, also allowing a controlled distribution.

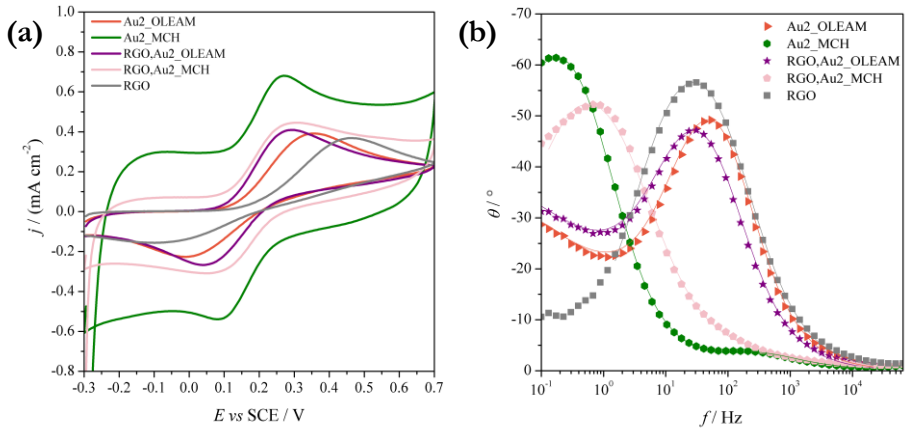

Figure 5.1.11: (**a**) Cyclic Voltammetry of the hybrid materials recorded in 0.1 M PBS as supporting electrolyte, at 100 mV s^{-1}, in the presence of 3 mM $K_4[Fe(CN)_6]$ (**b**) Bode plots recorded at +0.25 V.

Electrochemical Application of the PA-RGO/AuNPs Modified Electrodes in the detection of dopamine

The different modified electrode systems previously characterized were tested as electrochemical sensors for the detection of dopamine. **Figure 5.1.12** resumes experiments conducted on different modified C-SPEs in which it is possible to clarify and understand how the various parameters that can change in the hybrids structure effectively reflect in different electroanalytical performances. In particular, the role of the capping agent, of the dimension of the gold nanoparticles and the way in which these nano-objects are grown onto the graphene platform are kept into consideration and analyzed separately. In **Figure 5.1.12 (a)**, **(b)**, and **(c)** the different electrodes are in the presence of an equal concentration of dopamine, namely 10^{-5} M, in PBS (at a pH value of 7.4) as supporting electrolyte.

Figure 5.1.12 (a) clearly shows the effect of the AuNPs ligand on the electroanalytical performances of the device. In fact, hybrid materials with AuNPs of the same dimensions (in this case, the "Au3" sample, of 19 nm mean size) without ligand (**RGO_Au3**), with oleylamine (**RGO_Au3_OLEAM**) and with mercapthoexanol (**RGO_Au3_MCH**) as capping agents, respectively, are compared. The RGO_Au3_MCH system is not able to detect dopamine in a comparable way to the other two systems. Among these two, the electrode treated by spin coating and so without the oleylamine capping agent, has a response higher than the one without treatment. It is clear how the presence of the ligand is hiding the electrochemical activity of AuNPs and RGO towards dopamine. It is important to have naked nanoparticles free from the capping agent in order to have them more available to react with the target analyte. **Figure 5.1.12 (b)** shows the importance of having a real hybrid instead of a simple layer-by-layer deposition of the two materials (graphene and gold nanoparticles). The hybrid treated with CH_3OH/CH_3COOH (**RGO_Au2**) is compared with the non-treated hybrid (**RGO_Au2_OLEAM**) and with the corresponding counterparts, that are only AuNPs (of the same dimensions

and synthesized in the same way as the hybrid, so in the presence of the reducing and oleylamine capping agent, **Au2_OLEAM**) and only PA-RGO platform (**RGO**). It can be observed that RGO alone is active towards the analyte, in accordance to what is already evidenced in the literature,[32,33] and also gold nanoparticles alone have a response when they are in the presence of dopamine. By the way, the signal, keeping in mind that the concentration of the analyte is the same for all the different experiments, is lower for AuNPs than RGO. This could be related to the insulating effect played by the presence of the long aromatic chain of the oleylamine ligand. The presence of this effect is confirmed also by the decreased signal in the case of **RGO,Au2** system, with respect to the RGO one, like the second layer of AuNPs is hiding the response of RGO towards the analyte. The same decreased signal is observed comparing the hybrid **RGO_Au2_OLEAM** with the overlayered **RGO,Au2_OLEAM**. This observation confirms the importance of having a hybrid following the novel synthetic procedure here reported, in which the nanoparticles are grown *in situ* on the RGO platform. Moreover, the dramatic increase in the performances of the system obtained when the nanoparticles are free from the ligand deserves a particular explanation. It could be that the novel synthetic procedure ensures the obtainment of an optimal distribution of gold nanoparticles on the graphene platform and then the treatment to remove the oleylamine ligand allows to exploit the electroanalytical performances of both the components of the systems, with synergistic effects. These effects reflect in performances for the treated hybrid that are much better than the correspondent single components.

A deeper investigation is done in order to recognize the best electrode in general. **Figure 5.1.12 (c)** shows how the dimensions of the nanoparticles affect the electroanalytical response: the smaller, the better. Considering all these facts, the best system for the detection of the neurotransmitter resulted to be the hybrid with the smaller size of nanoparticles and treated by spin coating the mixture of methanol and acetic acid (**RGO_Au2**). With this system, several experiments were conducted and the concentration of the target analyte was lowered gradually, until the lowest LOD

was achieved. **Figure 5.1.12 (d)** reports the response of the electrode in a solution with dopamine in a really low concentration (from 2 to 20 ppb), with the relative calibration curve in the inset. A final LOD of 3.3 ppb was reached, in accordance with the benchmarck of the Literature for this molecule and even better than the majority of works in the literature.[34,35]

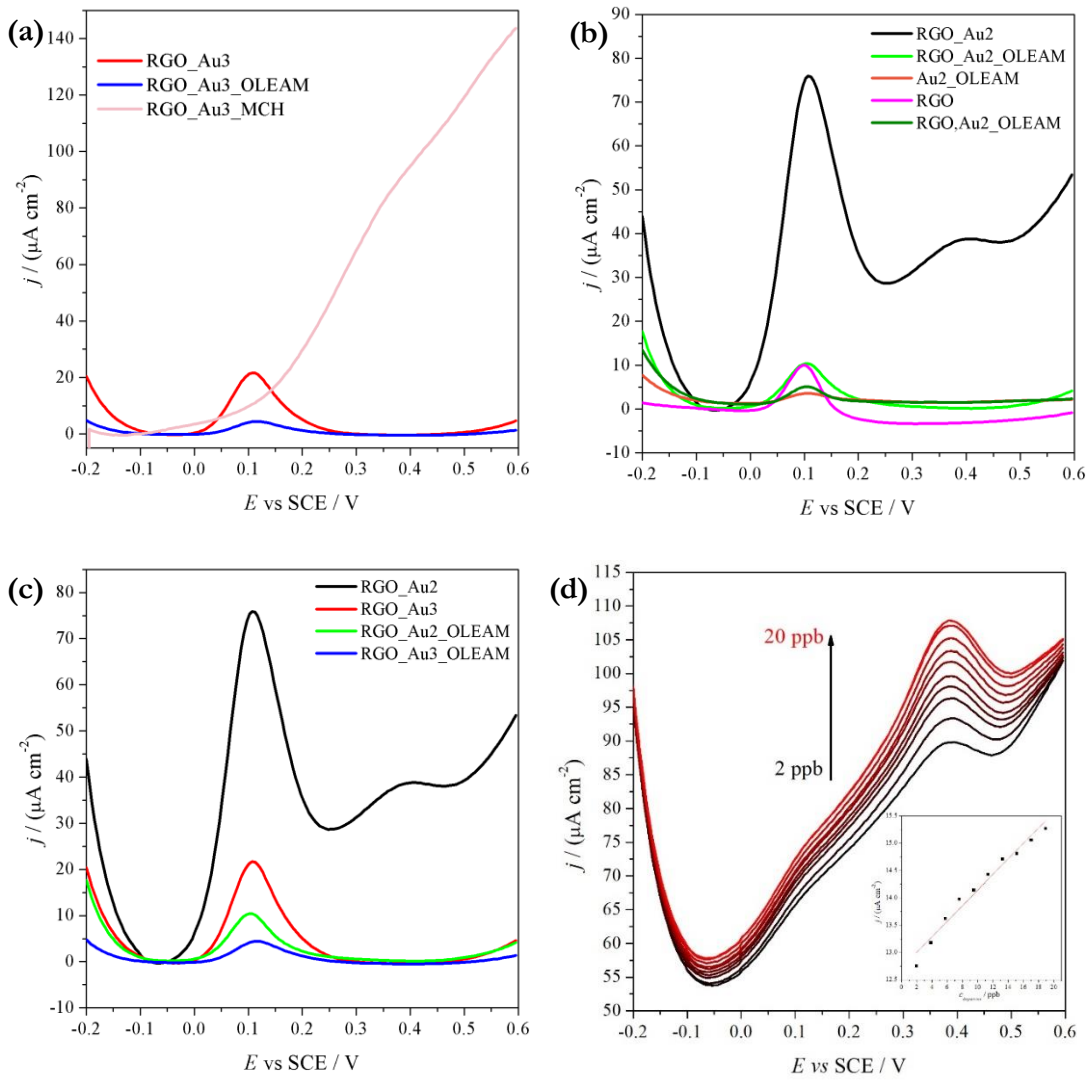

Figure 5.1.12: (**a**) Differential Pulse Voltammetry of the hybrid materials with different capping agent for AuNPs, (**b**) DPV of the hybrids compared with the single counterparts, (c) DPV of hybrid with different sizes of AuNPs, recorded in 0.1 M PBS, in the presence of 10^{-5} M Dopamine. (**d**) Response of the RGO_Au2 hybrid towards successive additions of dopamine in the range 2-20 ppb, with DPV analysis recorded in 0.1 M PBS.

It can be noticed that the "RGO_Au2" hybrid is the only one in which a double signal is present towards dopamine: a first one, more intense at high concentration of the analyte, at about +0.1 V (SCE), and a second one at about +0.4 V (SCE). It was found (**Figure 5.1.12 (d)**) that the second peak is more sensitive when lowering the concentration of dopamine and it was then utilized to build the calibration curve.

Electrochemical Characterizations of the PA-RGO/AuNPs Modified Electrodes

In order to understand deeply all the differences among the materials investigated, all the modifies electrodes were subjected to a deep electrochemical characterization, by Cyclic Voltammetry (CV) and Electrochemical Impedance Spectroscopy (EIS), as previously explained in "Materials and Methods" section of this Chapter.

Briefly, all the materials were studied in three different supporting electrolyte solutions ($NaClO_4$, KCl and PBS), at a concentration of 0.1 M, in the absence and in the presence of the redox probe $K_4[Fe(CN)_6]$. The reason of the choice of such a molecule is that it is already known to be an *inner-sphere* redox probe, towards carbonaceous supports.[36–40] It means that the molecule is sensitive not only to the electronic density of state of the electrode, but it is affected also by the electrode surface structure, also in terms of morphology. In this way, by studying the electrochemical answer of the probe toward a particular electrode it is possible to gain information and make suggestions onto the structure of the electrode surface, particularly interesting when dealing with graphene-based materials.

From the previous study, the best hybrid was found to be the "RGO_Au2" one. It was underlined at first how the ligand exchange procedure with MCH was detrimental and how, on the contrary, the performances after the treatment with spin coating are drastically enhanced. Moreover, the layer-by-layer deposition did not result in a better system. In conclusion, the key point in order to obtain the best

device was highlighted to be the presence or the absence of the OLEAM ligand . For this reason, comparison in the electrochemical characterization of the hybrids with the different AuNPs capping agent will be here discussed.

For each of the above-mentioned supporting electrolyte solutions, Cyclic Voltammetry on the background and in the presence of 3 mM of the redox probe was registered. In the presence of the probe, the scan rate was varied in the range 10 – 500 mV s^{-1}, in order to verify the dependency of the peak current with the voltage scan rate, to verify or not the Randles-Sevcik behavior (see **Chapter 2** and **Chapter 8** for more details) and understand if the system is in electrochemical reversible or irreversible conditions. In more details, the voltage scan rate was varied in the following way: 100, 200, 300, 400, 500, 100, 50, 20, 10, 100 mV s^{-1}. Three scans at 100 mV s^{-1} were repeated, in order to see if the system undergoes some modifications after being stressed with high and low voltage scan rates. EIS spectra were recorded on the background and after the redox probe addition at three different potential values: -0.10 V, +0.10 V and +0.25 V (SCE).

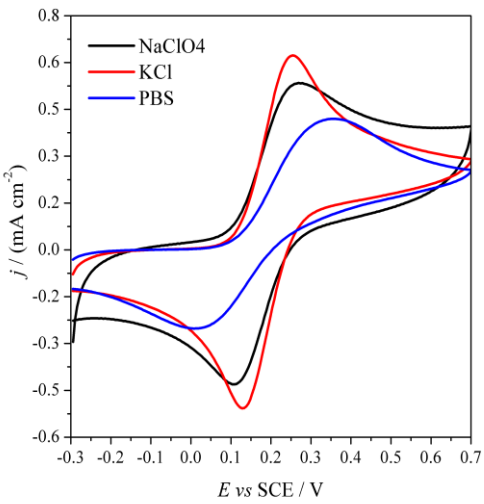

Figure 5.1.13: CV at 100 mV s^{-1} of the RGO_Au2 hybrid in the presence of 3mM $K_4[Fe(CN)_6]$ in three different electrolytes.

In **Figure 5.1.13** the comparison of Cyclic Voltammetries of the hybrid **RGO_Au2** in the presence of 3 mM potassium ferrocyanide in three different electrolytes, at 100 mV s^{-1} is reported. The most defined peak is registered with KCl, showing also one of the most electrochemically reversible behavior. An intermediate behavior is observed when $NaClO_4$ is used, while in case of PBS a shift of the oxidation and reduction peaks in terms of potential values is reported. This result could be ascribed to the presence of some absorption phenomena between the graphene platform and

the phosphate counter ion in the electrolyte solution, which could hinder a bit the reaction of the probe. By the way, the results gained from the characterization (See **Figures 5.1.14** and **5.1.15**) are not so different, giving the confidentiality to work later on in PBS. In fact, keeping in mind that the final application of the device is the detection of dopamine, a neutral and physiological pH value should be maintained over the experiments. Both KCl and $NaClO_4$ are a bit acidic (pH around 5.5), while PBS is synthesized and controlled at pH 7.4. Moreover, potassium ferrocyanide is used with the particular intention to highlight also the little differences that may be present among the experimental proofs, differences that could be not so relavant when dopamine is determined, since this molecule is not an *inner-sphere* probe as $K_4[Fe(CN)_6]$.

From the electrochemical characterization (**RGO_Au2** as example, again), it was found that current intensities of the anodic peak, relative to the oxidation of the probe, are linearly dependent to the square root of the scan rate in all the three electrolytes (**Figure 5.1.14 (a)**, **(b)**, and **(c)**), meaning that no probe adsorption phenomena are occurring at the electrode.

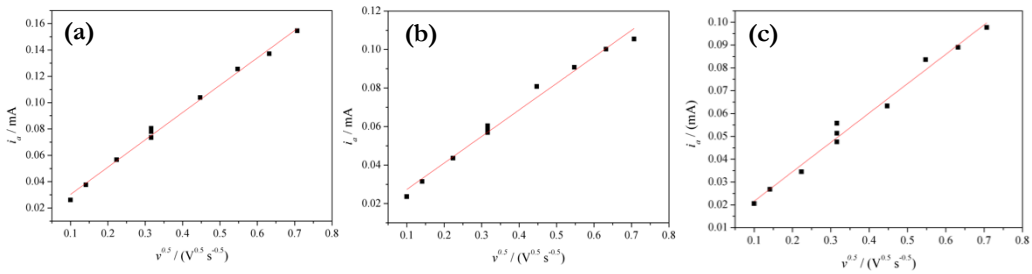

Figure 5.1.14: Linear Dependency of the intensity current values (of the anodic peak relative to $K_4[Fe(CN)_6]$ oxidation) with the square root of the voltage scan rate for the hybrid "RGO_Au2" in KCl (**a**), $NaClO_4$ (**b**) and PBS (**c**).

In order to verify the Randles-Sevcik equation (see **Chapter 2** and **8**) and to understand if the electrochemical process is controlled by planar diffusion towards the electrode or not, also the *log-log* graphs were analysed and reported in **Figure 5.1.15**. The values of the slope (α) of the three curves close to the ideal 0.5 value,

typical of planar diffusion mechanism, in the case of KCl electrolyte (see **Table 5.1.1**). Passing to $NaClO_4$ and PBS, this value is more distant from the ideal one, meaning that other diffusional mechanism are occurring.

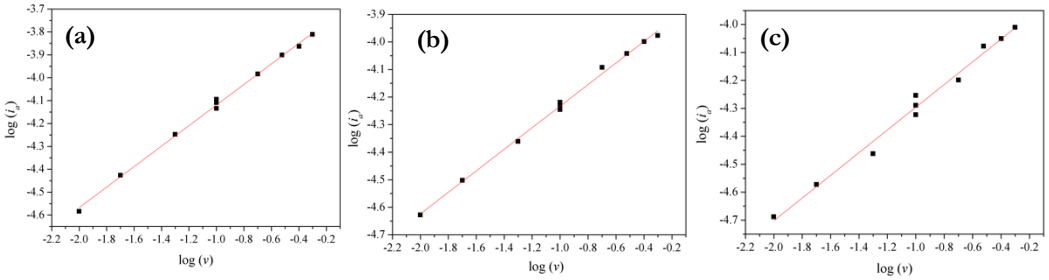

Figure 5.1.15: log(i_a) *vs* log(v) graph for the hybrid "RGO_Au2" in KCl (**a**), $NaClO_4$ (**b**) and PBS (**c**).

Table 5.1.1: α values deriving from the slope of the log-log graphs in **Figure 5.1.15**.

Electrolyte	α
KCl	(0.448 ± 0.008)
$NaClO_4$	(0.391 ± 0.008)
PBS	(0.41 ± 0.02)

Since the results with PBS are not so different from the other two electrolytes, the following comparisons between the hybrids will be done considering the results in PBS (**Table 5.1.2**).

Table 5.1.2: Values derived from the electrochemical characterization (CV) of the different hybrid materials in PBS. Effect of the scan rate on different parameters.

Hybrid	***i vs* $v^{0.5}$ dependency**	**α (log(*i*) *vs* log(*v*) slope)**	***ΔE vs* log(*v*) dependency**	**($E_p - E_{p/2}$) *vs* log(*v*) dependency**
RGO_Au2	Linear	(0.41 ± 0.02)	Variable **(0.1 V s^{-1}: 157 mV)**	Variable
RGO_Au3	Linear	(0.40 ± 0.01)	Variable **(0.1 V s^{-1}: 162 mV)**	Variable
RGO_Au2_OLEAM	Linear	(0.41 ± 0.01)	Variable **(0.1 V s^{-1}: 201 mV)**	Variable
RGO_Au3_OLEAM	Linear	(0.394 ± 0.007)	Variable **(0.1 V s^{-1}: 221 mV)**	Variable
RGO_Au2_MCH	Linear	(0.30 ± 0.04)	Variable **(0.1 V s^{-1}: 186 mV)**	Variable
RGO_Au3_MCH	Linear	(0.24 ± 0.04)	Variable **(0.1 V s^{-1}: 176 mV)**	Variable

From the values reported in **Table 5.1.2**, it is evident how the dependency of the intensity current of the anodic peak of $K_4[Fe(CN)_6]$ with the square root of the voltage scan rate is linear. This behaviour could be addressed both to reversible and irreversible reactions. For this reason, the dependency of the peak-to-peak separation (ΔE = difference between the potential values of the anodic and cathodic peaks) with the logarithm of the voltage scan rate is analysed. In the same way, the trend of the wave shape of the forward peak ($E_p - E_{p/2}$ = difference in potential between the voltage corresponding to the peak current, E_p, and the one corresponding to half the peak current) *vs* the logarithm of the scan rate is considered. In a reversible mechanism, these two parameters should be independent with the scan rate. Here, it is reported how in all cases there is a correlation and a variation with the voltage scan rate. It means that in all cases the mechanism is going towards a situation of electrochemical irreversibility, the peaks are broader and lower with respect to a perfect reversible situation. For a comparison, the ΔE value for all the hybrids recorded at 0.1 V s^{-1} is reported in brackets. It can be seen that the lowest value (157 mV) is present for the hybrid RGO_Au2 and so this is the system which shows the best electrochemical reversibility. Moreover, the value of $E_p - E_{p/2}$ is different from the ideal 57 mV (for a monoelectronic reaction). It is interesting to notice that the slope of the *log-log* graph, α, is far from the 0.5 value (ideal for planar diffusion control) especially in the case of the hybrid treated with the ligand exchange procedure with MCH, confirming once more the detrimental effect of this treatment on the electrochemical performance of the device. The same systems were analysed by Electrochemical Impedance Spectroscopy, both on the background and in the presence of 3 mM of the redox probe $K_4[Fe(CN)_6]$. Results from the comparison among the hybrids, in PBS, at +0.25 V are reported (**Figure 5.1.16 (a)** and **(b)** for the background and **Figure 5.1.18 (a)** and **(b)** with the probe). The equivalent circuits, reported in **Figure 5.1.17** and **5.1.19** were obtained by using the ZView 3.2 software.

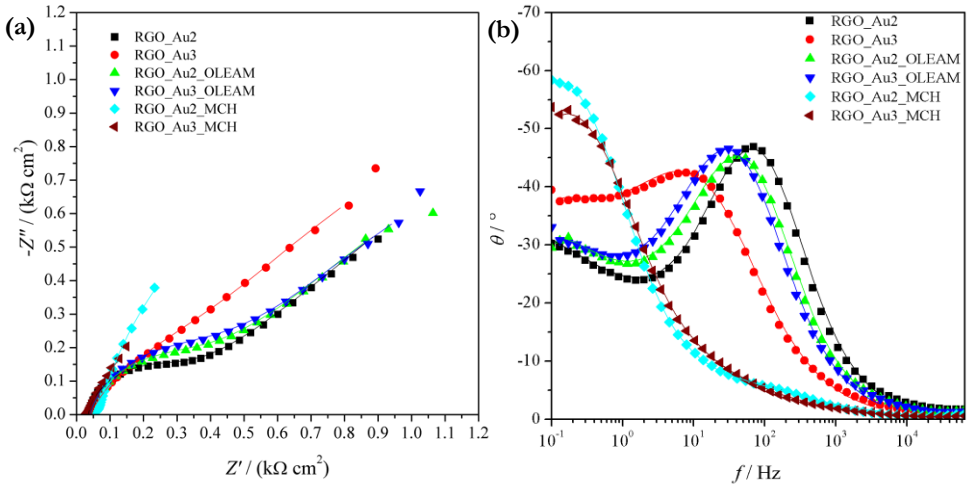

Figure 5.1.16: (**a**) Complex Plane plot at +0.25 V of the hybrid materials recorded in 0.1 M PBS as supporting electrolyte. (**b**) Analogous Bode plots recorded at +0.25 V.

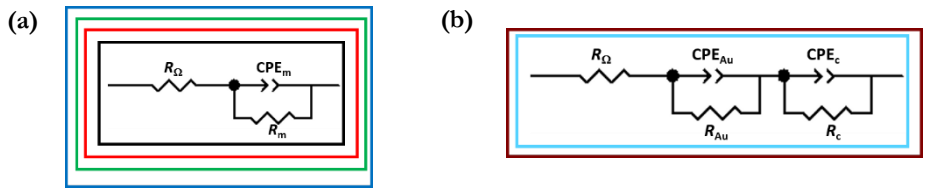

Figure 5.1.17 Equivalent circuits for (**a**) RGO_Au2, RGO_Au3, RGO_Au2_OLEAM and RGO_Au3_OLEAM hybrids and (**b**) RGO_Au2_MCH and RGO_Au3_MCH, at +0.25 V in 0.1 M PBS. $\boldsymbol{R_\Omega}$ = cell resistance, $\mathbf{CPE_m}$ = material capacitance (Constant Phase Element), $\boldsymbol{R_m}$ = material resistance, $\mathbf{CPE_{Au}}$ = capacitance related to AuNPs covered by MCH (Constant Phase Element), $\boldsymbol{R_{Au}}$ = resistance related to AuNPs covered by MCH, $\mathbf{CPE_c}$ = capacitance related to the carbonaceous support (Constant Phase Element), $\boldsymbol{R_c}$ = resistance related to the carbonaceous support. *Colors of the squares around the circuits are related to the colors of the lines and dots in the EIS spectra*.

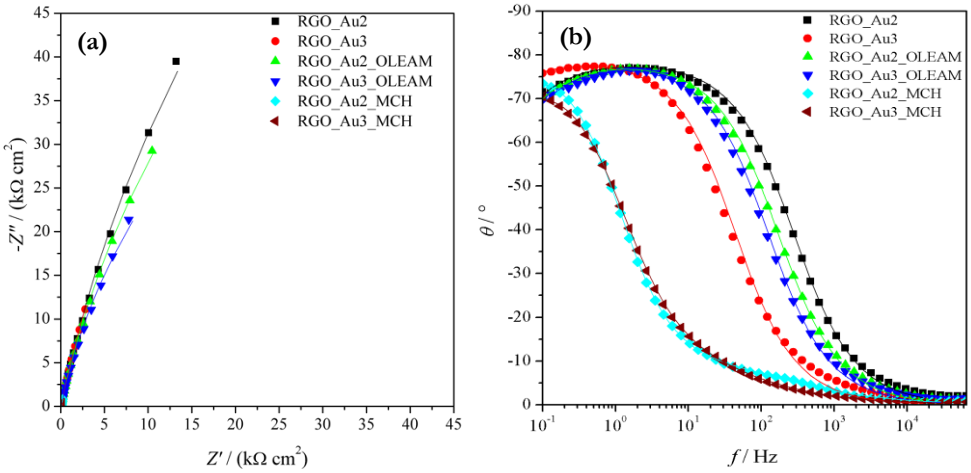

Figure 5.1.18: (**a**) Complex Plane Plots, at +0.25 V of the hybrid materials recorded in 0.1 M PBS + 3mM $K_4[Fe(CN)_6$. (**b**) Analogous Bode plots recorded at +0.25 V.

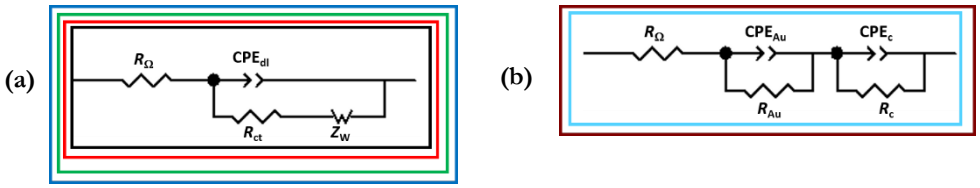

Figure 5.1.19: Equivalent circuits for (**a**) RGO_Au2, RGO_Au3, RGO_Au2_OLEAM and RGO_Au3_OLEAM hybrids and (**b**) RGO_Au2_MCH and RGO_Au3_MCH, at +0.25 V in 0.1 M PBS + 3mM $K_4[Fe(CN)_6]$. $\boldsymbol{R_\Omega}$ = cell resistance, $\mathbf{CPE_{dl}}$ = double layer capacitance (Constant Phase Element), $\boldsymbol{R_{ct}}$ = charge transfer resistance, $\boldsymbol{Z_w}$ = Warburg resistance, $\mathbf{CPE_{Au}}$ = capacitance related to AuNPs covered by MCH (Constant Phase Element), $\boldsymbol{R_{Au}}$ = resistance related to AuNPs covered by MCH, $\mathbf{CPE_c}$ = capacitance related to the carbonaceous support (Constant Phase Element), $\boldsymbol{R_c}$ = resistance related to the carbonaceous support. *Colors of the squares around the circuits are related to the colors of the lines and dots in the EIS spectra.*

Since from EIS results it may be possible to gain information about the structural insight of the electrode platform, a look also at the bare RGO and bare AuNPs, together with the layer-by-layer relative deposition was given with this technique. In fact, the possible instauration of additional circuits could be responsible for the instauration of a real link between the components of the hybrid. On the other hand, same behavior of the composite and of the single component could be related to the absence of any relations between the materials. Results in the absence and in the presence of the redox probe, at +0.25 V (SCE) are shown in **Figure 5.1.20** and **5.1.22**, respectively. The related equivalent circuits are reported in **Figure 5.1.21** and **5.1.23**.

The results obtained from the EIS spectra fitting are listed in **Table 5.1.3** and **5.1.4**, distinguishing the ones with the treatment with MCH from all the other materials. In fact, since the equivalent circuits for those systems are different, also the physical parameters associated need to be defined in a different way. In particular, for the first circuit the parameters will be defined as contribution from Au and so they will be listed as CPE_{Au} and R_{Au}, for the second circuit the contributes will be addressed to the carbonaceous support and so they will be listed as CPE_c and R_c.

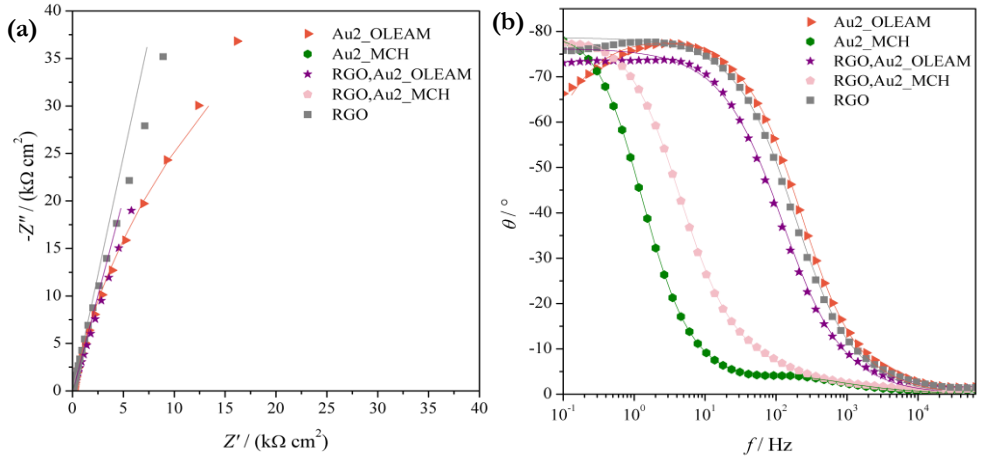

Figure 5.1.20: (**a**) Complex Plane plot at +0.25 V of the RGO, Au and (RGO, Au) materials recorded in 0.1 M PBS as supporting electrolyte. (**b**) Analogous Bode plots recorded at +0.25 V.

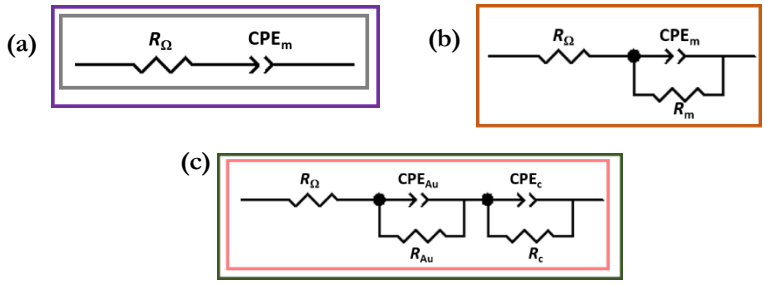

Figure 5.1.21 Equivalent circuits for (**a**) RGO, and RGO,Au2_OLEAM (**b**) Au2_OLEAM and (**c**) Au2_MCH and RGO,Au2_MCH at +0.25 V in 0.1 M PBS. $\boldsymbol{R_\Omega}$ = cell resistance, $\mathbf{CPE_m}$ = material capacitance (Constant Phase Element), $\boldsymbol{R_m}$ = material resistance, $\mathbf{CPE_{Au}}$ = capacitance related to AuNPs covered by MCH (Constant Phase Element), $\boldsymbol{R_{Au}}$ = resistance related to AuNPs covered by MCH, $\mathbf{CPE_c}$ = capacitance related to the carbonaceous support (Constant Phase Element), $\boldsymbol{R_c}$ = resistance related to the carbonaceous support. *Colors of the squares around the circuits are related to the colors of the lines and dots in the EIS spectra.*

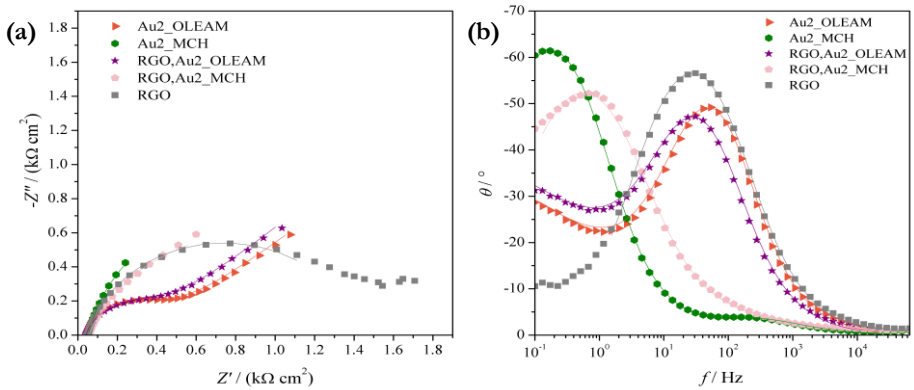

Figure 5.1.22: (**a**) Complex Plane Plots, at +0.25 V of the RGO, Au and (RGO, Au) materials recorded in 0.1 M PBS + 3mM $K_4[Fe(CN)_6]$. (**b**) Analogous Bode plots recorded at +0.25 V.

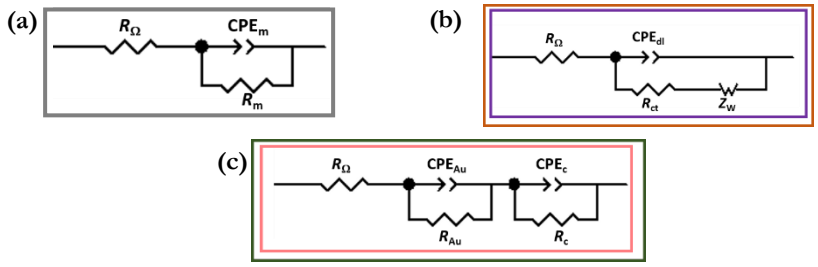

Figure 5.1.23 Equivalent circuits for (**a**) RGO (**b**) Au2_OLEAM and RGO,Au2_OLEAM and (**c**) Au2_MCH and RGO,Au2_MCH at +0.25 V in 0.1 M PBS + 3mM $K_4[Fe(CN)_6]$. $\boldsymbol{R_\Omega}$ = cell resistance, $\mathbf{CPE_m}$ = material capacitance (Constant Phase Element), $\boldsymbol{R_m}$ = material resistance, $\mathbf{CPE_{dl}}$ = double layer capacitance (Constant Phase Element), $\boldsymbol{R_{ct}}$ = charge transfer resistance, $\boldsymbol{Z_w}$ = Warburg resistance, $\mathbf{CPE_{Au}}$ = capacitance related to AuNPs covered by MCH (Constant Phase Element), $\boldsymbol{R_{Au}}$ = resistance related to AuNPs covered by MCH, $\mathbf{CPE_c}$ = capacitance related to the carbonaceous support (Constant Phase Element), $\boldsymbol{R_c}$ = resistance related to the carbonaceous support. *Colors of the squares around the circuits are related to the colors of the lines and dots in the EIS spectra*.

Focusing at first on the background results (**Table 5.1.3**), the "MCH" systems show the presence of two equivalent circuits, in series, in which in the first one the capacitance values are really high (CPE_{Au}). No particular differences are highlighted among the hybrids (RGO_Au2_MCH and RGO_Au3_MCH), the relative single component (Au2_MCH) and the layer-by-layer depositions (RGO,Au2_MCH), being the proof that in these systems the activity of gold nanoparticles covered by MCH is governing the overall activity. In the case of the hybrid in which the ligand exchange procedure is performed, the high affinity of MCH to AuNPs could lead to the detachment of AuNPs from the graphene platform (also with the breaking of the ligand between the gold nanoparticles and the NH_2 moieties of amino-pyrene) resulting in a system that it is not so different from the simple layer-by-layer one. This is verified also by the similar values of the physical parameters associated to the circuit components. The aggregation of all the nanoparticles (as already verified in Physico-Chemical characterization of the previous Paragraph) with the formation of a single entity, well ordered and covered by 1-mercapto-6-hexanol could behave like a sort of capacitor and that is why a high Capacitance (CPE_{Au}) is observed. The low Resistance, on the contrary, could be addressed to the presence of big aggregates of metallic AuNPs, that are covered by MCH and not particularly hindered. The presence of the second circuit could be addressed to a second contribution from the

carbonaceous electrode platform (bare C-SPE or the C-SPE together with the RGO deposited on it).

For what concern the hybrids treated or not treated with spin coating of MeOH and AcOH, and so the hybrid in which the AuNPs are covered or not by OLEAM ligand, the presence of a single circuit is highlighted. In this case, the treatment does not lead to the detachment of AuNPs from the graphene platform and the link between the nanoparticles and the NH_2 moieties of amino-pyrene is still present. This link could be responsible for the introduction of a resistance in the system, and that is why in these cases the *R* values (R_m, resistance of the overall material) are higher with respect to the correspondent MCH-treated materials. As previously observed, the hybrids without the external layer of OLEAM (RGO_Au2 and RGO_Au3) show more differences among them (in particular for the Capacitance values, since the resistance are for all the materials in the same order of magnitude), because in these cases the different dimensions of the AuNPs is a dominant factor. When the nanoparticles are covered by OLEAM, the two electrodes behave practically in the same way. This effect was verified at first by a simple look at the graphs (CV and EIS), but it is here verified also by the EIS fitting results. Regarding the single components and the layer-by-layer depositions, RGO corresponds only to an RC circuit, behaving like a pure capacitor. The only AuNPs, covered by OLEAM ligand, behave like the correspondent hybrids, meaning again that in these cases is gold that is governing the overall activity. When looking at the layer-by-layer depositions, in the case of RGO,Au2_OLEAM, the results are equal to the single RGO. In this case, the ligand between the AuNPs and the RGO platform is not present, since the nanoparticles are covered by the correspondent capping agent and are not grown onto the functionalized PA-RGO. For what concern the OLEAM coated ones, it could be that the hindering effect is too strong that the result is the reaction with the only RGO platform, since the molecules in the background solution are sensing only this part of the material and are not able to sense AuNPs.

Concerning the results in the presence of the redox probe (Table 5.1.4), again the hybrids treated with MCH behave differently from the other materials and that is why they are listed in a separated Table. In fact, in these cases, the reaction of the probe is not visible, since the presence of the Warburg element (associated to the mass transfer mechanism) is not verified. Moreover, the values of the CPE_{Au} and R_{Au} are in the same order of magnitude of the ones observed in the background solution and are typical of the material, not of the charge transfer mechanism of the probe towards the electrode. Also here, as happening for the background, a second circuit is present and could be addressed to the carbonaceous electrode support.

Regarding the materials treated with spin coating, the reaction of the redox probe is visible from the presence of the Warburg element. In more details, in the case of the hybrids and for which the differences in the gold nanoparticles dimensions are an important feature (RGO_Au2 and RGO_Au3), a lower resistance to the mass transport (Zw) is registered for the bigger AuNPs (RGO_Au3). It could be imagined that if the nanoparticles are smaller, a thicker layer is created into the RGO platform and the mass transfer of the probe is more hindered, while it is less hindered for bigger nanoparticles that could lead to a more "porous" layer onto the RGO platform.

Looking at the single contributions and the layer-by-layer depositions, RGO has only the resistance to the charge transfer but maybe the resistance to the mass transfer is too high to be detected. RGO,Au2_OLEAM is not behaving like on the background, similarly to the only RGO, but it is behaving like a sum of the contribution from single RGO and single AuNPs, being more similar to the only AuNPs. In the presence of the probe it could be that the favoured reaction Au-Probe prevails on the hindering effect of OLEAM and so the probe is able to react with both the component and not only with graphene.

Table 5.1.3: Impedance parameters deriving from the fitting of the equivalent circuits of the hybrids in the background solution.

	R_Ω / (Ω cm²)	CPE_m / (μF cm^{-2} s$^{\alpha-1}$)	α_m	R_m / (kΩ cm²)
RGO_Au2	41.6	35.6	0.87	296
RGO_Au3	53.2	135	0.88	223
RGO_Au2_OLEAM	49.4	46.6	0.87	208
RGO_Au3_OLEAM	47.9	62.8	0.87	135
RGO	51.8	40.7	0.87	
Au2_OLEAM	49.0	33.5	0.88	138
RGO,Au2_OLEAM	47.9	74.9	0.85	

	R_Ω / (Ω cm²)	CPE_{Au} / (μF cm^{-2} s$^{\alpha-1}$)	α_{Au}	R_{Au} / (kΩ cm²)	CPE_c / (mF cm^{-2} s$^{\alpha-1}$)	α_c	R_c / (kΩ cm²)
RGO_Au2_MCH	52.6	2087	0.53	0.035	1.82	0.93	10.3
RGO_Au3_MCH	28.5	6524	0.54	0.015	3.43	0.89	5.05
Au2_MCH	50.1	915	0.66	0.011	2.19	0.96	11.8
RGO,Au2_MCH	52.8	3136	0.49	0.020	0.65	0.92	29.5

Table 5.1.4: Impedance parameters deriving from the fitting of the equivalent circuits of the hybrids in the presence of the redox probe.

	R_Ω / (Ω cm²)	CPE_m / (μF cm^{-2} s$^{\alpha-1}$)	α_m	R_{ct} / (Ω cm²)	Z_W / (kΩ cm²)	τ / s	α_W
RGO_Au2	34.8	45.4	0.89	267	6.45	164.2	0.45
RGO_Au3	42.1	342	0.74	450	2.82	11.31	0.50
RGO_Au2_OLEAM	42.1	64	0.86	324	2.81	15.96	0.47
RGO_Au3_OLEAM	41.4	10.6	0.85	366	2.74	15.41	0.47
RGO	48.4	50.4	0.85	1384			
Au2_OLEAM	42.7	42.6	0.90	386	7.21	166	0.45
RGO,Au2_OLEAM	42.0	81.2	0.87	377	6.97	113	0.48

	R_Ω / (Ω cm²)	CPE_{Au} / (μF cm^{-2} s$^{\alpha-1}$)	α_{Au}	R_{Au} / (Ω cm²)	CPE_c / (mF cm^{-2} s$^{\alpha-1}$)	α_c	R_c / (kΩ cm²)
RGO_Au2_MCH	46.8	2583	0.54	19.7	0.413	0.84	179.46
RGO_Au3_MCH	26.1	8270	0.53	10.2	0.702	0.80	716.0
Au2_MCH	45.7	491	0.74	8.36	2.90	0.88	1.90
RGO,Au2_MCH	48.1	1515	0.58	8.22	1.23	0.78	1.68

Conclusions

A novel colloidal hybrid nanocomposite having as basic components graphene and gold nanoparticles is here synthesized. In particular, a multilayer network of oleylamine (OLEAM)-capped Au NPs, 10 to 20 nm in size, highly densely coats Reduced Graphene Oxide flakes, modified on the surface with 1-amminopyrene (PA). The NPs heteronucleation and growth is achieved by an *in situ* colloidal reduction of a Au precursor, in presence of OLEAM. This synthetic procedure ensures a high control on the nanoparticles size and distribution, which reflects on the overall control of the nanostructured morphology of the final decorated PA-RGO flakes. In the hybrid structure, each component has a particular and dedicated role. OLEAM acts both as reducing and capping agent of the gold nanoparticles, while PA acts as linker and coupling agent between the RGO flakes and the AuNPs. This is possible thanks to the π-π interactions of its aromatic structure with the RGO platform and, concomitantly to its amino moieties, serving as coordinating active sites for the AuNPs.

These hybrid nanostructures have been used for the modification of Carbon Screen Printed Electrodes, to be applied for the detection of the neurotransmitter dopamine. The best device was found to be the hybrid synthesized with the smaller nanoparticles and then subjected to a treatment of spin coating with methanol and acetic acid in order to remove the OLEAM capping agent. In this way, the most suitable distribution of AuNPs on the graphene platform was ensured and the best electroanalytical performances were achieved, thanks to the absence of the insulating hydrophobic chain of oleylamine and to the increased availability of both AuNPs and RGO flakes to react with the target analyte. LODs in accordance and even lower than other analytical techniques for the detection of dopamine were achieved, underlying the enhanced performances in the use of a hybrid with respect to the single separate components.

Bibliography

(1) Grace, A. A. Phasic versus Tonic Dopamine Release and the Modulation of Dopamine System Responsivity: A Hypothesis for the Etiology of Schizophrenia. *Neuroscience* **1991**, *41*, 1–24.

(2) Baskerville, T. A.; Douglas, A. J. Dopamine and Oxytocin Interactions Underlying Behaviors: Potential Contributions to Behavioral Disorders. *CNS Neurosci. Ther.* **2010**, *16* (3), 92–123.

(3) Huys, Q. J. M.; Tobler, P. N.; Hasler, G.; Flagel, S. B. *The Role of Learning-Related Dopamine Signals in Addiction Vulnerability*; 2014; Vol. 211.

(4) Chaudhury, D.; Walsh, J. J.; Friedman, A. K.; Juarez, B.; Ku, S. M.; Koo, J. W.; Ferguson, D.; Tsai, H. C.; Pomeranz, L.; Christoffel, D. J.; et al. Rapid Regulation of Depression-Related Behaviours by Control of Midbrain Dopamine Neurons. *Nature* **2013**, *493* (7433), 532–536.

(5) Chaudhuri, K. R.; Schapira, A. H. V. Non-Motor Symptoms of PD Diagnosis and Management. *Lancet Neurol.* **2006**, *5* (March), 235–245.

(6) Harrison, P. J.; Weinberger, D. R. Schizophrenia Genes, Gene Expression, and Neuropathology: On the Matter of Their Convergence. *Mol. Psychiatry* **2005**, *10* (1), 40–68.

(7) Schultz, W. Predictive Reward Signal of Dopamine Neurons. *J. Neurophysiol.* **2017**, *80* (1), 1–27.

(8) Lima, H. R. S.; da Silva, J. S.; de Oliveira Farias, E. A.; Teixeira, P. R. S.; Eiras, C.; Nunes, L. C. C. Electrochemical Sensors and Biosensors for the Analysis of Antineoplastic Drugs. *Biosens. Bioelectron.* **2018**, *108* (February), 27–37.

(9) Kimmel, D. W.; LeBlanc, G.; Meschievitz, M. E.; Cliffel, D. E. Electrochemical Sensors and Biosensors. *Anal. Chem.* **2011**, No. November, 685–707.

(10) Zhang, X.; Ju, H.; Wang, J. *Electrochemical Sensor, Biosensors and Their Biomedical Applications*; Academic Press, 2008.

(11) Georgakilas, V. M.; Otyepka, A.; Bourlinos, A. B.; Chandra, V.; Kim, N.; Kemp, K. C.; Hobza, P.; Zboril, R.; Kim, K. S. Functionalization of Graphene: Covalent and Non-Covalent Approaches, Derivatives and Applications. *Chem. Rev.* **2012**, *122*, 6156–6214.

(12) Ingrosso, C.; Bianco, G. V.; Pifferi, V.; Guffanti, P.; Petronella, F.; Comparelli, R.; Agostiano, A.; Striccoli, M.; Palchetti, I.; Falciola, L.; et al. Enhanced Photoactivity and Conductivity in Transparent TiO2 Nanocrystals/Graphene Hybrid Anodes. *J. Mater. Chem. A* **2017**, *5* (19), 9307–9315.

(13) Ingrosso, C.; Bianco, G. V.; Corricelli, M.; Comparelli, R.; Altamura, D.; Agostiano, A.; Striccoli, M.; Losurdo, M.; Curri, M. L.; Bruno, G. Photoactive Hybrid Material Based on Pyrene Functionalized PbS Nanocrystals Decorating CVD Monolayer Graphene. *ACS Appl. Mater. Interfaces* **2015**, *7* (7), 4151–4159.

(14) Chen, Q.; Zhang, L.; Chen, G. Facile Preparation of Graphene-Copper Nanoparticle Composite by in Situ Chemical Reduction for Electrochemical Sensing of Carbohydrates. *Anal. Chem.* **2012**, *84* (1), 171–178.

(15) Ingrosso, C.; Corricelli, M.; Bettazzi, F.; Konstantinidou, E.; Bianco, G. V.; Depalo, N.; Striccoli, M.; Agostiano, A.; Curri, M. L.; Palchetti, I. Au Nanoparticle: In Situ Decorated RGO Nanocomposites for Highly Sensitive Electrochemical Genosensors. *J. Mater. Chem. B* **2019**, *7* (5), 768–777.

(16) Saha, K.; Agasti, S. S.; Kim, C.; Li, X.; Rotello, V. M. Gold Nanoparticles in Chemical and Biological Sensing. *Chem. Rev.* **2012**, *112* (5), 2739–2779.

(17) Turcheniuk, K.; Boukherroub, R.; Szunerits, S. Gold-Graphene Nanocomposites for Sensing and Biomedical Applications. *J. Mater. Chem. B* **2015**, *3* (21), 4301–4324.

(18) Chen, X.; Wang, L.; Sheng, S.; Wang, T.; Yang, J.; Xie, G.; Feng, W. Coupling a Universal DNA Circuit with Graphene Sheets/Polyaniline/AuNPs Nanocomposites for the Detection of BCR/ABL Fusion Gene. *Anal. Chim. Acta* **2015**, *889* (1), 90–97.

(19) An, X.; Simmons, T.; Shah, R.; Wolfe, C.; Lewis, K. M.; Washington, M.; Nayak, S. K.; Talapatra, S.; Kar, S. Stable Aqueous Dispersions of Noncovalently Functionalized Graphene from Graphite and Their Multifunctional High-Performance Applications. *Nano Lett.* **2010**, *10* (11), 4295–4301.

(20) Konios, D.; Stylianakis, M. M.; Stratakis, E.; Kymakis, E. Dispersion Behaviour of Graphene Oxide and Reduced Graphene Oxide. *J. Colloid Interface Sci.* **2014**, *430*, 108–112.

(21) Hiramatsu, H.; Osterloh, F. E. A Simple Large-Scale Synthesis of Nearly Monodisperse Gold and Silver Nanoparticles with Adjustable Sizes and with Exchangeable Surfactants. *Chem. Mater.* **2004**, *16* (13), 2509–2511.

(22) Hinnemo, M.; Zhao, J.; Ahlberg, P.; Hägglund, C.; Djurberg, V.; Scheicher, R. H.; Zhang, S. L.; Zhang, Z. Bin. On Monolayer Formation of Pyrenebutyric Acid on Graphene. *Langmuir* **2017**, *33* (15), 3588–3593.

(23) Zhang, M.; Parajuli, R. R.; Mastrogiovanni, D.; Dai, B.; Lo, P.; Cheung, W.; Brukh, R.; Chiu, P. L.; Zhou, T.; Liu, Z.; et al. Production of Graphene Sheets by Direct Dispersion with Aromatic Healing Agents. *Small* **2010**, *6* (10), 1100–1107.

(24) Muszynski, R.; Seger, B.; Kamat, P. V. Decorating Graphene Sheets with Gold Nanoparticles. *J. Phys. Chem. C* **2008**, *112* (14), 5263–5266.

(25) Ferrari, A. C. Raman Spectroscopy of Graphene and Graphite: Disorder, Electron-Phonon Coupling, Doping and Nonadiabatic Effects. *Solid State Commun.* **2007**, *143* (1–2), 47–57.

(26) Chua, C. K.; Pumera, M. Chemical Reduction of Graphene Oxide: A Synthetic Chemistry Viewpoint. *Chem. Soc. Rev.* **2014**, *43* (1), 291–312.

(27) Li, L.; Zheng, X.; Wang, J.; Sun, Q.; Xu, Q. Solvent-Exfoliated and Functionalized Graphene with Assistance of Supercritical Carbon Dioxide. *ACS Sustain. Chem. Eng.*

2013, *1* (1), 144–151.

(28) Yang, Z.; Wang, M.; Shi, Y.; Song, X.; Lin, Z.; Ren, Z.; Bai, J. The Impact of Chemical Treatment on Optical and Electrical Characteristics of Multipod PbSe Nanocrystal Films. *J. Mater. Chem.* **2012**, *22* (39), 21009–21016.

(29) Jung, I.; Shin, K.; Kim, N. R.; Lee, H. M. Synthesis of Low-Temperature-Processable and Highly Conductive Ag Ink by a Simple Ligand Modification: The Role of Adsorption Energy. *J. Mater. Chem. C* **2013**, *1* (9), 1855–1862.

(30) Lakbub, J.; Pouliwe, A.; Kamasah, A.; Yang, C.; Sun, P. Electrochemical Behaviors of Single Gold Nanoparticles. *Electroanalysis* **2011**, *23* (10), 2270–2274.

(31) Singh, A. N.; Devnani, H.; Jha, S.; Ingole, P. P. Fermi Level Equilibration of Ag and Au Plasmonic Metal Nanoparticles Supported on Graphene Oxide. *Phys. Chem. Chem. Phys.* **2018**, *20* (41), 26719–26733.

(32) Pumera, M.; Ambrosi, A.; Bonanni, A.; Chng, E. L. K.; Poh, H. L. Graphene for Electrochemical Sensing and Biosensing. *TrAC - Trends Anal. Chem.* **2010**, *29* (9), 954–965.

(33) Zhou, M.; Zhai, Y.; Dong, S. Electrochemical Sensing and Biosensing Platform Based on Chemically Reduced Graphene Oxide. *Anal. Chem.* **2009**, *81* (14), 5603–5613.

(34) Ribeiro, J. A.; Fernandes, P. M. V.; Pereira, C. M.; Silva, F. Electrochemical Sensors and Biosensors for Determination of Catecholamine Neurotransmitters: A Review. *Talanta* **2016**, *160*, 653–679.

(35) Sajid, M.; Baig, N.; Alhooshani, K. Chemically Modified Electrodes for Electrochemical Detection of Dopamine: Challenges and Opportunities. *TrAC - Trends Anal. Chem.* **2019**, *118*, 368–385.

(36) Brownson, D. A. C.; Kampouris, D. K.; Banks, C. E. *Graphene Electrochemistry: Fundamental Concepts through to Prominent Applications*; 2012; Vol. 41.

(37) Lounasvuori, M. M.; Rosillo-Lopez, M.; Salzmann, C. G.; Caruana, D. J.; Holt, K. B. Electrochemical Characterisation of Graphene Nanoflakes with Functionalised Edges. *Faraday Discuss.* **2014**, *172* (Cv), 293–310.

(38) McCreery, R. L. Advanced Carbon Electrode Materials for Molecular Electrochemistry. *ChemInform* **2008**, *39* (41), 2646–2687.

(39) Patel, A. N.; Collignon, M. G.; OConnell, M. A.; Hung, W. O. Y.; McKelvey, K.; MacPherson, J. V.; Unwin, P. R. A New View of Electrochemistry at Highly Oriented Pyrolytic Graphite. *J. Am. Chem. Soc.* **2012**, *134* (49), 20117–20130.

(40) Ambrosi, A.; Pumera, M. Electrochemistry at CVD Grown Multilayer Graphene Transferred onto Flexible Substrates. *J. Phys. Chem. C* **2013**, *117* (5), 2053–2058.

5.2 PCA-RGO/DMBT-AuNPs Hybrids

Focus

In parallel to what concern the previous **Paragraph 5.1**, a similar hybrid based on gold nanoparticles and graphene flakes is here the subject of investigation. In this case, the Reduced Graphene Oxide flakes (RGO) are modified on their surface with 1-pyrene carboxylic acid (PCA). The application of a non-covalent approach allowed again to reach the functionalization of graphene platforms with densely and uniformly *in situ* decoration of gold nanoparticles (AuNPs). These are concomitantly coordinated to the PCA carboxylic group and to an aromatic thiol, 3,4-dimethylbenzenethiol (DMBT), which is used as reducing agent in the synthetic procedure. The thiol (DMBT) ensures the non-covalent anchorage of the nanoparticles onto the RGO flakes and promotes an interparticle electron coupling along the nanoparticles network. The colloidal solution is again used to modify Carbon Screen Printed Electrodes.

In a previous work, such material was involved in the creation of an electrochemical biosensor for the detection of the biotinylated miRNA-221 and for its determination in spiked human blood serum samples.[1] The excellent performances of such hybrid as nucleic acid biosensing platform moved the interest in the use of this material also in other fields. In fact, such a hybrid is here applied as simple sensor, without the need of any further modification after the synthetic procedure. The colloidal solution from the synthesis is deposited onto C-SPEs platform and then used in the electrochemical detection of Arsenic.

Arsenic belongs to the family of *heavy metals ions (HMIs)*, which are non-biodegradable and responsible of the contamination of most of the natural resources occurring in the environment, including water. Arsenic (As), together with Lead (Pb), Mercury (Hg), Chromium (Cr) and Cadmium (Cd), in their different oxidation states, are already known to be highly toxic and hazardous to human health even at trace levels. HMIs derive mostly from cosmetics, fertilizers and other chemicals generated from

industrial or household waste.[2] Moreover, HMIs could be find also in rocks, as natural components, but, particularly from industrial wastes, in contaminated soils.[3,4] They are highly dangerous since they do not decompose and have the tendency to accumulate in living organisms, being responsible of various diseases and disorders to the nervous, immune, reproductive and gastrointestinal systems.[5,6] Considering all these facts, the development of detection methods and tools to analyse HMIs in environmental samples is of extremely interest and it is spreading in the scientific community as a priority. This is also to follow the Directives of several international organizations such as the World Health Organization (WHO), the Joint Food and Agricultural Organization (FAO), the US Environmental Protection Agency (EPA), the Centre for Disease Control (CDC) and the European Union (EU) [*U.S, 2009. EPA National Primary Drinking Water Regulations; Directive, 2013. 2013/35/EU of the European Parliament and of the Council; Standard methods for the examination of water & wastewater, 2012. American Public Health Association (APHA), American Water Works Association (AWWA) & Water Environment Federation 22 (WEF)*].

Nowadays, several analytical techniques are involved in the detection of heavy metals in complex matrices, such as AAS[7], ICP-MS[8], ICP-OES[9], usually preceded by solid or liquid phase extractions. The advantages of all these methods reside in the fact that they are applicable for a wide range of elements and they allow also simultaneous determinations, with the possibility to reach very low detection limits. By the way, even if they are suitable for quantitative analysis, they often require to be coupled with other chromatographic techniques to perform ions speciation. Moreover, they suffer from being expensive and they sometimes require multisampling, with difficult analytical procedures. Therefore, trained personnel are needed and they result in being time-consuming techniques. Other tools for the detection of heavy metals in water are the optical techniques, even if they are costly and require complex equipment (such as photodetectors), high precision and high power operations[6]. In order to overcome all these disadvantages, electrochemical methods represent good candidates being more economic, user friendly and reliable. Moreover, the possibility

to miniaturize electrodes and easily modify their surface, together with the compact and portable instrumentation setup, made electrochemistry a perfect candidate for the detection of heavy metals in water samples[10,11] also allowing *on-line*, *on-site* and *continuous* measurements, which represent an actual need and a big challenge of the last few years. In fact, the increase in population together with the rise of resources and development of industry and agriculture has led to a dramatic excess of wastewater with the most various composition, toxicity and texture. The integrated processes ensure a novel risk-based approach to assess environmental status including chemical quality, morphological conditions and ecological safety (in Europe, this is specially requested by the Water Framework Directive, WFD, 2000).

The only disadvantage of electrochemical methods with respect to the other commonly involved analytical techniques, is that they suffer from lower sensitivity and higher detection limits. In order to overcome these problems, however, apart from the development of biosensing platforms (immunosensors, enzymatic sensors, etc.), the use of nanomaterials is considered to be a good solution. Therefore, the coupling of electrochemical techniques with nanomaterials could enhance the sensitivity, lower the limit of detections, and increase robustness of the specific sensors[12].

Considering all these facts, in this part of the Project, nanomaterial based electrochemical sensors are involved in the detection of Arsenic. All the different components of the hybrid are analysed in order to understand their peculiarities and their effectiveness in the final device performances. The peculiarities of the hybrid with respect to the single counterparts are underlined and deeply investigated by means of electrochemical characterizations supported by other physico-chemical analyses. Particular attention was also paid on the possibility to speciate among the two different oxidation states of As, namely As(III) and As(V), since the first one is ten times more dangerous than the other form and for this reason it is particularly interesting to find analytical tools able to differentiate between the two ions.

Materials and Methods

Chemicals

Commercial Reduced Graphene Oxide (RGO) (1.6 nm flakes) was purchased from Graphene Supermarket. 1-Pyrene Carboxylic Acid (PCA, 97%), n-methyl-2-pyrrolidone (NMP, 99%), tetraoctylammonium bromide (TOAB, 99%), hydrogen tetrachloroaurate(III) trihydrate ($HAuCl_4 \times 3H_2O$, 99.999%), 3,4-dimethylbenzenethiol (DMBT, 98%), 2-phenylethanethiol (98%), sodium borohydride (NaBH4, 99.99%) toluene and methanol were purchased from Sigma Aldrich.

Exfoliation and functionalization of RGO

Commercial RGO was exfoliated and functionalized with 1-Pyrenecarboxylic acid (PCA) by sonicating, in an ice bar, a mixture of RGO powder and PCA in n-methyl-2-pyrrolidone (NMP). The excess of PCA was removed by cycles of centrifugation and re-dispersed in methanol. Finally the purified PCA-RGO powder was dispersed in NMP. [13]

Synthesis of the PCA-RGO/AuNPs hybrid materials

For the synthesis of the PCA-RGO/AuNPs hybrid a two-phase method was used, following the one from Brust et al. [14] for the synthesis of gold nanoparticles, with some little modifications. In more details, 5 to 15 mg of the PCA modified RGO powder were dissolved in NMP and then added to a solution prepared by mixing 1.1872 g – 3.548 g of TOAB in 35 – 80 cm^3 of toluene, and left under stirring for 30 minutes. Then, 0.1770 g – 0.354 g of $HAuCl_4 \cdot 3H_2O$, dispersed in 15 - 30 cm^3 of milli-Q water, were added to the solution and left again 30 minutes to stir. After this passage, ensuring the transfer of the gold precursor from water to toluene, water was removed from the reaction flask and 60 – 120 μL of DMBT were added to the synthetic mixture and left to stir for one hour. In this way, the reduction from Au(III) to Au(I) is controlled and the coordination of the thiol to gold nanoparticles is

achieved. DMBT acts, in this way, as capping and reducing agent. In order to complete the reduction from Au(I) to Au(0), 0.189 g – 0.378 g of $NaBH_4$ in 12- 25 cm^3 of Milli-Q water were added. The growth of the AuNPs was allowed to proceed overnight. The whole process was conducted at room temperature. The PCA-RGO/Au NPs dispersions were then purified with methanol by cycles of centrifugation to remove the excess of DMBT aromatic ligand. In a final step, in order to separate the hybrid nanocomposite flakes from the gold nanoparticles homonucleated in the supernatant of the reaction mixture, a precipitation step was achieved, by adding methanol and inducing a gradual flocculation of the larger PCA-RGO/AuNPs flakes. The isolated pellet containing the hybrid, separated from the supernatant containing the free DMBT-capped gold nanoparticles by centrifugation, was then re-dispersed in toluene.

Characterization techniques

- **UV-Vis-NIR** absorption spectroscopy was performed to characterize the PCA-RGO/Au NP hybrid material dispersed in toluene, by using a Cary Varian 5000 spectrophotometer.
- **Mid-infrared** spectra were acquired with a Varian 670-IR spectrometer equipped with a DTGS (Deuterated Tryglycine Sulfate) detector, having a spectral resolution of 4 cm^{-1}. For attenuated total reflection (ATR) measurements, the used internal reflection element (IRE) was a one-bounce 2 mm diameter diamond microprism. The samples were cast directly on the upper face of the diamond crystal and the solvent was allowed to evaporate.
- **Transmission Electron Microscopy** (TEM) images of the PCA-RGO/Au NP hybrid flakes were acquired by using a JEOL JEM-1011 microscope, working at an accelerating voltage of 100 kV and equipped with a high-contrast objective lens, and a W filament as electron source. Under these conditions, the ultimate point resolution of the microscope was equal to 0.34 nm. The TEM images were collected by a Gatan SC-1000 Orius Camera,

equipped with a fiber-optical coupled 11 Mp CCD. The samples were prepared by dipping the 300 mesh amorphous carbon-coated Cu grid in PCA-RGO/Au NP toluene dispersions, and letting the solvent to evaporate. Size statistical analysis (NP average size and size distribution) of the samples was performed by means of a freeware Image J analysis program.

- Topography and phase mode **Atomic Force Microscopy** (AFM) measurements were performed in air and at room temperature, by means of a PSIA XE-100 SPM system operating in tapping mode. A silicon Scanning Probe Microscope (SPM) sensor for noncontact AFM (Park Systems), having a spring constant of 42 N m^{-1} and a resonance frequency of 330 kHz, was used. Micrographs were collected on six distinct areas of the sample, with a scan size area of 5 μm × 5 μm, by sampling the surface at a scan rate between 1.0–0.5 Hz, and a resolution of 256 × 256 pixels. Topography AFM images were processed by using the XEI software to obtain statistical data.

Electrodes Preparation

The colloidal dispersions in toluene were left under stirring for one hour, then, 1.8 μL of the colloid were deposited by drop casting, using an automatic micropipette (Kartell, Noviglio, Milano, Italy), onto the C-SPE (purchased from Metrohm DropSens) surface and let dry in air at room temperature. The final hybrid (PCA-RGO/DMBT-AuNPs) and the single components were deposited on different electrodes in order to study their relative characteristics (only PCA-RGO flakes solution and only DMBT-AuNPs). Apart from RGO and AuNPs samples alone, also a subsequent deposition (layer-by-layer) of RGO and then AuNPs was done, by drop casting 1.8 μL of RGO first and then, when dry, the same amount of AuNPs colloidal solution.

Electrochemical Characterizations

Electrochemical Characterizations by Cyclic Voltammetry (CV) and Electrochemical Impedance Spectroscopy (EIS) were performed using a PGStat30 (Metrohm AutoLab, Utrecht, The Netherlands) equipped with NOVA 2.1 Software (Metrohm AutoLab, Utrecht, The Netherlands). The experiments were carried out in a conventional three-electrodes cell using a Saturated Calomel Electrode (SCE) and a Platinum wire as reference (RE) and counter (CE) electrodes, respectively. The working electrode (WE) was the modified Carbon Screen Printed Electrode (C-SPE) with the different RGO and AuNPs colloidal solutions. 0.1 M solution of KCl, $NaClO_4$ and PBS (Phosphate Buffer, pH 7.4) were used as supporting electrolytes and $K_4[Fe(CN)_6]$ was selected as molecular redox probe. EIS measurements were conducted at -0.1 V, +0.1 V and +0.25 V (SCE), on the background and in the presence of the probe, in the same three above-mentioned electrolytes.

Electroanalytical Applications

Electrochemical detection of Arsenic, starting from mother solutions of As_2O_3 (Fluka) and As_2O_5 (Arsenic(V) oxide hydrate, Sigma Aldrich), was performed by using a μ-AutoLab III (Metrohm AutoLab, Uthrecht, The Netherlands), equipped with the NOVA 2.1 Software (Metrohm AutoLab, Utrecht, The Netherlands). Anodic Stripping Voltammetry (ASV) was used as electroanalytical technique, consisting of a preliminary accumulation step at cathodic potential in order to reduce As(III) or As(V) ions in solution, followed by a Linear Sweep in the anodic scan direction. The analyses were performed in different electrolytes, at different pH values, namely PBS (pH 7.4) and HCl 0.1 M. The experimental parameters, such as the potential of accumulation step and the potential range of the linear scan, were then adapted to the particular analysis (see next Paragraph).

Results and Discussion

Synthesis and Characterization of the PA-RGO/AuNPs Hybrids

The RGO commercial flakes were exfoliated in the presence of PCA in a NMP solution. NMP was chosen as solvent, because of its ability to disperse RGO flakes[15]. Pyrene was chosen, as already done in the parallel hybrid synthesis (Paragraph 5.1), for its ability to link the graphene *via* π–π stacking interactions, which are strong and practically irreversible. Pyrene acts as "molecular wedge", entering from the sides of the multi-stacks of graphene, in depth, and exfoliating them. In this case, PCA is chosen for its carboxylic moieties, necessary for the following nucleation and growth of gold nanoparticles. The out of plane –COOH functional groups are also suited to keep separated the graphene sheets, preventing their re-stacking, and allowing dispersion of the PCA modified RGO complex in solvents.[15,16]

Regarding the next creation of the hybrid, a step of phase-transfer was necessary. In fact, since the gold precursor is soluble in water, but the synthesis is carried out in toluene, TOAB was used in order to transfer $HAuCl_4 \cdot 3H_2O$ from water to toluene: it links gold nanoparticles by electrostatic interactions and interacts also with the carboxylic moieties of the PCA.

In this synthesis, the choice of the PCA and DMBT is thought with attention in order to achieve a perfect functionalization of graphene with gold nanoparticles; in fact, a pyrene without any alkyl group and a thiol with the -SH group directly linked to the aromatic ring were chosen. In this way, the attachment of AuNPs, linked to DMBT with the –SH moieties, to graphene platform is assisted by the instauration of π–π stacking interactions.

A sketch of the final hybrid is represented in **Figure 5.2.1**, where the link between the carboxylic moieties of PCA and AuNPs is marked, together with π–π interactions among the benzene ring of the thiol and the graphenic platform, ensuring the interconnection among the components of the hybrid.

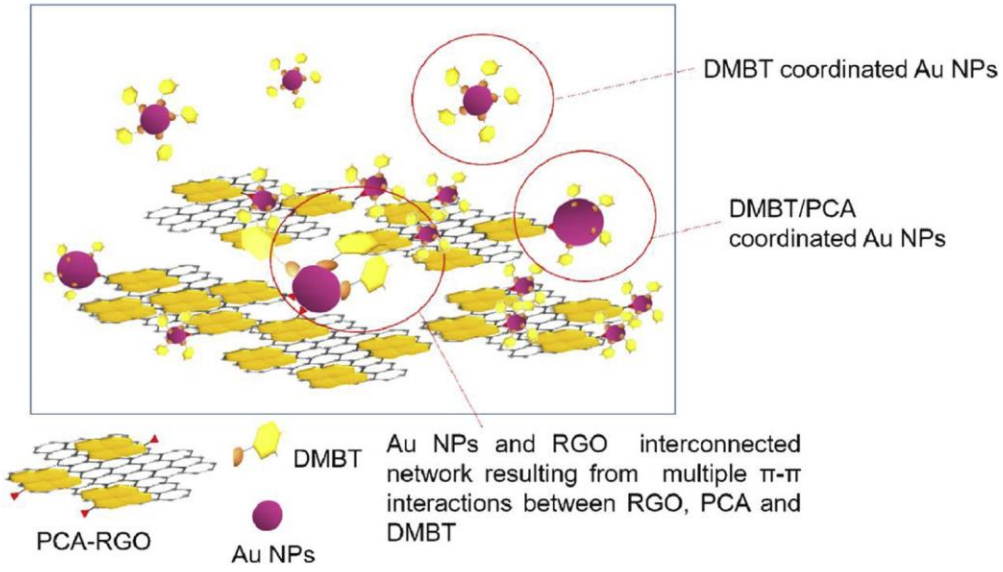

Figure 5.2.1: Sketch of the anchoring of the DMBT-capped Au NPs onto the PCA-RGO flakes. Adapted with permission, Copyright 2019 ©, Carbon

Figure 5.2.2 (**a**) reports a TEM image of the PCA-RGO/AuNPs flakes, where a micro-meter large sheet structure is evident, clearly coated by round-shaped nano-objects, AuNPs, higher in contrast. From the statistical analysis and size distribution (**Figure 5.2.2** (**b**)), the mean diameter was calculated to be 2.8 ± 0.6 nm.

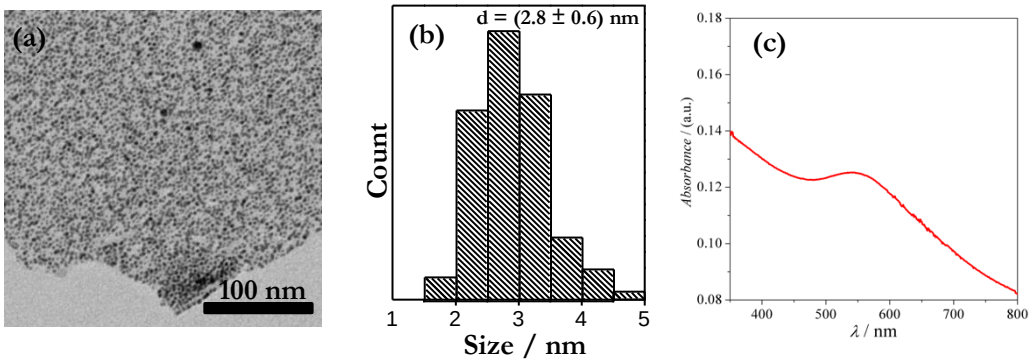

Figure 5.2.2: (**a**) TEM Image of the hybrid composite, (**b**) statistical size distribution of gold nanoparticles on the hybrid and (**c**) UV-Vis spectra of the hybrid.

From the UV-Vis spectra of the hybrid nanocomposite (**Figure 5.2.2** (**c**)), an absorption signal at about 564 nm is evident. This can be ascribed to the Localized Surface Plasmon Resonance (LSPR) peak of the AuNPs [14]. The position of this peak is at lower energy with respect to the one relative to AuNPs of comparable size in solution. This could be due to the differences in the dielectric constant of the environment, when AuNPs are functionalized onto the graphene platform, and also to the instauration of electron coupling effect among the nanoparticles assisted by the presence of the DMBT ligand [1].

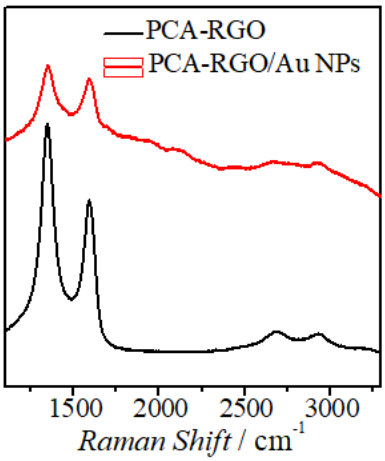

Figure 5.2.3: Raman spectra of the PCA-RGO and the final hybrid PCA-RGO/AuNPs.

Figure 5.2.3 shows the Raman spectra of the final hybrid compared with the only PCA-RGO flakes. In both cases, the G and D peaks, typical of RGO, are present. The strong difference between the two spectra is that in the case of the AuNP modified platform, a high background signal is present, originated by the PCA photoluminescence. The D peak of RGO is due to the defects on its surface, like ripples, edges, impurities (like oxygen functionalities, C heteroatoms and hydrocarbons). In the hybrid, the ratio between the D and G peaks is lower in intensity, being representative of a less defective material, with a higher domain of conjugated C-sp^2 atoms. This is ascribable to the final reduction step of gold carried out with $NaBH_4$ at room temperature[1].

In order to verify the role of the PCA linker during the synthesis of the hybrid material, a control experiment was done. In more details, AuNPs were synthesized following the *in situ* procedure, in toluene solutions of DMBT and bare RGO flakes, without any pyrene functionalities on them. TEM image of the achieved flakes is reported in **Figure 5.2.4 (a)**, while **Figure 5.2.4 (b)** reports the TEM images of the

flakes related to the synthesis of AuNPs conducted in the presence of the functionalized PCA-RGO platforms.

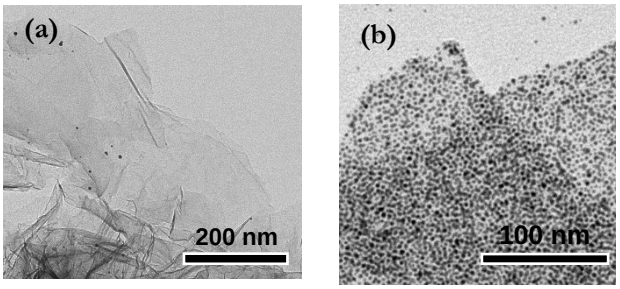

Figure 5.2.4: TEM images of the AuNPs grown onto bare RGO (**a**) and PCA-RGO (**b**) flakes.

This experiment shows that gold nanoparticles do not heteronucleate onto the bare RGO flakes, while they are densely and uniformely anchored onto the functionalized PCA-RGO. In conclusion, the presence of the pyrene linker is crucial and essential for the effective creation of the hybrid.

Other intended experiments were performed in order to understand the most suitable PCA:RGO w/w ratio, the $HAuCl_4 \cdot 3H_20$: TOAB and the $HAuCl_4 \cdot 3H_2O$: DMBT molar ratio (**Figure 5.2.5**). The morphological properties of the different obtained hybrids were monitored via TEM analysis. It was found that the PCA:RGO w/w ratio drastically affects the uniformity and density of the gold nanoparticles coverage on the graphene flakes. Moreover, different populations in terms of dimensions of the nanoparticles were found by varying the ratio between the pyrene acid and the RGO flakes. This fact is a confirmation of the action of PCA, not only in the functionalization of RGO, but also as assistant in the nucleation and growth of the AuNPs (when the amount of PCA is too high, also the nucleation of gold nanoparticles is too much). The best parameter was then fixed as a ratio of 17:1 PCA:RGO (w/w).

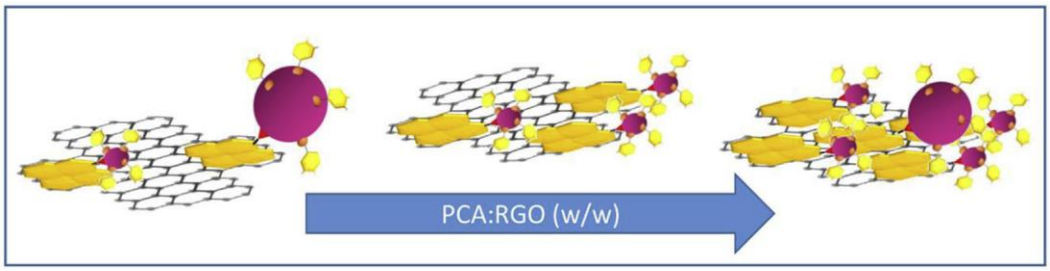

Figure 5.2.5: Sketch of the AuNPs morphology and coating density onto the PCA-RGO flakes by increasing the PCA:RGO (w:w) ratio. Adapted with permission, Copyright 2019 ©, Carbon

Regarding the molar ratio between the gold precursor ($HAuCl_4 \cdot 3H_20$) and the phase transfer reagent (TOAB), it was found that a 1:2 ratio was not sufficient and a complete transfer of the monomer from the aqueous phase to toluene was achieved by using 1:4 to 1:6 molar ratio. Finally, the 1:4 was used as the best synthetic parameter. For what concern the $HAuCl_4 \cdot 3H_20$: DMBT molar ratio, it was found that an excess of the thiol ligand was beneficial in order to achieve small nanoparticles and to favour the heteronucleation on the graphene platform.

The final proportion between all the reagents were then fixed as 1:4 $HAuCl_4 \cdot 3H_2O$: TOAB and 1:2 $HAuCl_4 \cdot 3H_2O$:DMBT molar ratio, respectively and 17:1 PCA:RGO w/w.

Electrochemical Characterization of the PCA-RGO/AuNPs Hybrids

In order to study the properties of the hybrid and, above all, to understand its peculiarities when compared to its single counterparts, different kind of electrodes were subjected to a deep electrochemical characterization. Cyclic Voltammetry (CV) and Electrochemical Impedance Spectroscopy (EIS) were conducted on four kind of modified C-SPEs, both on the background and in the presence of 3mM $K_4[Fe(CN)_6]$ (*inner-sphere* redox probe towards carbonaceous supports)[17] in three different aqueous electrolytes, namely 0.1 M KCl, $NaClO_4$ and PBS. The modified electrode will be hereafter named in the following way:

- **Hybrid:** C-SPE modified by drop casting 1.8 μL of the hybrid colloidal solution in toluene. Here, the complete PCA-RGO/DMBT-AuNPs system is investigated.
- **Au:** C-SPE modified with the colloidal solution (1.8 μL) with only DMBT-AuNPs, without the RGO flakes.
- **RGO:** C-SPE modified with the colloidal solution (1.8 μL) of only PCA-RGO flakes, without gold nanoparticles grown on them.
- **RGO,Au:** C-SPE modified by casting subsequently (layer by layer) the RGO colloidal solution and then the AuNPs one, 1.8 μL of each.

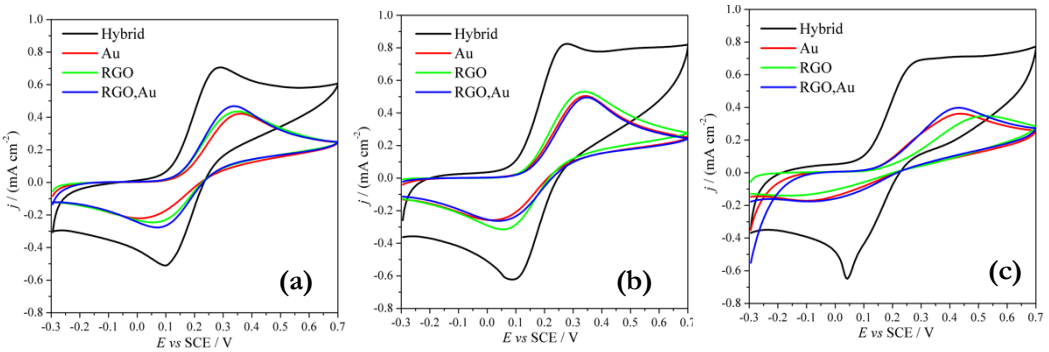

Figure 5.2.6: Cyclic Voltammetry recorded on the four different electrodic platform, at 100 mV s^{-1}, in the presence of 3 mM $K_4[Fe(CN)_6]$ in a 0.1 M aqueous solution of (**a**) KCl, (**b**) $NaClO_4$ and (**c**) PBS as supporting electrolytes.

The most appreciable difference among the systems are related to their reactions with the redox probe. **Figure 5.2.6** (**a**), (**b**) and (**c**) report the CVs of the four above-mentioned systems in KCl, $NaClO_4$ and PBS, respectively, in the presence of 3 mM potassium ferrocyanide.

At a first glance, it can be claimed that in all the three electrolytes the hybrid behaves differently from its counterparts (**Table 5.2.1**). In particular, the current density values (normalized for the geometric area of the electrodes, 0.126 cm^2) are higher for the hybrid (*electroactivity* effect). Moreover, the peak potential position of the anodic oxidation of the redox probe of the hybrid is shifted towards less positive values (it is closer to zero) with respect to the other materials, observing a shift of about 100-150 mV. For all the different electrolytes, the peak position for the oxidation of the

probe towards the hybrid is the same. In this case, a possible *electrocatalytic* effect is present. It is not possible to claim that electrocatalysis is the only reason of the anticipation of the peak, because effect of *convergent diffusion* and thin layer diffusion are here reasonably present, and they can be themselves responsible for both the increased current and for the anticipated peak position. In fact, it is possible to imagine that in the case of the hybrid, when gold nanoparticles are effectively grown onto the functionalized graphene platform, they are uniformly distributed and separated in a suitable distance one to the other. As a consequence, they can act as electroactive spots onto the graphene platform, forming a microarray of electrodes, resulting in the instauration of the so called *convergent diffusion*. The presence of such an effect is also supported by the changed shape of the oxidation peak of the probe, which resembles more a step than a peak (more visible in $NaClO_4$ and particularly PBS).[18]

Table 5.2.1: Peak position (*E*) and density current values (*j*) relative to the oxidation of $K_4[Fe(CN)_6]$ in three different electrolytes. Concentration of the probe = 3 mM; Voltage scan rate = 100 mV s^{-1}; Geometric Area = 0.126 cm^2.

	KCl		**$NaClO_4$**		**PBS**	
	***E* / V**	***j* / (mA cm^{-2})**	***E* / V**	***j* / (mA cm^{-2})**	***E* / V**	***j* / (mA cm^{-2})**
Hybrid	**0.28**	**0.599**	**0.28**	**0.750**	**0.28**	**0.546**
Au	0.35	0.355	0.34	0.482	0.43	0.300
RGO	0.35	0.408	0.33	0.496	0.52	0.318
RGO,Au	0.33	0.402	0.35	0.472	0.42	0.309

Figure 5.2.6 (**c**) clearly shows how the only RGO platform is the one that reacts more difficulty with the probe, having the anodic peak position at the highest potential values (**Table 5.2.1**). AuNPs alone seems to react in a better way and seems also to govern the situation in the RGO,Au system. In any case, the hybrid has a drastic enhancement in the electrochemical response. When using PBS, possible absorption phenomena of the phosphate counter ion on the graphene platform must be kept into consideration. This could be responsible also of the strange reduction signal for the hybrid: the phosphate could have been adsorbed[19] and then stripped

away leaving more available sites for the redox probe to react and then leading to a rapid enhanced of current.

Cyclic Voltammetry has been performed at different voltage scan rates, in the range 10 to 500 mV s^{-1}, in order to clarify the electrochemical reversibility and the kind of diffusional mechanism involved for the redox probe . Results and comparisons in the case of the $NaClO_4$ electrolyte solution are shown in **Table 5.2.2**.

Table 5.2.2: Values deriving from the electrochemical characterisation (CV) of the different materials in $NaClO_4$ 0.1 M + 3 mM $K_4[Fe(CN)_6]$. Effect of the scan rate on different parameters.

Electrode	***I vs v*$^{0.5}$ dependency**	**α (log(*i*) *vs* log(*v*) slope)**	***ΔE vs* log(*v*) dependency**	**($E_p - E_{p/2}$) *vs* log(*v*) dependency**
Hybrid	Linear	(0.39 ± 0.01)	Variable **(0.1 V s^{-1}: 268 mV)**	Variable
Au	Linear	(0.47 ± 0.02)	Variable **(0.1 V s^{-1}: 302 mV)**	Variable
RGO	Linear	(0.412 ± 0.005)	Variable **(0.1 V s^{-1}: 272 mV)**	Variable
RGO,Au	Linear	(0.47 ± 0.02)	Variable **(0.1 V s^{-1}: 292 mV)**	Variable

In all cases, the dependency of the current with the square root of the scan rate is linear, but the variability of the wave-shape and the peak-to-peak current with the voltage scan rate is an evidence of an electrochemical irreversibility of the system. For a comparison, the Δ*E* value for all the hybrids recorded at 0.1 V s^{-1} is reported in brackets. It can be seen that the lowest value (268 mV) is present for the hybrid and so this is the system which shows the best electrochemical reversibility. The highest value (302 mV) is reported for the only AuNPs modified system and in the case of the layer-by-layer deposition the value is in the middle between the one of only RGO and only Au. The fact that in the hybrid the situation is better than the single component is another confirmation of the good performances of this system and of the effectiveness of the synthetic route. Looking at the α values, that is the slope of the log(*i*) *vs* log(*v*) graph, interesting consideration can be drawn. In fact, in case of **Au**, the value is really close to the expected 0.5 for a planar diffusive

mechanism of the redox probe towards the electrode. The value is the same in the case of the **RGO,Au** electrode, meaning that gold is the main actor in such a device, covering the contribute from **RGO**. The **Hybrid**, on the contrary, is the material for which the α value is the most distant and lower than 0.5 being a confirmation of the instauration of a different diffusive mechanism of the redox probe towards the electrode, for example, the previously mentioned *convergent diffusion or thin layer effect*.

To better understand this conclusion, it is useful to come back to the difference between planar (or linear) and convergent (or radial) diffusion, as already discussed in **Chapter 2**: in the first case, current lines are perpendicular to the surface of the electrode and parallel one to the other, while in the second case they are not linear. This second situation is normally encountered when dealing with microelectrodes, where the diameter of the electrode is small, particularly, smaller than the diffusion layer, and the current lines come to the electrodes from every direction and they are not parallel one to the other. As a consequence, the diffusion layer thickness is high and it is higher than the time-scale of the performed voltammetry. In this case, a steady-state current is normally reached, resulting in a step-shaped voltammetric signal. In the present case, a more particular and complex situation can be imagined, that is the one of the *microelectrodes' array* (see **Chapter 2** for more details). It is possible to imagine to be in a situation like the category 2 or 3 of Figure 1.3, in which the hybrid is composed by a layer of RGO on which the gold nanoparticles are in a suitable distance one to the other to act as electroactive independent spots on the graphene flakes.

The same materials were analyzed by Electrochemical Impedance Spectroscopy. **Figure 5.2.7** reports the Complex plane (a) and Bode Phase (b) plots of the four modified electrodes in the presence of the redox probe, at +0.25 V (SCE), showing at a first glance a strong different behavior for the hybrid with respect to the other materials. The equivalent circuits, derived by using the Software ZView, are reported in **Figure 5.2.8** and the relative mathematical values are summarised in Table 5.2.3.

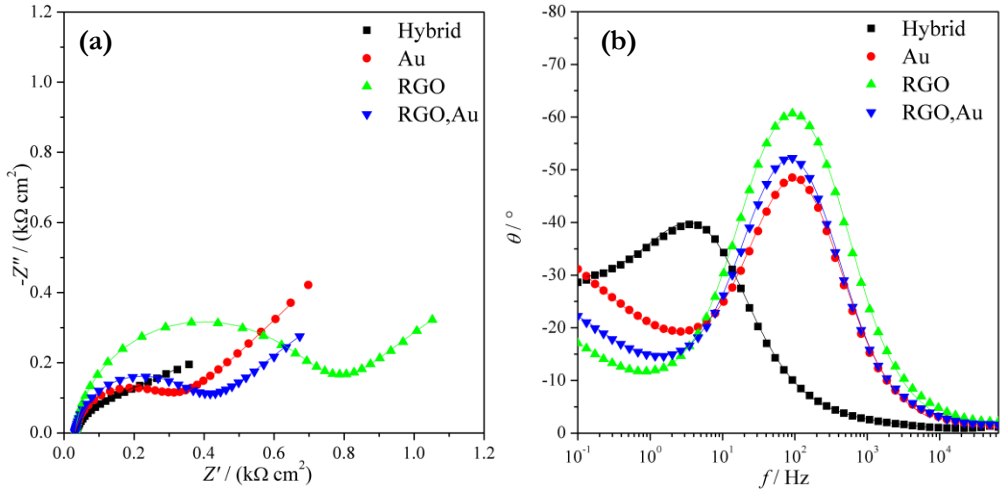

Figure 5.2.7: Complex plane (**a**) and Bode Phase (**b**) plots of the hybrid, Au, RGO and RGO,Au electrodes in $NaClO_4$ 0.1 M + 3 mM $K_4[Fe(CN)_6]$ recorded at +0.25 V (SCE).

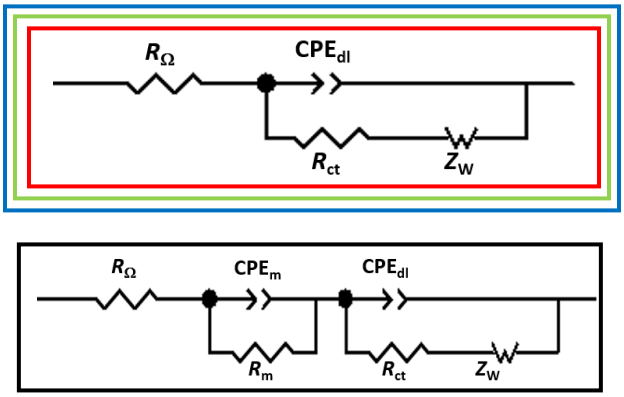

Figure 5.2.8: Equivalent circuits relative to the EIS spectra of **Figure 5.2.7.** R_Ω = cell resistance, CPE_{dl} = double layer capacitance (Constant Phase Element), R_{ct} = charge transfer resistance, Z_w = Warburg resistance, CPE_m = material capacitance (Constant Phase Element), R_m = material resistance. *Colors of the squares around the circuits are related to the colors of the lines and dots in the EIS spectra.*

Table 5.2.3: EIS mathematical parameters.

	R_Ω (Ω cm^2)	CPE_m (mF cm^{-2} s$^{\alpha-1}$)	α_m	R_m (Ω cm^2)	CPE_{dl} (μF cm^{-2} s$^{\alpha-1}$)	α_{dl}	R_{ct} (Ω cm^2)	Z_w (Ω cm^2)	α_w	τ_w (s)
Hybrid	31.16	2.78	0.55	3.48	684.16	0.86	**126**	2.55	0.38	422
Au	32.71	-	-	-	29.85	0.92	260	3.04	0.50	42
RGO	31.55	-	-	-	18.46	0.93	676	1.50	0.47	18
RGO,Au	31.85	-	-	-	29.09	0.92	334	1.42	0.46	24

It can be immediately observed that in the case of the hybrid the equivalent circuit is strongly different from the single components (RGO and Au) and from the two materials deposited one over the other (RGO, Au). The second part of the total equivalent circuit, which is a typical Randles circuit, is composed by a Constant Phase Element (replacing the ideal capacitance of the double layer) and the total impedance relative to the Faradaic reaction of the probe toward the electrode. The first resistance, occurring at higher frequencies, is relative to the charge transfer mechanism ($\boldsymbol{R}_{ct}$) connected with the passage of electrons between the probe and the support. What can be immediately observed is that this value is, among the four materials, the lowest for the hybrid and the highest for the only RGO platform. In particular, it can be noticed that in the case of only AuNPs the resistance is quite low, and in the case of the two materials deposited one to the other the effect seems mediated between the only RGO and the only AuNPs. The fact that for the hybrid the resistance is lowered again with respect to the bare AuNPs it could be related to the strong interaction between the two materials RGO and AuNPs. Moreover, the possible *convergent* or *thin layer diffusion* effect, previously discussed also for the CV results, could be responsible for this lower resistance values, being these processes energetically favoured. RGO deposited onto the C-SPE is ordered and AuNPs onto it are ordered again and strictly connected to the carbonaceous platform. The resistance of the electronic transfer from the probe to the electrode is so assisted by this particular structure and it is lowered. Moreover, looking at the Bode plots (**Figure 5.2.7** (**b**)), it can be noticed that in the case of the hybrid the maximum of the phase angle is shifted at lower frequencies, meaning that the reaction is more favoured (at lower frequencies the system is less perturbed). This could reflect also the possibility to see another circuit in addition of the Randles one, for the hybrid, which is probably related to the interfacial region between the C-SPE support and the Hybrid material deposited onto it.

Regarding the mass transfer resistance, which is expressed by the Warburg element (Z_w), it is the highest in the case of Au alone and the lowest in the case of RGO

alone. In the hybrid the effect seems mediated while in the RGO,Au system it seems that the contribute of RGO wins on the global behaviour of the system. In this case, since the resistance is relative to the massive transport and not only to the electronic one, sterical and hindering effects could play a crucial role. In the case of RGO, this reaction could be favoured thanks to the instauration of a *thin layer* diffusion effect, which is absent in the case of only Au (considering also that the single nanoparticles are functionalized with the aromatic thiol and so there could be a hindrance effect).

Electroanalytical Applications of the PCA-RGO / AuNPs Hybrids

As previously mentioned (See "**Focus**"), the materials under investigation were involved in the electroanalytical detection of Arsenic. Considering the chosen analyte, to perform these analyses, Anodic Stripping Voltammetry was chosen as the best electroanalytical technique.

The first approach was devoted to the detection of arsenic starting from his arsenate form, As_2O_3. A mother solution of this salt was prepared, by dissolving it in NaOH 0.1 M; then, it was added to an aqueous solution of PBS 0.1 M (at pH 7.4), which was the supporting electrolyte in the electrochemical cell. This last equipment was composed by a conventional three-electrode cell (See "Materials and Methods") in which the working electrode was the modified Carbon Screen Printed Electrode. The WE was modified with the four different materials previously analysed via electrochemical characterisations (namely, **Hybrid**, **Au**, **RGO** and **RGO,Au**). The experiments were carried out in a deaerated environment, previously achieved by bubbling N_2 in the solution for 15 minutes. The stripping procedure was composed by a pre-concentration step in which the As(III) in solution is expected to be reduced, and then by a linear anodic scan which ensures a reoxidation of the species in its metallic form. The best accumulation potential (in the cathodic region) was found to be -0.8 V (SCE); in fact, above this potential it was not possible to effectively reduce As(III), because under -0.8 V (SCE) problems related to the concomitant evolution

of hydrogen at the electrodes were encountered. In this way, it would have been impossible to accumulate the metallic ion at the working electrode surface and no signal would have been then registered.

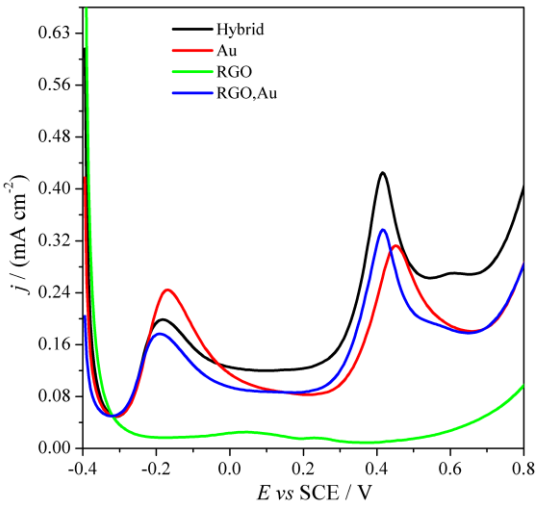

Figure 5.2.9: Comparisons between the four materials tested. Anodic Stripping Voltammetry in the presence of 10^{-5} M of As_2O_3. Accumulation step at -0.8 V (SCE) for 60s, in 0.1 M of PBS solution.

Figure 5.2.9 shows a general comparison of the four materials under investigation, in the presence of the same amount of As_2O_3 in solution (10^{-5} M), with the same accumulation time (60 s) and voltage (-0.8 V (SCE)). It can be observed how the presence of gold nanoparticles is essential, since in the case of RGO no signals are visible; moreover, when AuNPs are deposited onto the RGO solution, they govern the analytical answer. What it can be observed is that two distinct signals are present. In order to understand the nature of these signals, different experiments with and without the accumulation step, followed by an anodic scan in different voltage ranges were conducted. In more details, the voltage range -0.4 V (SCE) to +0.1 V (SCE) and the one from +0.1 V (SCE) to +0.8 V (SCE) were analysed after the addition of the arsenic salt and after performing or not the accumulation (reduction) step.

It was observed that the first signal, at about -0.2 V (SCE) is not present when the accumulation step is not performed (**Figure 5.2.10** (**a**)), while the second signal, around +0.4 V (SCE) is present also without the reduction step at -0.8 V (SCE) (**Figure 5.2.10** (**b**)). Successive additions of the As_2O_3 solution were done and subsequent ASV were performed, but only in the second scan it was possible to see a signal growing, while in the first range no signal were obtained, also growing the

concentration of arsenic in solution. Such an evidence let reasonably deduce that the first signal is related to the oxidation from As(0) to As(III) and the second one is related to the oxidation of As (III), already present in solution, to As(V). In fact, if the reduction step is not performed, the As(III) is not reduced and therefore not oxidized and detected in the following anodic scan.

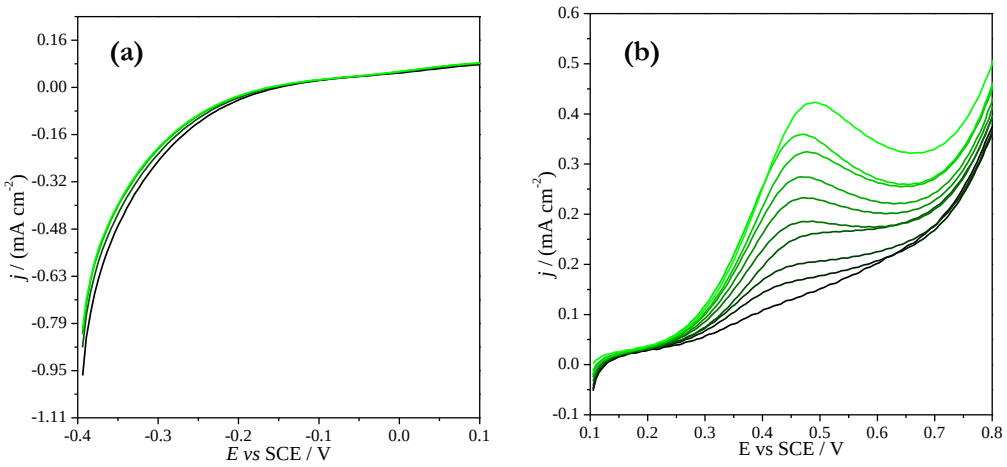

Figure 5.2.10: Successive addition of As_2O_3 (from 3.5 10^{-5} M to 3.2 10^{-4} M) in the (**a**) first range of the anodic scan and in the (**b**) second range, without accumulation step at -0.8 V (SCE).

A general consideration from the **Figure 5.2.9** is that no particular enhancement in the performances of the hybrids seems evident when compared with the only AuNPs modified electrodes. A first thing to be kept in mind is that in the case of the only AuNPs material, the concentration of gold nanoparticles is much higher than the hybrid, in which AuNPs are distributed and grown onto the graphene flakes. Since in this case is gold that reacts with Arsenic (because RGO is not able to give any signal), it means that in the case of the hybrid, the same answer is obtained, but with a lower amount of electroactive species. This could be due to the beneficial effect of the distribution of AuNPs on the graphene platform. RGO, that is not electroactive towards arsenic, assists and stimulates the final response of the AuNPs in the hybrid. It is not a simple spectator but, being a suitable platform, it helps in the detection of the target analyte, thanks maybe to the instauration of particular diffusional

mechanisms which helps in the enhancement of the faradaic current. This evidence is a great result, since it means that by creating a hybrid, it is possible to use less electroactive gold material (which is expensive and not so easily accessible) and to achieve the same results obtained with much more material. It is also a confirmation of the intimate contact between RGO and AuNPs, meaning that a real hybrid, with the instauration of heterojunctions is effectively created and active.

In order to understand which kind of electrode is the best and to try to achieve the lowest LOD, different measurements were done, by lowering the initial concentration of arsenic in solution and subsequently adding it in the electrolyte. The lowest initial concentration of As(III) in the cell was achieved as 10^{-7} M. The electroanalytical experiment was then carried out by adding As_2O_3 in solution and covering the concentration range between 10^{-7} M to 10^{-4} M. Calibration curves were recorded for the modified C-SPEs with **Hybrid**, **Au** and **RGO,Au** solutions (since with **RGO** it was impossible to get results) and the analytical parameters are shown in **Table 5.2.3**. As evident from these results, the best material is the Hybrid, considering all the parameters in one time. In fact, it is the electrode with the highest sensitivity and the lowest detection limits, both on the first peak (signal relative to the oxidation of As(III)) and on the second one (signal relative to the successive oxidation of As(III)). These results are promising, since they are in line (in the same order of magnitude) of the limits imposed by the Directives and Laws on the maximum amount of Arsenic in public water supplies (*i.e.* 10 ppb as established by U.S. EPA). It is interesting to underline the fact that with the layer-by-layer deposition the results are not comparable to the ones obtained with the hybrid and in this case it seems a better system the only AuNPs modified electrode. This observation confirms the importance of having a strict connection between RGO and Au, which is responsible of an enhancement of the analytical performances of the system.

Table 5.2.3: Sensitivity (*S*), Detection Limit (*LOD*) and Quantification Limit (*LOQ*) achieved with the different materials under investigation for the detection of As(III) in PBS 0.1 M.

E = - 0.2 V (SCE)				
Electrode	***S* / (A cm^{-2} ppm^{-1})**	***R*^{2}**	***LOD* / ppb**	**LOQ / ppb**
Hybrid	**1.8 * 10^{-2}**	**0.98**	**26**	**80**
Au	3.5 * 10^{-3}	0.99	25	76
RGO,Au	5.2 * 10^{-4}	0.97	270	820
E = + 0.4 V (SCE)				
Hybrid	**1.4 * 10^{-2}**	**0.98**	**19**	**58**
Au	7.7 * 10^{-3}	0.95	22	67
RGO,Au	1.13* 10^{-3}	0.96	480	1500

Figure 5.2.11 (**a**) reports the graph relative to the subsequent additions relative to the hybrid with the lowest achievable concentration of As(III) in solution. Next, in **Figure 5.2.11** (**b**) the relative calibration curve obtained with results of the second oxidation peak (+0.4 V (SCE)) is reported.

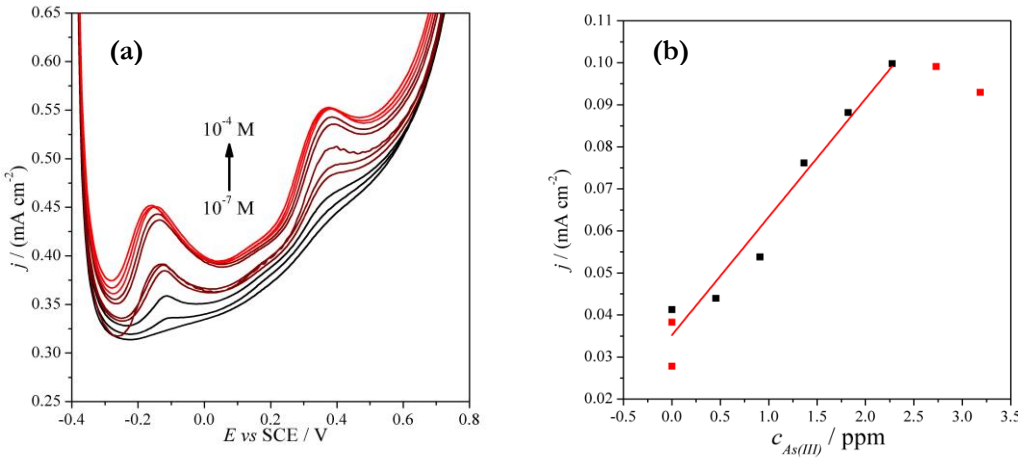

Figure 5.2.11: (**a**) Consecutive additions of As_2O_3 in solution, in the concentration range 10^{-4} to 10^{-7} M, (**b**) calibration curve obtained with the density current values relative to the oxidation signal at +0.4 V (SCE).

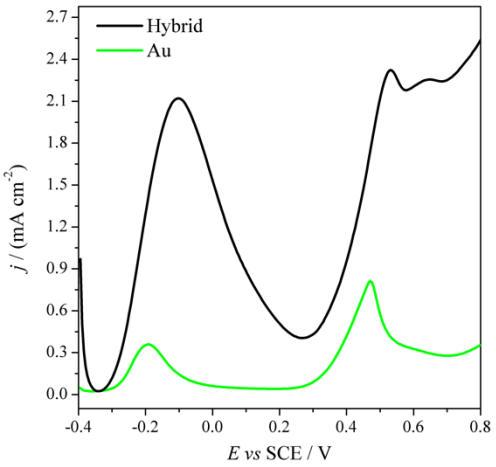

Figure 5.2.12: As(III) detection in PBS, at the same concentration (57 ppm), with the Hybrid (dark line) and Au (green line) modified electrodes.

At this point, the experimental procedure was tried to be refined repeatedly. It was found, in fact, that a preliminary Cyclic Voltammetry step, before the stripping procedure, was beneficial to the electrode. This evidence is probably related to the fact that, by cycling the potential, the AuNPs surface is renewed and cleaned, being more available for the detection of As. This fact was found to be beneficial especially when dealing with the hybrid. In **Figure 5.2.12**, in fact, a comparison between the Hybrid and the Au alone, after being treated with CV after each As(III) addition in solution is shown. In this case, the excellent performances of the hybrid with respect to its single counterpart is evident, also considering that the concentration of AuNPs, that is the electroactive material, is much more higher in "**Au**" than in the "**Hybrid**".

Speciation and Detection of As_2O_5 (As(V))

Since for the detection of As_2O_3 good results were achieved, the interest then moved to the possibility to speciate between the two ions (As(III) and As(V)) and try to detect also the presence of As_2O_5 in solution (As(V)). A first interesting thing observed is that it is necessary, in order to detect As_2O_5 in solution, to change the electrolyte. In fact, by working in PBS no signal were achieved. It was necessary to open the potential window to wider values, until +1.3 V (SCE), in order to see a small shoulder, but effectively no clear signal were detectable. Searching in the Literature,[20–22] several works reported the detection of Arsenic by working in acidic media, like HCl or citric acid. For this reason, the electrolyte solution in use was then

changed in HCl 0.1 M. Surprisingly, the same amount of As_2O_5 added in PBS was then clearly detectable in HCl, as evident in **Figure 5.2.13**.

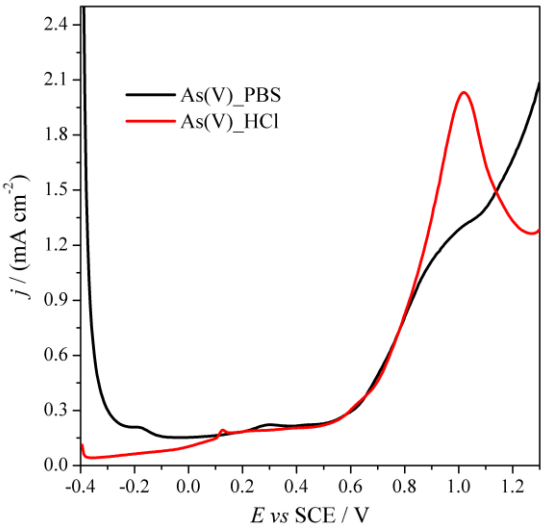

Figure 5.2.13: As_2O_5 in PBS (dark like) and in HCl (red line), detected by ASV with a preliminar reduction step at -0.5 V for 60s and then anodic scan from -0.4 to +1.3 V (SCE)).

The evidence that in PBS was impossible to see As(V) while this was possible in HCl, lets reasonably think that simply by changing the electrolyte solution it is possible to effectively distinguish between the two ions present in solution. A control experiment was carried out: As(III) was added in HCl solution and then a stripping voltammetry was achieved.

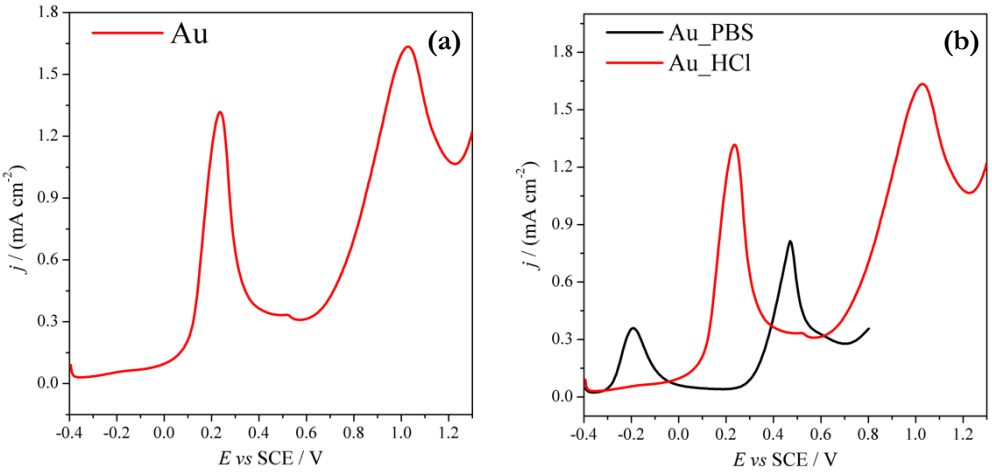

Figure 5.2.14: As_2O_3 in HCl (**a**) detected by ASV with a preliminar reduction step at -0.5 V for 60 s and then anodic scan from -0.4 to +1.3 V (SCE)). (**b**) Comparison with the previous experiments for the detection of As(III) in PBS 0.1 M.

As evident from **Figure 5.2.14** (**a**), two clear peaks are present, meaning that As(III) is detectable also in this electrolyte. In order to reach this result, with respect to the experiment carried out in PBS, it was necessary to change the potential window width

until +1.3 V (SCE) (**Figure 5.2.14** (**b**)) and to change the accumulation step to -0.5 V (SCE). This step was necessary because at potential values under this limit, evolution of hydrogen was observed. In this case, in fact, the high amount of available H^+ ions in solutions (since the electrolyte is HCl) could be easily reduced and favour this side reaction. This fact effectively limits the accumulation step of As(V) onto the electrode platform and it is one of the biggest obstacles encountered in the detection of such ions in solution. In fact, As(V) needs really low voltage to be reduced and the accumulation at -0.5 V (SCE) may not be sufficient for the complete and effective transformation of As(V) to As(0). For this reason, in some work a previous chemical reduction step is carried out, then followed by an electrochemical one.[21]

Since As(III) was detectable in an easy way also in HCl, as it was previously done for the analysis in PBS, it was tried to achieve the best sensitivity and detection limit with both the electrodes that are sensitive to this target analyte (Hybrid and Au). The concentration of As_2O_3 added in HCl was lowered until a value of 10^{-6} M. **Table 5.2.4** reports the analytical parameters obtained for both the electrodes, considering the first signal, at about +0.2 V (**Figure 5.2.14** (**a**)).

Table 5.2.4: Statistical parameters (Range of Linearity, LOD, LOQ, Sensitivity) achieved with the different materials under investigation for the detection of As(III) in HCl 0.1 M.

Electrode	***Range of Linearity* / ppm**	***S* / (μA cm^{-2} ppm^{-1})**	***R*^{2}**	***LOD* / ppm**	***LOQ* / ppm**
Au	0.118 - 2.29	(162 ± 8)	0.98	(0.37 ± 0.02)	(1.13 ± 0.06)
Hybrid	0.118 - 4.63	(116 ± 4)	0.98	(0.63 ± 0.02)	(1.89 ± 0.07)

In this case, it is evident how the statistical parameters are comparable for both the hybrid and the only AuNPs modified electrodes, with slightly better results in the case of Au. Following experiments, at lower concentrations, were not achievable for the hybrid and so they will not be taken into account. By the way, excellent detection limit in this experiments were reached, even if one order of magnitude higher than

the previous ones obtained with the analysis in PBS. It was possible to lower again the concentration only with the "Au" electrode and in this case a detection limits of (5.9 ± 0.2) ppb was achieved, even lower than the one imposed by laws (10 ppb for As(III)) (U.S. EPA). Efforts will be done in order to reach analogous results also with the "Hybrid" electrode. At this point, in fact, when recording the preliminary Cyclic Voltammetry, a strange and high resistive behaviour was registered, meaning that maybe the solution was damaged by changes in temperature and subsequent changes in the concentration of the colloidal solution, mining the stability of the same. The following experiments were carried out by using the electrode modified with only AuNPs, for a practical reason of availability of the materials. However, since it is defined that Au is effective towards the detection of arsenic, is expected that also the hybrid will behave in the same way, or even better, like already verified for the detection of As(III).

As previously done for As(III), also with As(V) it was tried to lower the concentration of the arsenic salt added in solution, in order to gain the lowest detection limits achievable. Since with the "Au" electrode it was found that the signal relative to As(V) was concomitant with the one relative to the oxidation of gold, it was necessary to perform the subtraction of the background signal to all the additions, and then to calculate the calibration curve on the differential values of the current intensities. In this way, it is possible to be sure that the signal calculated is relative only to the addition of Arsenic and not to the formation of gold oxide. The lowest achievable addition of As_2O_5 in solution was around 4 10^{-8} M. **Figure 5.2.15** (**a**) reports the consecutive additions of As(V) in solution, while **Figure 5.2.15** (**b**) shows the relative calibration curve, with the statistical and analytical parameters collected in **Table 5.2.5**.

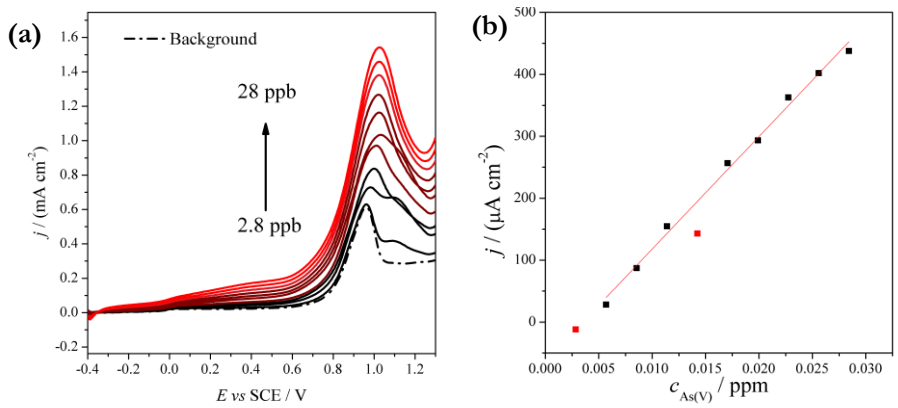

Figure 5.2.15: (**a**) Consecutive additions of As_2O_5 in solution, in the concentration range 2.8 ppb to 28 ppb (**b**) calibration curve obtained with the density current values relative to the oxidation signal at about +1 V (SCE).

Table 5.2.5: Statistical parameters (Range of Linearity, LOD, LOQ, Sensitivity) achieved with the Au electrode for the detection of As(V) in HCl 0.1 M.

Electrode	***Range of Linearity* / ppb**	***S* / (mA cm^{-2} ppm^{-1})**	***R*²**	***LOD* / ppb**	***LOQ* / ppb**
Au	5.69 – 28.4	(0.182 ± 0.5)	0.995	(2.11 ± 0.06)	(6.4 ± 0.2)

Also with this analyte, As(V), it was possible to achieve really excellent LOD, in the ppb range and so in accordance with the Directives and Laws.

Since good results both with As(III) and As(V) were achieved, an experiment when both of the ions species were present in solution was done. In fact, the final goal of the so-created sensor is to be able to detect Arsenic in water, but also to differentiate between the ionic species, when they are both present. In more details, the detection of an equal concentration, in two different experiments, of As(III) and As(V) was done. Then, both the mother solutions of As(III) and As(V) were added, in another experiment, in order to achieve a comparable global concentration of arsenic with respect to the "single" proof. The results are shown in **Figure 5.2.16**.

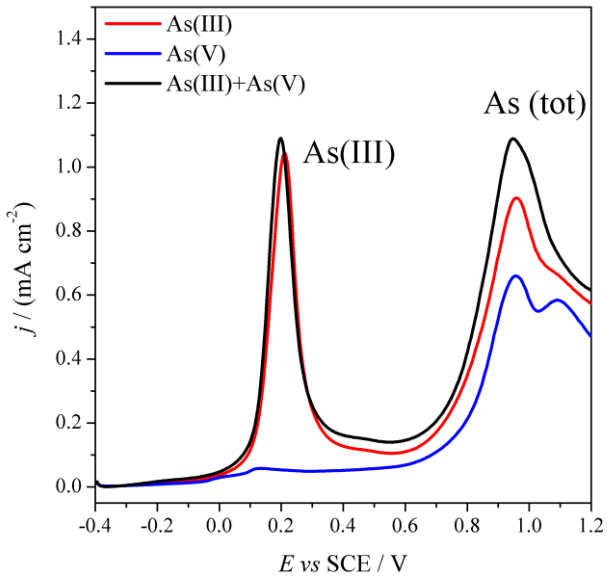

Figure 5.2.16: Anodic Stripping Voltammetry of As(III), As(V) and a mixture of the two ions, at the same concentration, in HCl 0.1 M.

From this proof it is evident how the first signal, at about +0.2 V (SCE) is relative to the oxidation of As(0) to As(III), which is not achieved when starting with As(V) in solution, or it is achieved in really low amount. No signal is present when only As(V) is in solution and in the case of the mixture, the intensity of current is the same as the one achieved when only As(III) is in solution, meaning that this is the only ion that at this potential is re-oxidized. Regarding the second signal, at about +1 V (SCE), it is present in all the three cases and it is in higher amount in the case of the mixture. This means that the signal is related to the whole arsenic present in solution, which is reasonably the As(III) that is oxidised to As (V), deriving both from As(III) still in solution and to the As(V) that was slightly reduced at that potential during the stripping procedure.

Conclusions

In this part of the Thesis Project, a novel hybrid nanocomposite, based on 1-pyrene-carboxylic acid (PCA) modified RGO flakes and 3,4-dimethylbenzenethiol (DMBT)-capped gold nanoparticles has been synthesized, via an *in situ* colloidal route. All the synthetic parameters and the chemicals involved in the reaction were intentionally studied and their role was deeply demonstrated with effectiveness. The short aromatic thiol was demonstrated to be involved in the reduction of Au(III) to Au(I), which is then reduced to Au(0) by $NaBH_4$. Moreover, the thiol, acting as reducing and capping agent at the same time, favours the anchorage of the NPs onto the flakes by π–π stacking interactions, enabling also a potential coupling between the AuNPs and the RGO flakes. The role of PCA was to couple the AuNPs onto the RGO sheets, behaving as coordinating agent (like DMBT) and accomplishing a fine control over the heteronucleation and growth of the AuNPs onto its exposed carboxylic moieties. In general, PCA contributes in narrowing the nanoparticles size distribution (which were finally distributed in the range of 2-3 nm mean size).

The created hybrid was demonstrated to be particularly suitable for the detection of Arsenic, one of the most toxic and dangerous pollutant in water. Excellent detection limits were achieved, in the same order of magnitude and sometimes even lower than the limits imposed by the Directives and Laws. It was demonstrated also the possibility to speciate between As(III) and As(V), by changing the aqueous media in which the experiment is carried out and accordingly adjust the experimental conditions.

In general, the enhanced performances of the hybrid with respect to the single counterparts were highlighted. This fact could be due to the suitable distribution of gold nanoparticles onto the graphene platform, which acts not only as a simple spectator, but it enhances the response of the material toward the analyte, thanks maybe to the instauration of particular diffusional mechanism, like the *convergent diffusion and thin layer effect*. The intimate contact between gold and graphene is again

underlined, verifying the previously mentioned *electron coupling* between the two materials.

The high performances of the materials open also the venue of other future application in metal-doped graphene Field-Effect-Transistors (FETs), other sensors, (photo)catalysts, memory devices, photodetectors and photovoltaic cells.

Bibliography

(1) Ingrosso, C.; Corricelli, M.; Bettazzi, F.; Konstantinidou, E.; Bianco, G. V.; Depalo, N.; Striccoli, M.; Agostiano, A.; Curri, M. L.; Palchetti, I. Au Nanoparticle: In Situ Decorated RGO Nanocomposites for Highly Sensitive Electrochemical Genosensors. *J. Mater. Chem. B* **2019**, *7* (5), 768–777. https://doi.org/10.1039/c8tb02514b.

(2) Callender, E. *Heavy Metals in the Environment - Historical Trends*; 2013; Vol. 11. https://doi.org/10.1016/B978-0-08-095975-7.00903-7.

(3) Wuana, R. A.; Okieimen, F. E. Heavy Metals in Contaminated Soils: A Review of Sources, Chemistry, Risks and Best Available Strategies for Remediation. *ISRN Ecol.* **2011**, *2011*, 1–20. https://doi.org/10.5402/2011/402647.

(4) Maskall, J. E.; Thornton, I. Chemical Partitioning of Heavy Metals in Soils, Clays and Rocks at Historical Lead Smelting Sites. *Water. Air. Soil Pollut.* **1998**, *108* (3–4), 391–409.

(5) Gumpu, M. B.; Sethuraman, S.; Krishnan, U. M.; Rayappan, J. B. B. A Review on Detection of Heavy Metal Ions in Water - An Electrochemical Approach. *Sensors Actuators, B Chem.* **2015**, *213*, 515–533. https://doi.org/10.1016/j.snb.2015.02.122.

(6) Aragay, G.; Merkoçi, A. Nanomaterials Application in Electrochemical Detection of Heavy Metals. *Electrochim. Acta* **2012**, *84*, 49–61. https://doi.org/10.1016/j.electacta.2012.04.044.

(7) Ghaedi, M.; Ahmadi, F.; Shokrollahi, A. Simultaneous Preconcentration and Determination of Copper, Nickel, Cobalt and Lead Ions Content by Flame Atomic Absorption Spectrometry. *J. Hazard. Mater.* **2007**, *142* (1–2), 272–278. https://doi.org/10.1016/j.jhazmat.2006.08.012.

(8) Huang, C.; Hu, B. Silica-Coated Magnetic Nanoparticles Modified with γ-Mercaptopropyltrimethoxysilane for Fast and Selective Solid Phase Extraction of Trace Amounts of Cd, Cu, Hg, and Pb in Environmental and Biological Samples Prior to Their Determination by Inductively Co. *Spectrochim. Acta - Part B At. Spectrosc.* **2008**, *63* (3), 437–444. https://doi.org/10.1016/j.sab.2007.12.010.

(9) Faraji, M.; Yamini, Y.; Saleh, A.; Rezaee, M.; Ghambarian, M.; Hassani, R. A Nanoparticle-Based Solid-Phase Extraction Procedure Followed by Flow Injection Inductively Coupled Plasma-Optical Emission Spectrometry to Determine Some Heavy Metal Ions in Water Samples. *Anal. Chim. Acta* **2010**, *659* (1–2), 172–177. https://doi.org/10.1016/j.aca.2009.11.053.

(10) Bansod, B. K.; Kumar, T.; Thakur, R.; Rana, S.; Singh, I. A Review on Various Electrochemical Techniques for Heavy Metal Ions Detection with Different Sensing Platforms. *Biosens. Bioelectron.* **2017**, *94* (March), 443–455. https://doi.org/10.1016/j.bios.2017.03.031.

(11) Barton, J.; García, M. B. G.; Santos, D. H.; Fanjul-Bolado, P.; Ribotti, A.; McCaul, M.; Diamond, D.; Magni, P. Screen-Printed Electrodes for Environmental Monitoring of Heavy Metal Ions: A Review. *Microchim. Acta* **2016**, *183* (2), 503–517. https://doi.org/10.1007/s00604-015-1651-0.

(12) Kumar, P.; Kim, K. H.; Bansal, V.; Lazarides, T.; Kumar, N. Progress in the Sensing Techniques for Heavy Metal Ions Using Nanomaterials. *J. Ind. Eng. Chem.* **2017**, *54*, 30–43. https://doi.org/10.1016/j.jiec.2017.06.010.

(13) Ingrosso, C.; Corricelli, M.; Disha, A.; Fanizza, E.; Bianco, G. V.; Depalo, N.; Panniello, A.; Agostiano, A.; Striccoli, M.; Curri, M. L. Solvent Dispersible Nanocomposite Based on Reduced Graphene Oxide in Situ Decorated with Gold Nanoparticles. *Carbon N. Y.* **2019**, *152*, 777–787. https://doi.org/10.1016/j.carbon.2019.06.070.

(14) Brust, M.; Walker, M.; Bethell, D.; Schiffrin, D. J.; Whyman, R. Synthesis of Thiol-Derivatised Gold Nanoparticles in a Two-Phase Liquid–Liquid System. *J. Chem. Soc., Chem. Commun.* **1994**, No. 7, 801–802. https://doi.org/10.1039/C39940000801.

(15) Konios, D.; Stylianakis, M. M.; Stratakis, E.; Kymakis, E. Dispersion Behaviour of Graphene Oxide and Reduced Graphene Oxide. *J. Colloid Interface Sci.* **2014**, *430*, 108–112. https://doi.org/10.1016/j.jcis.2014.05.033.

(16) An, X.; Simmons, T.; Shah, R.; Wolfe, C.; Lewis, K. M.; Washington, M.; Nayak, S. K.; Talapatra, S.; Kar, S. Stable Aqueous Dispersions of Noncovalently Functionalized Graphene from Graphite and Their Multifunctional High-Performance Applications. *Nano Lett.* **2010**, *10* (11), 4295–4301. https://doi.org/10.1021/nl903557p.

(17) Ambrosi, A.; Pumera, M. Electrochemistry at CVD Grown Multilayer Graphene Transferred onto Flexible Substrates. *J. Phys. Chem. C* **2013**, *117* (5), 2053–2058. https://doi.org/10.1021/jp311739n.

(18) Compton, R. G.; Banks, C. E. *Understanding Voltammetry*; Imperial College Press, 2011.

(19) Vasudevan, S.; Lakshmi, J. The Adsorption of Phosphate by Graphene from Aqueous Solution. *RSC Adv.* **2012**, *2* (12), 5234–5242. https://doi.org/10.1039/c2ra20270k.

(20) Tupiti, W.; Chandra, S.; Prasad, S. Sensitive Inorganic Arsenic Speciation on a

Voltammetric Platform in Environmental Water Samples. *Microchem. J.* **2018**, *139*, 301–305. https://doi.org/10.1016/j.microc.2018.03.001.

(21) Lestarini, D. T.; Ivandini, T. A. Electrochemical Detection of As3+ and As5+ by Anodic Stripping Voltammetry at a Gold Electrode. *IOP Conf. Ser. Mater. Sci. Eng.* **2019**, *496* (1). https://doi.org/10.1088/1757-899X/496/1/012030.

(22) Pungjunun, K.; Chaiyo, S.; Jantrahong, I.; Nantaphol, S.; Siangproh, W.; Chailapakul, O. Anodic Stripping Voltammetric Determination of Total Arsenic Using a Gold Nanoparticle-Modified Boron-Doped Diamond Electrode on a Paper-Based Device. *Microchim. Acta* **2018**, *185* (7). https://doi.org/10.1007/s00604-018-2821-7.

Acknowledgments

I gratefully acknowledge Dr. C. Ingrosso and Dr. M. Corricelli from CNR-IPCF S. S. Bari, Department of Chemistry, Università di Bari (Bari, Italy) for the synthesis and physico-chemical characterizations of the RGO-Au hybrid materials (Chapter 5.1 and 5.2).

5.3 Gold and Graphene Hybrids for Biosensing

This part of the work was developed at ICN2 (Instut Català de Nanociencia y Nanotecnologia), Barcelona, in collaboration with Prof. Dr. Arben Merkoçi.

Focus

Over the last decades, the research interests have been focused onto technologies to facilitate diagnostic, drug discovery, food safety, defence, security and environmental monitoring.[1,2] Within these technologies, biosensing has become an important approach, since biosensors are highly selective and sensitive. Moreover, they provide fast results and have easy-to-operate capabilities. A part from all these advantages, biosensing techniques could suffer from the disadvantages of being expensive. In order to overcome this fact, the implementation of nanomaterials in biosensing platforms has opened the venue to a plethora of new applications and performances. In addition, the possibility to use abundant flexible substrates, like plastic or paper, could drop the cost of the techniques being suitable for the most variable applications, from sensing to electronics and optics.[3] In this context, nowadays, printed technologies are implementing new emerging materials and developing new patterning techniques with the possibility to produce ubiquitous flexible, cost effective and easy of manufacturing devices. These has led to the evolution of new systems such as flexible displays, NFC tags, wearable devices and so on.[4–6]

In such a context, considering all together the advantageous tools of printing techniques, the possibility to use flexible substrates and the final goal of biosensing, it is important to underline the power of graphene and graphene related materials.[7] Graphene is intended as layer of carbon atoms packed into a honeycomb lattice. Thanks to its 2D structure it exhibits unique electronic, optical, magnetic, thermal and mechanical properties, becoming an interesting and novel sensing material, as already mentioned in the Introduction of **Chapter 5** and **6**. In the particular field of biosensing, pristine graphene, polycristalline graphene, graphene quantum dots (GQDs) and (reduced) graphene oxide (GO and rGO) are the most commonly

involved graphene derivatives. GO is a lattice of sp^2 carbon atoms incorporating defects since it is disrupted by sp^3 carbon bonds and possesses oxygen-containing groups (carbonyl, carboxyl, hydroxyl, epoxy groups on the exposed edges or on the basal planes). rGO is composed by GO after being reduced through chemical or physical routes.[8] Depending on the final application, it can be obtained in aqueous dispersion (and this represents a huge advantage for biosensing applications) or in powder. It can also be reduced directly onto the specific substrate, if the final application does not requires transparent devices, otherwise a transfer procedure is needed, often requiring the use of solvents and chemical pre-treatment of the specific substrates.[9]

In this part of the Thesis Project, considering all the above-mentioned needs in the research field, a new technique for direct patterning and rGO transfer to flexible substrates (particularly plastic and paper-based ones) have been developed. A specific design was laser scribed onto a GO layer previously deposited onto a nitrocellulose membrane. Then, only the reduced part is transferred avoiding any treatment of the final substrates. Particularly, electrodes transferred on PET and nitrocellulose were developed. They were at first electrochemically characterized and then they were applied, as bare graphene electrodes, in the detection of dopamine. Particularly, nitrocellulose-based devices were then used for the development of immunoassays. The possibility to directly transfer the rGO platform onto nitrocellulose paper was a great deal in the possibility to directly functionalize the electrodic platform with the biomolecule under investigation, exploiting the high affinity of nitrocellulose to such materials like antigens and antibodies. The final device was an immunoassay in which the secondary antibody was functionalized with gold nanoparticles and the activity of such electroactive material toward the HER catalysis was exploited in biosensing applications.

Materials and Methods

Electrodes Preparation: Printing Procedure

Graphene Oxide suspension (Angstrom Materials, solution N002-PS-1.0, 10 mg/L) was diluted in Milli-Q water (Purelab Option-Q) in different concentrations. All the aqueous solutions were filtered with a vacuum pump through nitrocellulose hydrophilic membranes, with a pore size of 0.025 μm and 47 mm of diameter. The as prepared GO membranes were finally dried with N_2 flux and placed onto a CD by a double adhesive tape. The CD were then placed face down into a DVD-burner enabled with lightscribe technology. Thanks to Corel Draw software the electrodic pattern was designed and the reduction process proceeded thanks to laser technology (780 nm length, 600 dots per inch of resolution). The reduced pattern was then transferred on new substrates, previously subjected to a plasma cleaning (Harrick Plasm), using a laboratory hydraulic press machine (12 Tons of pressure).

For the particular preparation of electrodic platform, GO solution of 0.4 mg mL^{-1} in a total volume of 5 mL was filtered. Then, five reduction steps were chosen as best parameters. After the printing procedure, the final design was transferred on two different substrates: poly(ethylene terephtalate) (PET) film and nitrocellulose paper (8 μm, CNPF-SN12, 25 mm, ADVANCED MICRODEVICES PVT. LTD.). Silver paste ((C2100203D2), Gwent group/Sun Chemical (Pontypool, U.K.)) was used to make electric contacts and a layer of grey dielectric paste ((D2070423P5), Gwent group/Sun Chemical (Pontypool, U.K.)) was printed in order to insulate the working part and avoid possible contacts between the solution and the electric component.

Physico-Chemical Characterizations

Magellan 400L XHR SEM (FEI, Hillsboro, OR) and Quanta 650FEG ESEM (FEI, Hillsboro, OR) were used to performed SEM and EDX analysis, while the film thickness was measured with a profilometer (Alpha Step D-500 Stylus Profiler, KLA-Tencor) and Asylum MFP-3D Atomic Force Microscope. The reduction efficiency

was assessed via XPS measurements, using a Phoibos 150 hemispherical energy analyzer (SPECS GmbH, Berlin, Germany), and confocal Raman spectrometer equipped with a 488 nm laser, with 1.5 mW power, grating 600 gr/nm and objective 50x. Every single spectrum was collected for 10 s and 3 accumulations.

Electrochemical Characterizations and Electroanalytical Applications

All the the electrochemical measurements were performed using an AutoLab PGStat302 connected to a computer equipped with the software NOVA 2.1.3 (Metrohm AutoLab). The electrodes were electrochemically characterized by means of cyclic voltammetry (CV) in presence of $[Ru(NH_3)_6]Cl_3$ (Sigma Aldrich) and $K_4[Fe(CN)_6]$ (PanReac AppliChem, ITW Reagents) as redox probes, in a 0.01 M phosphate buffer saline solution (PBS) as supporting electrolyte. PBS was prepared starting from pallets (Sigma Aldrich) dissolved in Milli-Q water (Purelab Option-Q). CV was performed in a potential range between -0.8 V and +0.5 V (Ag pseudo reference) for $[Ru(NH_3)_6]Cl_3$ and from -0.8 V to +1 V (Ag) for $K_4[Fe(CN)_6]$. The scan rate was varied in the range from 10 mV s^{-1} to 750 mV s^{-1}.

The electrodes were involved, as a preliminary proof of concept, in the detection of dopamine hydrochloride (Sigma Aldrich) in a concentration of 10^{-4} M, prepared in PBS, using differential pulse voltammetry (DPV) as electroanalytical technique. The potential was scanned between -0.2 and +0.6 V (Ag) with a pulse of 5 mV and an amplitude of 50 mV.

Biosensor Preparation

- *AuNPs Synthesis*

20 nm AuNPs were synthesized following the already known Turkevich method.[10] Briefly, 50 mL of 0.25 mM $HAuCl_4$ is heated up until boiling point under vigorous stirring. Then, 1.25 mL of 1% sodium citrate is added quickly to the solution. At this point, a gradual changing of the color of the solution is observed passing from purple

to bright red. At this point, the heating is switched off. Finally, the solution is cooled down and stored at 4°C.

- *AuNPs Conjugation to anti H-IgG antibody*

1.5 mL of 20 nm AuNPs previously synthesized were mixed with 100 μL of 250 μg/mL antibodies (Anti-Human IgG, whole molecule, antibody produced in goat, Sigma Aldrich), following a previous procedure developed in the group. The Gold Aggregation Test (GAT) previously conducted verified this concentration of antibodies as sufficient to cover the whole AuNPs). Then, the solution was shacked overnight, with a ThermoShaker (VELP), at 4°C, 650 rpm. The day after, 100 μL of Bovine Serum Albumine (BSA) 1 mg mL^{-1} was added as blocking agent and shacked for 20 minutes in the same condition as before. Finally, the AuNPs were centrifuged at 14000 rpm for 30 minutes at 4°C. The NPs were suspended in PBS, pH 7.4.

- *Immunoassay Creation*

The nitrocellulose-based electrodes were subjected to several steps in order to create the final immunoassay. At first, a drop of 4 μL of different concentrations of the antigene H-IgG was placed onto the working electrode and let it dry for about 30 minutes. Then, a drop of 4 μL of blocking agent (ETA or BSA, Sigma Aldrich) was placed onto the working electrode and let it dry. The electrodes were then washed three times in PBS (pH 7.4). At this point, 4 μL of the conjugated AuNPs with the antibody anti-H-IgG are added and let it dry. The electrode is finally washed three times in PBS (pH 7.4).

- *Electrochemical Proof*

The as-prepared biosensors were then used as electrochemical platform. 60 μL of HCl 0.5 M were placed onto the electrode (which actually behaves as a complete electrochemical cell, being equipped with a working (WE), counter (CE), and

reference (RE) electrodes) and a chronoamperometry at -1 V (Ag) was recorded for 300 s.

Results and Discussion

Physico-Chemical, Electrochemical Characterizations and Electroanalytical Applications

The concentration of GO solution filtered onto the nitrocellulose membrane and the number of reduction steps to which the as-prepared membrane was subjected were deeply studied and optimized, in order to obtain a high thickness control and to ensure the transfer of only the outermost rGO layers. Different reduction steps (and also different GO concentrations) were tested. SEM images of the different materials showed that the most uniform surface was achieved with samples that were reduced five times. Moreover, using a four-point-probe method an in-depth electrical analysis was performed allowing us to follow the evolution of the conductive behaviour of the material while varying the concentration of GO and the degree of reduction. From a contour map it was possible to see the conductivity trend for different concentrations of GO in a 5 mL solution as the number of reduction steps increases For concentrations lower than 0.1 mg/mL it was not possible to obtain good results since the reduction process was too aggressive for the thin surface: it was immediately damaged, the transfer was not homogeneous and the result was a non-conductive material. On the contrary, for concentrations higher than 0.8 mg/mL the rGO layer transferred was too thick and the conductivity was very low. For concentrations between 0.3 and 0.7 mg/mL, the conductivity of the material increases with the number of reduction steps until the degree of reduction reaches a threshold value. The best and most stable result is obtained for concentrations around 0.4 mg/mL five times reduced. Results were also compared with Raman (**Figure 5.3.1**) and XPS analysis.

Before the transfer process onto PET and Nitrocellulose, these two substrates were cleaned into an oxygen plasma cleaner, in order to remove dust and other residues

from their surface. Moreover, this process could also lead to the formation of surface functional groups which can then interact with the oxygen functionalities eventually present as residues in the rGO pattern, enhancing the transfer process. The membrane with the pattern-reduced GO is fixed faced down onto the selected substrates with adhesive tape. The created sandwich is put between PDMS discs and after that pressed with a hydraulic press machine. In this way, the only reduced part (the outermost layers) are transferred into the new substrates and separate from the GO mesh, which remains attached to the membrane. It was found that lowering the GO initial concentration and enhancing the reduction steps lead to a complete rGO transfer. GO is reduced because it is already known that rGO possesses higher performances when applied in electronics and sensing applications, starting from its enhanced conductivity and its lower concentration of defects.[11,12] In this particular case, the laser of the DVD burner used to reduce GO acts at 780 nm, where photothermal processes are responsible for the reduction. It means that the laser locally reduces GO by heating its surface and then changing GO structure and bonds.[13]

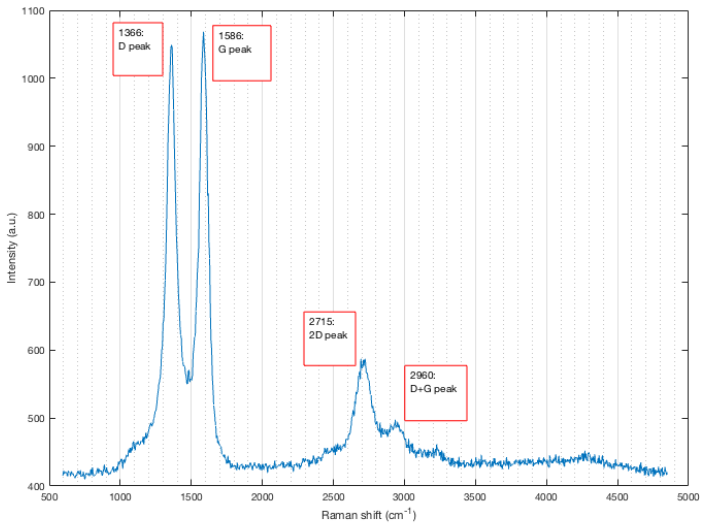

Figure 5.3.1: Raman Spectrum of the rGO membrane reduced for five times.

The effective structure of the obtained reduced graphene oxide film was investigated via Raman spectroscopy (See **Figure 5.3.1**). In such spectra the characteristic G band at 1580 cm^{-1} and D band at 1350 cm^{-1} are present. The I_D / I_G ratio, that gives an index of the disorder of graphene-based materials, decreases as the number of reduction steps increases. This may be due to the removal of the oxygen-functional groups and to the restoration of sp^2 domain. The strong increase in the 2D band intensity further supports this behavior.

Other spectroscopic techniques (AFM, XPS) were involved in order to study the physico-chemical properties of the device, but this is out of the particular topic of this PhD Thesis, since the selected material was then further used for other application in electronics and optics.

As previously reported, the rGO patterns were transferred onto PET (hereafter shortened as "rGO on PET") or Nitrocellulose (hereafter shortened as "rGO on NITRO") substrates, in order to be used as electroanalytical platforms. **Figure 5.3.2** reports the final hand-made devices.

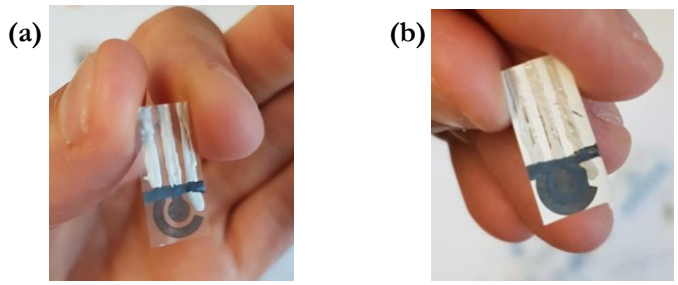

Figure 5.3.2: Final devices on PET (a) and Nitrocellulose (b).

Electrochemical characterizations of the rGO electrodes were performed in the presence of the so-called "*inner sphere*" ($K_4[Fe(CN)_6]$) and "*outer sphere*" ($[Ru(NH_3)_6]Cl_3$) redox probes. These definitions are relative to different mechanisms involved between the electrode (a carbonaceous material) and the redox probe present in solution. With "outer sphere", it is defined a molecule that interacts only with the electronic density of state (DOS) of the electrode. On the contrary, an "inner sphere" redox probe is a molecule that is sensitive also to the surface structure

of the electrode itself and not only to the DOS of the material.[14–18] The differences in the behaviour of the electrodes with these molecules let suppose and conclude that differences in the surface structure are present, which could be exploited for electroanalytical and sensing applications in general.

Figure 5.3.3 reports the comparison between the two different electrode platforms towards $K_4[Fe(CN)_6]$ (**a**) and towards $[Ru(NH_3)_6]Cl_3$ (**b**), respectively. What it can be immediately seen is that the most appreciable difference between the two materials are visible when dealing with the *inner sphere* redox probe, being this molecule effectively affected by changes in the surface structure of the electrode. Such difference let us suppose that a different surface structure of the materials is present, when dealing with PET or NITRO substrates.

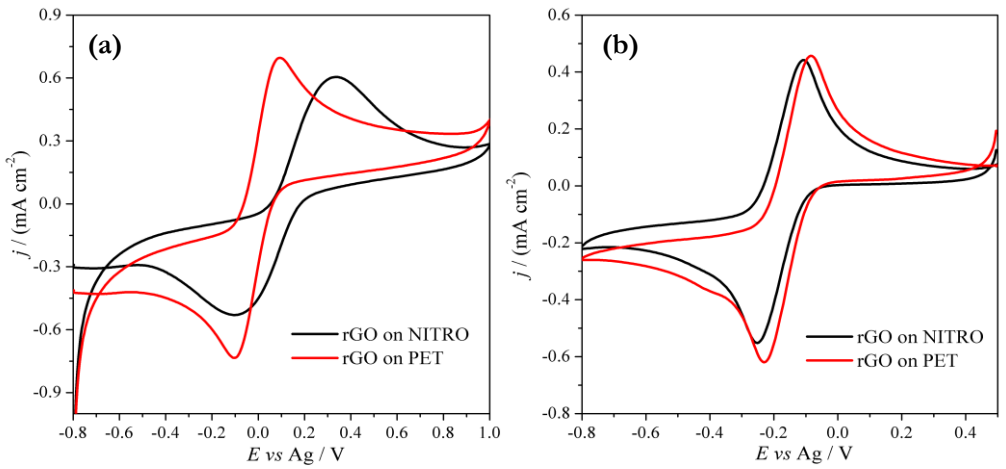

Figure 5.3.3: Cyclic Voltammetries (CV) of the different electrodic platform recorded in 0.01 M PBS, at 50 mV s^{-1}, in the presence of 3 mM of $K_4[Fe(CN)_6]$ (**a**) and $[Ru(NH_3)_6]Cl_3$ (**b**).

In particular, looking at the response with the inner-sphere redox probe, on the anodic (forward) peak position and current, it is evident a strong effect of both electrocatalysis and electroactivity when dealing with PET substrates. It seems that in this case, the amount of edge planes is higher with respect to the one of nitrocellulose, where more basal planes are expected by looking at its response towards the redox probe. It could be that, in the case of nitrocellulose, that is a more

porous material, the transfer of the rGO surface is more effective and creates a final homogeneous layer. On PET, which is a less porous material, it could happen that the transfer procedure is less complete and leads to more flakes than homogeneous layer, resulting in a higher amount of edges. This is evident also from SEM image in **Figure 5.3.4**, where in the case of PET (**a**) the transfer is not completely homogeneous and there is not a perfect adhesion of the rGO to the substrate like in the case of nitrocellulose (**b**).

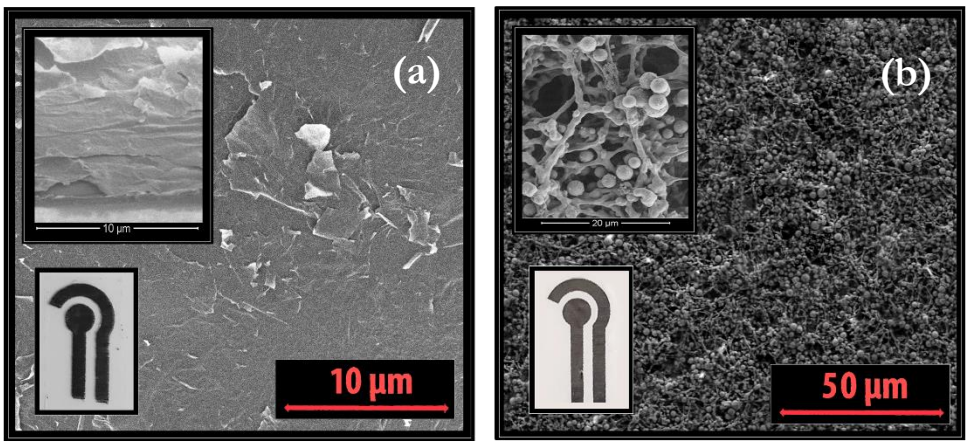

Figure 5.3.4: SEM Images of the rGO transferred onto PET (a) and Nitrocellulose (b) platforms.

It is known that the edge planes in a graphene-like structure are more active than basal planes and in fact this reflects in anticipated peak positions and higher current density values. The current values are normalised for the geometric area of the electrodes, which is 0.07065 cm^2. The effective surface area was calculated by applying the Randles-Sevcik equation $I_p = 2.69 \cdot 10^{-5} A D^{1/2} [A] v^{0.5}$, assuming to be under perfect reversible behaviour and in a complete diffusive control. In the equation, I_p is the current intensity at the maximum, A is the electrodic area (to be calculated), D is the diffusion coefficient of the molecule under investigation, [A] is the concentration of the probe and v is the voltage scan rate. The characterizations were done in the presence of 3 mM ([A]) $[Ru(NH_3)_6]Cl_3$ ($D = 6.5 \cdot 10^{-6}$ cm^2 s^{-1}),[18] by varying the voltage scan rate and calculating the relative current intensities of the cathodic peak. The effective area resulted equal (considering the error range) for both

the nitrocellulose ((0.7 ± 0.1) cm^2) and PET ((0.7 ± 0.2) cm^2) electrodes and one order of magnitude higher than the geometric one, being representative of a high number of defects and roughness of the surface with respect to the bare substrates. By the way, since both the geometrical and the effective areas were the same for PET and NITRO electrodes, it was decided to leave the density current values as normalized for the geometric area.

The PET and NITRO rGO based electrodes were characterised by varying the voltage scan rate, on the background (0.01 M PBS solution, pH 7.4) and in the presence of 3 mM of the two redox probes. By observing how the capacitive current (background current) varies with the voltage scan rate it was possible to calculate the Capacitance (*C*) of the electrodes, while from the elaboration of the data in the presence of the probes it was possible to gain more information on the diffusional mechanism and on the electrochemical reversibility or irreversibility of the reaction. In particular, linear dependency of the oxidation current values of the Fe(II)/Fe(III) redox probe versus $v^{0.5}$ for the two different types of electrodes was found. This fact could be responsible for both a reversible than an irreversible system. The fact that the peak-to-peak distance (ΔE_{pp}) varies with the scan rate, together with the wave shape of the oxidation peak (that is the E_p - $E_{p/2}$ value), is the evidence of an irreversible or quasi-reversible electrochemical behaviour. ΔE value for all the hybrids recorded at 0.1 V s^{-1} is reported in brackets: the highest values are recorded for the nitrocellulose based systems, especially in the presence of potassium ferrocyanide probe, being this materials the ones with the most marked electrochemical irreversibility behaviour. Moreover, by plotting log(*i*) *vs* log(*v*) a deviation from the perfect linear diffusion behaviour is observed. In fact, the slope of the curve (α) is lower than 0.5, meaning that other diffusional mechanisms (maybe *convergent* or *thin layer* diffusion) are here present. These considerations are done also with the Ru(III)/Ru(II) redox couple, observing in this case parameters closer to the conventional ones, confirming once more the independency of the electrochemical behaviour of this probe toward the surface structure of the electrode. Regarding the

Capacitance values, they are similar for both electrodes, being the same order of magnitude, a little bit higher for NITRO than for PET. By the way, the values are really low meaning that the capacitive current is not an obstacle to the observation of Faradaic phenomena towards the electrode and so the devices act as suitable sensing platforms.

Table 5.3.1: Analytical Parameters derived from the electrochemical characterizations of the rGO platforms in 0.01 M PBS, as background electrolyte solutions, and in the presence of two different redox probes, namely $K_4[Fe(CN)_6]$ and $[Ru(NH_3)_6]Cl_3$.

	rGO on PET	**rGO on NITRO**
Capacitance	$(5.24 \pm 0.07) \cdot 10^{-6}$ F	$(7.8 \pm 0.1) \cdot 10^{-6}$ F
	$K_4[Fe(CN)_6]$	
α ($\log(i)$ *vs* $\log(v)$) slope	(0.31 ± 0.02)	(0.53 ± 0.03)
ΔE_{pp}	Scan rate dependent **(0.1 V s^{-1}: 221 mV)**	Scan rate dependent **(0.1 V s^{-1}: 534 mV)**
$E_p - E_{p/2}$	Scan rate dependent	Scan rate dependent
	$[Ru(NH_3)_6]Cl_3$	
α ($\log(i)$ *vs* $\log(v)$) slope	(0.460 ± 0.004)	(0.46 ± 0.02)
ΔE_{pp}	Scan rate dependent **(0.1 V s^{-1}: 162 mV)**	Scan rate dependent **(0.1 V s^{-1}: 171 mV)**
$E_p - E_{p/2}$	Scan rate dependent	Scan rate dependent

In order to understand if these electrodic platforms are effectively performant, a comparison in the response with other Carbon Based Screen Printed Electrodes on plastic support (C-SPEs on PET), commonly involved in the group was done and the results shown in **Figure 5.3.5** (**a**). The response towards the *inner sphere* redox probe $K_4[Fe(CN)_6]$ was done and a strong effect of electrocatalysis and electroactivity was observed. In this case, it is reasonable to assert that the electrodes are made of a more performant material from the electrochemical point of view, namely rGO instead of normal Carbon Ink.

The excellent properties of the rGO electrodes with respect to the conventional C-SPEs were also verified by an experimental proof of concept. The electrodes were used to detect dopamine and their response, at the same concentration of the analyte (10^{-4} M in 0.01 M PBS, pH 7.4) is compared in **Figure 5.3.5** (**b**). The electroanalytical technique is, in this case, a Differential Pulse Voltammetry (DPV). It is clearly evident how, in the case of the rGO electrodes, a four-time higher current response is registered. Also in this case, the values are normalized for the geometric area, since not so many differences were calculated for the three different electrodic platforms in terms of effective area. This huge result effectively confirms the enhanced performances of the graphene-based electrode as electroanalytical sensor; the high current response of the devices let reasonably suppose that the concentration of the analyte could be lowered and lowered until the best LOD for the technique is found.

The electrodes resulted to be really reproducible and stable over time. It was possible to perform characterizations over several hours. The only thing to be kept in consideration is the evaporation and absorption of the solvent, especially in the nitrocellulose electrodes.

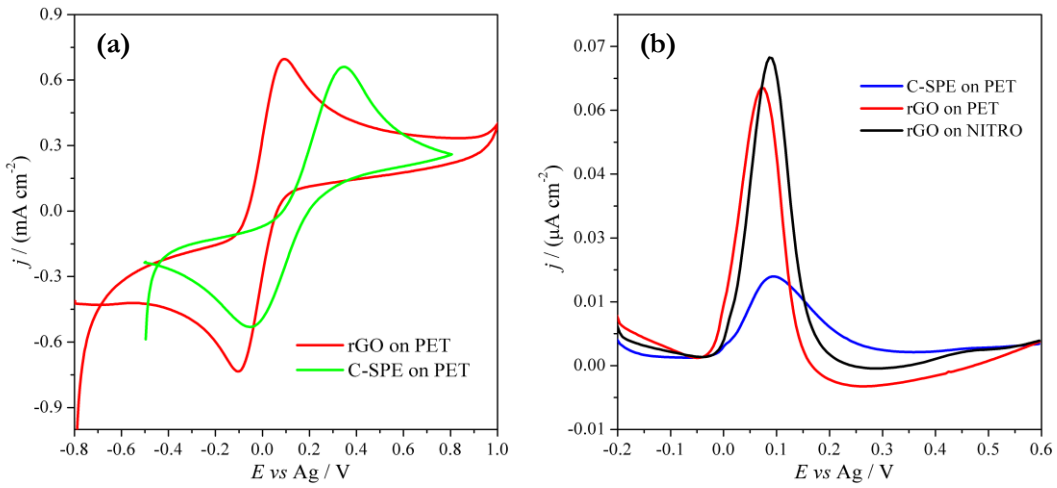

Figure 5.3.5: (**a**) CV of the rGO PET platform compared with C-SPE on PET, in the presence of 3 mM $K_4[Fe(CN)_6]$, at 50 mV s^{-1}, in 0.01 M PBS (pH 7.4). (**b**) DPV of the two rGO electrodes compared with the C-SPE on PET, in the presence of 10^{-4} M of dopamine, in PBS 0.01 M (pH 7.4).

Biosensing Applications

The synthesized rGO electrodes, after being deeply characterized both from a physico-chemical and electrochemical point of view, were used to build, finally, a biosensor. In this case, the electrodes under investigation are the ones with Nitrocellulose as substrate. The negatively charged nitrate groups of this support are the most important functional groups able to interact with biomacromolecules (such as antigens and antibodies) which are typical positively charged proteins due to the amino acids in their structure. The connection can occur simply to nitrate ester by electrostatic bonds.[19] The activation of the substrate,[20] usually known as a procedure able to increase the capacity to capture biomacromolecules, it is however time consuming and can be in this way avoided.

A scheme of the final device is reported in **Figure 5.3.6**, showing how an antigen (H-IgG) is directly attached to the electrodic platform, then an antibody (anti- H-IgG), labelled with AuNPs is attached to the selected antigen. The presence of gold nanoparticles is then exploited for their ability to catalyse the Hydrogen Evolution Reaction (HER). A higher amount of AuNPs reflects in a higher concentration of the antigen, which is observed by an enhancement of the chrono-current registered.

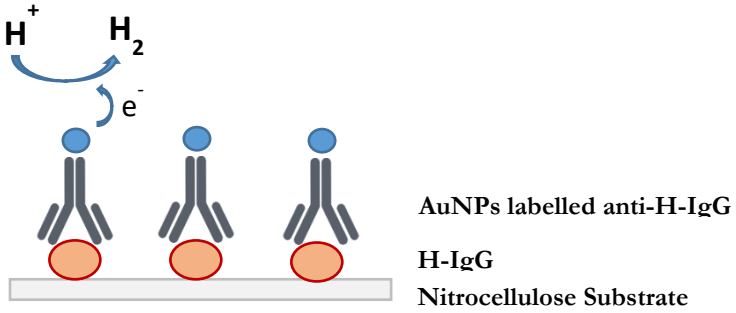

Figure 5.3.6: Schematic Representation of the created Immunosensor.

The created biosensor is, in particular, an *immunosensor*, a sensor in which the recognition is obtained by *Affinity Interactions*. These interactions involve reversible multiple binding of two chemical species through noncovalent bonds (ionic bonds, hydrogen bonds and Van der Waals interactions). The product of an affinity

interaction is a molecular association complex, which is formed only if the involved species are complementary with respect to shape and chemical reactivity. A real example of affinity interaction is, in fact, the *antigen-antibody* interaction, which is an *immunochemical reaction*. [21]

The experimental procedure to create the immunoassay was previously reported in the "Materials and Methods" Paragraph. The first step is the deposition, via drop casting, of the antigen (in different concentrations) on the electrode platform. In order to understand if the antigen is effectively attached to the surface of the electrode, it is a common procedure to record an Impedance spectrum (EIS) before and after the addition of the molecule, in the presence of a redox probe, in this case $K_4[Fe(CN)_6]$. The attachment of the antigen reflects in an enhanced charge transfer resistance, which is visible from the increased diameter of the semicircle in the Complex plane plot. This effect was observed and it meant that the functionalization of the electrode surface was effective (see **Figure 5.3.7**).

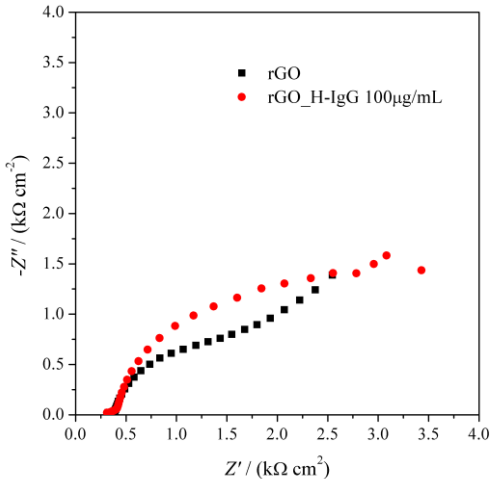

Figure 5.3.7: Complex plane plot of the bare rGO (dark dots) and of the antigen-modified one (red dots).

After the deposition of the antigen, a blocking step is necessary. In fact, it is important to cover the surface of the electrode that is not functionalized with the antigen, in order to prevent unspecific attachment of the secondary antibody directly onto the electrode and not onto the target antigen. Two different blocking agents were tried, at first ETA (Ethanolamine) and then BSA (Bovine Serum Albumine). In both cases an effective blocking step was achieved. As an example, **Figure 5.3.8** reports the effect played by different concentration of BSA. A chronoamperometry of the bare rGO electrode, as blank, was registered. Then, an rGO modified directly

with AuNPs labelled anti-H-IgG, without any blocking step, was used as the other reference. In the middle, different concentrations of BSA on different electrodes, which are then functionalized with the AuNPs-labelled antibodies, were tried. The goal is to reach the same current obtained with the electrode that is non-blocked and non-functionalized with AuNPs-labelled antibody (rGO in the Figure). In this case, in fact, it means that the blocking step is effective and no antibody is effectively attached to the surface of the electrode. In the present work, a concentration of BSA equal to 0.5 % was found to be necessary in order to get a complete blocking of the surface. This is evidenced in a better way if looking at the current intensity values, registered at 150s, for all the different electrodic platforms. It is clear that from a concentration of 0.5% of BSA the intensity current values of the bare rGO are comparable with the blocked ones.

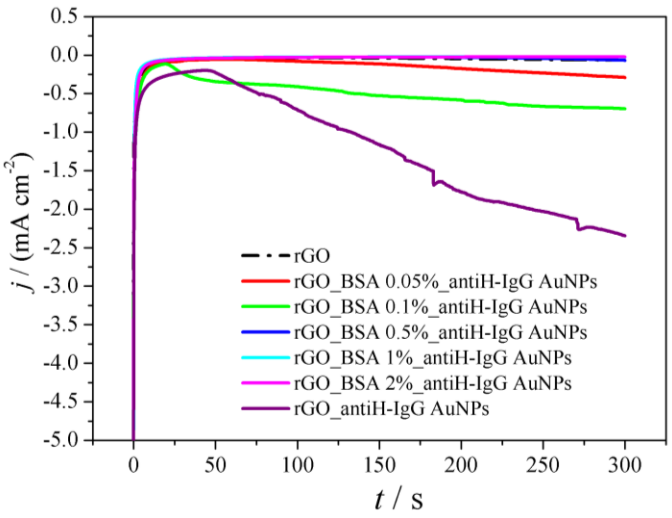

Figure 5.3.8: Chronoamperometry of different electrodes blocked with higher amount of BSA.

Table 5.3.2: Intensity current values (at 150 s) of the electrodes blocked with different concentrations of BSA.

Electrode	***i* / mA (at 150 s)**
rGO	**-2.79**
rGO_BSA 0.05%_antiHIgG-AuNPs	-8.27
rGO_BSA 0.1%_antiHIgG-AuNPs	-37.4
rGO_BSA 0.5%_antiHIgG-AuNPs	**-1.93**
rGO_BSA 1%_antiHIgG-AuNPs	**-1.76**
rGO_BSA 2%_antiHIgG-AuNPs	**-1.91**
rGO_antiHIgG-AuNPs	-82.2

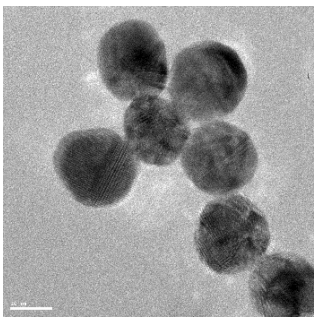

Figure 5.3.9: TEM Image of the synthesized AuNPs.

Once that the blocking step is performed, the next modification is with the AuNPs-labelled antibodies. Also in this case the procedure is explained in the previous paragraph. **Figure 5.3.9** reports a TEM image of the gold nanoparticles synthesized, confirming their dimensions of about 10-20 nm.

When the immunosensor is complete, a chronoamperometry at -1 V (Ag pseudo reference), for 300 s, in HCl 0.5 M was recorded. The use of the acidic media was necessary in order to let the nanoparticles active towards the HER.

A first preliminary test was recorded using an antigen concentration range between 0.2 and 0.6 μg mL^{-1}. In this case (**Figure 5.3.10** (**a**)), the linearity is maintained between 0.2 and 0.5 μg mL^{-1} (**Figure 5.3.10** (**b**)) and the electrodes showed a good reproducibility, giving the same results in a triplicate experiment. The intensity current values, to get the calibration curve in **Figure 5.3.10** (**b**) were registered at 150 s.

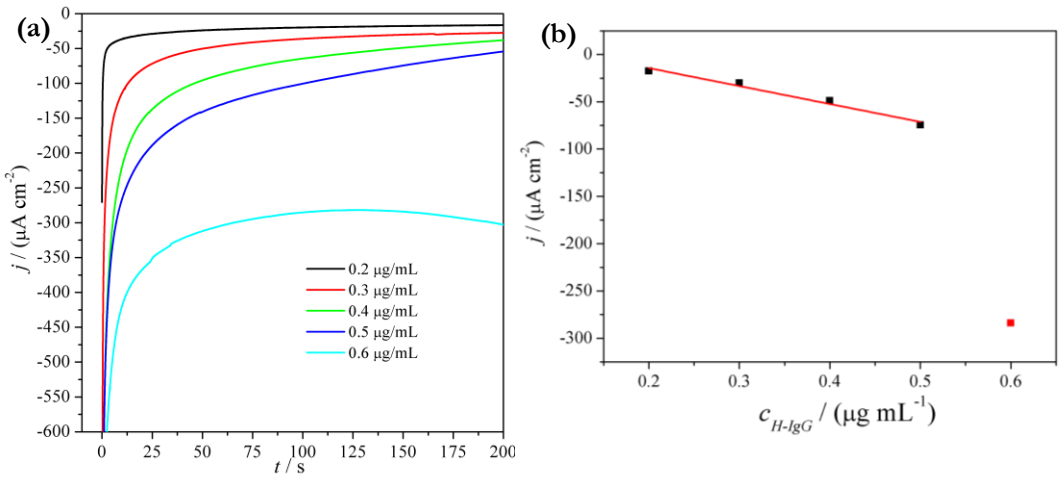

Figure 5.3.10: (**a**) Chronoamperometry at different concentration of antigen H-IgG. (b) Linearity obtained for the range 0.2 – 0.5 μg mL^{-1}.

These good results let reasonably think that it is possible to lower the concentration of the antigen in order to get the best LOD for the technique, that is still far from other work in the Literature.[22] Unfortunately, several problems were encountered in the repetition of the analysis. It was found later that a beneficial step, in order to get a stable and reproducible current, is represented by a preliminary oxidation before the chronoamperometry at reducing potential. In fact, thanks to this passage, some gold atoms in the outer layer of AuNPs surface are transformed into Au(III) ions. These ions could also exert a catalytic effect on hydrogen evolution.[23]

Conclusions

In this part of the Thesis Project, graphene based materials were used for the final construction of an immunosensor, in which the role of AuNPs was determinant.

At first, a novel route to produce and print the electrodes was optimized, then, a deep physico-chemical and electrochemical characterization of the electrodes was done. The novelty of the work is in the possibility to transfer onto the selected substrate only the reduced part, obtained by laser irradiation, from a mesh of Graphene Oxide. The rGO electrodes were transferred onto different supports, in particular PET and Nitrocellulose paper. They resulted in being more performant than other C-SPEs normally involved in the group, both in terms of electrochemical activity and catalysis and also in the response toward a target analyte, which was selected to be dopamine.

The Nitrocellulose electrodes were then used to construct an immunoassay, in which the antigen was directly attached onto the paper support and then it reacted with the related antibody. Such an antibody was labelled with gold nanoparticles, which act as electrocatalytic reagent towards the Hydrogen Evolution Reaction.

Good results were obtained and paved the way towards the use of these devices in a plethora of applications involving flexible substrates, from sensing to electronics and optics, passing through the novel field of wearable devices.

Bibliography

(1) Dragone, R.; Grasso, G.; Muccini, M.; Toffanin, S. Portable Bio/Chemosensoristic Devices: Innovative Systems for Environmental Health and Food Safety Diagnostics. *Front. Public Heal.* **2017**, *5* (MAY), 1–6. https://doi.org/10.3389/FPUBH.2017.00080.

(2) Long, F.; Zhu, A.; Shi, H. Recent Advances in Optical Biosensors for Environmental Monitoring and Early Warning. *Sensors (Switzerland)* **2013**, *13* (10), 13928–13948. https://doi.org/10.3390/s131013928.

(3) Morales-Narváez, E.; Baptista-Pires, L.; Zamora-Gálvez, A.; Merkoçi, A. Graphene-Based Biosensors: Going Simple. *Adv. Mater.* **2017**, *29* (7), 1–7. https://doi.org/10.1002/adma.201604905.

(4) Kenry; Yeo, J. C.; Lim, C. T. Emerging Flexible and Wearable Physical Sensing Platforms for Healthcare and Biomedical Applications. *Microsystems Nanoeng.* **2016**, *2* (October 2015). https://doi.org/10.1038/micronano.2016.43.

(5) Stoppa, M.; Chiolerio, A. Wearable Electronics and Smart Textiles: A Critical Review. *Sensors (Switzerland)* **2014**, *14* (7), 11957–11992. https://doi.org/10.3390/s140711957.

(6) An, B. W.; Shin, J. H.; Kim, S. Y.; Kim, J.; Ji, S.; Park, J.; Lee, Y.; Jang, J.; Park, Y. G.; Cho, E.; et al. Smart Sensor Systems for Wearable Electronic Devices. *Polymers (Basel).* **2017**, *9* (8). https://doi.org/10.3390/polym9080303.

(7) Jo, G.; Choe, M.; Lee, S.; Park, W.; Kahng, Y. H.; Lee, T. The Application of Graphene as Electrodes in Electrical and Optical Devices. *Nanotechnology* **2012**, *23* (11). https://doi.org/10.1088/0957-4484/23/11/112001.

(8) Li, Z. J.; Xia, Q. f. Recent Advances on Synthesis and Application of Graphene as Novel Sensing Materials in Analytical Chemistry. *Rev. Anal. Chem.* **2012**, *31* (1), 57–81. https://doi.org/10.1515/revac-2011-0039.

(9) Eda, G.; Fanchini, G.; Chhowalla, M. Large-Area Ultrathin Films of Reduced Graphene Oxide as a Transparent and Flexible Electronic Material. *Nat. Nanotechnol.* **2008**, *3* (5), 270–274. https://doi.org/10.1038/nnano.2008.83.

(10) Turkevich, J.; Stevenson, P. C.; Hillier, J. A Study of the Nucleation and Growth Processes in the Synthesis of Colloidal Gold. *Discuss. Faraday Soc.* **1951**, *11*, 55–75. https://doi.org/10.1039/DF9511100055.

(11) Sharma, V.; Jain, Y.; Kumari, M.; Gupta, R.; Sharma, S. K.; Sachdev, K. Synthesis and Characterization of Graphene Oxide (GO) and Reduced Graphene Oxide (RGO) for Gas Sensing Application. *Macromol. Symp.* **2017**, *376* (1), 1–5. https://doi.org/10.1002/masy.201700006.

(12) Hidayah, N. M. S.; Liu, W. W.; Lai, C. W.; Noriman, N. Z.; Khe, C. S.; Hashim, U.; Lee, H. C. Comparison on Graphite, Graphene Oxide and Reduced Graphene Oxide: Synthesis and Characterization. *AIP Conf. Proc.* **2017**, *1892* (October).

https://doi.org/10.1063/1.5005764.

(13) Trusovas, R.; Račiukaitis, G.; Niaura, G.; Barkauskas, J.; Valušis, G.; Pauliukaite, R. Recent Advances in Laser Utilization in the Chemical Modification of Graphene Oxide and Its Applications. *Adv. Opt. Mater.* **2016**, *4* (1), 37–65. https://doi.org/10.1002/adom.201500469.

(14) Brownson, D. A. C.; Kampouris, D. K.; Banks, C. E. *Graphene Electrochemistry: Fundamental Concepts through to Prominent Applications*; 2012; Vol. 41. https://doi.org/10.1039/c2cs35105f.

(15) Lounasvuori, M. M.; Rosillo-Lopez, M.; Salzmann, C. G.; Caruana, D. J.; Holt, K. B. Electrochemical Characterisation of Graphene Nanoflakes with Functionalised Edges. *Faraday Discuss.* **2014**, *172* (Cv), 293–310. https://doi.org/10.1039/c4fd00034j.

(16) McCreery, R. L. Advanced Carbon Electrode Materials for Molecular Electrochemistry. *ChemInform* **2008**, *39* (41), 2646–2687. https://doi.org/10.1002/chin.200841279.

(17) Patel, A. N.; Collignon, M. G.; OConnell, M. A.; Hung, W. O. Y.; McKelvey, K.; MacPherson, J. V.; Unwin, P. R. A New View of Electrochemistry at Highly Oriented Pyrolytic Graphite. *J. Am. Chem. Soc.* **2012**, *134* (49), 20117–20130. https://doi.org/10.1021/ja308615h.

(18) Ambrosi, A.; Pumera, M. Electrochemistry at CVD Grown Multilayer Graphene Transferred onto Flexible Substrates. *J. Phys. Chem. C* **2013**, *117* (5), 2053–2058. https://doi.org/10.1021/jp311739n.

(19) Ahmadi, H. S.; Heiat, M.; Rashedi, H.; Latifi, A. M. Utilizing Different Supports and Comparing Their Performances in the Construction of Morphine Rapid Detection System Based on Lateral Flow Assay. *J. Appl. Biotechnol. Reports* **2015**, *2* (1), 199–202.

(20) Janissen, R.; Oberbarnscheidt, L.; Oesterhelt, F. Optimized Straight Forward Procedure for Covalent Surface Immobilization of Different Biomolecules for Single Molecule Applications. *Colloids Surfaces B Biointerfaces* **2009**, *71* (2), 200–207. https://doi.org/10.1016/j.colsurfb.2009.02.011.

(21) Banica, F.-G. *Chemical Sensors and Biosensors - Fundamentals and Applications*; Wiley, 2012.

(22) Baradoke, A.; Jose, B.; Pauliukaite, R.; Forster, R. J. Properties of Anti-CA125 Antibody Layers on Screen-Printed Carbon Electrodes Modified by Gold and Platinum Nanostructures. *Electrochim. Acta* **2019**, *306*, 299–306. https://doi.org/10.1016/j.electacta.2019.03.081.

(23) Costa, M. M. Da; La Escosura-Muñiz, A. De; Merkoçi, A. Electrochemical Quantification of Gold Nanoparticles Based on Their Catalytic Properties toward Hydrogen Formation: Application in Magnetoimmunoassays. *Electrochem. commun.* **2010**, *12* (11), 1501–1504. https://doi.org/10.1016/j.elecom.2010.08.018.

6.

Graphene-Semiconductor Hybrids

Introduction

In recent years, many efforts have been focused on the implementation of solution-based procedures for the synthesis of hybrid materials to be integrated in electronic and optoelectronics devices (field effect transistors (FET), photodetectors, light emitting diodes, etc.) and sensors.[12] The use of carbon-based devices, in particular graphene based ones (pristine or on its derivative forms), has widespread in this context thanks to the attractive and outstanding properties of such fascinating material. To mention some: high surface area, optical transparency in the visible and NIR spectral range, high mobility and low recombination time of charge carriers photogenerated under light illumination.[3] The high reactivity of graphene and graphene-based materials opened the venue to a large variety of strategies of hybridization by means of molecular decoration approaches. This is done in general to enhance the pristine functionalities of graphene and extending its potential applicability. In this context, the decoration of graphene with colloidal nanocrystals (NCs) is rapidly growing, since this approach is responsible for a combination of the functionalities of the carbonaceous platform with the original size-dependent properties of the nanosized inorganic matter.[4] Colloidal nanocrystals are particularly suitable in this field because they are normally surface functionalized with surfactants, whose chemistry can be tuned by implementing suitable ligand exchange procedures. Moreover, they allow to immobilize nano-objects on different surfaces and create in this way hierarchical structures [5] with outstanding and new properties from the single components, to be conveniently exploited in the final devices.[6] In recent years, the type of nanocrystals often involved in the construction of graphene-based hybrids are semiconductor materials. The general aim is to implement them in solar cells, sensors, (bio)imaging and photodetectors.[2,78–10] In such nanocomposites, thanks to the creation of a proper interface between the nanocrystals and the graphene platform, the electron coupling between the components is allowed and assisted, as well as the charge transfer process from the photo-excited NCs to the

aromatic compound. The result is a hybrid with a photoresponse ranging from visible to infrared and a conductivity increased with respect to that of bare graphene.[8,9]

The manufacturing of such objects can be done following different routes. These can be divided essentially in two main families: *ex situ* or *in situ* approaches. With the first approach, pre-synthesized highly crystalline colloidal nanocrystals are bound by means of molecular linkers to highly crystalline graphene. In this case, the synthesis of the nano-objects is done in a separated moment from the effective functionalization. With the second approach, on the contrary, the semiconductor and graphene precursors are mixed together: NCs nucleate and grow directly onto the graphene oxide platform, which can be possibly transformed into reduced graphene oxide.[11] In a different way, the *in-situ* synthesis of the nano-objects can be done directly on pre-existing graphene sheets.[10]

In the following **Chapters 6.1** and **6.2**, both the *ex situ* and the *in situ* techniques for the manufacturing of graphene-semiconductor hybrids will be considered. In the first case, CVD-graphene modified with colloidal TiO_2 NCs will be the subject, while in the second case, Reduced Graphene Oxide platform modified, in situ, by PbS colloidal NCs will be the object of the study.

Bibliography

(1) Wang, J.; Mu, X.; Sun, M.; Mu, T. Optoelectronic Properties and Applications of Graphene-Based Hybrid Nanomaterials and van Der Waals Heterostructures. *Appl. Mater. Today* **2019**, *16*, 1–20. https://doi.org/10.1016/j.apmt.2019.03.006.

(2) Koppens, F. H. L.; Mueller, T.; Avouris, P.; Ferrari, A. C.; Vitiello, M. S.; Polini, M. Photodetectors Based on Graphene, Other Two-Dimensional Materials and Hybrid Systems. *Nat. Nanotechnol.* **2014**, *9* (10), 780–793. https://doi.org/10.1038/nnano.2014.215.

(3) Bonaccorso, F.; Sun, Z.; Hasan, T.; Ferrari, A. C. Graphene Photonics and Optoelectronics. *Nat. Photonics* **2010**, *4* (9), 611–622. https://doi.org/10.1038/nphoton.2010.186.

(4) Ingrosso, C.; Bianco, G. V.; Corricelli, M.; Comparelli, R.; Altamura, D.; Agostiano, A.; Striccoli, M.; Losurdo, M.; Curri, M. L.; Bruno, G. Photoactive Hybrid Material Based on Pyrene Functionalized PbS Nanocrystals Decorating CVD Monolayer Graphene. *ACS Appl. Mater. Interfaces* **2015**, *7* (7), 4151–4159. https://doi.org/10.1021/am5081925.

(5) Niu, T.; Li, A. From Two-Dimensional Materials to Heterostructures. *Prog. Surf. Sci.* **2015**, *90* (1), 21–45. https://doi.org/10.1016/j.progsurf.2014.11.001.

(6) Curri, M. L.; Comparelli, R.; Striccoli, M.; Agostiano, A. Emerging Methods for Fabricating Functional Structures by Patterning and Assembling Engineered Nanocrystals. *Phys. Chem. Chem. Phys.* **2010**, *12* (37), 11197–11207. https://doi.org/10.1039/b926146j.

(7) Lü, K.; Zhao, G. X.; Wang, X. K. A Brief Review of Graphene-Based Material Synthesis and Its Application in Environmental Pollution Management. *Chinese Sci. Bull.* **2012**, *57* (11), 1223–1234. https://doi.org/10.1007/s11434-012-4986-5.

(8) Konstantatos, G.; Badioli, M.; Gaudreau, L.; Osmond, J.; Bernechea, M.; Garcia de Arquer, F.; Gatti, F.; Koppens, F. Hybrid Graphene-Quantum Dot Phototransistors with Ultrahigh Gain. *Nat. Nanotechnol.* **2012**, *7* (6), 363–368. https://doi.org/10.1038/nnano.2012.60.

(9) Huang, Y. Q.; Zhu, R. J.; Kang, N.; Du, J.; Xu, H. Q. Photoelectrical Response of Hybrid Graphene-PbS Quantum Dot Devices. *Appl. Phys. Lett.* **2013**, *103*, 143119.

(10) Bi, H.; Huang, F.; Liang, J.; Xie, X.; Jiang, M. Transparent Conductive Graphene Films Synthesized by Ambient Pressure Chemical Vapor Deposition Used as the Front Electrode of CdTe Solar Cells. *Adv. Mater.* **2011**, *23* (28), 3202–3206.

(11) Cao, A.; Liu, Z.; Chu, S.; Wu, M.; Ye, Z.; Cai, Z.; Chang, Y.; Wang, S.; Gong, Q.; Liu, Y. A Facile One-Step Method to Produce Craphene-CdS Quantum Dot Nanocomposites as Promising Optoelectronic Materials. *Adv. Mater.* **2010**, *22* (1), 103–106. https://doi.org/10.1002/adma.200901920.

6.1 CVD-Graphene/PBA-TiO_2 NCs Hybrids

Focus

Objects of the study of this Chapter are hybrids based on graphene and titanium dioxide nanocrystals. The excellent properties of graphene have been already discussed in the Introduction of **Chapter 5** and **6.** For what concern TiO_2, already involved in another hybrid in this Thesis Project (see **Chapter 4**), it is a high band gap semiconductor, widely used in electrochemical sensors, solar cells and photocatalytic systems for its low toxicity, optical transparency, low cost, biocompatibility, photostability and for its photocatalytic and photoelectrochemical activity.[1,2]

Colloidal nanocrystals (NCs), prepared by means of solution-based colloidal chemistry routes, are functional nano-objects, exhibiting unique size- and shape-dependent properties, extremely flexible for chemically decorating graphene, and hence, for transferring to it the functionalities of the inorganic nano-sized matter, promising for advanced technological applications.[3,4] The surface of the colloidal NCs is here coated by surfactant molecules, whose chemistry can be modified by means of surface functionalization procedures for modulating interactions of the nano-objects towards specific surfaces or other nanostructures.

The synergistic combination of the properties of the TiO_2 NCs with those of carbon based nanostructured compounds has been found to provide hybrid materials with enhanced electrical conductivity, photoelectrical conversion efficiency, photocatalytic properties and environmental stability.[5] Indeed, on one side, the charge scavenger property of carbon based compounds decreases the recombination rate of photogenerated hole-electron pairs in TiO_2, and on the other hand, the photoexcited charges transferred to the carbon nanostructure improve its charge transport properties due to charge trap screening and doping effects.[6] The interface

between graphene and TiO_2 NCs is expected to play an essential role in determining the electron coupling of the components.[7]

In this part of the PhD Thesis work, CVD-grown graphene systems decorated with colloidal TiO_2 nanocrystals are the hybrid materials under investigation. The hybrids are synthesized with particular attention on the number of graphene layers, from monolayer to pentalayer, and on the effect that these differences in the carbonaceous platform have on the electrochemical performances of the final device. In particular, starting from a previous work focused on the structural and electrochemical differences between monolayer and bilayer graphene,[7] the research is here expanded on the study of tri- and penta-layer graphene. It is known, in fact, that the properties of graphene, especially its electrochemistry, are strictly dependent from its number of layers. From five layers of graphene, it is more likely to have a graphite-like structure instead of graphene, with a strong difference in the ratio between basal and edge planes with respect to the single-layered graphene hybrids, reflecting in different sensing and catalytic activities.

The application of these materials as photoanode, at first, and in general as electroanalytical sensors for neurotransmitters (dopamine, norepinephrine) are finally the topic of this Chapter. For more details on the interest about the detection and the properties of such analytes, see **Chapter 5.1**.

Materials and Methods

Chemicals

For the synthesis of the hybrid materials, oleic acid (OLEA, 90%), titanium tetraisopropoxide ($Ti(OiPr)_4$ or TTIP, 98.9%) and trimethylamino-N-oxide dehydrate (TMAO, 98%) were purchased from Fluka. 1-Pyrene butyric acid (PBA), methanol and chloroform were purchased from Aldrich. All the reagents were used as the highest purity available and as received.

For the electrochemical characterizations and applications, $NaClO_4$ (ACS reagent, ≥98%), $[Ru(NH_3)]Cl_6$ and $K_4[Fe(CN)_6]$ were purchased by Sigma Aldrich. Phosphate Buffer Solution was prepared from Na_2HPO_4 (Sigma Aldrich) and KH_2PO_4 (J. T. Baker Chemicals B.V., Denver, Holland). Dopamine Hydrochloride was purchased from Fluka, L-norepinephrine (≥98%) and Ascorbic acid were purchased from Aldrich.

(OLEA)-TiO_2 NCs synthesis

The synthetic procedure to produce TiO_2 nanocrystals involved dried and degassed reactants and it was conducted under N_2 atmosphere, at low temperature (80-100 °C).[8] The TiO_2 precursor (TTIP) hydrolysis was conducted in the presence of the surfactant OLEA, in ethylene glycol and with the addition of TMAO base as catalyst for the polycondensation reaction. The as-prepared TiO_2 nanocrystals coated with OLEA were isolated from the reaction mixture by precipitation with methanol and were finally dispersed in chloroform in order to obtain optically transparent solutions.[7]

(PBA)-TiO_2 NCs synthesis

The previously prepared OLEA-TiO_2 nanocrystals were washed repeatedly with methanol in order to remove the excess of OLEA surfactant coordinating the NCs surface. Then, a chloroform solution of PBA was added to the washed TiO_2 NCs ($5\ 10^{-2}$ M, in a 1:5 TiO_2:PBA molar ratio) and left stirring overnight. After that, the NCs

were washed with methanol to remove the excess aromatic ligand and then dispersed again in chloroform. The obtained transparent solution of PBA-TiO_2 NCs (in a concentration of 10^{-3} M) is stable over months without further addition of PBA molecules.

Grown of Graphene via Chemical Vapour Deposition (CVD) technique and functionalization with (PBA)-TiO_2 NCs

Monolayer graphene with 50–110 mm^2 grain sizes was grown by CVD on 25 mm thick copper foils (Alfa Aesar, item no. 13382) in a typical quartz tube CVD reactor at 1000 °C using CH_4/H_2 as precursors. The prepared graphene was then transferred onto 300 nm SiO_2/Si or ITO/glass substrates by using a thermal release tape and an aqueous solution of ammonium persulfate (0.1 M) as copper etchant. Before graphene transfer, the SiO_2/Si substrates were treated with O_2 plasma for improving adhesion.

Bilayer graphene samples were fabricated by transferring an additional graphene layer onto the monolayer graphene. In the same way, tri-, quadri- and penta-layer graphene were synthesized simply by repeating the CVD procedure three, four and five times, respectively. All graphene samples were dipped in a toluene/ethanol/anisole (1/1/1) solution for removing any organic impurities of thermal tape traces.

CVD grown graphene on SiO_2/Si substrate or on ITO was incubated in a 10^{-3} M chloroform solution of PBA-TiO_2 NCs for 48 h and finally rinsed with chloroform to remove NCs not specifically adsorbed.

Physico-Chemical Characterizations

- **UV-Vis** absorption spectra were recorded using a Cary 5000 (Varian) UV/Vis/NIR spectrophotometer. All optical measurements were performed at room temperature.

- **Mid-infrared** spectra were acquired with a Varian 670-IR spectrometer equipped with a deuterated triglycine sulphate (DTGS) detector. The spectra resolution used for all experiments was 4 cm^{-1}. For ATR measurements (attenuated total reflection), the internal reflection element was a one-bounce 2 mm diameter diamond microprism. The solution or suspension of interest (3-5 μL) was casted directly onto the internal reflection element, on the upper face of the diamond crystal.
- **Raman** spectra were collected using a Lab-RAM HR Horiba-Jobin Yvon spectrometer with a 532 nm excitation laser source. The measurements were carried out under ambient conditions at a low laser power (1 mW) to avoid laser-induced damage. The Raman band recorded from a silicon wafer at 520 cm^{-1} was used to calibrate the spectrometer and the accuracy of the spectral measurements was estimated to be 1 cm^{-1}.
- **Transmittance** spectra of CVD graphene as bare and modified with PBA and PBA-TiO_2 NCs were recorded by means of an optical setup composed of a white light source, a light collecting system and an optical spectrometer (HR4000, Ocean Optics).
- **Transmission Electron Microscopy (TEM)** analyses were performed by using a Jeol Jem-1011 microscope, operated at 100 kV. The TEM images were acquired using a Quemesa Olympus CCD 11 Mp Camera. The TEM images of organic-coated TiO_2 NCs were collected by dipping a 300 mesh amorphous carbon-coated Cu grid in chloroform solutions of TiO_2 NCs and leaving the solvent to evaporate. Statistical analyses of the size (NP average size and size distribution) of the samples were performed using a freeware ImageJ analysis program. At least 150 NCs were counted for each sample.
- **Scanning Electron Microscopy (SEM)** analyses (in particular, Field-Emission SEM) were performed by using a Zeiss Sigma microscope operating in the range of 0–10 keV and equipped with an in-lens secondary electron detector and an INCA Energy Dispersive Spectroscopy (EDS)

detector. Samples were mounted onto stainless-steel sample holders using double-sided carbon tape and ground with silver paste.

- **Atomic Force Microscopy (AFM)** phase mode and topography were performed by means of a PSIA XE-100 SPM system in air and at room temperature, in tapping mode. A silicon SPM sensor for noncontact AFM (Park Systems), having a spring constant of 42 N m^{-1} and a resonance frequency of 330 kHz, was used. Micrographs were collected on six distinct areas of samples, with a scan size area of 5 mm x 5 mm, by sampling the surface at a scan rate between 1.0 and 0.5 Hz and a resolution of 256 x 256 pixels. The AFM topography images were processed by using XEI software to obtain statistical data.
- **Electrical measurements** were carried out using a four-probe contact geometry in the van der Pauw configuration on a sample area of 4 x 4 mm^2 using a fully automated Hall system (MMR Technologies, Inc.).

Electrochemical Measurements

- **Electrochemical characterizations** were carried out using an Autolab PGStat 30 (EcoChemie, Utrecht, The Netherlands) potentiostat/galvanostat equipped with the Software Nova 2.0 (Metrohm Autolab). All the measurements were done in a conventional three-electrode cell equipped with a Saturated Calomel Electrode (SCE) and a Platinum wire as Reference (RE) and Counter (CE) electrodes, respectively. The working electrode (WE) was a modified ITO glass with the CVD graphene (as bare or functionalized with the PBA-TiO_2 NCs). An aqueous solution with 0.1 M $NaClO_4$ was chosen as supporting electrolyte and $[Ru(NH_3)]Cl_6$ and $K_4[Fe(CN)_6]$ were the selected redox probes for the characterization of the materials. Cyclic Voltammetry (CV) was performed by scanning the potential in different potential ranges (by changing the probe and the materials) with a step of 5

mV at different voltage scan rates (form 0.01 V s^{-1} to 0.750 V s^{-1}). Electrochemical Impedance Spectroscopy (EIS) was performed at different potentials in the presence and in the absence of the redox probes. Frequencies were varied between 650000 and 0.1 Hz and a sinusoidal potential curve with an amplitude of 10 mV was applied in all cases. All the impedance data were processed by using Z-View 3.1 software.

- **Photocurrent measurements** were performed (on the mono- and bi-layer graphene) using a UV Jelosil HG500 iron halogenide lamp, having a power density of 45 mW cm^{-2}, placed at a distance of 40 cm from the sample. All the measurements were carried out in a N_2 atmosphere after having degassed the cell with nitrogen flux for at least 10 minutes. The procedure was in accordance with the method already optimized in the literature, used also to treat the photocurrent transients and extract the time values τ for charge recombination processes.[9,10]
- **Electroanalytical Applications:** Cyclic voltammograms were registered, in Phosphate Buffer solution (PBS), at a physiological pH of 7.4, at 100 mV s^{-1}. Dopamine hydrochloride (Fluka) and L-norepinephrine hydrochloride (Sigma, ≥ 98.0%) were used as analytes. Ascorbic acid (Sigma) was chosen as interferent for dopamine determination.

Results and Discussion

Synthesis and Morphological Characterizations

The synthesis of the OLEA-TiO_2 NCs was carried out by following a known procedure already reported in [8] and then, the surface was modified *via* a ligand exchange with 1- pyrenebutirric acid. The schematic representation of the synthesis is reported in **Figure 6.1.1**. The choice of PBA as capping agent was done because this surfactant is expected to connect the nanocrystals to the graphene platform *via* π–π stacking interactions and concomitantly to coordinate the NCs surface by means of its end carboxylic moieties.[7]

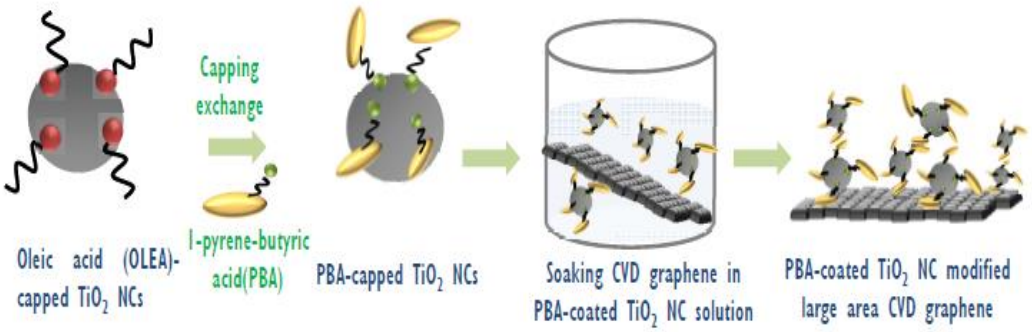

Figure 6.1.1: Schematic representation of the synthetic procedure of the G/PBA-TiO_2 NCs hybrids.

The morphological and optical characterizations of the material were done before and after the ligand exchange, in order to assess the effectiveness of this procedure to modify the surface chemistry of the nanocrystals and any possible change in their spectroscopic and structural properties. It was verified that both the morphology and the spectroscopic characteristics of the NCs were preserved after the ligand exchange with PBA. The PBA-TiO_2 nanocrystals resulted to be spherical in shape and about (6.0 ± 0.3) nm. All the morphological and optical characterizations, as already mentioned in the introduction of the Paragraph (see Focus) were already performed and reported in [7]. The electrochemical characterizations will be discussed deeper, because the ones relative to mono- and bi-layer graphene were the starting point for the study of the other materials (tri and penta-layer), serving as reference and confirmation of hypothesis.

Mono- and Bi-layer Graphene: (Photo) Electrochemical Characterizations

Four different ITO glass modified electrodes have been (photo)electrochemically characterized and applied in the field of electroanalytical sensing:

1) CVD-grown monolayer graphene (hereafter in the graph shortened as 1G);

2) CVD-grown bilayer graphene (hereafter in the graph shortened as 2G);

3) CVD-grown monolayer graphene decorated with PBA-TiO_2 NCs (1G + TiO_2);

4) CVD-grown bilayer graphene decorated with PBA-TiO_2 NCs (2G + TiO_2).

At first, Cyclic Voltammetry was performed in the dark, in the absence of any redox probe, in order to see the background behaviour of each working electrode. It was found that the immobilized TiO_2 NCs affect the anodic potential window limit of graphene, anticipating the oxidation of the medium. Such a down-shift of the anodic potential (ca. 0.16 V) can be reasonably ascribed to the shift of the graphene Fermi level ΔE_F of ca. 0.17 eV, verified also by Hall measurements. This shift of the graphene Fermi level is due to the enrichment of holes transferred from the nanocrystals to graphene, which makes the oxidation of the medium more energetically favorable.[7]

Then, cyclic voltammetry profiles have been recorded in the presence of an outer- and an inner-sphere redox probe, namely $[Ru(NH_3)_6]Cl_3$ and $K_4[Fe(CN)_6]$, respectively. The outer sphere redox probe is expected to react only with the electronic density of state of the electrode, while the inner sphere one is expected to show changes also related to the electrode surface structure.[11–15] These experiments were done, in fact, in order to study the electron transfer and the structural properties of the prepared hybrid material based working electrodes. **Figure 6.1.2** reports the voltammograms of the different electrodes in the presence of the $K_4[Fe(CN)_6]$ redox probes, since with $[Ru(NH_3)_6]Cl_3$ no great differences were highlighted among the electrode platforms, which seems to behave like a macroelectrode.[7] The absence of

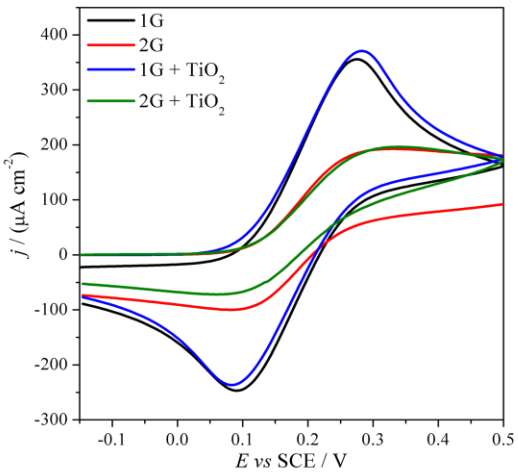

Figure 6.1.2: CV in 0.1 M $NaClO_4$ of the bare and NCs-modified graphene electrodes in the presence of 3 mM $K_4[Fe(CN)_6]$, recorded at 100 mV s^{-1}.

any difference among the four electrodes is a confirmation of the outer sphere character of the redox probe. On the contrary, in the presence of $K_4[Fe(CN)_6]$, monolayer and bilayer graphene electrodes show a different electrochemical behavior. Monolayer graphene (dark line) presents a peak-shaped curve typical of the electrochemically inert side basal plane of a high quality and almost "perfect" monolayer graphene.[16,17] Bilayer graphene (red line), instead, present a step-shaped curve, explained by the sensitivity of the probe to the electroactive carbon-oxygen functionalities located at the edge plane-like sites/defects of the separated graphitic island, which grow on the underlying continuous monolayer graphene film. These islands are responsible for a convergent diffusion mechanism of the redox probe molecule to the electrode surface and result in the observed sigmoidal cyclic voltammograms, typical of an "*array of microelectrodes*" (See **Chapter 2** for theoretical explanation and **Figure 6.1.3** for a schematic representation).

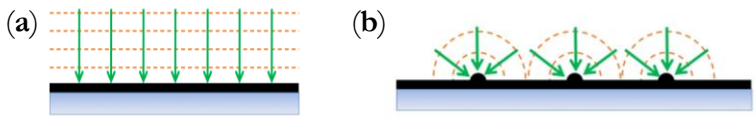

Figure 6.1.3: Schematic representation of the current lines in the case of planar (**a**) and convergent (**b**) diffusion at the electrode platform, observed for monolayer (**a**) and bilayer (**b**) graphene. Adapted with permission, Copyright 2017, Royal Society of Chemistry.[7]

The immobilization of the nanocrystals does not lead to any modification neither in the line shape, nor in the current densities (green line for the modified monolayer and blue line for the modified bilayer), being another confirmation of the fact that

the decoration procedure does not lead to structural defects on the graphene platform.

Electrochemical Impedance Spectroscopy was also recorded and supports the hypothesis previously explained from cyclic voltammetries. **Figure 6.1.4 (a)** reports the Bode phase plots of the different electrodes in 0.1 M $NaClO_4$, at -0.1 V, in the absence of any redox probe. The relative equivalent circuits, extrapolated by a data fitting with the Software ZView 3.1, are reported in **Figure 6.1.4 (b)**.

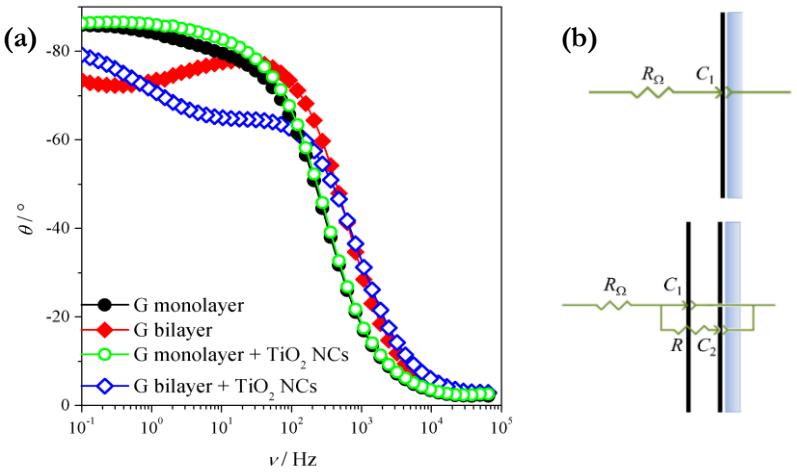

Figure 6.1.4. (**a**) Bode-phase plots of modified ITO glass working electrodes registered at -0.1 V. (**b**) Monolayer (on the top) and bilayer (on the bottom) graphene equivalent circuits used to fit the EIS spectra. Adapted with permission, Copyright 2017 ©, Royal Society of Chemistry.[7]

What it can be immediately seen is that also in this case, monolayer and bilayer graphene electrodes behave differently. In the case of monolayer, a sigmoidal EIS curve is registered, while a peak-shaped curve is obtained in the case of bilayer graphene. The equivalent circuit for monolayer graphene is based on a resistance R_Ω of the solution, in series with a capacitance C_1 (Constant Phase Element). This last capacitance is attributed to the "Debye layer", that is an accumulation of ions in proximity of the electrode, which behaves like a parallel-plate capacitor and occurs for compensating the charge accumulated at the graphene surface. Conversely, the equivalent circuit of bilayer graphene based electrodes (on the bottom of **Figure 6.1.4 (b)**) presents, in parallel with the interfacial capacitance C_1, a resistance R, which

originates mostly from the turbostratic regions, that are the graphitic islands of the second layer of graphene which are not aligned with the underlying monolayer graphene basal planes. Such a misalignment leads to the occurrence of a contact resistance *R* between the graphene layers that can vary by more than one order of magnitude, depending on the angular alignment of the two graphene lattices.[18] In addition, in series with such a contact resistance *R*, the circuit presents also a capacitance C_2, originated from the charge separation between the two graphene layers of the turbostratic regions. A more detailed explanation on the nature and the values of these capacitances, divided in two contributions (C_H and C_Q)[19] acting in an opposite way, is reported in [7].

Photocurrent experiments were also performed on the different electrodes, in 0.1 M $NaClO_4$, at a bias voltage of +1 V (SCE), irradiating with a UV light source (λ = 365 nm). In all cases, as shown in **Figure 6.1.5**, an anodic photocurrent is registered, meaning that the oxidation of the medium is occurring with the concomitant transfer of the photogenerated electrons from the photoanode to the ITO supporting electrodes. The bare graphene based working electrodes have a photocurrent signal originated from the π-π* transition of the graphene C=C bond[20] occurring under UV light. In particular, the bilayer graphene shows a photocurrent density higher than that of the monolayer, namely 0.30 μA cm^{-2} against 0.15 μA cm^{-2}. This is explained by the linear increase of the broadband absorption of graphene increasing the number of layers. With the immobilization of the PBA-coated TiO_2 NCs on graphene, the working electrodes show an improvement of the photocurrent density. Such a finding is

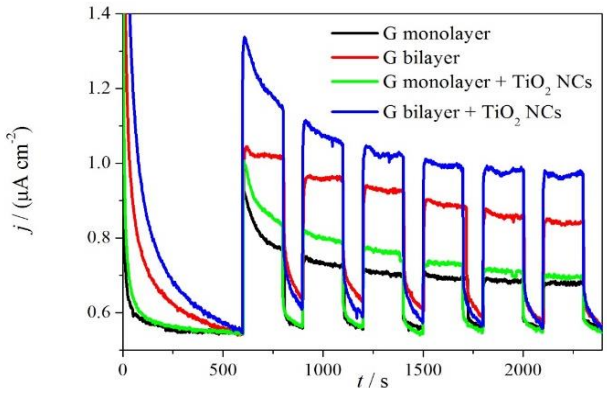

Figure 6.1.5: Photocurrent measurements on the four different working electrodes. Adapted with permission, Copyright 2017 ©, Royal Society of Chemistry.

particularly evident in the case of the functionalized bilayer graphene, which shows a photocurrent density increased up to 0.45 μA cm^{-2}. This result is ascribed to the intrinsic UV light activity of the TiO_2 NCs film, that provides generation and separation of electron-hole pairs, that are then transferred to graphene thanks to the pyrene mediated electron coupling. Indeed, pyrene linker stabilizes the photoelectrons by its π-ring system and transfers them to graphene where they are stored in the huge π-π network of the aromatic platform. In addition, the Fermi level of graphene lies in between the conduction band of TiO_2 and that of ITO, and hence it decreases the injection barrier at the ITO/TiO_2 NCs interface. Finally, graphene, behaving as a charge acceptor and fast transporter, facilitates further photoelectron withdrawn from the nano-oxide film to the ITO supporting electrode, suppressing both hole/electron recombination processes at the defect states of the nanocrystalline oxide film and back reactions at the interface with the electrolyte, thus resulting in an increase of the photocurrent.

Tri- and Penta-layer Graphene: Electrochemical Characterizations

The interesting features derived from the study of mono and bi-layer graphene moved the attention in the investigation of multilayer graphene platforms (from three to five layers). The interest was again in the understanding of any structural difference in the electrode surface and the relative difference in the electrochemical response towards selected redox probes and analytes.

Also in this case, the electrodes were tested in the presence of an *inner-sphere* and *outer-sphere* redox probes (namely, $K_4[Fe(CN)_6]$ and $[Ru(NH_3)_6]Cl_3$). As already observed for mono and bilayer, in the presence of the outer sphere redox probe the electrodes, both bare and modified with TiO_2 NCs, do not show any relevant differences (**Figure 6.1.6 (a)**). In fact, they present the same peak-shape and peak-position. The only difference is in the current density values (normalized, like in any case, for the geometrical area of the electrodes), which decrease passing from 3G to 5G

electrodes. This effect could be related to the effective nature of the graphene materials. Passing from 3G to 5G, in fact, the graphene behaviour is changing to a graphitic one. It is known that graphene is more conductive than graphite and that is verified by an increased current toward the probe ($j_{(3G)} > j_{(5G)}$). The correspondent modified electrodes with titania possess density current values that are lower than the related bare graphene platforms ($j_{(3G + TiO2)} < j_{(3G)}$ and $j_{(5G + TiO2)} < j_{(5G)}$). This could be ascribed to the intrinsic semiconductive character of TiO_2 NCs, which could mask a bit the highly conductive character of the bare graphene. The fact that no differences in the position of the oxidation and reduction peaks of the probe are present is a confirmation of the *outer-sphere* behaviour of the probe, which remains insensitive to the surface structure of the electrodes.

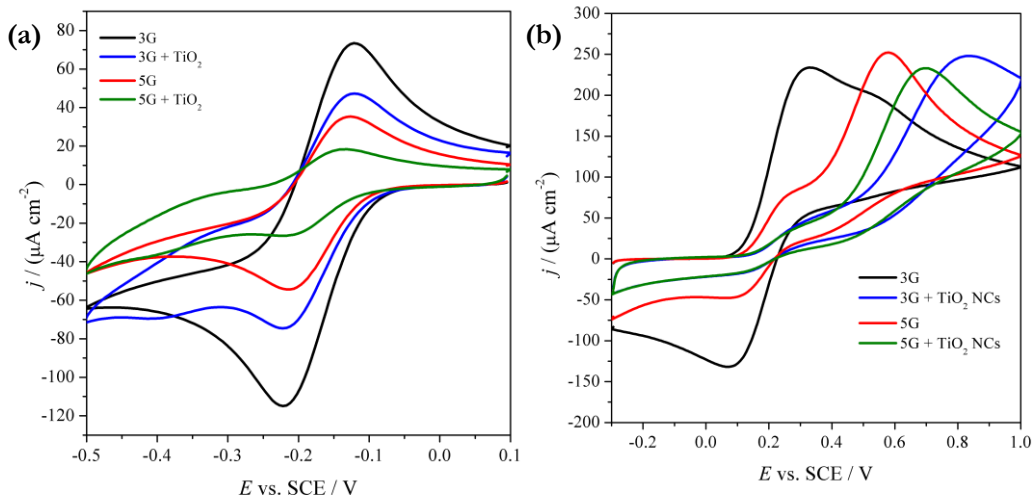

Figure 6.1.6: CVs at 100 mV s^{-1} in the presence of 3 mM of $[Ru(NH_3)_6]Cl_3$ (**a**) and $K_4[Fe(CN)_6]$ (**b**) for bare and modified tri-layer and penta-layer graphene electrodes.

On the contrary, in the case of $K_4[Fe(CN)_6]$, huge differences among the electrodes can be found (**Figure 6.1.6 (b)**). In more details, focusing at first on the behaviour of bare tri- and penta-layer graphene (3G and 5G), the presence of two signals in the oxidation scan can be observed: a first peak, at about +0.3 V (SCE), more marked for the tri-layer graphene, and a second one, at about +0.6 V (SCE), more marked for the penta-layer graphene. These signals could be representative of two different active sites of graphene, on which the redox probe could react, and in general are the

proof of having an inhomogeneous surface. It seems that tri-layer graphene possesses a higher concentration of edge plane-like sites, which are known to present an electrocatalytic effect, while penta-layer has a higher concentration of basal plane sites (less reactive). This could be due to the fact that the repeated cycles of CVD (from three to five) lead to a covering of some defects and to the creation of a sort of "graphitic" structure for the penta-layer, which presents a less-defective surface with a lower amount of electroactive sites. Another explanation could be also given by reasoning from an energetic point of view. In more details, tri-layer graphene has the tendency to receive electrons (from the redox probe in solution, which is undergoing an oxidation reaction and so it is donating its electrons to the electrode platform) at lower potential with respect to penta-layer. This could be explained by the fact that, passing from few layers of graphene to more layers the conduction pass from being through electrons and holes (ambipolar) to only electrons. It is likely that penta-layer graphene is more charged with electrons with respect to tri-layer and then it is less available to receive more electrons from the external and that is why the oxidation of the probe occurs (with higher intensities) at higher potentials. It could be that passing from tri-layer to penta-layer the energy to let the probe oxidized is growing because the charge transfer probe/graphene is changing. Further investigations on the electron transfer rate and on the energy levels will be done in order to clarify this aspect. As previously mentioned, tri-layer graphene is expected to have an ambipolar behaviour while penta-layer is more likely a graphitic electrode. The ambipolar effect could be linked also to the presence of a more marked reversibility in the case of tri-layer than in the case of penta-layer, in which the reduction peak of the reverse scan is less marked than the one of tri-layer.

Regarding the modified graphene platform with PBA-TiO_2 NCs, the electrochemical behaviour is different from the relative bare graphene. In fact, in these cases, both tri-layer and penta-layer present the same voltammetric shape, shifted at higher potentials with respect to the one of the un-modified graphene electrodes. The presence of a unique peak could be related to a "patching effect" played by the

pyrene linkers of TiO_2 NCs, which cover the defects of the bare graphene platform and create a sort of homogeneous surface for both tri-layer and penta-layer without showing structural difference among the two.

Table 6.1.1 lists all the capacitance values (*C*) derived from the characterization on the background. For more details on how the electrochemical characterization was carried out see **Chapter 8 (Appendix)**. For what concern bare electrodes, the *C* values are equals (considering the error), while they differ when the electrodes are functionalised with titania nanocrystals: they are higher than the correspondent bare platforms and they increase passing from three layers to five layers. This effect could be explained again by the "patching" played by the pyrene linkers of the nanocrystals, which act as an additional carbonaceous film and help to create a more "perfect" platform that here act as a more performant capacitor.

Table 6.1.1: Capacitance values of the multilayer graphene platforms derived from the elaboration of the data on the background

	***C* / μF**
3G	(2.96 ± 0.07)
3G + TiO₂	(5.45 ± 0.04)
5G	(2.85 ± 0.08)
5G +TiO₂	(8.5 ± 0.1)

From the characterization in the presence of the redox probes the other parameters, listed in **Table 6.1.2** are derived. In case of potassium ferrocyanide, in which the presence of two different oxidation peaks was observed, the elaboration was conducted on the first peak. In more details, α values are derived from the slope of the log(*i*) *vs* log(*v*) curve (see for more details on the elaboration of the electrochemical data **Chapter 8: Appendix**). The deviation from the 0.5 value, expected for processes that undergo a perfect linear diffusive behaviour, is responsible for the instauration of other diffusional mechanisms of the probe toward the electrode, probably related to the highly defective surface structure of the

different electrodes. It is interesting to notice that, passing from the bare graphene (3G, 5G) to the TiO_2 modified ones (3G + TiO_2, 5G + TiO_2), the related α values decrease a bit, meaning that the surface functionalization reflects also in a different electrochemical response (in terms of diffusional mechanism) of the probe toward the electrodes. In general, a deviation from the 0.5 value, responsible of a perfect linear diffusion of the probe toward the electrode, is registered. This effect means that different diffusional mechanisms are present for all the platforms, maybe convergent diffusion or thin layer diffusion effects. For sure, the fact that the results are strongly different from an electrode to the other are another confirmation of the different surface morphology of these systems. The scan-rate dependence of the distance between the anodic and cathodic peaks (*ΔEp*) and the values of the peak width at half height ($E_p - E_{p/2}$) are indicative of a process that is moving towards electrochemical irreversibility. For a comparison, the *ΔEp* registered for all the materials at a scan rate equal to 0.1 V s^{-1} is reported in brackets. It is clear how the materials modified with titania nanocrystals (3G + TiO_2 *vs* bare 3G and 5G + TiO_2 *vs* bare 5G) show a more electrochemical reversible behaviour (the *ΔEp* values are lower). This trend is verified with both the redox probes even if with a more rational way in the case of ruthenium hexaamminochloride.

In the case of the electrochemical characterization in the presence of $[Ru(NH_3)_6]Cl_3$, α values are definitely closer to the 0.5 for a perfect linear diffusion, attesting again the insensibility of this probe to the electrode surface diversity among the samples.

Table 6.1.2: Statistical parameters derived from the electrochemical characterization of the multilayer graphene platforms. *ΔEp* values at 0.1 V s^{-1} are reported in brackets.

$K_4[Fe(CN)_6]$			
	α	***ΔE_p / V***	***$(E_p - E_{p/2})$ / V***
3G	(0.34 ± 0.02)	*Scan Rate Dependent* (187 mV)	*Scan Rate Dependent*
3G + TiO_2	(0.30 ± 0.03)	*Scan Rate Dependent* (146 mV)	*Scan Rate Dependent*
5G	(0.34 ± 0.02)	*Scan Rate Dependent* (227 mV)	*Scan Rate Dependent*
5G +TiO_2	(0.16 ± 0.03)	*Scan Rate Dependent* (121 mV)	*Scan Rate Dependent*

$[Ru(NH_3)_6]Cl_3$			
	α	ΔE_p / V	$(E_p - E_{p/2})$ / V
3G	(0.481 ± 0.007)	*Scan Rate Dependent* (101 mV)	*Scan Rate Dependent*
3G + TiO₂	(0.46 ± 0.01)	*Scan Rate Dependent* (81 mV)	*Scan Rate Dependent*
5G	(0.48 ± 0.01)	*Scan Rate Dependent* (76 mV)	*Scan Rate Dependent*
5G +TiO₂	(0.51 ± 0.02)	*Scan Rate Dependent* (60 mV)	*Scan Rate Dependent*

All these electrodes were then characterized by Electrochemical Impedance Spectroscopy, in the absence and in the presence of the $K_4[Fe(CN)_6]$ redox probe, which is the one capable to give information about the electrode surface structure, as already evidenced from the results gained from the Cyclic Voltammetries. **Figure 6.1.7 (a)** and **(b)** present the Complex Plane and Bode Phase plots of the different materials registered at -0.1 V (SCE) in a background solution of 0.1 M $NaClO_4$, respectively. These proofs were done in order to have a comparison with the results previously reported for the mono and bilayer systems (**Figure 6.1.4**). The related equivalent circuits, gained by using the Software ZView, are shown in **Figure 6.1.8**.

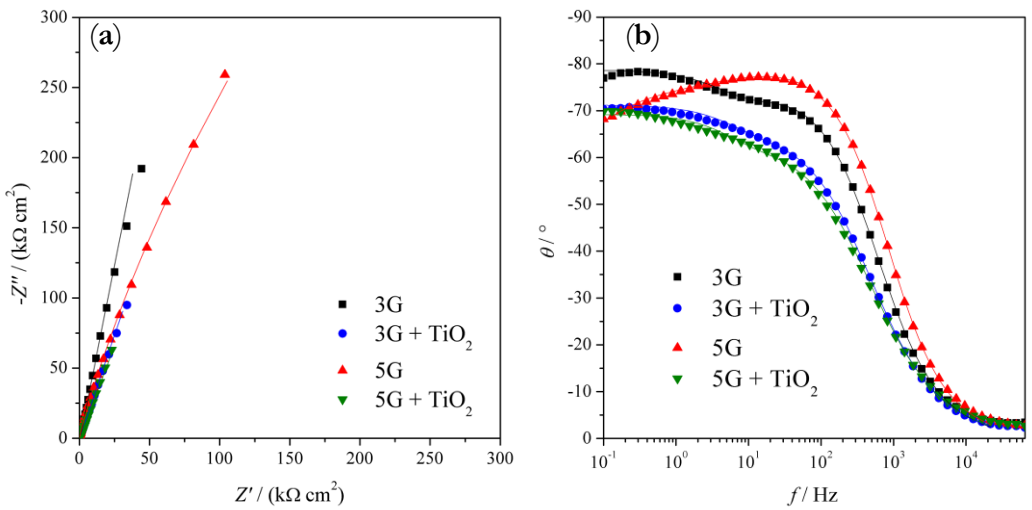

Figure 6.1.7: (**a**) Complex Plane plot at -0.1 V of the hybrid materials recorded in 0.1 M $NaClO_4$ as supporting electrolyte. (**b**) Analogous Bode plots.

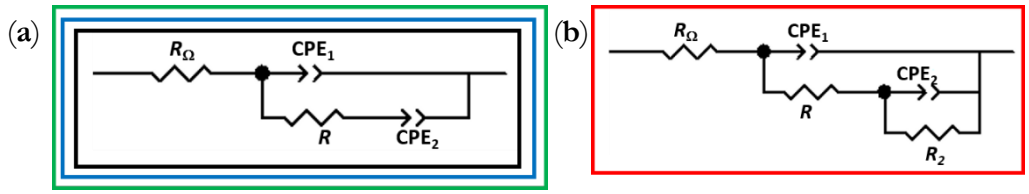

Figure 6.1.8: Equivalent circuits for (**a**) 3G, 3G +TiO_2, 5G + TiO_2 and (**b**) 5G systems. $\boldsymbol{R_\Omega}$ = cell resistance, $\mathbf{CPE_1}$ = "Debye Layer" capacitance (Constant Phase Element), $\boldsymbol{R}$ = contact resistance (from the turbostratic region), $\mathbf{CPE_2}$ = charge separation capacitance (Constant Phase Element), $\boldsymbol{R_2}$ = additional resistance. *Colors of the squares around the circuits are related to the colors of the lines and dots in the EIS spectra.*

As it can be immediately seen, comparing the results with the ones of **Figure 6.1.4**, all the materials behave like the bilayer system, being again different from the simple monolayer graphene. In more details, the addition of a Resistance (R_1) and a Capacitance (CPE_2) to the single RC circuit of the monolayer is addressed to the presence of defects originated at the turbostratic regions. These are a consequence of the mismatch between the different graphene layers, which are not perfectly superimposed and can create wrinkles, edges, steps and so on. In the case of pentalayer graphene (5G), another additional resistance (R_2) is present. This could be related to the highly graphitic structure of the material, which becomes less conductive. This effect is less evident for the 5G + TiO_2 material, thanks to the patching effect played by the nanocrystals already discussed in the Paragraph. 5G + TiO_2 is behaving like a less defective graphite, as also the "α_2" values related to each system suggest (see **Table 6.1.3**). This parameter is indicative of the deviation from the ideal and pure capacitor of a CPE element. The more α is closer to 1, the more the material behaves as a pure capacitor. If α is far from the unit, a defective surface can be reasonably imagined. The related Capacitance values (CPE_1) are in accordance with what previously observed for the mono and bilayer materials and stated in [7]. Briefly, the total Capacitance is the final sum of two contributions: the Helmoltz layer capacitance (C_H) and the quantum capacitance (C_Q), intrinsic to graphene.[19] These components act in an opposite way, since C_H decreases while C_Q rises with the

increasing number of layers, resulting in a total capacitive behaviour presenting a maximum for intermediate layers. Moreover, C_Q is strongly influenced by the carrier density of graphene and so, in this case, by the p-doping TiO_2 nanocrystals. The final balance, in the case of 1G and 2G systems, was the prevailing C_H contribute in the case of bare graphene and C_Q in the case of the functionalized systems. For multilayer systems, it is happening the same, since the total capacitance is decreasing passing from bare 3G to 5G, while it is increasing passing from 3G + TiO_2 to 5G + TiO_2 (see **Table 6.1.3**).

Table 6.1.3: EIS mathematical parameters from the fitting of the spectra at -0.1 V on the background solution of 0.1 M $NaClO_4$.

	R_Ω (Ω cm^2)	CPE$_1$ (μF cm^{-2} s$^{\alpha-1}$)	α_1	R (kΩ cm^2)	CPE$_2$ (μF cm^{-2} s$^{\alpha-1}$)	α_2	R_2 (MΩ cm^2)
3G	115	6.85	0.87	26.2	0.966	0.93	-
3G + TiO_2	141	13.9	0.78	17.9	1.24	0.90	-
5G	113	3.76	0.90	55.5	1.64	0.62	2.95
5G + TiO_2	117	20.5	0.76	13.3	1.89	0.90	-

Concerning the resistance (R) values (**Table 6.1.3**), the more disordered materials (bare 3G and 5G) are more resistive than the related functionalized ones (3G + TiO_2) and (5G + TiO_2).

For what concern the experiments in the presence of the redox probe, the EIS spectra were registered at two different voltage values, namely +0.25 V and +0.6 V (SCE). At these values, in fact, different behaviours for the materials were highlighted in the CVs (see **Figure 6.1.6 (b)**) and further investigation on the mechanisms that are occurring at these electrodes could be explained using this technique. **Figure 6.1.9 (a)** and **(b)** reports the Complex Plane and Bode Phase plots registered at +0.25 V (SCE), with the relative equivalent circuits in **Figure 6.1.10**. Then, **Figure 6.1.11** shows the plots recorded at +0.6 V (SCE) with the relative equivalent circuits in

Figure 6.1.12. All the mathematical parameters are then listed in **Table 6.1.4** and **Table 6.1.5**.

Regarding the behaviour at +0.25 V (SCE), where the reaction of the probe is favoured in the case of the bare graphene (Figure 6.1.8), just from a simple look at the EIS spectra, a different behaviour among the bare and modified electrode can be highlighted. In fact, different equivalent circuits are derived for the materials without the functionalization. In particular, in those cases also the mass transfer reaction is visible (Warburg element, see **Figure 6.1.10 (a)**)

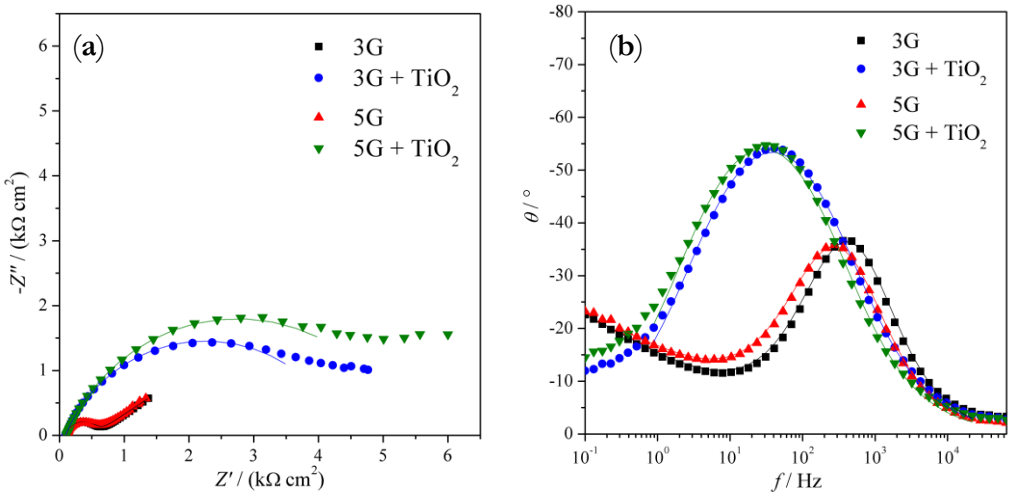

Figure 6.1.9: (**a**) Complex Plane plots at +0.25 V of the hybrid materials recorded in 0.1 M $NaClO_4$ as supporting electrolyte + 3mM of $K_4[Fe(CN)_6]$. (**b**) Analogous Bode plots.

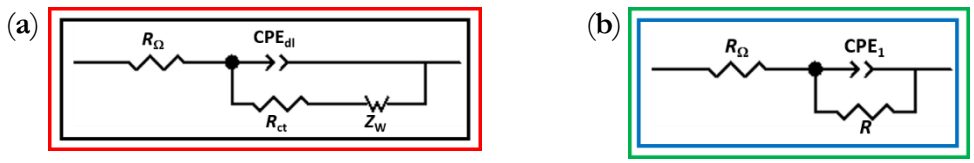

Figure 6.1.10: Equivalent circuits for (**a**) 3G, 5G and (**b**) 3G +TiO2, 5G +TiO_2 systems, related to the spectra at +0.25 in the presence of 3mM $K_4[Fe(CN)_6]$. $\boldsymbol{R_\Omega}$ = cell resistance, $\mathbf{CPE_{dl}}$ = double capacitance (Constant Phase Element), $\boldsymbol{R_{ct}}$ = charge transfer resistance, $\boldsymbol{Z_W}$ = Warburg resistance, $\mathbf{CPE_1}$ = "Debye Layer" capacitance (Constant Phase Element), $\boldsymbol{R}$ = contact resistance. *Colors of the squares around the circuits are related to the colors of the lines and dots in the EIS spectra.*

The presence of the nanocrystals in this case (and so in the presence of a redox probe that is interacting with the electrode surface structure) acts as a hindering effect, since the resistance of the functionalized materials (*R*) are higher with respect to the bare ones (Table 6.1.4). Moreover, the mass transfer process seems favored in the case of the bare 5G and this could be ascribed to a more defective structure with a more "porous" surface that could let the probe react in an easier way with respect to the analogous 3G system.

Table 6.1.4: EIS mathematical parameters from the fitting of the spectra at +0.25 V in 0.1 M $NaClO_4$ + 3 mM $K_4[Fe(CN)_6]$.

	$R\Omega$ (Ω cm^2)	CPE_1 (μF cm^{-2} s$^{\alpha-1}$)	α_1	R (kΩ cm^2)	Z_w (Ω cm^2)	α_w	τ_w
3G	113	4.01	0.90	0.432	4.39	0.38	76.6
3G + TiO_2	92.9	25.5	0.75	5.40			
5G	111	6.58	0.88	0.414	1.96	0.38	7.87
5G + TiO_2	110	25.7	0.76	5.30			

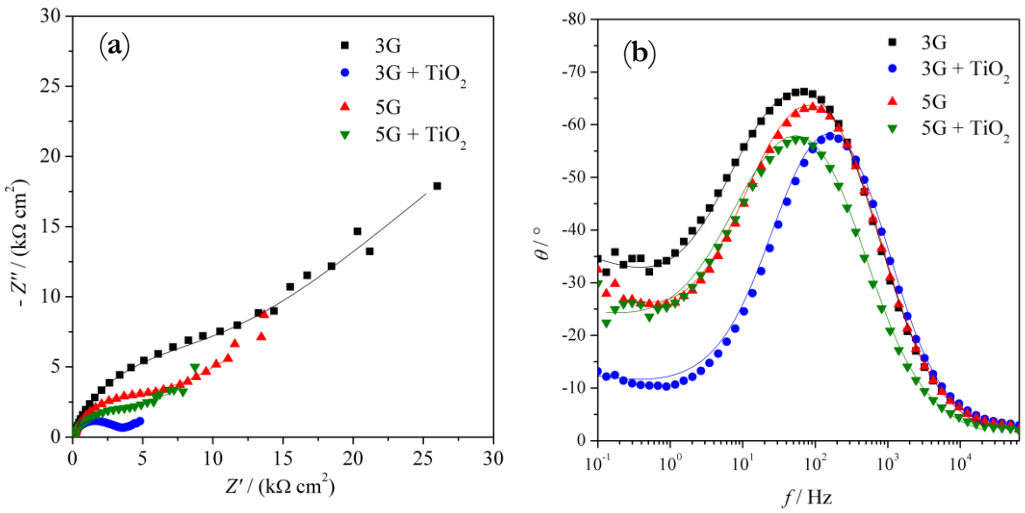

Figure 6.1.11: (**a**) Complex Plane plots at +0.6 V of the hybrid materials recorded in 0.1 M $NaClO_4$ as supporting electrolyte + 3mM of $K_4[Fe(CN)_6]$. (**b**) Analogous Bode plots.

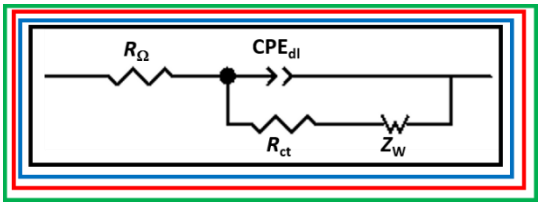

Figure 6.1.12: Equivalent circuits for all the investigated systems recorded at +0.6 V in the presence of 3mM of $K_4[Fe(CN)_6]$. R_Ω = cell resistance, CPE_{dl} = double capacitance (Constant Phase Element), R_{ct} = charge transfer resistance, Z_W = Warburg resistance, CPE_1 = "Debye Layer" capacitance (Constant Phase Element), R = contact resistance. *Colors of the squares around the circuits are related to the colors of the lines and dots in the EIS spectra.*

Considering the spectra recorded at +0.6 V (SCE) (**Figure 6.1.11**), where all the materials react with the probe, but the highest current density was registered for the functionalized systems (**Figure 6.1.6**), the situation is different from the one observed at +0.25 V (SCE). Regarding the resistance values, in fact, the situation is opposite to the previous one and the materials functionalized are the ones with the lower resistance to the charge transfer reaction (see **Table 6.1.5**). Moreover, at this voltage value, for all the materials it is possible to see also the mass transfer process of the redox probe, with the addition of a Warburg element in the equivalent circuits (**Figure 6.1.12**). By the way, since from the experimental results, especially in the case of the functionalized trilayers graphene, the fitting of the Warburg element was derived with few points, the mathematical results cannot be discussed further since they are not particularly affordable. In this case, a simple empirical explanation is done, and a general trend is verified.

Table 6.1.5: EIS mathematical parameters from the fitting of the spectra at +0.25 V in 0.1 M $NaClO_4$ + 3 mM $K_4[Fe(CN)_6]$.

	R_Ω (Ω cm^2)	CPE_1 (μF cm^{-2} s$^{\alpha-1}$)	α_1	R (kΩ cm^2)	Z_w (kΩ cm^2)	α_w	τ_w
3G	139	4.41	0.88	9.31	120	0.47	46.2
3G + TiO_2	118	3.51	0.90	1.77	0.940	0.12	0.019
5G	121	4.48	0.89	4.73	35.1	0.40	23.8
5G + TiO_2	120	9.81	0.85	3.01	21.9	0.35	43.4

Electroanalytical Applications

Sensing

One particular area where graphene has had a significant impact is electroanalysis, where it has been used as sensor receptor for a variety of analytes[21,22] and has the potential for utilisation in the development of cost effective, sensitive and selective electrochemical sensors of the future.[23] In particular, all the materials under investigation were used in the detection of two molecules of biomedical interest, namely dopamine and norepinephrine. They both belong to the family of catecholamine neurotransmitters and their determination is of high importance since an altered level and concentration of such molecules lead to several diseases of neural and cardiovascular systems. Besides their low physiological concentration, which demands very sensitive detection systems, high concentration of interfering substances such as ascorbic acid (AA) and uric acid (UA) requires the sensing platforms to be highly specific as well.

Both the pristine and the TiO_2 NCs-modified electrode platforms were tested as preliminary proof of concept by recording a Cyclic Voltammetry in the presence of Dopamine and Norepinephrine, in a 0.1 M solution of Phosphate Buffer (PBS) at a physiological pH value of 7.4. All the electrodes resulted to be suitable for the detection of the selected molecules. In **Figure 6.1.13** the voltammetric signals of the different electrodes in the presence of 3 mM dopamine are reported. It can be immediately observed that in the case of the modified graphene platforms, with both monolayer and bilayer (1G + TiO_2 and 2G + TiO_2), a strong electrocatalytic effect is present. In fact, both the

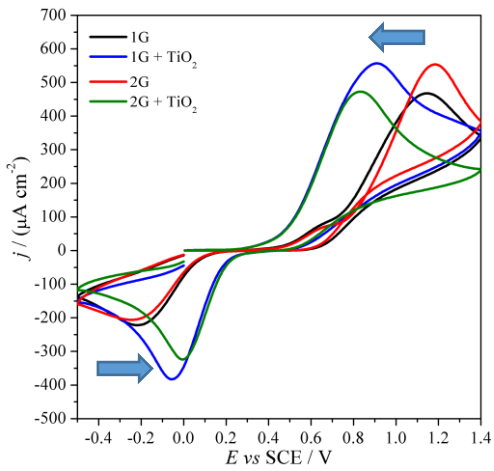

Figure 6.1.13: CV of the bare and modified graphene electrodes in the presence of 3mM of dopamine.

oxidation and reduction peaks relative to dopamine are at potential values closer to zero, as evidenced by the arrow depicted in **Figure 6.1.13**. This fact means that the presence of TiO_2 favours the reaction of the molecule toward the electrode, maybe because they favour the electron/holes exchange at the interface with respect to what concern the bare graphene. As already mentioned, in fact, TiO_2 NCs donate holes to the platform and then favouring the oxidation of the species in solution.

A more detailed look at the oxidation part shows that a small signal at about +0.65 V (SCE) for bare mono and bilayer graphene is present, while in the case of the NCs-modified electrode the signal is only one. Apart from the electrocatalytic effect played on the signal at about +1.2 V (SCE) of the bare graphene, also a sort of patching effect is evidenced: the pyrene linker that functionalises TiO_2 nanocrystals could cover the defect sites of the bare graphene and effectively creates a more homogeneous surface with less electroactive sites toward dopamine.

As preliminary results, also the multilayer graphenes were employed for the detection of dopamine and results are reported in **Figure 6.1.14**. In this case, no reduction peaks are present. By the way, the general trend observed in the case of mono- and bi-layer graphene is again confirmed. On the bare graphene platforms (3G and 5G) two peaks are visible, with the first one more marked with respect to the same of mono and bi-layer, while in the case of the TiO_2 NCs modified

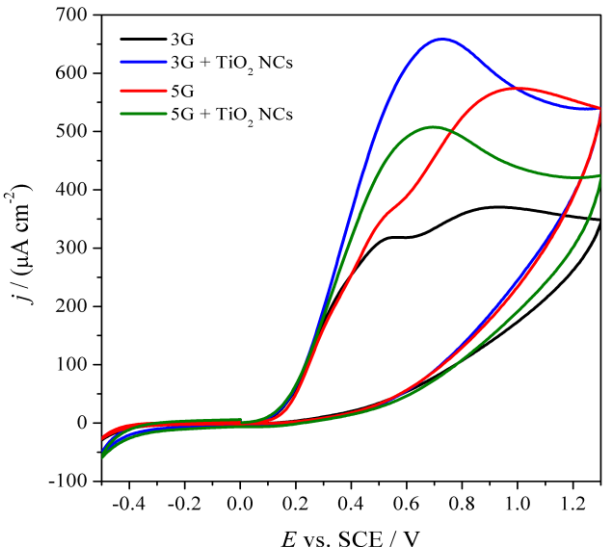

Figure 6.1.14: CV of the bare and modified multilayer graphene electrodes in the presence of 3mM of dopamine.

electrodes, a single peak, at more favourable potential with respect to the second one of the bare graphene, is observed. This aspect is again a confirmation of the electronic transfer between the two components of the hybrid and of the patching effect played by the pyrene linker of the nanocrystals.

- *Selectivity*

Among the desired features of an electrochemical sensor, there is the selectivity, which describes the ability of a device to detect clearly in a distinguished way different analytes. Since dopamine and norepinephrine possess a similar chemical formula, differing just for the presence of a hydroxyl group (see **Figure 6.1.15**), finding a sensor able to detect and speciate among the two molecules is an actual challenge. For this reason, the answers of the four electrodes under investigation (monolayer and bilayer graphene, bare and modified) towards dopamine and norepinephrine were overlapped and results are shown in **Figure 6.1.16**.

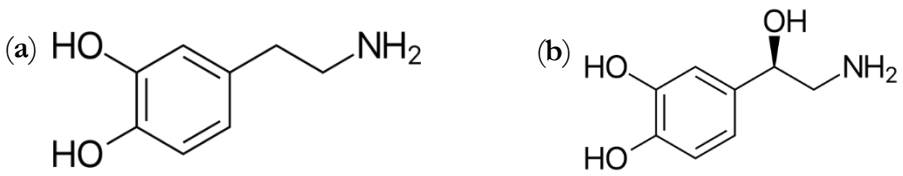

Figure 6.1.15: Molecular structures of (a) dopamine and (b) norepinephrine.

Figure 6.1.16 (a) and **(c)** are related to the bare graphene platform and clearly show that the electrodes are able to distinguish between the two molecules, since the oxidation reactions occur at different potentials. For what concern the TiO_2-modified graphenes (**Figure 6.1.16 (b)** and **(d)** for monolayer and bilayer, respectively), unfortunately, the distinction in the detection of the two molecules is not so clear. It could be that the presence of PBA-capped TiO_2 creates a sort of "patching" on the graphene platform, uniforming the surface and covering defects, due to the presence of the pyrene linker. The different reactivity of the two molecules

of the bare graphene could be connected, in fact, to a different reactivity that the analytes have towards basal, edge planes, wrinkles, steps, folded, edges, missing atoms and so on. All these defects could be hidden by the presence of the functionalities on PBA-TiO_2 NCs.

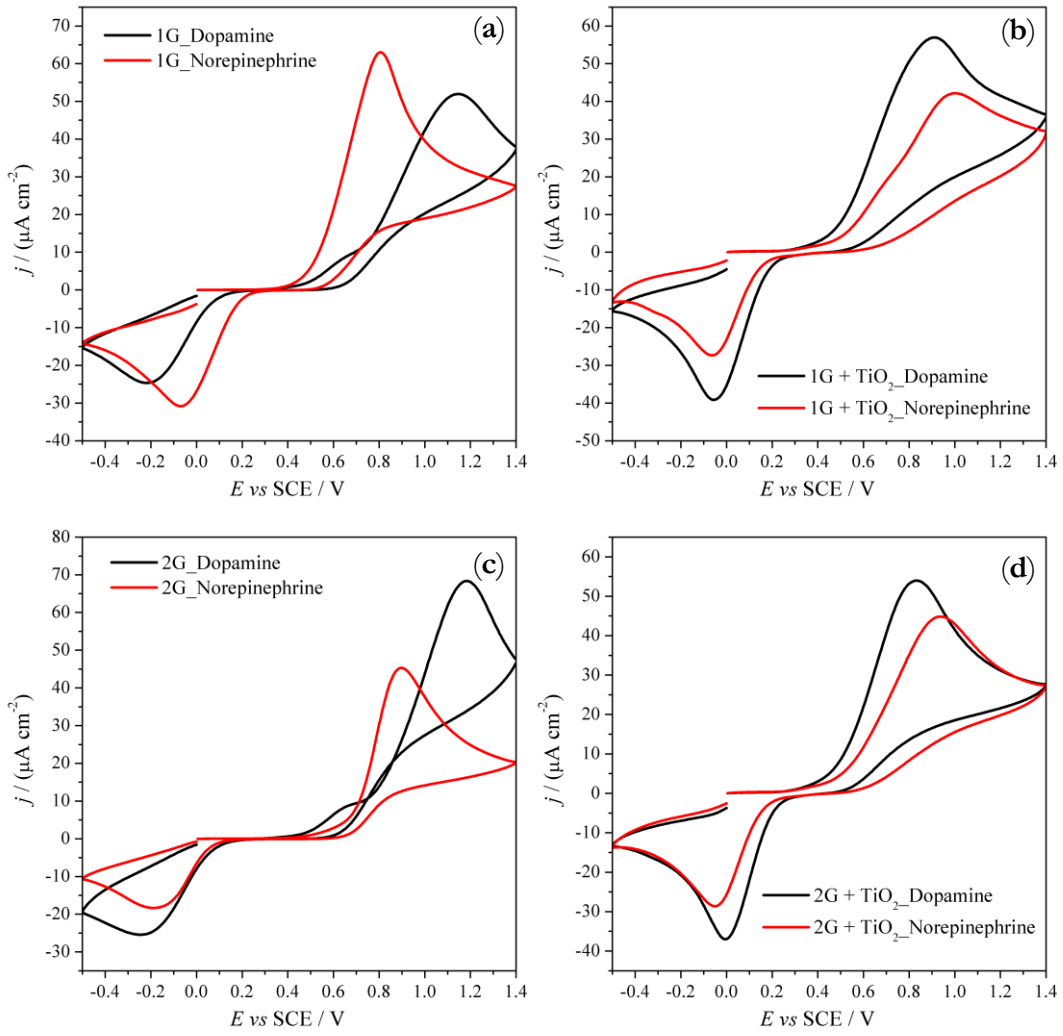

Figure 6.1.16: CV of the bare monolayer (a), bilayer (b) graphene and the relative TiO_2 modified platforms (c) and (d), in the presence of 3 mM of dopamine (black lines) and norepinephrine (red lines), recorded at 100 mV s^{-1} in 0.1 M PBS (pH 7.4).

Unfortunately, with multilayer graphene it was not possible to effectively distinguish among the two molecules. In fact, the answers toward dopamine and norepinephrine

show basically the same trend, with a double peak for the bare graphene platforms and a single, shifted, signal in the case of the TiO_2 modified ones (see **Figure 6.1.17**). It could be that, by moving toward more graphitic electrodes, more similar among themselves and more different from the single graphene, it is practically impossible to distinguish among two molecules that are really similar one to the other (dopamine and norepinephrine, in fact, differ only for the presence of an -OH group).

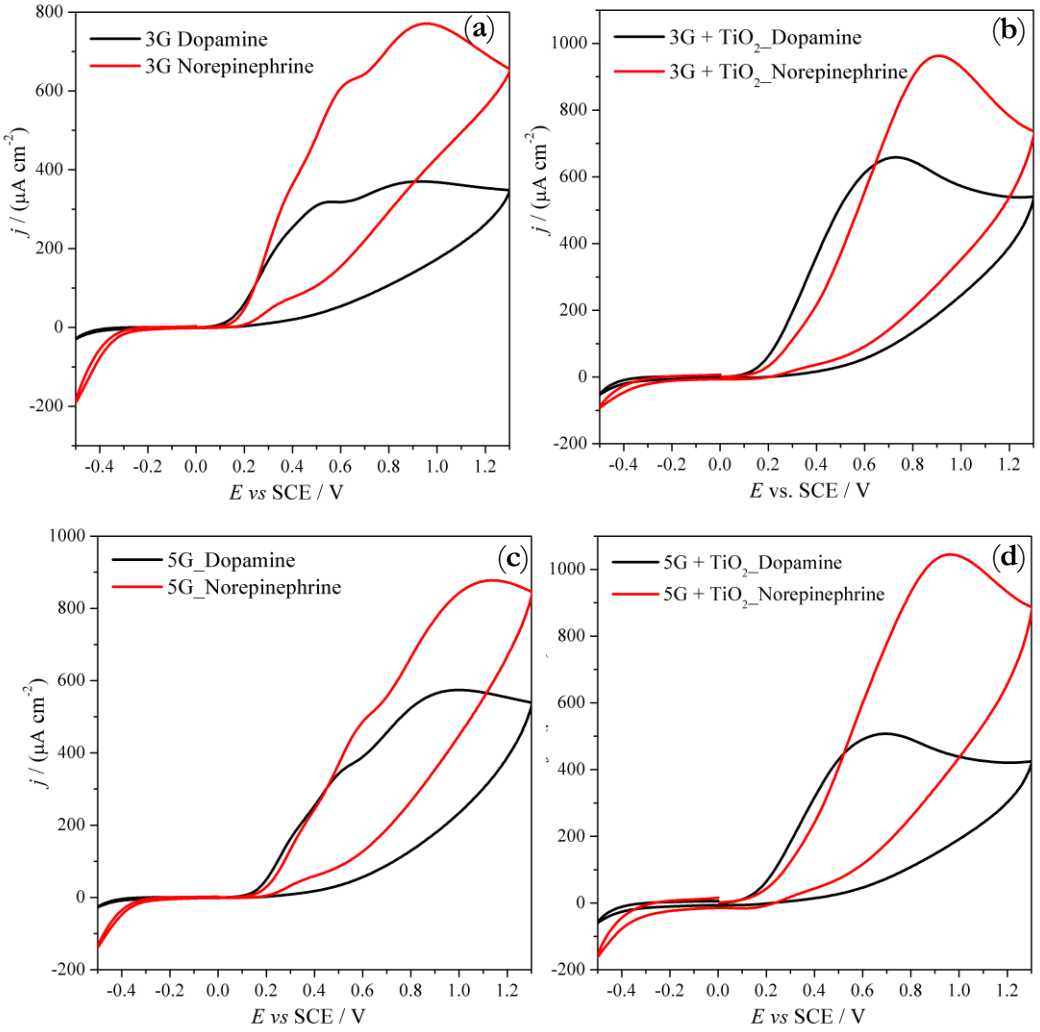

Figure 6.1.17: CV of the bare trilayer (a), pentalayer (b) graphene and the relative TiO2 modified platforms (c) and (d), in the presence of 3 mM of dopamine (black lines) and norepinephrine (red lines), recorded at 100 mV s^{-1} in 0.1 M PBS (pH 7.4).

Considering the sensitivity of a single electrode toward an analyte, like what it was observed in the case of dopamine (**Figure 6.1.16** and **Figure 6.1.17**), the presence of TiO_2 nanocrystals is beneficial, because it generates electrocatalytic effects. If dealing with more than one analyte, and so looking at the selectivity of the platform, the presence of the nanocrystal is no more beneficial as before. By the way, the presence of TiO_2 nanocrystals was verified to be beneficial not only for the construction of a performant photo-anode, but also for the creation of an electroanalytical sensor. Moreover, the intrinsic semiconductor nature of the nanocrystals could be exploited for the development of a photo-renewable sensor, as already reported for analogous systems in the literature.[24,25] In fact, one of the biggest problem related to the detection of organic molecules like dopamine, is the fouling and passivation of the electrode surface after the detection. The possibility to irradiate the electrode and favour the generation of photoexcited electrons, could accelerate the reduction of the molecule deposited on the surface of the electrode and concomitantly could promote the cleaning and renewal of the device.

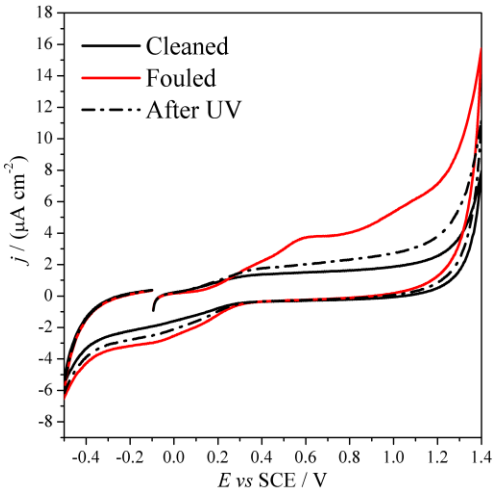

Figure 6.1.18: CV of the background of bare 5G electrode before the detection of dopamine (black filled line), after (red line) and after 1h UV (black dotted line).

As a proof of concept, the effect of light irradiation onto a fouled electrode was verified in case of penta-layer graphene. In more details, the electrode was used in the detection of dopamine, then, it was washed with Milli-Q water and put in a background electrolytic solution, without any addition of the analyte. The presence of a signal related to dopamine was verified, meaning that the electrode was fouled and that its surface was passivated. Then, the

electrode was left under UV light for one hour and the CV was recorded again, showing the disappearance of the signal relative to the analyte and ensuring the cleanliness of the electrode surface. Results are shown in **Figure 6.1.18**.

- *Specificity*

As already mentioned, the detection of dopamine and norepinephrine could be disturbed by the presence in human body of high concentration of interfering substances such as ascorbic acid (AA) and uric acid (UA). For this reason, the device requires to be highly specific, apart from being selective and sensitive.

As a reference, results obtained in the case of detection of dopamine in the presence of ascorbic acid with monolayer graphene and the relative PBA-TiO_2 NCs modified monolayer are shown. In the experiment, additions of dopamine (1 mM each) were made in a 0.5 mM solution of ascorbic acid and results are shown in **Figure 6.1.19**.

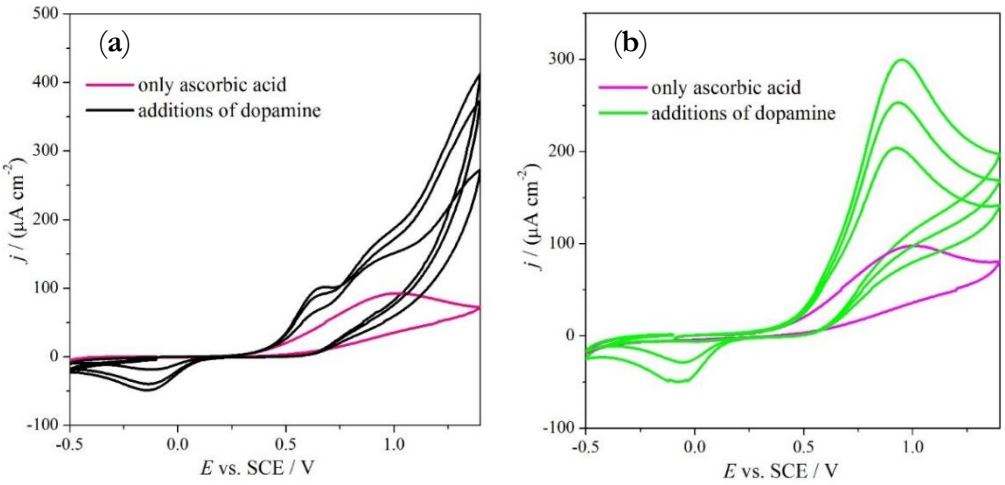

Figure 6.1.19: Detection of dopamine in the presence of ascorbic acid with bare monolayer graphene (**a**) and TiO_2 modified monolayer graphene (**b**).

From the results shown in **Figure 6.1.19**, it is possible to claim that the detection of dopamine in the presence of ascorbic acid is possible looking at the cathodic peak. In fact, in case of the only interferent, this signal is absent. Probably the oxidation product of dopamine (namely leuco-dopaminoquinone, **Figure 6.1.20**)[26,27] is able to interact by means of π–π interactions with graphene and consequently to be

detected. This does not happen with ascorbic acid. The oxidation peak, unfortunately, is more or less at the same position for both the interferent and the analyte and cannot be significant of the presence of one or the other molecules in solution.

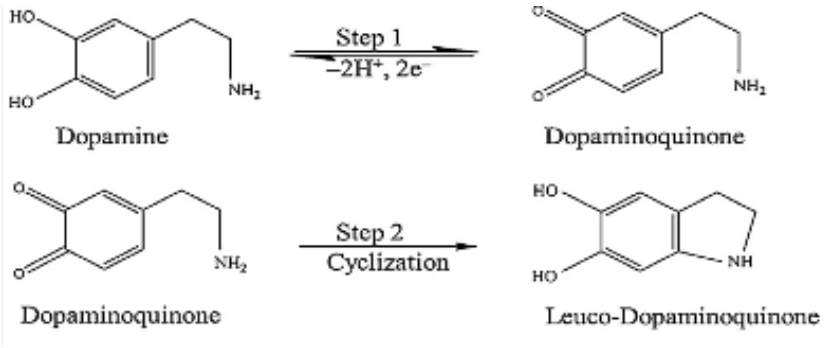

Figure 6.1.20: EC mechanism for dopamine oxidation.[26] Adapted with permission, Copyright 2017, Elsevier.

Conclusions

In this work, a straightforward and facile solution-based approach has been optimized to fabricate a transparent hybrid material formed of a large area of CVD grown monolayer graphene film, decorated with a dense multi-layered nanoporous coating of 1-pyrene butyric acid (PBA)-coated TiO_2 nanocrystals. The interest was focused onto the understanding differences among materials synthesized with a different number of graphene layers (from one to five) in their electrochemical performances. It was found that by changing the number of graphene layers, the electronic structure of the material is drastically changed: strong differences are highlighted among mono- and bi-layer graphene, in which a strong effect of convergent diffusion, due to the presence of graphitic island and defect, on the bi-layered platform, is verified. Passing to multi-layered graphene (tri- and penta-layer) the presence of different electroactive sites is highlighted, and it is possible to effectively distinguish among a graphene or a graphitic-like structure. These differences in the electrochemical response are reflected also when the electrodes are

used, as a preliminary proof of concept, for the detection of neurotransmitters of particular interest in the biomedical field (dopamine and norepinephrine). The signal related to the target molecule is registered at different potential positions by changing the electrode and this aspect could be further applied for selectively detect one molecule instead of other interferents. Future works will be focused on the improvement of the electroanalytical techniques, with the general aim to create a performant, selective and sensitive sensor. The presence of TiO_2 NCs and the transparent aspect of the electrodes make them also suitable for application under UV-light, being good candidate to create photoanodes to be integrated in solar cells, photodetectors, catalytic systems, FETs and photoelectrochemical and capacitive sensors.

Bibliography

(1) Soliveri, G.; Pifferi, V.; Panzarasa, G.; Ardizzone, S.; Cappelletti, G.; Meroni, D.; Sparnacci, K.; Falciola, L. Self-Cleaning Properties in Engineered Sensors for Dopamine Electroanalytical Detection. *Analyst* **2015**, *140*, 1486–1494.

(2) Pifferi, V.; Soliveri, G.; Panzarasa, G.; Ardizzone, S.; Cappelletti, G.; Meroni, D.; Falciola, L. Electrochemical Sensors Cleaned by Light: A Proof of Concept for on Site Applications towards Integrated Monitoring Systems. *RSC Adv.* **2015**, *5* (87), 71210–71214.

(3) Ingrosso, C.; Bianco, G. V.; Corricelli, M.; Comparelli, R.; Altamura, D.; Agostiano, A.; Striccoli, M.; Losurdo, M.; Curri, M. L.; Bruno, G. Photoactive Hybrid Material Based on Pyrene Functionalized PbS Nanocrystals Decorating CVD Monolayer Graphene. *ACS Appl. Mater. Interfaces* **2015**, *7* (7), 4151–4159.

(4) Katsukis, G.; Malig, J.; Schulz-Drost, C.; Leubner, S.; Jux, N.; Guldi, D. M. Toward Combining Graphene and QDs: Assembling CdTe QDs to Exfoliated Graphite and Nanographene in Water. *ACS Nano* **2012**, *6* (3), 1915–1924.

(5) Jeong, H. J.; Kim, H. Y.; Jeong, H.; Han, J. T.; Jeong, S. Y.; Baeg, K. J.; Jeong, M. S.; Lee, G. W. One-Step Transfer and Integration of Multifunctionality in CVD Graphene by TiO2/Graphene Oxide Hybrid Layer. *Small* **2014**, *10* (10), 2057–2066.

(6) Han, J. T.; Kim, B. J.; Kim, B. G.; Kim, J. S.; Jeong, B. H.; Jeong, S. Y.; Jeong, H. J.; Cho, J. H.; Lee, G. W. Enhanced Electrical Properties of Reduced Graphene Oxide Multi Layer Films by In-Situ Insertion of a TiO2 Layer. *ACS Nano* **2011**, *5* (11),

8884–8891.

(7) Ingrosso, C.; Bianco, G. V.; Pifferi, V.; Guffanti, P.; Petronella, F.; Comparelli, R.; Agostiano, A.; Striccoli, M.; Palchetti, I.; Falciola, L.; et al. Enhanced Photoactivity and Conductivity in Transparent TiO 2 Nanocrystals/Graphene Hybrid Anodes. *J. Mater. Chem. A* **2017**, *115*, 10307.

(8) Cozzoli, P. D.; Kornowski, A.; Weller, H. Low-Temperature Synthesis of Soluble and Processable Organic-Capped Anatase TiO2 Nanorods. *J. Am. Chem. Soc.* **2003**, *125* (47), 14539–14548.

(9) Dholam, R.; Patel, N.; Santini, A.; Miotello, A. Efficient Indium Tin Oxide/Cr-Doped-TiO2 Multilayer Thin Films for H2 Production by Photocatalytic Water-Splitting. *Int. J. Hydrogen Energy* **2010**, *35* (18), 9581–9590.

(10) Spadavecchia, F.; Ardizzone, S.; Cappelletti, G.; Falciola, L.; Ceotto, M.; Lotti, D. Investigation and Optimization of Photocurrent Transient Measurements on Nano-TiO2. *J. Appl. Electrochem.* **2013**, *43* (2), 217–225.

(11) McCreery, R. L. Advanced Carbon Electrode Materials for Molecular Electrochemistry. *ChemInform* **2008**, *39* (41), 2646–2687.

(12) Patel, A. N.; Collignon, M. G.; OConnell, M. A.; Hung, W. O. Y.; McKelvey, K.; MacPherson, J. V.; Unwin, P. R. A New View of Electrochemistry at Highly Oriented Pyrolytic Graphite. *J. Am. Chem. Soc.* **2012**, *134* (49), 20117–20130.

(13) Ambrosi, A.; Pumera, M. Electrochemistry at CVD Grown Multilayer Graphene Transferred onto Flexible Substrates. *J. Phys. Chem. C* **2013**, *117* (5), 2053–2058.

(14) Brownson, D. A. C.; Kampouris, D. K.; Banks, C. E. *Graphene Electrochemistry: Fundamental Concepts through to Prominent Applications*; 2012; Vol. 41.

(15) Lounasvuori, M. M.; Rosillo-Lopez, M.; Salzmann, C. G.; Caruana, D. J.; Holt, K. B. Electrochemical Characterisation of Graphene Nanoflakes with Functionalised Edges. *Faraday Discuss.* **2014**, *172* (Cv), 293–310.

(16) Brownson, D. a. C.; Kampouris, D. K.; Banks, C. E. *Graphene Electrochemistry: Fundamental Concepts through to Prominent Applications*; 2012; Vol. 41.

(17) Li, W.; Tan, C.; Lowe, M. A.; Abruña, H. D.; Ralph, D. C. Electrochemistry of Individual Monolayer Graphene Sheets. *ACS Nano* **2011**, *5* (3), 2264–2270.

(18) Paulson, S.; Helser, A.; Nardelli, M. B.; Taylor, R. M.; Falvo, M.; Superfine, R.; Washburn, S. Tunable Resistance of a Carbon Nanotube-Graphite Interface. *Science* **2000**, *290* (5497), 1742–1744.

(19) Ji, H.; Zhao, X.; Qiao, Z.; Jung, J.; Zhu, Y.; Lu, Y.; Zhang, L. L.; MacDonald, A. H.; Ruoff, R. S. Capacitance of Carbon-Based Electrical Double-Layer Capacitors. *Nat. Commun.* **2014**, *5* (Cmcm).

(20) Li, L.; Zheng, X.; Wang, J.; Sun, Q.; Xu, Q. Solvent-Exfoliated and Functionalized Graphene with Assistance of Supercritical Carbon Dioxide. *ACS Sustain. Chem. Eng.* **2013**, *1* (1), 144–151.

(21) Brownson, D. A. C.; Banks, C. E. Graphene Electrochemistry: An Overview of Potential Applications. *Analyst* **2010**, *135* (11), 2768–2778.

(22) Pumera, M.; Ambrosi, A.; Bonanni, A.; Chng, E. L. K.; Poh, H. L. Graphene for Electrochemical Sensing and Biosensing. *TrAC - Trends Anal. Chem.* **2010**, *29* (9), 954–965.

(23) Brownson, D. A. C.; Banks, C. E. CVD Graphene Electrochemistry: The Role of Graphitic Islands. *Phys. Chem. Chem. Phys.* **2011**, *13* (35), 15825–15828.

(24) Pifferi, V.; Soliveri, G.; Panzarasa, G.; Cappelletti, G.; Meroni, D.; Falciola, L. Photo-Renewable Electroanalytical Sensor for Neurotransmitters Detection in Body Fluid Mimics. *Anal. Bioanal. Chem.* **2016**, *408* (26), 7339–7349.

(25) Soliveri, G.; Pifferi, V.; Panzarasa, G.; Ardizzone, S.; Cappelletti, G.; Meroni, D.; Sparnacci, K.; Falciola, L. Self-Cleaning Properties in Engineered Sensors for Dopamine Electroanalytical Detection. *Analyst* **2015**, *140* (5), 1486–1494.

(26) Ejaz, A.; Joo, Y.; Jeon, S. Fabrication of 1,4-Bis(Aminomethyl)Benzene and Cobalt Hydroxide @ Graphene Oxide for Selective Detection of Dopamine in the Presence of Ascorbic Acid and Serotonin. *Sensors Actuators B Chem.* **2017**, *240*, 297–307.

(27) Palomäki, T.; Chumillas, S.; Sainio, S.; Protopopova, V.; Kauppila, M.; Koskinen, J.; Climent, V.; Feliu, J. M.; Laurila, T. Electrochemical Reactions of Catechol, Methylcatechol and Dopamine at Tetrahedral Amorphous Carbon (Ta-C) Thin Film Electrodes. *Diam. Relat. Mater.* **2015**, *59*, 30–39.

Acknowledgments

This Project was partially supported by the National Project (PRIN 2012, prot. 20128ZZS2H).

I gratefully acknowledge Dr. C. Ingrosso and Dr. M. L. Curri from CNR-IPCF S. S. Bari, Dr. G. V. Bianco and Dr. G. Bruno from CNR-NANOTEC, Department of Chemistry, Università di Bari (Bari, Italy) for the synthesis and physico-chemical characterizations of the hybrid materials.

6.2 PCA-RGO/OLEA-PbS NCs Hybrids

Focus

As already mentioned in the **Introduction** of this **Chapter 6**, the interest in constructing graphene-based hybrids with semiconductor has rapidly expanded in recent years. More than bare graphene, the use of its derivative RGO (Reduced Graphene Oxide) is growing, thanks to its processability in solution, also aqueous ones, which represents a huge advantage especially when dealing with the synthesis of nanocomposites.[1] These nanocomposites, which for different applications were already discussed in Chapter 5, can be prepared by *non-covalent* approaches. Thanks to these procedures, the decoration of graphene is carried out without detrimental effect on the structural properties of the carbonaceous platform, which is retained and often enhanced thanks to the functionalization with the other components of the hybrid.[2]

Interesting materials to prepare nanocomposites with RGO are Nanocrystals (NCs), thanks to their outstanding *size*- and *shape*-dependent properties[3] and their high chemical and photophysical stability. Moreover, they possess a processable surface, which makes them suitable candidates for the implementation of solution-based routes for functionalizing graphene derivatives.[4] In particular, colloidal PbS NCs are among the most widely studied nanostructured semiconductors in optoelectronics, for the strong-confinement of their small band-gap, the size-tunable absorption (which covers the visible and the near-infrared (NIR) spectral region), the high extinction coefficient, and the narrow photoluminescence emission signal.[5] The functionalization of graphene with colloidal PbS NCs semiconductors leads to the band alignment between the Dirac point of graphene and the LUMO of the PbS NCs. This effect reflects in the creation of hybrid materials with the UV-Vis-NIR light harvester property of the nano-objects, combined with the capability of graphene to extract, and transfer, the exciton photogenerated in the PbS NCs.[2,6] In such a hybrid structure, the exciton radiative recombination processes, typically

occurring in the light absorbing NCs film, is suppressed and hence, light-energy conversion efficiencies, enhanced with respect to those of the single components, are reached.[7–9]

In this part of the Thesis Project, a *one-pot* and *in situ* colloidal approach to create RGO-PbS hybrids is deeply studied and optimized. In particular, the PbS nanocrystals are capped with oleic acid surfactant (OLEA) and are anchored onto the RGO flakes, which are themselves functionalized with pyrene carboxyl acid (PCA). This linker allows a strong electron coupling between graphene and PbS nanocrystals and this results in a strong quenching of the NCs emission and in a high photoresponsivity, enhanced with respect to the single components. These excellent properties of the hybrid with respect to its single counterparts let us suppose that this material could be reasonably applied also as sensing platform, with enhanced performances and features.

Materials and Methods

Chemicals

Lead(II) oxide (PbO, powder 99.99%), hexamethyldisilathiane (HMDS, synthesis grade), toluene (laboratory reagent, ≥99.3%), tetrachloroethylene (TCE, >99%), 1-pyrenecarboxylic acid (PCA, 97%),1-Octadecene (ODE, 90% technical grade), oleic acid (OLEA, technical grade 90%), $NaClO_4$ and N-Methyl-2-pyrrolidone (NMP anhydrous, 99.5%) were purchased from Sigma-Aldrich, and used as received. Ethanol and tetrachloroethylene (TCE) were purchased from Sigma-Aldrich and used at the highest purity available. Commercial Reduced Graphene Oxide (RGO, 1.6 nm flakes) was provided by Graphene Supermarket. ITO supporting electrodes having a surface resistivity of 30-60 Ω sq^{-1} were purchased from Sigma Aldrich.

Preparation of the 1-pyrenecarboxylic acid (PCA) surface modified Reduced Graphene Oxide (RGO) complex

5 mg of commercial RGO have been functionalized on its surface and exfoliated in a solution of 1-pyrenecarboxylic acid (PCA). The PCA:RGO weight ratio was fixed as 30:1 and 3:1, in N-Methyl-2-pyrrolidone (NMP). The procedure was adapted from a previously reported one[10], with some modifications, particularly focused on the cycles of bath sonication and stirring. The excess of PCA, not chemically adsorbed onto the RGO flakes, has been removed by cycles of centrifugation at 10000 rpm for 15-20 min and re-dispersion in methanol. The effective removal of the non-chemically adsorbed PCA was verified looking at the UV-Vis absorption spectra of the PCA-RGO complex, collected after each washing step. This is expected to remain unchanged and to show only the absorption of the PCA anchored onto the RGO sheets. Moreover, the TEM images of the dispersion do not show PCA crystallites on the RGO flakes[10]. Then, the dark pellets of the PCA-RGO complex have been isolated and dried under vacuum.

Synthesis of the PCA-RGO/PbS NCs hybrid material

Following the procedure previously reported for the preparation of the oleic acid (OLEA)-coated PbS NCs, by Corricelli et al. and Hines et al.[11,12], the synthesis of the PCA-RGO/PbS NC hybrid material was performed, with some modifications. In more details, in a three-neck flask, 3 mg or 10 mg of the PCA-RGO complex were added and dispersed in 13 mL of ODE and 45 mg of PbO powder (corresponding to a 15:1 and 4.5:1 Pb:PCA-RGO weight ratio, respectively). Then, 100 μL to 2 mL of OLEA were added (reaching a Pb:OLEA molar ratio between 1:1.5 to 1:30). The mixture was degassed for about 20 min at the temperature of 120°C, until decomposition of PbO was observed, due to the formation of the lead-oleate complex precursor[11]. Then, the temperature was decreased down to 110°C and the sulphur precursor solution (21 μl of hexamethyldisilathiane (HMDS) in 2 mL of ODE, that is a Pb:S molar ratio of 2:1) was rapidly injected under stirring. Then, the temperature was suddenly cooled down to room temperature. This passage is essential in order to prevent further nucleation and promote the growth of the PbS NCs anchored onto the surface of the PCA-RGO flakes. The reaction was stopped when the flask reached room temperature. The obtained PCA-RGO/PbS NCs hybrid material was purified from the excess of OLEA by cycles of centrifugation, using a non-solvent precipitation procedure. This technique was carried out by adding methanol or ethanol in excess and a black pellet was finally isolated and dispersed in toluene or TCE, to achieve optically transparent solutions.

A size selective fractional precipitation procedure was performed on the as-synthesized PCA-RGO/PbS NCs solution, to separate the free OLEA-capped PbS NCs, homonucleated in solution and not anchored onto the RGO flakes, from the PCA-RGO/PbS NCs hybrid flakes. This was achieved by centrifuging at 4500 rpm for 20 minutes, with the addition of methanol in excess. Then, the isolated PCA-RGO/PbS NCs hybrid flakes were dispersed in toluene or TCE.

Characterization techniques

- **UV-Vis-NIR** absorption spectroscopy was performed to characterize the PCA-RGO/PbS NCs hybrid material dispersed in TCE, by using a Cary Varian 5000 spectrophotometer. UV-Vis-NIR PL (Photoluminescence) emission measurements were carried out with a Horiba Jobin Yvon Fluorolog-3 spectrofluorimeter, by using a 450 Xe lamp as excitation source, coupled with a double grating Czerny–Turner monochromator for wavelength selection. The detection system relies on a TBX-PS detector in the visible range and a Peltier-cooled InGaAs detector in the NIR range.
- **Mid-infrared** spectra were acquired with a Varian 670-IR spectrometer equipped with a DTGS (Deuterated Tryglycine Sulfate) detector, having a spectral resolution of 4 cm^{-1}. For attenuated total reflection (ATR) measurements, the internal reflection element (IRE) used was a one-bounce 2 mm diameter diamond microprism. The samples were cast directly on the upper face of the diamond crystal and the solvent was allowed to evaporate.
- **Transmission Electron Microscopy** (TEM) images of the PCA-RGO/PbS NCs hybrid flakes were acquired by using a JEOL JEM-1011 microscope, working at an accelerating voltage of 100 kV and equipped with a high-contrast objective lens, and a W filament as electron source. Under these conditions, the ultimate point resolution of the microscope was equal to 0.34 nm. The TEM images were collected by a Gatan SC-1000 Orius Camera, equipped with a fiber-optical coupled 11 Mp CCD. The samples were prepared by dipping the 300 mesh amorphous carbon-coated Cu grid in PCA-RGO/PbS NCs toluene dispersions and letting the solvent to evaporate. Size statistical analysis (NP average size and size distribution) of the samples were performed by means of a freeware Image J analysis program.
- **Field Emission Scanning Electron Microscopy** (FE-SEM) was performed with a Zeiss Sigma microscope, operating in the range of 0.5−20

kV and equipped with an in-lens secondary electron detector and an INCA Energy Dispersive Spectroscopy (EDS) detector. FE-SEM samples were prepared by casting a drop of the PCA-RGO/PbS NCs toluene dispersion, at a proper concentration, onto a silicon slide. Finally, the samples were mounted onto stainless-steel sample holders by a double-sided carbon tape and grounded by silver paste.

- **Electrochemical** and **spectro-electrochemical measurements** of the bare RGO flakes, the OLEA-capped PbS NCs and the RGO/PbS NCs hybrid material were performed by drop-casting the sample solutions onto the ITO supporting electrode and letting the solvent dry under ambient conditions. A three-electrode cell, integrating the modified ITO as working electrode (WE), a saturated calomel electrode (SCE, AMEL) and a Pt wire, as reference (RE) and counter (CE) electrodes, respectively, was used. A 0.1 M $NaClO_4$ solution was used as supporting electrolyte. Photocurrent intensities were measured in air under the potentials of +0.8 and -0.3 V (SCE) by repeating six cycles of irradiation of the samples with a UV-Vis-NIR light lamp (Deuterium 30 W and Tungsten 150 W, Spectral Products), equipped with a monochromator (CM110, Spectral Products). For the measurements, the hybrid samples were placed at 10 cm from the monochromator and illuminated at the wavelength of 900 nm and light irradiance of about (4.794 $\pm$ 0.002) $\mu W\ cm^{-2}$. All the electrochemical measurements were performed using an AutoLab PGStat30 (Metrohm AutoLab, Utrecht, The Netherlands) connected with a computer equipped with the NOVA 2.1 Software (Metrohm AutoLab, Utrecht, The Netherlands).

Results and Discussion

The use of PCA ligand is essential to exfoliate the RGO sheets and to stack onto their platform by aromatic π–π interactions.[2,6] Moreover, the carboxylic moieties, acting as out-of-plane pendants, allow the stable dispersion of the PCA-RGO in solution, preventing the π–π restacking. The complex is expected to be in single-, few- and multi- layered sheets.[13]

Subsequently, the PbS nanocrystals are synthesized *in situ*, by a heteronucleation and growth process onto the carboxylic functionalities of the PCA-RGO complex. In this passage, the presence of the OLEA surfactant (oleic acid) is essential, since it acts as capping ligand for the nanocrystals and concomitantly it controls the NCs growth. A control experiment was performed in order to verify the effectiveness of the OLEA reagent. The synthesis was conducted also without the addition of the surfactant and it was verified that in its absence the PbO precursor remains in the reaction flask as yellow powder. As a consequence, OLEA is essential to dissolve PbO in the lead oleate monomer complex. In parallel, also the effectiveness of the PCA linker on RGO was verified, always carrying out the reaction without the addition of such a reagent. It was found that in this case, the flakes of RGO result mainly aggregated and without the formation of the nanocrystals.

In order to have a reliable control on the synthesis of the PCA-RGO/PbS NCs hybrids, the effect of the different synthetic parameters on the resulting nanocomposite properties has been explored. In particular, the Pb:OLEA ratio was varied, as well as the PCA:RGO and Pb:PCA-RGO w/w ratio. In this way, the effectiveness and the role of each component onto the final synthetic procedure was verified and it was possible to effectively control the formation of a hybrid densely and uniformly decorated by PbS NCs, with a narrow size distribution and regular morphology.

The variation of the Pb:OLEA molar ratio was studied by following the UV-Vis-NIR absorption and photoluminescence (PL) spectroscopy, together with TEM analyses, of the as-generated NCs onto the flakes. It was found that by varying the molar ratio between the lead precursor and the surfactant, the absorption and photoluminescence peaks change, together with the mean size of the nanocrystals calculated from statistics performed into TEM micrographs. The size of NCs seems to increase when increasing the PbO:OLEA ratio (the growth is preferred to the heteronucleation).

Another set of experiments has been performed by investigating the morphology and size distribution of the OLEA-coated PbS NPs synthesized onto the PCA-RGO flakes, by tuning the PCA:RGO and the PbO:PCA-RGO w/w. In this case, a decreasing in the PCA:RGO w/w leads to a less effective exfoliation of the RGO flakes, appearing as mostly aggregated nanostructures. Moreover, keeping fixed the PbO:OLEA molar ratio and the PbO:PCA-RGO w/w, an increase in the PCA-RGO complex feed leads to a shift of the absorption and PL peaks towards the lower energy side and to an increase of the dimensions of the OLEA-coated PbS NCs. These results assess the cooperative effect of OLEA and of the -COOH moieties of PCA in dissolving the PbO precursor and in generating the lead monomer in the reaction solution. Indeed, the increase of the concentration of the PCA molecules leads to lower nucleation events, and hence, to a smaller number of larger in size PbS NCs.[12]

Spectroscopic investigations were also performed onto the nanostructures growth on the PCA-RGO sheets in order to study their chemical composition and surface chemistry. EDS analysis of the hybrid (pellet casted from a toluene solution on a silicon substrate) (**Figure 6.2.1**), recorded in the range of 0-20 keV, showed typical features of Pb and S elements (Kα line of S at 2.30 keV and the Mα and Lα lines of Pb at 2.34 and 10.55 keV). This evidence allows to effectively assume that the nanostructures immobilized onto the PCA-RGO sheets are PbS nanocrystals.

In the inset of the EDS spectrum a SEM image of the hybrid itself is reported, in which a sheet-like structure with corrugations and bright contrasting wrinkles and folded edges is evident. This aspect is ascribed to the PCA-RGO flake, coated by the bright contrasting PbS NCs, meaning that a dense and uniform coating is effective onto the graphene platform by the semiconductor nanocrystals.

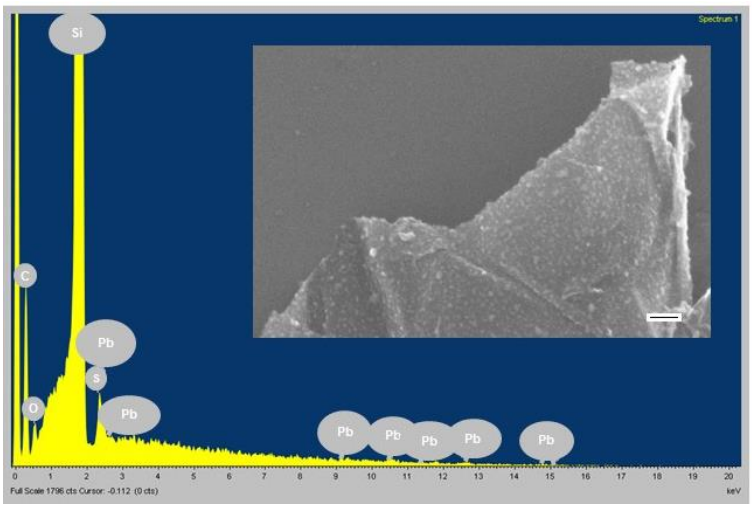

Figure 6.2.1: EDS spectrum of the PCA-RGO/PbS NCs hybrid. SEM images of the same sample in the inset.

Figure 6.2.2 compares the FTR-ATR spectra of the surnatant and of the PCA-RGO/PbS NCs hybrid flakes isolated in the pellet. In the surnatant sample, the typical stretching vibration of the OLEA ligand coordinated to the surface of the PbS NCs are present. Namely, the symmetric stretching of =CH at 3077 cm^{-1}, the asymmetric stretching of $–CH_3$ at 2960 cm^{-1}, and the symmetric and asymmetric stretching of $-CH_2$ at 2922 cm^{-1} and 2853 cm^{-1}, respectively. In the low wavenumber region, the stretching of –C=C- at 1640 cm^{-1}, the $-CH_3$ bending vibrations at 1465 cm^{-1}, the asymmetric and symmetric stretching of the carboxylate ion coordinated to the NC surface at 1565 cm^{-1} and 1403 cm^{-1}, respectively, are evident. Moreover, the asymmetric -C-O-C- stretching at 1259 cm^{-1}, the bending of –CH and $–CH_2$ between 1200 cm^{-1} and 930 cm^{-1} and the bending of –CH at 800 cm^{-1} are visible. Regarding the infrared spectrum of the hybrid flakes in the pellet, most of the same features can be noticed. This demonstrates the presence of the OLEA molecules coordinated to the

surface of the PbS NCs immobilized onto the PCA-RGO complex. It is worthwhile to notice that the presence of such a ligand coordinated onto the surface of the NCs is responsible for the dispersion of the hybrid material in organic solvents.

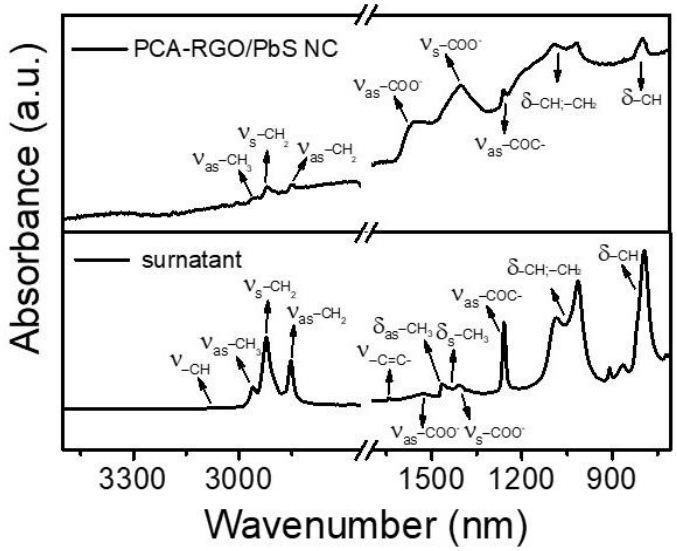

Figure 6.2.2: FT-ATR spectra of the PCA-RGO/PbS NCs hybrid (on top) and of the surnatant from the synthesis (on the bottom).

(Photo)Electrochemical Characterizations

In order to investigate the photoelectrochemical properties of the hybrid, compared to its relative counterparts (bare PCA-RGO and bare OLEA-capped PbS NCs), photocurrent measurements have been performed on the different materials.

The hybrid pellet under investigation possess the absorption maximum at 929 nm, as evidenced by the UV-Vis-NIR absorption spectrum in **Figure 6.2.3**. For this reason, the samples were irradiated at the wavelength of 900 nm, by using a UV-Vis-NIR light lamp equipped with a monochromator. The photocurrent measurements were carried out by performing a chronoamperometry at two different bias voltages, namely +0.8 V (SCE) and -0.3 V (SCE), expected to be higher and lower than the flat band potential of this semiconductor material. The experiments were carried out in a 0.1 M aqueous solution of $NaClO_4$ as supporting electrolyte.

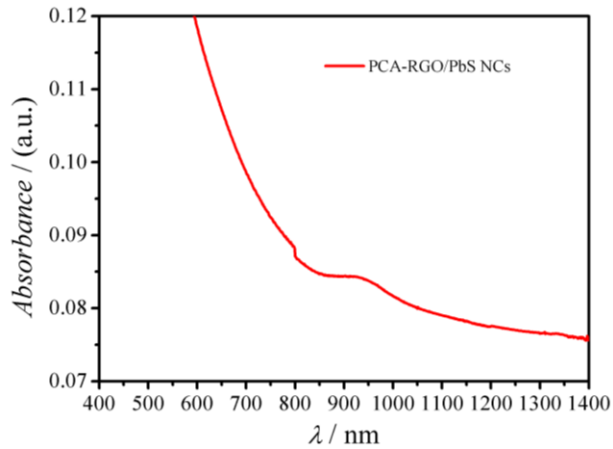

Figure 6.2.3: UV-Vis-NIR absorption spectrum of the PCA-RGO/PbS NCs hybrid, with the maximum of absorption registered at 929 nm.

It must be kept in mind that in this case, dealing with a hybrid and not with a bare PbS semiconductor, the standard values of the flat band potential could be drastically changed. In order to have a better comprehension of this parameter, Mott-Schottky plots on the bare OLEA-PbS NCs were registered, in $NaClO_4$ 0.1 M, by varying the potential between 0 V and -1 V (SCE) at different frequencies (namely, 10 Hz, 31.623 Hz, 100 Hz and 316.23 Hz). **Figure 6.2.4** reports the Mott-Schottky plot recorded at the frequency value of 100 Hz, for which the most linear trend could be fitted.

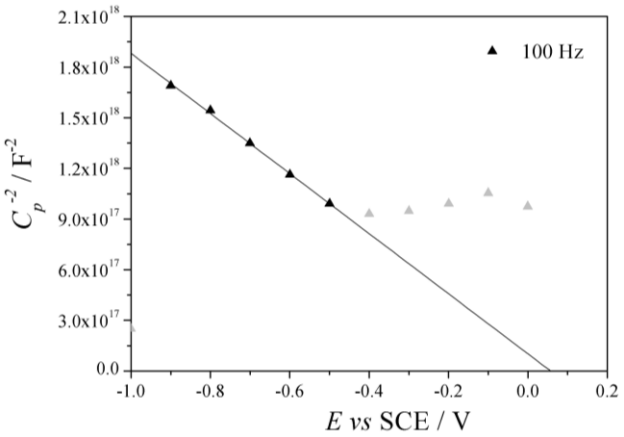

Figure 6.2.4: Mott-Schottky plot at 100 Hz, registered between 0 V and -1 V (SCE) in $NaClO_4$ 0.1 M. E_{FB} = 0.057 V (SCE).

The potential value of the intersection of the linear plot with the x-axys is the effective flat band potential. In this case, it is calculated to be equal to **0.057 V** (SCE). The negative slope of the curve is a confirmation of the p-type character of the PbS semiconductor[14].

In the photocurrent experiments, at the beginning the electrode was left in the dark and at the selected potential (-0.3 V or +0.8 V (SCE)) for 5400 s, in order to reach a situation of stationary background current. Then, the material was irradiated at the selected wavelength for a period of 600 s and then left in the dark for 1200 s. These cycles of light and dark were repeated for 6 times on each sample. **Figure 6.2.5** reports a comparison between the hybrid, the only PCA-RGO and the only OLEA-PbS NCs irradiated at +0.8 V (**a**) and -0.3 V (SCE) (**b**).

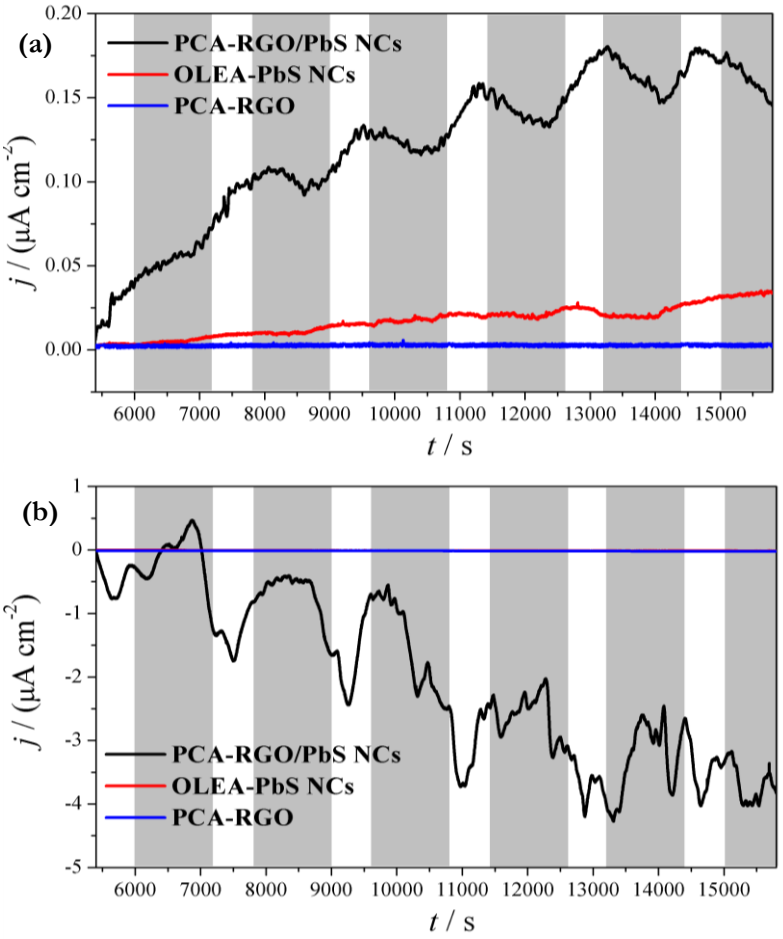

Figure 6.2.5: Photocurrent at +0.8 V (SCE) (**a**) and at -0.3 V (SCE) (**b**) for the hybrid and the relative counterparts. Grey part means "light off" while white part means "light on".

The grey parts of the graph are related to the period in which the materials are left in the dark, while the white parts are related to the periods of irradiation. The graphs start with the initial irradiation (from 5400 to 6000 s) from the beginning of the chronoamperometry experiment. The photocurrent intensity, on the y-axis, is normalized for the geometric area of the electrodes, which is in all cases equal to 1 cm^2.

As it can be noticed from **Figure 6.2.5** (**a**) and (**b**), bare PCA-RGO working electrodes do not show any photoresponse at both the investigated bias, because of the weak incident light absorption of graphene. Photocurrent signals of graphene are typically recorded under UV-light irradiation and originate from the π-π* transition of the graphene -C=C- bond[6]. Conversely, detectable anodic *I-t* signals have been collected for the OLEA-PbS NCs and PCA-RGO/PbS NCs hybrid material, at +0.8 V (SCE) (**Figure 6.2.5** (**a**)). These photocurrent densities are due to the intrinsic UV-Vis-NIR light harvesting capability of the NCs, which, under illumination, generate electron-hole pairs. These are then separated under the effect of the electric field, created in the accumulation layer of the electrode/solution junction, which predominates on the internal electric field generated at the graphene/NC interphase by their work function mismatch[15]. In the hybrid material, the electrons photogenerated in the NCs are transferred to graphene, yielding to an increase of its Fermi level, and concomitantly, the photogenerated holes are transferred to the electrode/electrolyte junction for oxidizing the medium, generating the observed anodic photocurrent. A schematic representation on what it is supposed to be generated in the hybrid is reported in **Figure 6.2.6**.

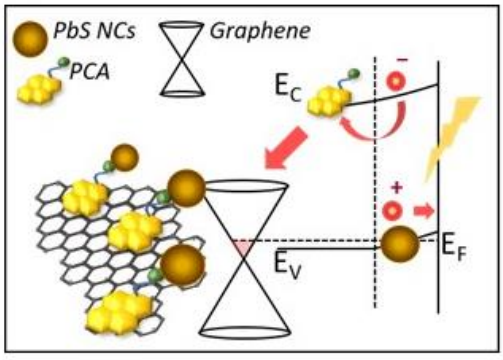

Figure 6.2.6: Scheme of what is happening at the hybrid materials under anodic bias voltage.

The charge transfer from the photoexcited PbS NCs and the PCA-RGO complex occurs thanks to the pyrene linker, which thus behaves as charge transport channel[2,6]. PCA stabilizes the photogenerated charges by the pyrene π system, and transfers them to RGO, where they can be stored in the extended π-π network of the aromatic platform[2,6]. An interesting feature to be noticed is that the anodic photocurrent density of the PCA-RGO/PbS NCs hybrid material is one order of magnitude higher than that of the bare OLEA-PbS NCs. This evidence can be ascribed to the fact that the Dirac point of graphene is lower than the LUMO level of the PbS NC semiconductor, and in addition, it lies in between LUMO of PbS and that of ITO. This fact, together with the extremely high electron mobility of graphene (10^4 cm^2/ V s at room temperature), promotes in general the exciton dissociation. The photogenerated electrons are favoured to pass from PbS to RGO and then to ITO while, concomitantly, the holes are accumulated at the interface electrode/electrolyte, where the reaction of the medium (oxidation) can take place, enhancing the anodic photocurrent density. In more details, thanks to the presence of graphene, the injection barrier at the ITO/PbS NCs interphase is decreased and the charge withdrawn from the photoexcited PbS NCs to ITO is favoured. As a consequence, the hole/electron recombination at the NCs defects is suppressed. Thanks to all these considerations, it is worthwhile noticing that in the case of the hybrid, the photogenerated current is drastically enhanced with respect to the one of the correspondent bare PCA-PbS.

Another peculiarity of the photocurrent density of **Figure 6.2.5** (**a**) is that the typical ON/OFF behaviour is not verified, but there is a steeply increasing photocurrent at each cycle of illumination until it reaches a plateau value, after five cycles of illuminations. Such a finding can be inferred to the fact that when the lamp is turned off, the process of recombination of the photogenerated carriers does not take place completely and the system does not reach the pristine equilibrium condition, resulting in holes trapping in the NCs and accumulation of electrons in the graphene sheets for capacitive coupling. Additionally, the incompletely recovered

photocurrent density increases, until the electric field, caused by the accumulation of charge between graphene and the NCs for charge coupling, balances the electric field at the electrode/electrolyte junction.

At – 0.3 V (**Figure 6.2.5 (b)**), the photocurrent density signal of the bare PCA-RGO complex is absent and the one of the bare OLEA-PbS NCs is negligible with respect to the one observed for the complete hybrid material, which presents a consistent cathodic photocurrent density. This is originated from the separation of the exciton in the NCs, induced by the electric field generated at the depletion layer of the electrode/electrolyte junction. This electric field combines with the internal electric field generated at the interphase between the NCs and graphene[15]. The result is the transfer of the photogenerated holes to graphene, which lead to a decrease of its Fermi level, and in the transfer of photogenerated electrons to the medium, yielding to the cathodic current (schematic representation in **Figure 6.2.7**).

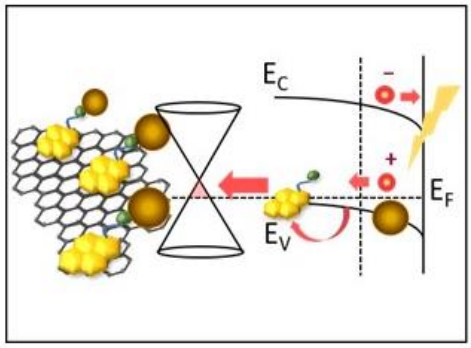

Figure 6.2.7: Scheme of what is happening at the hybrid materials under cathodic bias voltage.

An interesting fact that can be drawn from the comparisons of panel (**a**) and (**b**) of **Figure 6.2.5**, is that the cathodic photocurrent density, recorded at -0.3 V (SCE), of the hybrid is significantly higher than the anodic one, recorded at +0.8 V (SCE). Such a result can be reasonably explained considering the intrinsic *p-type* behaviour of the PbS semiconductor[16]. Such a material, in fact, has the photogenerated holes as majority carriers, and hence behaves as a photo-cathode. Furthermore, the cathodic photocurrent density steeply increases at each cycle of illumination and it is not switched off when the lamp is turned off, showing that also in this condition (as already observed for the anodic photocurrent) the photoelectrode does not reach the pristine equilibrium condition. It can be supposed that the photoelectrons are

accumulated in the NCs, inducing positive charge in the graphene sheets for capacitive coupling and hence the electric field generated at the graphene/NCs interphase. Moreover, the electric field at the electrode/electrolyte junction is in equilibrium, resulting in the plateau value of the cathodic photocurrent after five cycle of irradiation. This enhanced performance of the hybrid, with respect to the single components (in this case the active part under illumination, that is the OLEA-PbS NCs) can be an effective confirmation of the real intimate contact between the two components of the hybrid, in which the electron coupling is assisted and stimulated and in which the recombination process is delayed.

In order to clarify the effect of charging and discharging, and to support the evidences of the photocurrent density measurements, Cyclic Voltammetry (CV) of the working electrodes modified with the PCA-RGO complex, the OLEA-PbS NCs and the PCA-RGO/PbS NCs hybrid were recorded before and after the photocurrent experiments with irradiations.

The CV of the bare OLEA-coated PbS NCs, collected after the photocurrent analyses at + 0.8 V (**Figure 6.2.8 (a)**), presents a large cathodic peak at about – 0.3 V (SCE), which is instead not observed in the CV recorded before the photocurrent measurements (dark line, almost hidden because of the high signals of the other voltammetries). This peak is most likely due to the discharge of the holes accumulated at the electrode/electrolyte junction during the photocurrent experiments.

In fact, as previously mentioned, at this anodic bias voltage the photogenerated holes are accumulated at the electrode/electrolyte interface. These holes can be filled with electrons that are given from the external voltage scan in the cathodic region, resulting in a big discharging peak. The discharging effect is confirmed by the fact that in the second cycle this strong signal is almost disappeared, meaning that the holes were already filled with the first voltage scan.

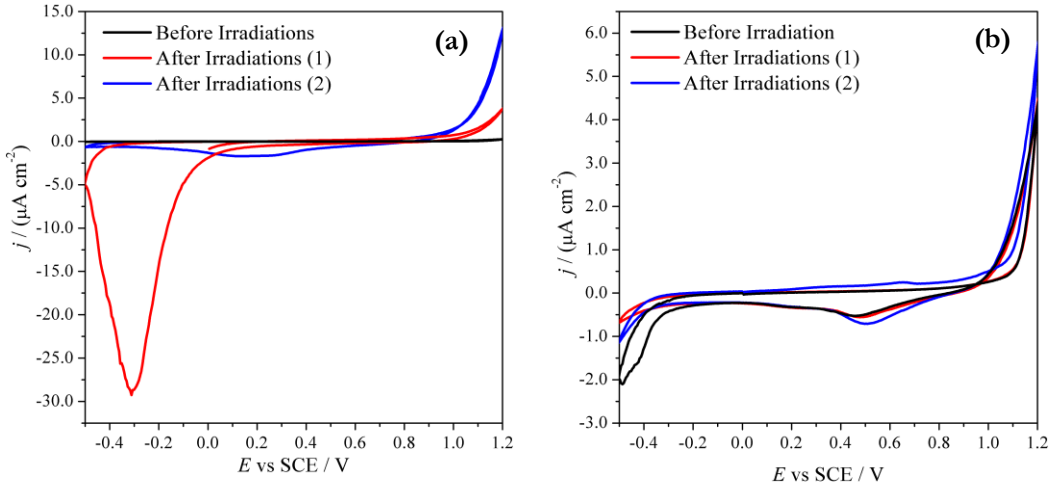

Figure 6.2.8: CV of the OLEA-PbS NCs, recorded at 100 mV s^{-1} in 0.1 M $NaClO_4$, before and after the photocurrent experiments at +0.8 V (**a**) and -0.3 V (**b**).

On the contrary, when the CVs of the OLEA-PbS NCs are collected at – 0.3 V (SCE), a weak cathodic peak, at ca. 0.4-0.5 V, is observed (**Figure 6.2.8 (b)**). Such a signal is observed both before and after the photoelectrochemical experiment, and thus, it is not consequent to the illumination of the electrode, but it is likely due to the reduction of the surface PbO layer, generated by oxidation phenomena occurring onto the PbS NC surface, under illumination and in air.

On the other hand, the CVs of the bare PCA-RGO complex do not show any cathodic signal after the photocurrent experiment at +0.8 V, but at -0.3 V, they show a large anodic peak maybe due to the oxidation of the –COOH and -OH functionalities of the PCA-RGO complex. The fact that this signal is related to an effective structure of the material and not to an accumulation of charges could be explained also by the fact that the peak is not disappearing after the first cycle, as on the contrary happened in the OLEA-PbS system. Even if with lower density current values, the signal is still well visible (**Figure 6.2.9 (a)** and **(b)**).

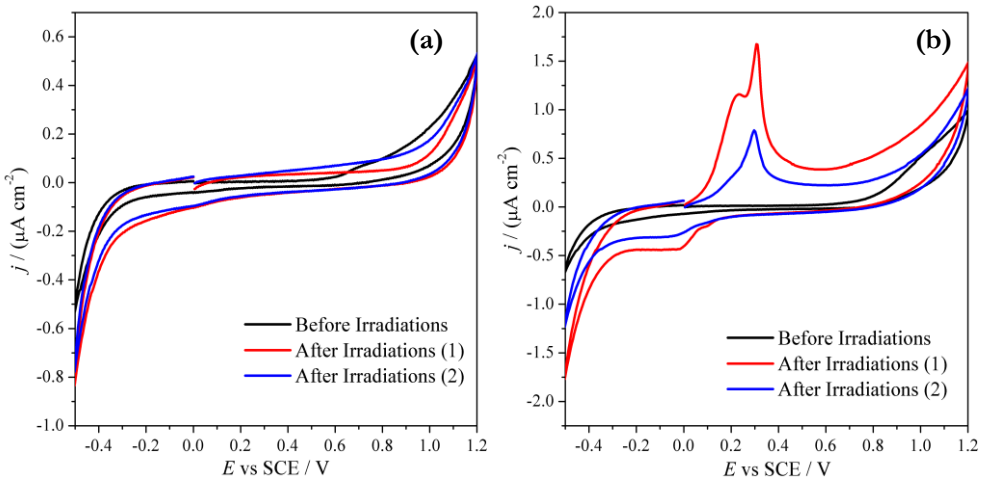

Figure 6.2.9: CV of the bare PCA-RGO complex, recorded at 100 mV s^{-1} in 0.1 M $NaClO_4$, before and after the photocurrent experiments at +0.8 V (**a**) and -0.3 V (**b**).

Finally, the PCA-RGO/PbS NC hybrid material does not present any red/ox signal, irrespectively of the applied bias, thanks to the capability of RGO, to collect, store and stabilize the charge in its extended π-π network (**Figure 6.2.10 (a)** and **(b)**).

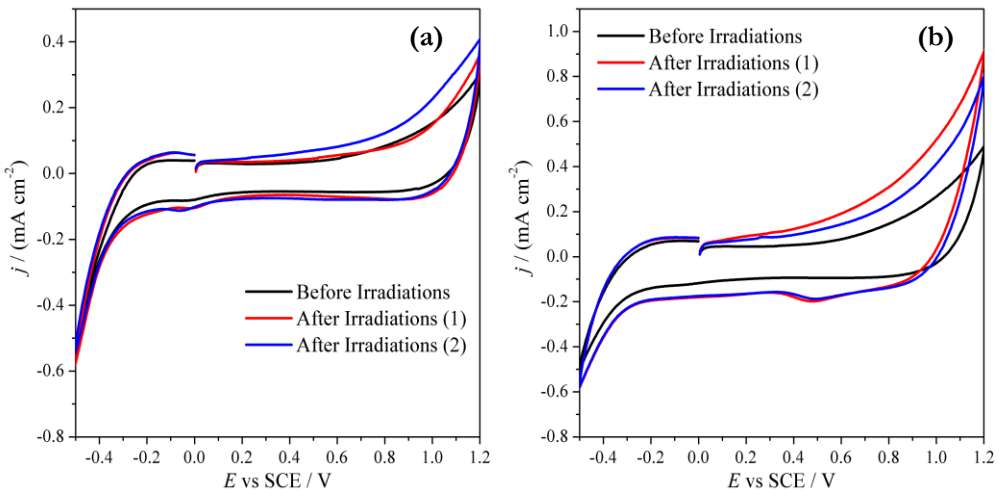

Figure 6.2.10: CV of the PCA-RGO/PbS NCs hybrid, recorded at 100 mV s^{-1} in 0.1 M $NaClO_4$, before and after the photocurrent experiments at +0.8 V (**a**) and -0.3 V (**b**).

Conclusions

In this part of the Thesis Project, a hybrid material based on reduced graphene oxide and semiconducting PbS nanocrystals has been deeply investigated, starting from the synthetic route to the final possible applications. In more details, UV-Vis-NIR light absorbing oleic acid (OLEA)-coated PbS NCs, anchored onto Reduced Graphene Oxide (RGO) flakes, whose surface is functionalized with 1-pyrene carboxylic acid (PCA) has been synthesized by a facile and reproducible *one-pot* and *in-situ* colloidal chemical approach. The principal intended application of such a material is the fabrication of highly photoactive cathodes, but its excellent feature made it a good candidate to be applied in other electronic and sensors (like spectro-electrochemical, photo-chemical) applications.

In the hybrid, both OLEA and PCA behave as capping ligands, allowing a reproducible control on the nano-object morphology. The carboxyl functionalities of the PCA-RGO complex act as nucleation and growth sites for the PbS nanocrystals, allowing a uniform coating density. Since the interlayer distance between PCA and RGO is short, also the coupling length between the nanocrystals and graphene is limited. This fact allows relaxation of the eventually photogenerated exciton in PbS NCs into RGO by charge transfers, resulting in a combination of the size tunable UV-Vis-NIR light-harvesting properties of the PbS NCs and the outstanding capability of graphene in extracting and transferring the photogenerated excitons. In this way, limitations of the relatively low conductive NCs films are overcome and the result is also a strong quenching of the NCs emission. Indeed, the manufactured photocathodes show a photoelectric conversion efficiency enhanced with respect to those of the single components, with a (cathodic) photocurrent density of -4 $\mu A\ cm^{-2}$ under the illumination of lamp source at 900 nm and light intensity of $(4.794 \pm 0.002)\ \mu W\ cm^{-2}$, resulting promising for photovoltaics, FETs and photodetectors.

Finally, the investigated synthetic strategy can be extended to the preparation of other hybrid materials made of colloidal NCs, having different sizes, shapes and

chemical compositions (metals, metal oxides, semiconductors), and hence exhibiting properties appealing for different technological applications.

Bibliography

(1) Zhu, Y.; Murali, S.; Cai, W.; Li, X.; Suk, J. W.; Potts, J. R.; Ruoff, R. S. Graphene and Graphene Oxide: Synthesis, Properties, and Applications. *Adv. Mater.* **2010**, *22* (35), 3906–3924.

(2) Ingrosso, C.; Bianco, G. V.; Corricelli, M.; Comparelli, R.; Altamura, D.; Agostiano, A.; Striccoli, M.; Losurdo, M.; Curri, M. L.; Bruno, G. Photoactive Hybrid Material Based on Pyrene Functionalized PbS Nanocrystals Decorating CVD Monolayer Graphene. *ACS Appl. Mater. Interfaces* **2015**, *7* (7), 4151–4159.

(3) Moreels, I.; Lambert, K.; Smeets, D.; De Muynck, D. Size-Dependent Optical Properties of Colloidal PbS Quantum Dots. *ACS Nano* **2009**, *3* (10), 3023–3030.

(4) Curri, M. L.; Comparelli, R.; Striccoli, M.; Agostiano, A. Emerging Methods for Fabricating Functional Structures by Patterning and Assembling Engineered Nanocrystals. *Phys. Chem. Chem. Phys.* **2010**, *12* (37), 11197–11207.

(5) Kang, I.; Wise, F. W. Electronic Structure and Optical Properties of PbS and PbSe Quantum Dots. *J. Opt. Soc. Am. B* **1997**, *14* (7), 1632.

(6) Ingrosso, C.; Bianco, G. V.; Pifferi, V.; Guffanti, P.; Petronella, F.; Comparelli, R.; Agostiano, A.; Striccoli, M.; Palchetti, I.; Falciola, L.; et al. Enhanced Photoactivity and Conductivity in Transparent TiO2 Nanocrystals/Graphene Hybrid Anodes. *J. Mater. Chem. A* **2017**, *5* (19), 9307–9315.

(7) Mnoyan, A.; Kim, K.; Kim, J. Y.; Jeon, D. Y. Colloidal Nanocomposite of Reduced Graphene Oxide and Quantum Dots for Enhanced Surface Passivation in Optoelectronic Applications. *Sol. Energy Mater. Sol. Cells* **2016**, *144*, 181–186.

(8) Kim, B. S.; Neo, D. C. J.; Hou, B.; Park, J. B.; Cho, Y.; Zhang, N.; Hong, J.; Pak, S.; Lee, S.; Sohn, J. I.; et al. High Performance PbS Quantum Dot/Graphene Hybrid Solar Cell with Efficient Charge Extraction. *ACS Appl. Mater. Interfaces* **2016**, *8* (22), 13902–13908.

(9) Martín-García, B.; Polovitsyn, A.; Prato, M.; Moreels, I. Efficient Charge Transfer in Solution-Processed PbS Quantum Dot-Reduced Graphene Oxide Hybrid Materials. *J. Mater. Chem. C* **2015**, *3* (27), 7088–7095.

(10) An, X.; Simmons, T.; Shah, R.; Wolfe, C.; Lewis, K. M.; Washington, M.; Nayak, S. K.; Talapatra, S.; Kar, S. Stable Aqueous Dispersions of Noncovalently

Functionalized Graphene from Graphite and Their Multifunctional High-Performance Applications. *Nano Lett.* **2010**, *10* (11), 4295–4301.

(11) Corricelli, M.; Altamura, D.; De Caro, L.; Guagliardi, A.; Falqui, A.; Genovese, A.; Agostiano, A.; Giannini, C.; Striccoli, M.; Curri, M. L. Self-Organization of Mono- and Bi-Modal PbS Nanocrystal Populations in Superlattices. *CrystEngComm* **2011**, *13* (12), 3988–3997.

(12) Hines, M. A.; Scholes, G. D. Colloidal PbS Nanocrystals with Size-Tunable Near-Infrared Emission: Observation of Post-Synthesis Self-Narrowing of the Particle Size Distribution. *Adv. Mater.* **2003**, *15* (21), 1844–1849.

(13) Konios, D.; Stylianakis, M. M.; Stratakis, E.; Kymakis, E. Dispersion Behaviour of Graphene Oxide and Reduced Graphene Oxide. *J. Colloid Interface Sci.* **2014**, *430*, 108–112.

(14) Lee, P. Y.; Chang, S. P.; Chang, S. J. Photoelectrochemical Characterization of N-Type and p-Type Thin-Film Nanocrystalline Cu2ZnSnSe4 Photocathodes. *J. Environ. Chem. Eng.* **2015**, *3* (1), 297–303.

(15) Cells, D. S.; Yang, N.; Zhai, J.; Wang, D.; Chen, Y.; Jiang, L. Two-Dimensional Graphene Bridges Enhanced Photoinduced Charge. *ACS Nano* **2010**, *4* (2), 887–894.

(16) Sun, Z.; Liu, Z.; Li, J.; Tai, G. A.; Lau, S. P.; Yan, F. Infrared Photodetectors Based on CVD-Grown Graphene and PbS Quantum Dots with Ultrahigh Responsivity. *Adv. Mater.* **2012**, *24* (43), 5878–5883.

Acknowledgments

I gratefully acknowledge Dr. C. Ingrosso and Dr. M. L. Curri from CNR-IPCF S. S. Bari, Department of Chemistry, Università di Bari (Bari, Italy) for the synthesis and physico-chemical characterizations of the hybrid material.

7.

Conclusions

This PhD Thesis Project was focused on the study of hybrid nanomaterials for the general purpose of creating electroanalytical sensors. The applications of such devices were verified to be the most various ones, from environmental to medical fields. The systems investigated were composed mainly by three big families of materials: *metals*, *graphene* and *semiconductors*, in different conformations and combinations. For each material, a preliminary electrochemical characterization permitted, in almost all cases, to effectively verify the presence of interfaces between the components, allowing to talk about real hybrid materials. Then, their subsequent application, when possible, for electroanalytical purposes strengthened the thesis that the hybrids possess enhanced performances with respect to their single components, allowing to increase the selectivity and sensitivity and to lower the detection limits of the electroanalytical techniques.

Concerning *metal-metal* hybrids, the creation of bimetallics that are completely new materials with respect to their starting monometallic components was verified. These systems showed strong electrocatalytic effects and different selectivity when applied for the detection of target analytes. Apart from these good results, in this part of the Thesis Project it was demonstrated how it is possible to involve electrochemistry not only as analytical technique, but also as a characterization tool. In fact, results obtained from the electrochemical data, compared to others gained by conventional physico-chemical characterization techniques, allowed to draw the same conclusions. Moreover, it was verified also the possibility to study the evolution of bimetallic systems during time: a result that it is not always achievable with other techniques. Such a finding is of great interest, since electrochemistry is serving here as a simple, easy to use, low cost and alternative tool to know the structure of a system, without applying other expensive and not so easily accessible techniques, in particular for a preliminary survey of the material.

Always concerning *metal* modified systems, the interest was then moved towards *metal-semiconductor* hybrids. In more details, Au/TiO_2 systems were verified not to be

real hybrids, since the presence of an interface is still to be clarified and seemed not to be created. By the way, the presence of both the components in the final system was exploited in any case, since a promising device for the detection of emerging contaminants in water was finalized. The presence of gold nanoparticles was essential to detect the target analyte (Diclofenac), while the presence of the top layer of titanium dioxide was essential to renew the electrode surface after its fouling and passivation. In this way, a suitable device for *on-line, on-site* and *continuous* monitoring of contaminants is created, also answering to the actual need expressed by the Legislation.

Passing to another fascinating material, that is *graphene*, hybrids composed by graphene (and its derivatives) and *metals* nanoparticles were involved for the finalization of sensors for environmental and diagnostic interest. In more details, device for the detection of Arsenic were optimized, achieving good detection limits, in the ppb range. It was verified the effective formation of a hybrid by deeply studying each component compared with the final system, always underlying the enhancement in the results gained with the hybrid. The same was observed for similar materials that were then applied for the detection of analytes of medical interest, such as the neurotransmitters family. Also in this case, good results (in the ppb range), in accordance with the benchmark of such molecules and comparable to other analytical techniques in the field were achieved. Among the *graphene-based* materials, also the bio-sensing field was investigated, by constructing *ad-hoc* nitrocellulose-based electrodes to be applied for the detection of immunoglobulins with promising results. An innovative printing technique was involved for the creation of the platforms and the electrodes were literally *hand-made* ultimated, evidencing the possibility to lower the production cost of the materials.

Graphene was studied also in combination with *semiconductor* nanomaterials, also employing the use of light in order to verify the effective presence of a hybrid structure. The final application of these systems was similar to the one previously

reported (in general, neurotransmitters detection). Apart from the encouraging results gained in this context, a deep characterization of the materials looking at the modification of the electrochemical response by changing the electrode surface morphology was conducted. It was verified how an electrochemical characterization could give important information on the surface structure of a material as well as on the presence of impurities (such as functional groups, defects and so on), supporting once more the previous thesis on the possibility to enrol electrochemistry not only as analytical technique but also as characterization tool.

Most of the works explained in the Chapters of this Thesis are still in progress and future developments could be planned for all the different projects. In fact, all the promising results obtained with the applications of the hybrids materials open the venue to their applications in the most various fields, from sensing to catalysis, from electronics to energetics, also allowing to think about multi-purpose, user-friendly and smart devices.

8.

Appendix

Analytical Parameters

All the analytical parameters were determined according to the IUPAC protocols:

- **Limit of detection:** inferior limit of concentration where the analyte can be distinguished from the blank.

$LoD = \frac{3.29\times \sigma_{Blank}}{S}$, where *S*, indicating the method calibration sensitivity, is the slope of the linear calibration plot, and σ_{blank} is the blank standard deviation. When no blank signal could be detected, σ_{blank} was estimated by the standard deviation of 10 repeated scans on the same solution of the lowest available standard;

- **Limit of quantification:** inferior limit of analyte concentration measured with an acceptable precision and accuracy level.

$LoQ = \frac{10\times \sigma_{Blank}}{S}$, where *S*, indicating the method calibration sensitivity, is the slope of the linear calibration plot, and σ_{blank} is the blank standard deviation. When no blank signal could be detected, σ_{blank} was estimated by the standard deviation of 10 repeated scans on the same solution of the lowest available standard;

- **Relative standard deviation:** absolute value of the coefficient of variation.

$RSD\ \% = \frac{\sigma_{Blank}}{\bar{x}} \times 100$, where σ_{blank} is the blank standard deviation, estimated by the standard deviation of 10 repeated scans on the same solution of the lowest available standard, and $\bar{x}$ is the average value, calculated on the 10 repeated scans;

- **Apparent recovery factor:** observed value, x_{obs}, derived from an analytical procedure by means of a calibration graph divided by reference value, x_{ref}, indicating the trueness of the method (higher trueness when close to 100%)

$$RF = \frac{x_{obs}}{x_{ref}} \times 100$$

Electroanalytical Techniques (outlines)

- **Cyclic Voltammetry (CV)**

In this technique, the potential of a working electrode is varied linearly with time until a step potential, where the potential ramp is inverted, and the resulting current is measured. This method allows characterizing the electrodes, in terms of capacitance, surface area, diffusion coefficient of the analyte, rate determining steps and reversibility.

Electrode capacitance ***C*** can be calculated varying the scan rate without the presence of the analyte, from the slope of the plot Δi *vs* scan rate, derived from the equation $\frac{i_a - i_c}{2} = Cv$. In more details, a fixed voltage value is chosen, in which no Faradaic current are present. The related anodic (i_a) and cathodic (i_c) capacitive current are read. Then, $((i_a - i_c)/2)$ is calculated and plotted against the voltage scan rate. From the slope of the relative curve capacitance values are derived.

When the analyte is present and is electroactive, several calculations could be done in order to understand the mechanism of diffusion of the probe towards the electrode and the electrochemical reversibility or irreversibility of the reaction. In more details, if the plot $\boldsymbol{i_p}$ ***vs*** $\boldsymbol{v^{0.5}}$, obtained by *Randles-Sevcik* equation $i_p = 0.4463\, nFAc\left(\frac{nFvD}{RT}\right)^{0.5}$, [where i_p is the peak current, n the number of electrons transferred in the redox event, A the electrode area, F the Faraday Constant, D the diffusion coefficient, c the bulk concentration and v the scan rate], is linear, the rate determining step is the diffusion of the analyte to the electrode. On the other hand, if the peak current is proportional to the scan rate the rate determining step is the absorption of the analyte on the electrode. Moreover, the slope of the Randles-Sevcik plot can give information about the diffusion coefficient of the analyte and the surface area of the electrode.

Information about the diffusion mechanism can be obtained also from the slope of the $\ln(i_p)$ *vs* $\ln(v)$ plot, since the perfect planar diffusional behaviour gives a slope of 0.5.

A detailed description of the technique can be found in many dedicated books (Bard & Faulkner, 2001; Bard, 2007; C. M. A. Brett & Oliveira Brett, 1993; R. G. Compton, C. E. Banks, 2011).

- **Electrochemical Impedance Spectroscopy (EIS)**

This technique measures the impedance (Z) of a system over a range of frequencies as a result of the perturbation of an applied potential or current. In this thesis, only the applied potential was employed to characterize electrodes. Impedance data can be presented using two types of plot: **complex plane** or **Nyquist** plot, the imaginary part of impedance (Z'') *vs* the real part (Z'), and the **Bode** plots: $|Z|$ *vs* frequency or phase angle *vs* frequency. Moreover, from the fitting of impedance data, information about the morphology of the electrode surface and the electrical properties can be obtained, after the choice of the electrical circuit corresponding to the electrochemical system.

In the equivalent circuit, capacitance and resistance can be found in series or in parallel and in different combinations. In more details, CPE (instead of normal capacitance, C) is defined as **constant phase element**. CPE = $[(Ci\omega)^{a}]^{-1}$, is modelled as pure capacitor in the case of $\alpha = 1$ or as non-ideal capacitor, due to the porosity and non-homogeneity of the surface, for $0.5 < \alpha < 1$. Other parameters than can be found in an equivalent circuit are the diffusional resistance R_W and the diffusional time constant τ of the Open Warburg Element, resulting from the equation $Z_W = R_W \mathrm{cth}[(\tau i\omega)^{a}](\tau i\omega)^{-a}$, where $\alpha < 0.5$.

A detailed description of the technique can be found in many dedicated books (Bard, 2007; Orazem & Tribollet, 2008).

- **Other voltammetric or amperometric techniques**

This is the list of all the employed electrochemical techniques with a brief description. A detailed description of all the techniques can be found in many dedicated books (Bard & Faulkner, 2001; Bard, 2007; C. M. A. Brett & Oliveira Brett, 1993) and it is out of the scope of this Thesis:

- **Linear Sweep Voltammetry (LSV)**: the potential of a working electrode is varied linearly with time and the resulting current is measured;
- **Linear Sweep** Anodic**Stripping Voltammetry (LSAdSV)**: preconcentration deposition is performed before LSV stripping;
- **Differential Pulse Voltammetry (DPV)**: a series of regular voltage pulses is superimposed on the potential linear sweep and the current is measured before and after the imposed pulse; the difference of the two measurements (differential measurement) is plotted against the voltage;
- **Chronoamperometry:** the potential is maintained at a chosen value and the resulting current is measured during time.

List of Papers and Communications produced during the PhD period

Papers:

Published:

Pifferi, V., Chan-Thaw, C.E., Campisi, S., Testolin, A., Villa, A., Falciola, L., Prati, L. "Au-based catalysts: Electrochemical Characterization for Structural insights", *Molecules*, (2016), 21, 261, doi: 10.3390/molecules21030261

Bettazzi, F., Laschi, S., Voccia, D., Gellini, C., Pietraperzia, G., Falciola, L., Pifferi, V., Testolin, A., Ingrosso, C., Placido, T., Comparelli, R., Curri, M.L., Palchetti, I., "Ascorbic acid-sensitized Au nanorods-functionalized nanostructured TiO_2 transparent electrodes for

photoelectrochemical genosensing", *Electrochimica Acta,* (2018), 276, 389-398, doi: 10.1016/j.electacta.2018.04.146.

Testolin, A., Cattaneo, S., Wang, W., Wang, D., Pifferi, V., Prati, L., Falciola, L., Villa, A. "Cyclic Voltammetry Characterization of Au, Pd, and AuPd Nanoparticles Supported on Different Carbon Nanofibers", *Surfaces*, (2019), 2, 205-215, doi: doi:10.3390/surfaces2010016

Giacomelli, C., Alvarez D., R., Testolin, A., Merkoci, A. "Laser Scribing of Graphene Oxide Yielding Multipurpose Stamped Nano Films", *2D Materials – accepted, in press*

In preparation:

Testolin, A., Pifferi, V., Prabhudev, S., Botton, G. A., Prati, L., Villa, A., Falciola, L. *"Investigating the formation and final structure of AuPt Bimetallic Nanoparticles by Cyclic Voltammetry"*

Ingrosso, C., Testolin, A., Pifferi, V., Falciola, L., Palchetti, I. et al. "*Colloidal Au NPs decorated Reduced Graphene Oxide based hybrid nanocomposite for (bio)sensors"*

Ingrosso, C., Valenzano, V, Corricelli M., Testolin, A., Pifferi, V., Comparelli, R., Depalo, N., Striccoli, M., Agostiano, A., Falciola, L., Curri, M.L. *"Highly Photoactive Colloidal PbS Nanocrystal/Reduced Graphene Oxide based Photocathode"*

Book Chapters:

Pifferi, V., Testolin, A., Falciola, L., "Metal-free Doped Carbons for Electroanalytical Sensors", (2018), pp.304-325, DOI:10.1039/9781788013116-00304, In *Metal-free Functionalized Carbons in Catalysis: Synthesis, Characterization and Applications* - ISBN:9781782628637

Falciola, L. Pifferi, V., Testolin, A., "Detection Methods of Wastewater contaminants: state of the art and role of nanotechnology" (2019) in *Nanomaterials for the detection and removal of wastewater pollutants* (Elsevier) - *accepted*

Communications:

The presenting author is underlined

Testolin A., Pifferi V., Chan-Thaw C.E., Campisi S., Villa A., Prati L., Falciola L. (2016) *"Electrochemical characterization of Au/Pd catalysts"* – Poster Contribution
Giornate dell'Elettrochimica Italiana (GEI) (Gargnano, BS, Italy, 11 – 14 September 2016)

Guffanti P., Testolin A., Pifferi V., Ingrosso C., Bianco G.V., Petronella F., Comparelli R., Agostiano A., Striccoli M., Palchetti I., Curri M.L., Bruno G., Falciola L. (2017). *"Synthesis and Electrochemical Characterization of TiO_2 Nanocrystals Decorated CVD Graphene Hybrid Materials"* – Poster Contribution
RSC Twitter Poster Conference (20 - 21 March 2017)

Testolin A., Guffanti P., Pifferi V., Chan-Thaw C.E., Campisi S., Villa A., Prati L., Falciola L. (2017). *"An Electrochemical Investigation for Structural Insights of Au/Pd Catalysts"* – Poster Contribution
RSC Twitter Poster Conference (20 - 21 March 2017)

Testolin A., Guffanti P., Pifferi V., Ingrosso C., Bianco G.V., Petronella F., Comparelli R., Agostiano A., Striccoli M., Palchetti I., Curri M.L., Bruno G., Falciola L. (2017). *"CVD graphene decorated with colloidal titanium oxide nanocrystals: (photo) electrochemical characterization and electroanalytical applications"* – Poster Contribution
21st ISE Topical Meeting (Szeged, Hungary, 23 - 26 April 2017)

Falciola, L., Guffanti, P., Pifferi, V., Testolin, A., Ingrosso, C., Petronella, F., Comparelli, R., Agostiano, A., Striccoli, M., Curri, M.L, Bianco G.V., Bruno G., Palchetti I., *"(Photo)Electrochemically Active Functional Hybrids of Multilayer CVD Graphene Decorated with Colloidal TiO_2 Nanocrystals"* – Invited Oral
68th ISE Annual Meeting (Providence, RI, 27 August – 1 September 2017)

Testolin, A., Pifferi, V., Falciola, L., Guffanti, P., Ingrosso, C., Petronella, F., Comparelli, R., Agostiano, A., Striccoli, M., Curri, M.L, Bianco G.V., Bruno G., Palchetti I., *"Functional hybrids of multilayer CVD graphene and colloidal anatase nanocrystals"* – Oral Contribution
Giornate dell'Elettrochimica Italiana (GEI) (Sestriere, TO, Italy, 21 – 25 January 2018)

Testolin, A., Pifferi, V., Falciola, L., Ingrosso, C., Petronella, F., Comparelli, R., Agostiano, A., Striccoli, M., Curri, M.L, Bettazzi F., Palchetti I., *"Electrochemical characterization and electroanalytical applications of RGO-AuNPs Hybrids"* – Poster Contribution
Giornate dell'Elettrochimica Italiana (GEI) (Sestriere, TO, Italy, 21 – 25 January 2018)

Falciola, L., Pifferi, V., Testolin, A., Turrisi, R., Bertoncello, S., Carminati, M., Turolla, A., Antonelli, M.., "*Photo-Renewable conductivity and pH electroanalytical sensors for on-line monitoring of drinking water quality"* - Poster Contribution
Giornate dell'Elettrochimica Italiana (GEI) (Sestriere, TO, Italy, 21 – 25 January 2018)

Testolin, A., Pifferi, V., Falciola, L., Ingrosso, C., Petronella, F., Comparelli, R., Agostiano, A., Striccoli, M., Curri, M.L, Bettazzi, F., Palchetti I., *"Understanding the Electrochemical Behaviour of RGO-AuNPs Hybrids: from Characterization to Applications"* – Poster Contribution
RSC Twitter Poster Conference (6 - 7 March 2018)

Testolin, A., Pifferi, V., Villa, A., Falciola, L., *"Cyclic Voltammetry as a powerful tool for the understanding of the evolution in time of bimetallic Au/Pt systems"* – Poster Contribution
69th ISE Annual Meeting (Bologna, BO, Italy, 2 – 7 September 2018)

Palchetti, I., Bettazzi, F., Falciola, L., Pifferi, V., Testolin, A., Ingrosso, C., Corricelli, M., *"Colloidal Nanoparticle modified Graphene-based Elecrochemical Platforms for Nucleic Acid Biosensing"*
69th ISE Annual Meeting (Bologna, BO, Italy, 2 – 7 September 2018)

Bettazzi, F., Laschi, S., Falciola, L., Pifferi, V., Testolin, A., Ingrosso, C., Placido, T., Comparelli, R., Curri, M.L., Palchetti, I., *"Au NRs-functionalized nanostructured TiO_2 Sensor for Photoelectrochemical Genosensing"*
69th ISE Annual Meeting (Bologna, BO, Italy, 2 – 7 September 2018)

Testolin, A., Pifferi, V., Falciola, L., Ingrosso, C., Petronella, F., Comparelli, R., Agostiano, A., Striccioli, M., Curri, M.L., Bettazzi, F., Palchetti, I., *"Exploring the potentiality of RGO-AuNPs hybrids towards electroanalytical sensor applications"* – Oral Contribution
69th ISE Annual Meeting (Bologna, BO, Italy, 2 – 7 September 2018)

Testolin, A., Pifferi, V., Falciola, L., Ingrosso, C., Petronella, F., Comparelli, R., Agostiano, A., Striccioli, M., Curri, M.L., Bettazzi, F., Palchetti, I., *"Potentialities of hybrid materials based on RGO and AuNPs towards electroanalytical applications"* – Oral Contribution
18th Merck & Elsevier Young Chemist Symposium (MEYCS) (Rimini, RN, Italy, 19 – 21 November 2018)

Pifferi, V., Ferrari, E., Testolin, A., Ranucci, E., Ferruti, P., Manfredi, A.G., Falciola, L., *"Cyclodextrins nanosponges as o-toluidine sorbents"* – Poster Contribution
Milan Polymers Days 2019 (MIPOL 2019) (Milano, MI, Italy, 11 - 13 March 2019)

Testolin, A., Pifferi, V., Cattaneo, S., Villa, A., Falciola, L. *"Investigation of Gold-Based Bimetallic System via Cyclic Voltammetry"* – Poster Contribution
RSC Twitter Poster Conference (5 - 6 March 2019)

Testolin, A., Pifferi, V., Falciola, L., Ingrosso, C., Corricelli, M., Agostiano, A., Striccioli, M., Curri, M.L., Bettazzi, F., Palchetti, I., *"Enhanced performances of RGO-AuNPs hybrids towards electroanalytical applications"* – Poster Contribution
International Workshop on Electrochemistry of Electroactive Materials (WEEM 2019) (Borovets, Bulgaria, 16 – 21 June 2019)

Testolin, A., Pifferi, V., Falciola, L., Ingrosso, C., Corricelli, M., Agostiano, A., Striccioli, M., Curri, M.L., Bettazzi, F., Palchetti, I., "*An Electrochemical Approach to Understand the Enhanced Performances of Gold-Based Hybrid Nanomaterials"* – Poster Contribution
Chemitry meets Industry and Society (CIS 2019) (Salerno, SA, Italy, 28-30 August 2019)

Testolin, A., Pifferi, V., Cattaneo, S., Balerna, A., Evangelisti, C., Villa, A., Falciola, L., "*Voltammetric Characterization of Gold-Based Bimetallic (AuPt; AuPd; AuAg) Nanoparticles"* – Poster Contribution
Giornate dell'Elettrochimica Italiana (GEI) (Padova, PD, Italy, 8 – 12 September 2019)

Pifferi, V., Di Liberto, G., Riva, A., Testolin, A., Falciola, L., "*Metal-Semiconductors Hybrids for Electroanalytical Purposes"* – Oral Contribution
Giornate dell'Elettrochimica Italiana (GEI) (Padova, PD, Italy, 8 – 12 September 2019)

Acknowledgements

At the end of these three years I have to thank many people who have accompanied me along the path and in some way have contributed to achieving this goal.

The first big thanks goes to the supervisor of this Thesis, Prof. Falciola. Luigi, thank you. I started working in your research group during the internship of the Bachelor Degree and since then I have never left. You made me grow up not only from a scientific point of view, supporting me always with extreme enthusiasm in all my decisions. You have believed in me since the beginning by allowing me to work independently, without ever letting me miss your support in times of need. You encouraged me to travel, to meet colleagues in Italy and abroad, which allowed me to enrich my cultural and personal background. Thanks.

Thanks Vale, for being my guide during the Bachelor's, the Master's thesis and finally during the PhD. Thank you for being my point of reference and above all for being before a colleague, a friend.

A sincere thanks to all the collaborators who have contributed to the realization of various projects in this Thesis: Alberto and Stefano of the MatHeC group of UniMi, Chiara and all the colleagues of the CNR-IPCF, Department of Chemistry, University of Bari, Ilaria and Francesca from UniFi, Antonella from INFN of Frascati, Claudio from the CNR of Milan and all their collaborators. Your contribution has been precious.

Thanks to my supervisor in Spain, Prof. Merkoçi, for allowing me to work in his research labs for nine months, during one of the best experiences of my life. The possibility of doing research in a forefront center, in an international context, has certainly enriched me professionally but above all personally. Thanks also to all the people in the group with whom I was able to work, with a particular thought for Bernardo, a reference electrochemist especially in the first period of setting in a new working context, and to Lorenzo, dispenser of scientific and survival advice.

Thanks to Caterina, brilliant mind and example of determination and enthusiasm. Thank you for being the best colleague, the best roommate and the best friend I could have ever desired during my time abroad.

I thank all the colleagues of the research groups of Prof. Ardizzone and Prof. Cappelletti, who have certainly contributed to making the workplace a welcoming place over the past three years. In particular thanks to Giuseppe, for all the valuable advices but also for the moments of leisure during the lunch break. Eleonora, the special colleague with whom I shared this PhD course from the beginning to the end. You are one of the most helpful people I know, always ready to help me and listen to me. I admire your determination and stubbornness in reaching a goal, never disrespecting anyone. I wish you all the best that the future is reserving.

Thanks to all the trainees who have populated the laboratory during these three years. Thank you for having chosen to work in our research group and above all for making the work environment so pleasant. I will not name you all because you are so many, but thank you, there is a small part of each of you in this Thesis.

A special thought to a particular trainee, by now a skilled chemist, Valentina. You came suddenly into our labs and suddenly you won me over. Although I was the PhD student, how many things I learned from you! Extremely curious, brilliant and resourceful mind. Thanks for the countless laughs, for the endless chats (even on Skype from one hemisphere to another) and for all the valuable advices. I have found in you a sincere friend.

And now a thought for those people who have shared the life with me outside the workplace.

Thanks to my friends, those of always and from always. Elo, to be by my side even if kilometers and nations separate us. Tina, Lallo, thank you for staying even after the worst storms. I know I can count on you.

Thanks Denis, for having found me in one of the most chaotic moments of my life and for having started, together with me, to put the pieces back in order. Everything is more beautiful and lighter since you are with me.

Thanks to my sister Silvia, an example from always. In silence and with extreme respect you have constantly supported me and understood me.

Finally, the biggest thanks goes to my parents. Mom, Dad, thanks for supporting and enduring me during this time (you are the real heroes of this PhD!). You have always supported me in all the choices I have made so far and I am sure that I will always have your support and your understanding whatever path I decide to take.

If I have arrived here, I owe it to you above all.

Anna

Ringraziamenti

Alla fine di questi tre anni sento di dover ringraziare numerose persone che mi hanno accompagnata durante il percorso e in qualche modo hanno contribuito al raggiungimento di questo traguardo.

Il primo grande e doveroso grazie va al relatore di questa tesi, Prof. Falciola. Luigi, grazie. Ho iniziato a lavorare nel tuo gruppo di ricerca durante il tirocinio triennale e da quel momento non me ne sono più andata. Mi hai cresciuta non solo scientificamente, supportandomi in ogni momento e sostenendomi con stima ed entusiasmo in tutte le mie decisioni. Hai creduto in me sin dall'inizio concedendomi di lavorare in autonomia, senza mai farmi mancare il tuo appoggio nei momenti di bisogno. Mi hai spronata a viaggiare, a conoscere colleghi in Italia e all'estero, che mi hanno consentito di arricchire il mio bagaglio culturale e personale. Grazie.

Grazie Vale, per essere stata la mia guida durante il tirocinio, la tesi magistrale e infine durante il dottorato. Grazie per essere stata il mio punto di riferimento e soprattutto per essere prima che una collega, un'amica.

Un doveroso ringraziamento a tutti i collaboratori che hanno contribuito alla realizzazione di diversi progetti in questa Tesi: Alberto e Stefano del gruppo MatHeC di UniMi, Chiara e tutti i colleghi del CNR-IPCF e CNR-NANOTEC, Dipartimento di Chimica, Università di Bari, Ilaria e Francesca da UniFi, Antonella dall' INFN di Frascati, Claudio dal CNR di Milano e tutti i loro collaboratori. Il vostro contributo è stato prezioso.

Grazie al mio supervisore in Spagna, Prof. Merkoçi, per avermi consentito di lavorare nei suoi laboratori di ricerca per nove mesi, durante una delle esperienze più belle della mia vita. La possibilità di fare ricerca in un centro all'avanguardia, in un contesto internazionale, mi ha sicuramente arricchito professionalmente ma soprattutto personalmente. Grazie anche a tutte le persone del gruppo con cui ho avuto modo di lavorare, con un particolare pensiero a Bernardo, elettrochimico di riferimento

soprattutto nel primo periodo di ambientazione in un nuovo contesto lavorativo, e a Lorenzo, dispensatore di consigli scientifici e di sopravvivenza. Grazie a Caterina, mente brillante ed esempio di determinazione ed entusiasmo. Grazie per essere stata la migliore collega, la migliore coinquilina e la migliore amica che mai avrei potuto desiderare durante il mio periodo all'estero.

Ringrazio tutti i colleghi dei gruppi di ricerca della Prof.ssa Ardizzone e Prof. Cappelletti, che lungo questi tre anni hanno sicuramente contribuito a rendere l'ambiente di lavoro un posto accogliente. Grazie Giuseppe, per tutti i preziosi consigli ma anche per i momenti di svago in pausa pranzo. Eleonora, la speciale collega con cui ho condiviso dall'inizio alla fine questo percorso di dottorato. Sei una delle persone più disponibili che io conosca, sempre pronta ad aiutarmi ed ascoltarmi. Di te ammiro la determinazione e la caparbietà nel raggiungere un obiettivo, senza mai mancare di rispetto a nessuno. Ti auguro tutto ciò che di più bello il futuro stia riservando.

Grazie a tutti i ragazzi, tesisti e tirocinanti, che durante questi tre anni hanno popolato il laboratorio. Vi ringrazio per aver scelto di lavorare nel nostro gruppo di ricerca e soprattutto per aver reso l'ambiente di lavoro così piacevole e spensierato. Non vi nomino tutti quanti perché siete davvero tantissimi, ma grazie, vi assicuro che c'è una piccola parte di ognuno di voi in questa tesi.

Un pensiero particolare ad una tesista particolare, ormai chimica affermata, Valentina. Sei arrivata all'improvviso nei nostri laboratori e all'improvviso mi hai conquistata. Nonostante io fossi la dottoranda, quante cose ho imparato da te! Estremamente curiosa, mente brillante e intraprendente. Grazie per le innumerevoli risate, per le chiacchierate infinite (anche su Skype da un emisfero all'altro) e per i preziosi consigli. In te ho trovato un'amica sincera.

Ed ora un pensiero a quelle persone che mi sono state accanto al di fuori del contesto lavorativo.

Grazie ai miei amici, quelli di sempre e da sempre. Elo, per essere al mio fianco anche se ci separano chilometri e nazioni. Tina, Lallo, grazie per essere rimasti anche dopo le peggiori tempeste. So di poter contare su di voi.

Grazie Denis, per avermi trovata in uno dei momenti più caotici della mia vita e per aver iniziato, insieme a me, a rimetterne in ordine i pezzi. È tutto più bello e più leggero da quando ci sei.

Grazie a mia sorella Silvia, esempio di sempre. In silenzio e con estremo rispetto mi hai costantemente sostenuta e capita.

Infine, il più grande ringraziamento va ai miei genitori. Mamma, Papà, grazie per avermi supportata e sopportata durante questo periodo (siete voi i veri eroi di questo dottorato!). Mi avete sempre sostenuta in tutte le scelte finora fatte e sono certa che avrò sempre il vostro appoggio e la vostra comprensione qualsiasi strada deciderò di intraprendere.

Se sono arrivata fino a qui, lo devo soprattutto a voi.

Anna